Max-Planck-Institut
für Meteorologie

MAX-PLANCK-GESELLSCHAFT

International Max Planck Research School
on Earth System Modelling

Glacial Climate Variability

Florian Andreas Ziemen

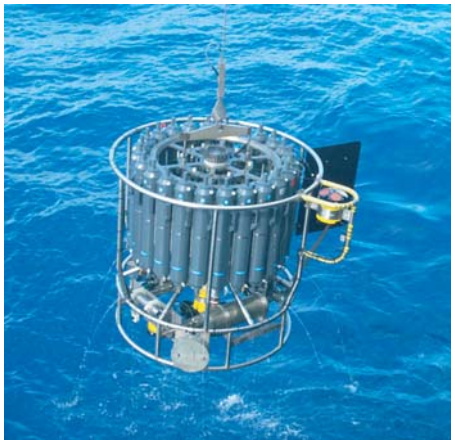

Berichte zur Erdsystemforschung 139
2013

Reports on Earth System Science

Hinweis

Die Berichte zur Erdsystemforschung werden vom Max-Planck-Institut für Meteorologie in Hamburg in unregelmäßiger Abfolge herausgegeben.

Sie enthalten wissenschaftliche und technische Beiträge, inklusive Dissertationen.

Die Beiträge geben nicht notwendigerweise die Auffassung des Instituts wieder.

Die "Berichte zur Erdsystemforschung" führen die vorherigen Reihen "Reports" und "Examensarbeiten" weiter.

Notice

The Reports on Earth System Science are published by the Max Planck Institute for Meteorology in Hamburg. They appear in irregular intervals.

They contain scientific and technical contributions, including Ph. D. theses.

The Reports do not necessarily reflect the opinion of the Institute.

The "Reports on Earth System Science" continue the former "Reports" and "Examensarbeiten" of the Max Planck Institute.

Anschrift / Address

Max-Planck-Institut für Meteorologie
Bundesstrasse 53
20146 Hamburg
Deutschland

Tel.: +49-(0)40-4 11 73-0
Fax: +49-(0)40-4 11 73-298
Web: www.mpimet.mpg.de

Layout:

Bettina Diallo, PR & Grafik

Titelfotos:
vorne:
Christian Klepp - Jochem Marotzke - Christian Klepp
hinten:
Clotilde Dubois - Christian Klepp - Katsumasa Tanaka

Berichte zur Erdsystemforschung 139/2013

Glacial Climate Variability

Florian Andreas Ziemen

aus Göttingen

Hamburg 2013

Reports on Earth System Science 139/2013

ISSN 1614-1199

Florian Andreas Ziemen
Max-Planck-Institut für Meteorologie
Bundesstrasse 53
20146 Hamburg

Als Dissertation angenommen
vom Department Geowissenschaften der Universität Hamburg

auf Grund der Gutachten von
Dr. Victor Brovkin
und
Dr. Uwe Mikolajewicz

Hamburg, den 29. Januar 2013
Prof. Dr. Jürgen Oßenbrügge
Leiter des Departments für Geowissenschaften

ISSN 1614-1199

Glacial Climate Variability

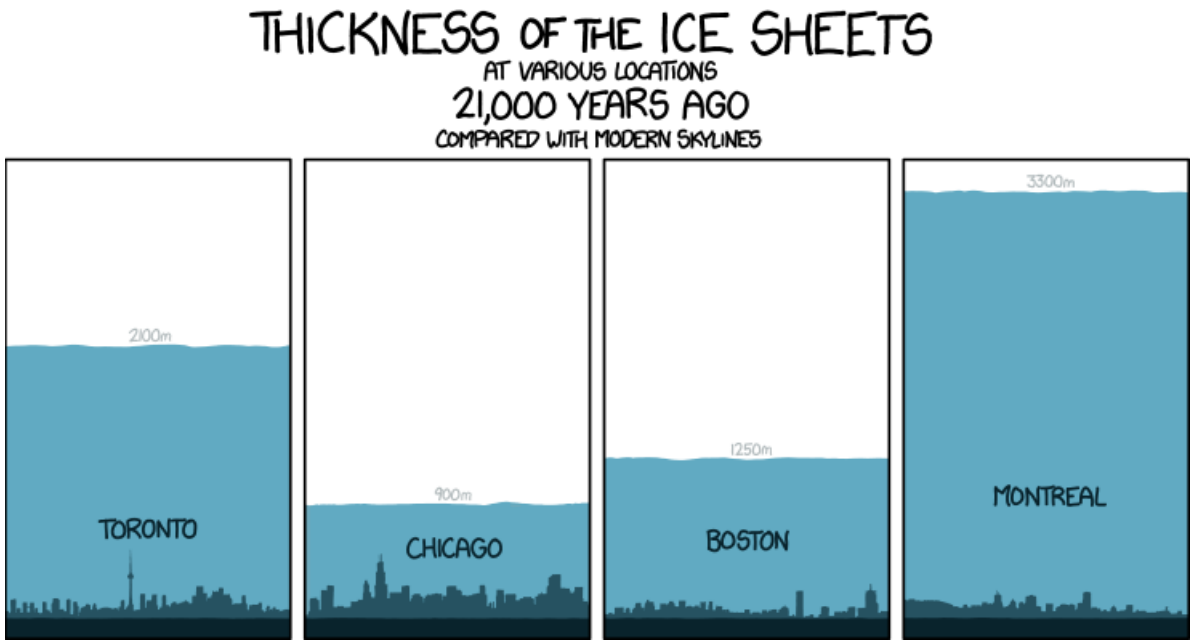

Image URL: http://xkcd.com/1225

Florian Andreas Ziemen

Hamburg 2013

All models are wrong, but some are useful.

George E. P. Box, 1979

Contents

List of Figures

Abstract

The topic of this study is the investigation of glacial climate variability with a coupled atmosphere–ocean general circulation model (AOGCM) – ice sheet model (ISM) system, focusing on one of the most prominent features of glacial climate variability, the Heinrich events. Modeling past climates and periods of past climate change is an important test of the capability of climate models to correctly represent future climate changes. Only if we can correctly represent past climates and climate changes, we can be confident about our predictions of future climate changes.

For this study, the Parallel Ice Sheet Model (PISM) was modified in order to prepare it for coupling to a climate model. The resulting model is called modified Parallel Ice Sheet Model (mPISM). It was coupled bidirectionally with the AOGCM ECHAM5/MPIOM/LPJ. ECHAM5 was run in T31 resolution ($\sim 3.75°$), MPIOM on a grid with a nominal resolution of 3° and poles over Greenland and Antarctica, mPISM on a Cartesian 20 km grid covering most of the northern hemisphere. The dynamical vegetation model LPJ uses the ECHAM5-grid and provides the vegetation for the computations in ECHAM5. In the models, as well as in the coupling, no flux correction or anomaly maps are applied. The ice sheet surface mass balance is computed using a positive degree day scheme with lapse rate correction and height desertification effect. The coupled system was validated by performing steady state experiments under last glacial maximum (LGM) and pre-industrial boundary conditions. In both cases, the results agree reasonably well with reconstructions and observations. This shows that the model system is able to adequately represent large climate perturbations that go well beyond the linear range.

The LGM simulations are not only the first coupled AOGCM–ISM LGM simulations so far, but they also are the first coupled AOGCM–ISM simulations where Heinrich event style surges occur as internal, model generated variability. In the model, several ice streams show repeated surges that are consequences of an internal instability mechanism suggested by MacAyeal (1993). The surges of the Hudson Strait Ice Stream reach discharge rates of 0.06 Sv and show a typical recurrence interval of 7 kyrs, matching the basic characteristics for Heinrich events inferred from proxy data.

The timescale of the repeat cycle is set by the time it takes surface accumulation to build up the ice sheets again after a surge. The surges initiate at the ocean boundary and propagate upstream, allowing for ocean-triggering and thus for an explanation for the occurrence of Heinrich events during the Dansgaard-Oeschger cold periods and for the observed synchronization of ice sheet discharges from different regions (e. g. Calov et al., 2002). The fact that no such triggering takes place in the simulations is, at least in parts, due to the lack of Dansgaard-Oeschger cycles in the coupled model, a general problem of modern AOGCMs (Valdes, 2011), but it is also due to the low sensitivity of the ice sheet model to ocean temperature changes.

The surges of the Hudson Strait Ice Stream cause changes in the climate system that are consistent with the proxy reconstructions for Heinrich events. The large ice discharge during a surge of the Hudson Strait Ice Stream causes an expansion of the sea ice cover. The freshwater, that is released when the ice melts, stabilizes the density stratification in the northern Atlantic. This weakens the north Atlantic deep water formation and the Antarctic Bottom Water cell strengthens. With the increase in sea ice cover and the decrease in deep water formation, the air temperatures over the northern Atlantic decrease. This cooling spreads downwind into Eurasia. The lower temperature and the increased sea ice cover cause a decrease in evaporation over the northern Atlantic and the Nordic Seas. This results in decreased precipitation over Eurasia and the forest cover over Eurasia decreases.

There are large scale surges in several parts of the ice sheets. They add long-term variability to the climate system by influencing the ocean circulation and the sea ice cover. The ice streams feeding into the Arctic Ocean dominate the variability of the sea ice discharge from the Arctic Ocean on decadal and longer timescales.

CHAPTER 1

Introduction

One of the key questions in future climate predictions is the evolution of the sea level. The ice sheets in Greenland and Antarctica store enough water to raise the global sea level by 63.9 m (Solomon et al., 2007). While at least Antarctica is not expected to melt completely, the contribution of the ice sheets to the global sea level rise is only poorly constrained and could sum up to several meters over the next centuries to millennia (e. g. Ridley et al., 2005; Vizcaíno et al., 2008; Bamber et al., 2009). Solomon et al. (2007, page 821) summarized: *Further accelerations in ice flow of the kind recently observed in some Greenland outlet glaciers and West Antarctic ice streams could increase the ice sheet contributions substantially, but quantitative projections cannot be made with confidence.* To predict the future sea level, it is crucial that we develop reliable coupled ice sheet – climate models.

From a European perspective, another key question regarding the future evolution of the climate system is the strength of the Atlantic Meridional Overturning Circulation (AMOC). It presently transports about 1.3 PW of heat northward across 26°N (Johns et al., 2011) and contributes strongly to the mild climate in Europe. Weaver et al. (2012) summarized that in the models participating in the Coupled Model Intercomparison Project Phase 5 (CMIP5), the AMOC weakens in the future with stronger changes for stronger greenhouse gas forcings. While all models show a weakening AMOC, they do not show a sudden collapse of the AMOC. Weaver et al. noted that none of the models in the CMIP5 comparison include the effects of the melting ice sheets. While the AMOC seems to have been stable in the Holocene, there is strong indication that during the last glacials the AMOC was not stable and fast changes of the AMOC caused strong, sudden climate changes (see Rahmstorf, 2002; Clement and Peterson, 2008 for reviews). According to our current understanding, these processes were strongly related to interactions of the atmosphere and oceans with ice sheets.

To gain confidence in our predictions of the future climate and the future interaction of ice sheets with the atmosphere–ocean system, it is necessary that we are able to correctly model the past periods with climates that are strongly different from the present-day climate and the past rapid climate change periods (Valdes, 2011; Braconnot et al., 2012). The last glacial is characterized by a climate that strongly differs from the present day climate and by rapid climate change events. Because the last glacial still is very recent from a geological perspective, the proxy coverage is comparatively good, so the model results can be compared to (albeit indirect) observations. The last glacial therefore is ideally suited for advancing our understanding of ice-climate interactions and putting ice sheet and climate models to the test.

1.1. Ice sheets

Ice sheets are continental scale ($> 50\,000\,\mathrm{km}^2$) ice bodies that move under their own weight. They gain mass by surface accumulation of precipitation and

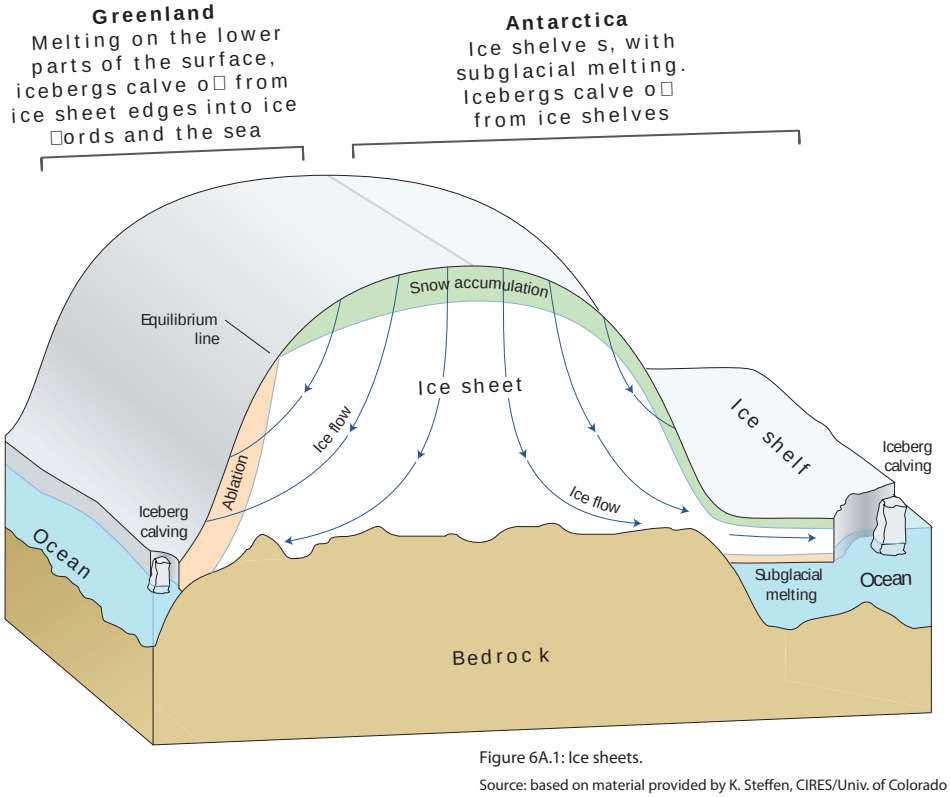

FIGURE 1.1. The most important processes in the present day ice sheets. Figure taken from Eamar et al. (2007)

lose mass by melt and by ice(berg) calving (fig. 1.1, see the textbooks by Paterson, 1994 and Benn and Evans, 2010). Presently, the only ice sheets on Earth are the Greenland Ice Sheet and the Antarctic Ice Sheet. During Glacials, further ice sheets covered large parts of North America, Scandinavia and northern Siberia (e. g. Peltier, 2004). Smaller ice masses that overlie the topography are called ice caps. Their even smaller relatives that are constrained by adjacent mountains are called glaciers.

Driven by its own weight, the ice moves from accumulation areas in the higher lying parts of a glacier or ice sheet to the low-lying margins. In most cases, the ice flow direction is determined by the surface gradient, in some regions of fast ice flow, membrane stresses inside the ice become dominant. The flow speed is controlled by a variety of factors, most notably the ice sheet thickness, the magnitude of the surface slope, the temperature distribution inside the ice, and, last but not least, sliding at the base of the ice sheet. This sliding can occur by sliding over a hard bedrock interface, or by deformation of subglacial sediments.

Snow that falls on the ice sheet slowly is compacted and turns into ice. Snow that has survived one summer melt season is called firn. It is considered ice, when the pore spaces between the snow grains become sealed off and air enclosed between the grains cannot move any longer. In Antarctica, where, in most parts, surface temperatures constantly are sub-freezing, this process can take thousands of years.

In the Vostok ice core the transition occurs at a depth of 95 m and a snow age of 2500 years (Barnola et al., 1987; Paterson, 1994). In areas with liquid precipitation or summer melt the transition from snow to ice occurs within a few years (Paterson, 1994). When rain falls on the surface of the ice sheet and the ice surface is sufficiently cold, the water can freeze on. This is most effective in snow, where the water is caught in the sponge-like matrix.

Ice is categorized based on its temperature as cold ice or temperate ice. Cold ice has a temperature below the pressure melting point and does not contain liquid water in the ice matrix. Temperate ice is at the pressure melting point and contains small amounts (up to a few percent) of liquid water in the ice matrix. In general, it is assumed that the viscosity of ice decreases exponentially with growing temperature (Paterson, 1994). When modeling temperate ice, it is possible to extend this into the temperate regime by using the combined enthalpy of ice and pore water (Aschwanden et al., 2012). This allows to seamlessly model the decreases in viscosity caused by the pore water.

At the surface of an ice sheet, the accumulation competes with ablation. When the air temperature exceeds the melting point, or when there is sufficient radiative heating, the snow at the surface melts and liquid water is released (see Hock, 2005 for a review). This water forms little rivers on top of the ice sheet that can cut into the ice and force their way to the base (Gulley et al., 2009). On its way down, the water can affect the ice sheet by warming and thus softening the ice adjacent to the channels (Phillips et al., 2010). Depending on the model used, studies with regional climate models show that between a third and half of the surface accumulation of the Greenland Ice Sheet melts before reaching the ocean (Ettema et al., 2009). The remainder flows into the ocean in outlet glaciers. In Antarctica practically all mass losses occur as iceberg calving and shelf basal melt (e. g. van de Berg et al., 2006; Rignot et al., 2008).

Regions in ice sheets, where the ice is sliding at the base and thus reaches high flow velocities are called ice streams. Basal sliding mainly occurs when the base of the ice sheet is temperate and there is water available to lubricate the flow (e. g. Lliboutry, 1968; Iken, 1981; Blankenship et al., 1986; Alley et al., 1986; Benn and Evans, 2010). While ice flow by internal deformation in an ice sheet usually stays in the range of a few meters per year, ice streams reach velocities of kilometers per year. They therefore strongly contribute to the ice discharge from ice sheets (see Rignot et al. (2008) for the velocities and drainage of the Antarctic Ice Sheet). This makes the representation of ice streams a key problem in ice sheet modeling.

The boundary between the ice sheet that is grounded on bedrock and the floating ice shelf is called the grounding line. While in the grounded ice sheet, the ice flow is slowed down by basal friction, the ice shelf is floating freely on the ocean, and thus only membrane stresses in the ice can act to slow down its spreading. These membrane stresses arise when the ice shelf (or the floating part of a glacier tongue) is in contact with lateral walls of an embayment (fig. 1.2) or is grounded locally on bedrock rises. The ice shelf acts as a plug, slows down the ice flow across the grounding line and thereby slows down the entire glacier or ice stream. This effect is called buttressing. For glaciers feeding into Larsen B Ice Shelf, Scambos et al. (2004) showed an up-stream increase in ice flow velocities following the breakup of the ice shelf. Similar effects have been observed at other outlets in Antarctica (Pritchard et al., 2012) and Greenland (Howat et al., 2005) when ocean melt thinned the ice shelves, respectively the floating tongues of outlet glaciers. The synchronous retreat of several southeast Greenland glaciers was linked to a

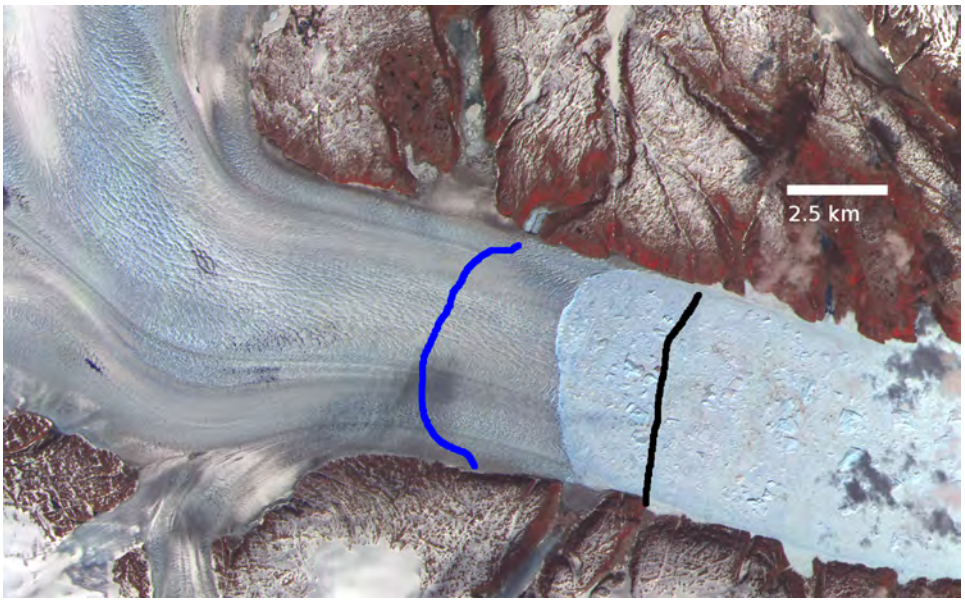

FIGURE 1.2. Helheim Glacier in southeast Greenland flowing from left to right. The photo was taken by the ASTER sensor on NASA's Terra satellite on July 7, 2003, the black line shows the glacier margin on May 12, 2001, the blue line shows the glacier margin on June 19, 2005. Image from `http://earthobservatory.nasa.gov/IOTD/view.php?id=6207`. See Howat et al. (2005)

brief period of enhanced access of warm Irminger Current water to the Greenland coast and, following from that, increased melting at the ice tongues of the glaciers. When the coastal waters cooled again, the glaciers slowed down again (Murray et al., 2010). Thus, the interaction between the ocean and the ice sheets is of prime importance for the prediction of the future ice sheet evolution and thus for the prediction of the sea level.

In an idealized, two-dimensional ice sheet extending infinitely in one horizontal direction, the buttressing effect is missing. In such a setup, the ice flow across the grounding line increases with the ice thickness at the grounding line. Weertman (1974) showed the instability of a two-dimensional ice sheet on a retrograde sloping bed, as it is the case for the West Antarctic Ice Sheet (WAIS). Since then, the question whether the WAIS is susceptible to a runaway collapse is an important question in Glaciology (e. g. Schoof, 2007). This question becomes even more important since we observe increasing shelf basal melt at Antarctica, and with it speed-ups of the glaciers feeding into the shelves (Pritchard et al., 2012). Furthermore, climate models predict an increase in shelf basal melt due to changing ocean currents for the future (Hellmer et al., 2012). Recent works by Gudmundsson et al. (2012) and Gudmundsson (2013) showed that in three-dimensions ice sheets can be stable on retrograde sloping beds, so the future of the WAIS remains unknown and models that have proven to correctly reproduce past ice-ocean interaction and ice sheet collapse events are needed.

1.2. Ice sheet models

Modeling ice sheets consists of solving the coupled thermomechanical problem inside the ice sheet and modeling the evolution of the boundary conditions at the ice sheet surface, the base and the lateral margins.

For each of these problems models with varying degree of sophistication exist. Simple models can model the evolution of Antarctica over millions of years (e. g. Pollard and DeConto, 2009), while complex models are used for modeling one time slice of a single outlet Glacier (e. g. Morlighem et al., 2010).

Depending on the time interval covered in a simulation, different methods are used to determine the surface mass balance ranging from empirical parametrizations based on latitude and height (Pollard and DeConto, 2009) to fully coupled AOGCM–ISM simulations with energy balance schemes operating on the six-hourly AOGCM output downscaled to the highly resolved ISM grid (Vizcaíno et al., 2010). More details on coupled models are given in section 1.6.

Inside the ice sheet, the ice flow is a coupled thermomechanical problem with non-newtonian rheology. The momentum balance in the Navier Stokes equation becomes a force balance by neglecting the time derivatives. The Coriolis force, that is important in atmosphere and ocean dynamics, is neglected too. The remaining equation is called the Full-Stokes equation (all terms in (1)). The divergence of the deviatoric stress tensor ($\nabla \cdot \tau$, left-hand side) balances the pressure gradient (∇p, right hand side) and gravitational force (ρg, right hand side). Full-Stokes models solve this equation but are computationally very expensive and usually only used to model single outlet glaciers. In so-called Higher Order (Blatter-Pattyn) Models (Blatter, 1995; Pattyn, 2003), only the gray terms in (1) are neglected. These models can nowadays be used in multi-millennial simulations of the Greenland Ice Sheet (e. g. Fürst et al., 2013). In most parts of the interior of an ice sheet, the ice is frozen to the base or the base is so rough that the ice can not slide over it. The driving stress is balanced locally. Therefore all membrane stresses can be neglected, and the stress balance in the ice is a purely local problem. This case is dealt with in the so-called shallow ice approximation (SIA), consisting of the red and black terms in (1) (Hutter, 1982). In contrast, in ice shelves and glaciers, the ice slides over its base and the vertical shear of the horizontal velocity can be neglected. The ice flow can be dealt with as a two-dimensional plug-flow problem and is described using the shallow shelf approximation (SSA, blue and black terms of (1), Hutter, 1982; MacAyeal, 1989).

$$
\begin{array}{ccccccccc}
\frac{\partial}{\partial x}\tau_{xx} & + & \frac{\partial}{\partial y}\tau_{xy} & + & \frac{\partial}{\partial z}\tau_{xz} & = & \frac{\partial}{\partial x}p & & \\
\frac{\partial}{\partial x}\tau_{xy} & + & \frac{\partial}{\partial y}\tau_{yy} & + & \frac{\partial}{\partial z}\tau_{yz} & = & \frac{\partial}{\partial y}p & & \\
\frac{\partial}{\partial x}\tau_{xz} & + & \frac{\partial}{\partial y}\tau_{yz} & + & \frac{\partial}{\partial z}\tau_{zz} & = & \frac{\partial}{\partial z}p & + & \rho g
\end{array} \tag{1}
$$

Schoof (2006) showed that the domains of SIA and SSA have practically no overlap in ice sheets and therefore the two approximations can be combined in one model. This is done in the Parallel Ice Sheet Model (PISM) (Bueler and Brown, 2009; Winkelmann et al., 2011; the PISM authors, 2013). A standard way to model the relationship between stress τ and strain rate $\dot{\varepsilon}$ is the use of Glen's flow law

$$
\dot{\varepsilon} = A(T)\tau_{II}^{(n-1)/2}\tau \tag{2}
$$

with $\tau_{II} = \frac{1}{2}\sum_{i,j}\tau_{ij}^2$ as second invariant of the stress tensor. The exponent n is usually assumed to be 3. The temperature dependence is commonly modelled using

an Arrhenius-type law

$$A(T) = A_0 \exp\left(-\frac{Q}{RT}\right) , \tag{3}$$

with A_0 being a constant in $\mathrm{Pa}^{-\mathrm{n}}/\mathrm{yr}$, and the Q activation energy (J/mol) and R the gas constant (J/mol/K).

Ice sheet models that can handle both cold and temperate ice are called polythermal. PISM uses the ice enthalpy instead of the temperature and thus can model cold and temperate ice without explicitly tracking the boundary between cold and temperate ice as it is done in the widely used polythermal ice sheet model SICOPOLIS (Greve, 1997).

The basal melt of ice shelves is usually prescribed, or uses simple parametrizations based on nearby ocean temperatures (e. g. Álvarez Solas et al., 2011), since there are only few observations (Jenkins et al., 2010) and correctly modeling the flow below ice sheets is very challenging because it requires (a) a very high model resolution, (b) knowledge of the seafloor topography and the base of the ice sheet on a high resolution, and (c) an ocean model that can handle the ice shelf as a boundary. While (a) and (b) are general modeling problems where some compromises can be made, (c) rules out most global ocean models. One exception is FESOM (Timmermann et al., 2009; Hellmer et al., 2012), the ocean model of the Alfred Wegener Institute for Polar and Marine Research (AWI). There are regional models ocean models that can handle ice shelves (e. g. Holland et al., 2008; Hellmer et al., 2012). A coupled ice-shelf ocean model study for an idealized geometry is presented in Goldberg et al. (2012a,b).

On the land, the isostatic response of the bedrock to the weight of the ice has to be taken into account. We still observe local sea level lowering in Canada and Scandinavia because of the post-glacial rebound from the last ice age. There are various ways of representing the properties of the lithosphere and the underlying Asthenosphere (Le Meur and Huybrechts, 1996). A common method in glaciology is to use a local rebound model with a rebound timescale of 3000 years, called Local Lithosphere, Relaxed Asthenosphere (LLRA) in Le Meur and Huybrechts (1996). This is the method we chose in our experiments.

1.3. The climate of the Last Glacial Maximum

About 2.5 million years ago, the first large ice sheets formed in the northern hemisphere. Since then, there was cyclic growth and decay of large-scale ice sheets, first with a dominant period of 41 kyrs. In the last ~ 1.2 Mio years the duration of the ice age cycles varied between 80 and 120 kyrs with a dominant period of 100 kyrs, matching the different periods of the Milanković cycles of insolation (Milanković, 1941; Clark et al., 1999). The concentration in greenhouse gases covaried with the growth and decay of the ice sheets with low greenhouse gas concentrations during times of large ice sheets, and high greenhouse gas concentrations during the interglacials (fig. 1.3). The last glacial ice sheets started growing about 116 kyrs ago (Waelbroeck et al., 2002). They reached a maximum volume about 21 kyrs ago during the Last Glacial Maximum (LGM) followed by a deglaciation between 20 kyrs ago and 7 kyrs ago (Denton et al., 2010). The shape of the ice sheets up to the LGM is only poorly constrained, since many proxies can only show when an area was ice-free again (Kleman et al., 2010). The deglaciation is much better covered (Stokes and Tarasov, 2010).

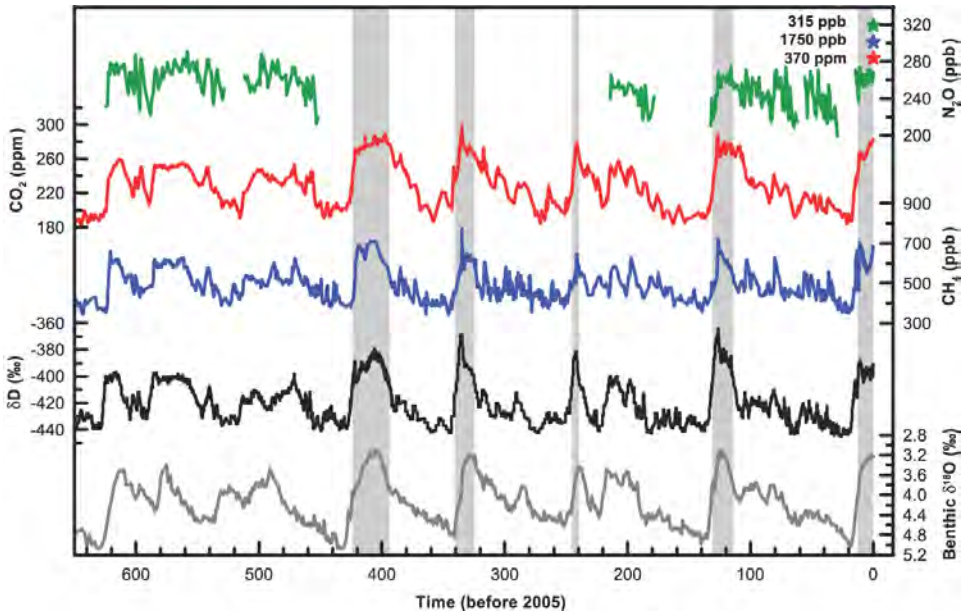

FIGURE 1.3. Variations of deuterium (δD; black), a proxy for local temperature, and the atmospheric concentrations of the greenhouse gases CO_2 (red), CH_4 (blue), and (N_2O; green) derived from air trapped within ice cores from Antarctica and from recent atmospheric measurements The stack of 57 globally distributed benthic δ^{18}O marine records (dark grey), a proxy for global ice volume fluctuations (Lisiecki and Raymo, 2005), is displayed for comparison with the ice core data. Downward trends in the benthic δ^{18}O curve reflect increasing ice volumes on land. Note that the shaded vertical bars are based on the ice core age model (EPICA Community Members, 2004), and that the marine record is plotted on its original time scale based on tuning to the orbital parameters (Lisiecki and Raymo, 2005). The stars and labels indicate atmospheric concentrations at year 2000. Figure taken from Solomon et al. (2007, Fig. 6.3), the caption was shortened.

The climate of the LGM was strongly shaped by the low greenhouse gas concentrations (fig. 1.3) and the large ice sheets (see figs. 3.9, 3.15, and 3.16 for reconstructions) covering present-day Canada (Laurentide Ice Sheet, the part covering the Canadian Arctic Archipelago is also called Innuitian Ice Sheet), Fennoscandinavia and the Barents Sea (Fennoscandian Ice Sheet). The Antarctic Ice Sheet also increased in volume during this period. The water stored in the ice sheets caused a sea level decrease by about 120 m (Peltier, 2002; Solomon et al., 2007). The low greenhouse gas concentration caused a global cooling and accounts for about half of the temperature difference between the pre-industrial and the LGM climate (Otto-Bliesner et al., 2006). The high altitude and albedo of the ice sheets led to a strong amplification of the cooling in the northern hemisphere (Abe-Ouchi et al., 2007). With the cooling came a decrease in precipitation. The forests on the northern hemisphere retreated southward and gave room to steppes (Prentice et al., 2000).

There is general agreement that the North Atlantic Deepwater (NADW) cell during the LGM was shallower than it is today. Because of its shallowness, this cell is often called Glacial North Atlantic Intermediate Water (GNAIW) cell (Lynch-Stieglitz et al., 2007). We will call it NADW cell in the following, since it corresponds to the NADW cell, and, in our simulations, is very similar to the present day NADW cell. While in a review article (Lynch-Stieglitz et al., 2007) came to the

conclusion, that the NADW cell was *neither extremely sluggish, nor an enhanced version of the present-day circulation*, even this basic statement is not consensus. Lippold et al. (2012) analyzed the ratio between ^{231}Pa and ^{230}Th in sediment cores from the Atlantic, and, using a zonally averaging forward proxy model, concluded that the NADW formation during the LGM was shallower than the present-day NADW formation, but stronger. They obtained optimal model-data fits for values between 22 and 30 Sv, compared to present-day values of 18.7 ± 2 Sv at 26.5°N (Kanzow et al., 2010). To test the behavior of climate models in this respect, as part of the Paleoclimate Modelling Intercomparison Project Phase II (PMIP 2, Crucifix et al., 2005), several climate models were forced with LGM boundary conditions and their NADW cell strength was compared (Weber et al., 2007). Some of the models in this comparison showed an increase in NADW cell strength while others showed a decrease. In ocean-only GCM experiments, with varying boundary conditions, Oka et al. (2012) analyzed the effect of the surface forcing on the NADW strength. They tested linear combinations of present-day and glacial maximum boundary conditions. In their experiments, the NADW cell strengthened for a moderate cooling. For a stronger cooling, the NADW cell reached a maximum and with further cooling switched into a weak mode. Depending on the other boundary conditions, this switching occurred for intermediate, or colder-than-glacial boundary conditions, indicating that coupled models that show a stronger NADW cell under LGM boundary conditions could show a weaker NADW cell for *colder* forcings. On the other hand, ocean-only models are known to show an overly strong switching behavior (Weaver et al., 1991; Zhang et al., 1993; Marotzke, 2012). While the NADW cell shallowed during the LGM, the Antarctic Bottom Water (AABW) cell increased in strength (Duplessy et al., 1988; Lynch-Stieglitz et al., 2007; Negre et al., 2010).

The glacial was not a smooth cooling up to the LGM and then a smooth warming back to present day conditions, but showed massive rapid climate change events. During the Dansgaard-Oeschger events, Greenland air temperatures increased by up to 10 K within a few decades (Dansgaard et al., 1984, 1993; see Clement and Peterson, 2008 for a recent review). This rapid warming was followed by a slow cooling over the next centuries. Dansgaard-Oeschger events recurred quasi-periodically with a repeat period of about 1500 years. The cold periods are called stadials, the warm periods are called interstadials. The events were not only recorded in Greenland but can be traced all over the globe. They commonly are linked to rapid reorganizations of the AMOC. Similar climate features have been created in Earth System Models of Intermediate Complexity (EMICs, Claussen et al., 2002) by prescribing alternating freshwater flux anomalies over the northern Atlantic (Ganopolski and Rahmstorf, 2001), but have not yet been observed as internal variability of climate models. Up to now, no modern AOGCM has shown such switching behavior. During some of the stadials, large amounts of ice rafted debris were deposited on the Atlantic seafloor. The events during which these layers were deposited are called Heinrich events.

1.4. Heinrich events

Heinrich events are climate change events that occurred quasi-periodically during glacials (e. g. Rahmstorf, 2002; Marshall and Koutnik, 2006; Clement and Peterson, 2008, for overview articles). Their duration is estimated anywhere between centuries and millennia. They are named after Hartmut Heinrich, who found sediment layers containing ice rafted debris (IRD) and cold-dwelling planktic foraminifera in

sediment cores from off the Iberian coast of the Atlantic. The increase in ice rafting and the cold surface water conditions were related to a strong reduction of the NADW formation that led to global climate changes. During the last glacial, six of these events occurred. They are commonly named H1–H6 with H1 as the youngest event. Hemming (2004) listed their ages as 16 800, 24 000 ∼31 000, 38 000, 45 000, and ∼60 000 years before present. The Younger Dryas event (13 000–11 500 years before present; Carlson et al. (2007)) sometimes is considered as seventh Heinrich event (H0).

While Heinrich (1988) dated the IRD layers to be matching the precessional cycles, later research indicated them to occur at multiples of 7000 years (Broecker et al., 1992; Bond et al., 1992; Grousset et al., 1993; Hemming, 2004; Clement and Peterson, 2008). Chemical analyses of the sediments and analyses of the thickness distribution of these sediment show that they mainly stem from the Hudson Strait Ice Stream. Recent analyses found contributions of several other ice stream systems, such as the McClure Strait Ice Stream (Stokes et al., 2005), Mackenzie and the Amundsen Gulf Ice Streams (all draining the Laurentide Ice Sheet into the Arctic ocean, see fig. 3.14(a)), and the Innuitian Ice Sheet covering the Canadian Arctic Arcipelago (Darby and Zimmerman, 2008), the British Islands Ice Sheet and the Fennoscandian Ice Sheet as well as from the Iceland and Greenland Ice Sheets (Peck et al., 2006). Hemming (2004) provides a thorough review of the compositions of the Heinrich layers, Stanford et al. (2011) detail on the sequence of events during HE1.

In 1993, Douglas R. MacAyeal proposed the Heinrich events to be the result of internal oscillations of the Laurentide Ice Sheet (MacAyeal, 1993). In his model, the Laurentide Ice Sheet grows until the insulating effect of the ice sheet together with the geothermal heat flux and shear heating in the ice cause the base of the ice sheet to melt and thereby create a sub-glacial layer of liquid water. In areas where the ice sheet base consists of sediments, an ice stream forms. The ice stream drains the ice sheet more efficiently and thereby lowers the ice sheet surface, creating a steeper temperature gradient between the base and the ice sheet surface. The drainage of the ice sheet and the basal melting advect cold ice downward. Together with the steepened thermal gradient, this cools the base of the ice sheet, so it refreezes and the ice sheet builds up again.

MacAyeal (1993) analyzed the binge-purge oscillations in an analytical model. The same concept was proved to work in a fully 3-D setup by the work of Calov et al. (2002), who showed that the combination of the ISM SICOPOLIS and the EMIC CLIMBER can generate quasi-periodic collapse events that match the basic requirements from proxy interpretations. They obtained surge repeat intervals of about 7000 years with surges lasting for centuries and discharging 5–10 m sea level equivalent of ice. They furthermore showed that their model is sensitive to triggering at the mouth of the Hudson strait and thus provides the basis for a mechanism that triggers surges during the Dansgaard-Oeschger cold periods and for synchronization of different ice streams through teleconnections.

One problem with the MacAyeal (1993)-model is that it does on its own not explain for the occurence of Heinrich events during Dansgaard-Oeschger stadials, nor for the synchronous surges of several different parts of the ice sheets. Christina L. Hulbe proposed two mechanisms based on ice shelves. In Hulbe (1997) she proposed a mechanism with constant discharge from the ice sheet. During the cold stadials, basal freeze-on on the ice shelf allows sediments to get enclosed in ice and then transported over larger distances. During the warmings following the Heinrich

events, the ice shelf would retreat again. This model has the advantage, that it explains the occurence of Heinrich layers during the stadials, but also has clear weaknesses. One is that it does not explain for sea level rises found to have occured during the Heinrich events (e. g. Chappell, 2002; Marshall and Koutnik, 2006). Although the error bars on the sea level rise estimates are of the same magnitude as the estimates, Hulbe (1997) has not found much support in the Heinrich event community and consequentially does not appear in the reviews by Marshall and Koutnik (2006) or Clement and Peterson (2008).

After the breakup of Larsen B, Hulbe et al. (2004) suggested an analogous ice-shelf breakup as cause of Heinrich events, but still maintained the ice sheet itself as stable. Again, an ice shelf would obviously be voulnerable to ocean forcings, making it easier to explain for the occurence of Heinrich events during stadials and for synchrounous timing of different ice rafted debris sources. Alley (2005) comment on this publication and explain their doubts against the model on several lines, including the occurence of planktonic foraminifera in the Labrador sea at the onset of Heinrich events. They point out their previous publications that suggest possibilities for triggering of a *loaded* MacAyeal (1993)-style oscillator. As mentioned before, this problem was also tackled successfully in Calov et al. (2002).

Álvarez Solas et al. (2010, 2011) picked up on Hulbe et al. (2004), but instead of keeping the ice sheet discharge constant, they proposed that the waxing and waining of a massive Labrador Sea Ice Shelf modulated the discharge from the Hudson Strait Ice Stream. The waxing and waining of the ice shelf is controlled by the shelf basal melt, which in turn is controlled by the ocean sub-surface temperature. The sub-surface ocean temperature is strongly influenced by the stability of the vertical stratification in the northern Atlantic, which is to a large degree controlled by the freshwater fluxes into the northern Atlantic. For HE1, Álvarez Solas et al. (2011) suggested that the deglacial melting of the Fennoscandian Ice Sheet provided a freshwater flux that was strong enough to stabilize the layering in the northern Atlantic and thus to cause a sub-surface warming. The warm sub-surface water would then remove the hypothesized Labrador Sea Ice Shelf and allow the Hudson Strait Ice Stream to flush the Hudson Bay into the Northern Atlantic. They support their hypothesis with simulations where the ice sheet model GRISLI is forced with results from the EMIC CLIMBER3α. By adjusting the surface windstress, CLIMBER3α was brought into a bistable regime, where moderate changes in the surface freshwater fluxes are able to force the model to transition between a state with active deepwater formation in the northern Atlantic and cold sub-surface conditions on the one hand, and a state with a stable stratification and warm sub-surface conditions on the other hand. These two states were then used as a forcing for GRISLI. With the cold sub-surface conditions, a massive ice shelf built up in the Labrador sea that reached over to Greenland with a thickness exceeding 500 m and pushed back on the Hudson Strait Ice Stream. When the boundary condition was switched to the warm sub-surface temperature the ice shelf disintegrated and the Hudson Strait Ice Stream sped up.

Barker et al. (2010) analyzed benthic foraminifera from the southern Atlantic. They found signals for an exceptionally deep NADW cell after HE1 and HE4, indicating a strong NADW formation that overshot after the Heinrich events. This matches with the exceptionally strong Dansgaard-Oeschger warmings following Heinrich events.

1.5. Freshwater hosing experiments

Before Heinrich events were found, the Younger Dryas event was known and its origin was related to massive freshwater discharges into the Atlantic ocean. This led to a series of experiments that investigated the bistability of the AMOC, its sensitivity to freshwater forcings and the consequences of an AMOC shutdown in the climate system. The experiments where an additional freshwater is applied to an ocean model became known as *(freshwater) hosing experiments*. In the following we briefly outline the research that led to this concept and the history of freshwater hosing experiments.

Manley (1965) analyzed European climate proxies and linked the Younger Dryas cold event to increased *pack-ice, drift-ice and cold water in the North Atlantic* (page 364) and *the onset of a vigorous zonal type of meteorological circulation, with its associated eastward displacement of the prevailing Icelandic low and with this a fall of the average summer temperature [...]* (page 365). Mercer (1969) picked up on these findings and *suggested that a sudden increase in the North Atlantic ice occurred when ice shelves that had formed in full-glacial time in the Arctic ocean, and probably in the northern Norwegian Sea also, began to disintegrate* (page 229).

Based on Mercer (1969), and the works by Stommel (1961) and Rooth (1982) who showed and analyzed the possibility of multiple steady states of the Atlantic Meridional Overturning Circulation (AMOC) in box models, and on a suggestion by Oeschger, that the oscillations found in Greenland ice cores (and later named Dansgaard-Oeschger cycles) were caused by cycling between *two modes of ocean-atmosphere-biosphere-cryosphere operation* (Broecker et al., 1985, page 25). Broecker et al. (1985) suggested that the climate oscillations in the Atlantic region are caused by an oscillation of the AMOC. They suggested that the normal and reversed mode of Stommel's box model correspond to the present day and a glacial AMOC, and that the Dansgaard-Oeschger cycles were caused by cycling between these two modes. Their proposed mechanism for this cycling involved the AMOC and the ice sheets at the Atlantic coasts. In its active mode, the AMOC transports large amounts of heat northward. They suggested that this heat melted the adjacent ice sheets and thereby caused a freshwater release that weakened the AMOC. The subsequent cooling reduced the ice sheet melt and allowed the ice sheets to recover. The reduced melt in turn allowed the AMOC to recover and the cycle started over again.

Bryan (1986) put the box model of Rooth (1982) to the test in an OGCM experiment with an idealized, 60° wide and 5000 m deep ocean basin. He found stable solutions for a symmetric and for an asymmetric ocean circulation depending on the initial salinity distribution. The experiment still suffered from the idealized geometry, the missing feedback between temperature and evaporation and the lack of an atmosphere model.

Manabe and Stouffer (1988) found two stable AMOC states in their coupled AOGCM. Started from two different sets of initial conditions, their model either showed an active or a collapsed AMOC. The experiment with the collapsed AMOC state showed a northern hemisphere cooling relative to the experiment with the active AMOC state. This cooling basically agrees with the proxy reconstructions of the Younger Dryas cold event.

Maier-Reimer and Mikolajewicz (1989) studied the amount of freshwater input into their OGCM necessary to shut off the AMOC. They showed that the ice sheet melt fluxes associated with the deglaciation would be strong enough to have caused

the Younger Dryas cold period. In their study, they varied the amount of freshwater released between 0.007 Sv and 0.6 Sv and tested three locations for the freshwater release (a) the St. Lawrence River, (b) the Mississippi and (c) a combination of St. Lawrence, Mississippi and the Norwegian sea. In (c), a 0.6 Sv forcing was applied and the thermohaline circulation collapsed within 10 years. The other freshwater releases were smaller but most of them were strong enough to severely reduce the northward heat transport. The ocean responded faster and more sensitive to freshwater releases at the St. Lawrence river than to releases at the Mississippi.

While Maier-Reimer and Mikolajewicz (1989) experimented with different time-constant freshwater forcings, the potential for multistability of the ocean circulation under the same forcing was shown by Mikolajewicz et al. (1993). To construct a climate forcing, they used the OGCM LSG to diagnose freshwater fluxes in an experiment with temperature and salinity restoring to present day values. When forced with temperature restoring and the diagnosed freshwater fluxes, LSG showed three different, stable ocean circulation states, (1) an *on* state, similar to the present day ocean circulation, (2) a *reduced* state with weak NADW formation and and stronger AABW formation than in the *on* state, and (3) an *off* state without NADW formation, similar to the present day Pacific Ocean.

In a simplified geometry setup with a parametrized atmosphere Rahmstorf (1994) obtained different NADW states in an OGCM for an identical surface forcing and was able to transition between them by applying freshwater forcings. The strength of the AMOC remained constant between the different states, while there was a shift in deep water formation areas and depth of the NADW cell. A southward shift of the NADW formation caused cooling in the north and a reduced heat transport in the NADW cell because the sinking water was warmer than in the case with high-latitude sinking.

Similar hysteresis behavior with regard to the freshwater forcing in the OGCM LSG was shown by Mikolajewicz and Maier-Reimer (1994). They furthermore demonstrated the strong influence of the formulation of the surface boundary condition on the stability of the AMOC in the model.

Several further experiments followed and the freshwater hosing experiments became part of the Coupled Model Intercomparison Project (CMIP). An overview of the results is given in Stouffer et al. (2006). They describe the results of standardized freshwater hosing experiments under pre-industrial boundary conditions with 9 AOGCMs and 4 EMICs. For all models a forcing corresponding to 0.1 Sv freshwater input was applied over the northern Atlantic between 50°N and 70°N for 100 years. Then the model was let to recover for another 100 years. In all models the NADW cell weakened. The weakening was strongly model-dependent and varied between 6% and 62% with an average of 30%. Some models showed a cooling over the Nordic seas, while others showed a northward shift of the deep convection areas with an associated warming over the Nordic Seas.

A synthesis of recent hosing experiments where a freshwater discharge of 0.1 Sv is distributed around Greenland to represent a future Greenland Ice Sheet melt is presented in Swingedouw et al. (2012). All models show a reduction in NADW strength within 40 years with changes ranging from about 0.5 to about 4.5 Sv. The strength of the reduction is correlated to the amount of freshwater leaking from the Subpolar Gyre into the Subtropical Gyre, with stronger leakage corresponding to less AMOC reduction.

There is a growing number of freshwater hosing experiments under LGM boundary conditions. Prange et al. (2002) performed OGCM experiments under glacial

boundary conditions in search for multiple steady states. They found that the glacial Atlantic meridional overturning circulation was monostable under the forcing derived from an AGCM simulation with ECHAM3, but had a small bifurcation zone for higher freshwater inputs. From their experiments, they concluded that during the deglaciation, a relatively small freshwater perturbation would be able to push the AMOC from its strong branch into the weak branch.

In an EMIC study, Wang and Mysak (2006) found two modes of the NADW formation. A strong mode, that was predominantly driven by the heat release effect on density and a weak mode that was predominantly driven by the brine rejection during sea ice formation.

Bitz et al. (2007) freshened the north Atlantic under pre-industrial, glacial, and $4\,\mathrm{x}\,\mathrm{CO}_2$ conditions down to a depth of 920 m with an average freshening of 2 psu and found that the recovery was fastest in the pre-industrial state and slowest in the glacial state. They concluded that the increased sea-ice cover in the glacial case was responsible for the slow recovery by cutting the heat fluxes over the deep water formation areas and by providing an additional freshening once deep water welled up and melted the ice.

Hu et al. (2008) studied the recovery times for hosing experiments with an open and a closed Bering Strait and found that the Bering Strait stabilized the AMOC in hosing scenarios by allowing for a net freshwater export from the Arctic Ocean into the Pacific. The open Bering Strait thus provides negative feedback for changes in Atlantic salinity and AMOC. Since the Bering Strait was closed for large parts of the last glacial, they speculated that the closed Bering Strait could have contributed to the Dansgaard-Oeschger and Heinrich events.

Otto-Bliesner and Brady (2010) investigated the influence of different freshwater input locations, strengths and durations on the climate in LGM simulations with CCSM3. As Maier-Reimer and Mikolajewicz (1989), they found that the climate system responded slower and less sensitive to a freshwater forcing in the Gulf of Mexico than to a forcing that is directly applied to the North Atlantic. A larger set of LGM hosing experiments is summarized in Kageyama et al. (2013). They analyzed an *ensemble of opportunity* where six climate models of different complexity were forced with different freshwater forcings under LGM boundary conditions. All models responded with a reduced NADW strength with reductions ranging from 5 Sv to 25 Sv, corresponding to relative anomalies of 20% to 95%. While weak forcings of 0.1 Sv caused a wide range of responses, the strong forcings consistently caused strong responses.

Kageyama et al. (2010) reviewed the state of modeling of Dansgaard-Oeschger and Heinrich events and provided a detailed overview of the existing freshwater hosing experiments under present day as well LGM boundary conditions, including the question of AMOC bistability and hysteresis. While several EMICs showed hysteresis behavior in the AMOC with relationship to freshwater forcings (Rahmstorf et al., 2005), up to 2010 no AOGCM had shown this behavior. (Hawkins et al., 2011) performed a set of freshwater hosing experiment with the low-resolution AOGCM FAMOUS. They found that the model showed hysteresis behavior for a narrow band (0.07 Sv) of freshwater forcings. This is the first published modern AOGCM simulation that showed an AMOC hysteresis. Furthermore, in their study, the net salt transport across the southern boundary of the Atlantic ocean was an indicator for the stability of the on-state of the AMOC, as suggested by Rahmstorf (1996), and shown in EMIC and ocean-only studies (de Vries and Weber, 2005; Marsh et al., 2007).

Among the modern AOGCMs there is a mixed picture with respect to the freshwater import at the southern boundary of the Atlantic. 12 of 25 CMIP5 models show negative freshwater imports in at least some of the emission scenarios (Weaver et al., 2012). In reality the freshwater balance is supposed to be negative (Pardaens et al., 2003; Huisman et al., 2010; Hawkins et al., 2011).

1.6. Coupled ice sheet – climate model experiments

An overview of coupled ice sheet – climate modeling is provided in Pollard (2010). The main challenge in this field is that the time scales of ice sheets are very long (millennia to hundreds of millennia) and most of the snowfall and melt occurs in a narrow band at the ice sheet margin. In principle, the margin zone calls for high-resolution modeling, while the long time scales make this impossible.

The importance of the forcing strategy for ice sheet simulations was nicely shown by Langen et al. (2012). They studied the effects of different strategies on the regrowth of a removed Greenland Ice Sheet under present-day conditions. Depending on the forcing strategy, they obtained a more or less complete regrowth of the Greenland Ice Sheet, reproducing several previous contradicting publications. Coupling the models once at an intermediate stage of the regrowth led to a substantially smaller Greenland Ice Sheet than the experiments with constant forcing.

The discrepancy between the need for high resolution modeling and long time spans leads to a variety of strategies. Some groups use simple models (EBMs or EMICs) to compute anomalies between the present day and the target climate and apply these anomalies to present day temperatures and precipitation (Tarasov and Peltier, 1997; Pollard and DeConto, 2009). Another way of using an EMIC consists in downscaling the fields obtained from the EMIC in an intermediate energy balance, or energy-moisture balance model. This is done in the group around Reinhard Calov and Andrey Ganopolski at the Potstam Institute for Climate Impact Research (PIK) (Calov et al., 2002, 2005a; Robinson et al., 2010). This combines the speed of an EMIC with a reasonably realistic representation of the surface mass balance. In Calov et al. (2002), the first coupled LGM simulation with Heinrich event style ice sheet collapses are presented. In this setup, the coupling is only done via the atmosphere, so the model cannot show the ocean response to freshwater forcings. The response of the ocean to freshwater fluxes had previously been investigated with CLIMBER in Ganopolski and Rahmstorf (2001). The next great challenge was the coupled modeling of the glacial inception presented in Calov et al. (2005a,b), and following from that full glacial cycles (Ganopolski et al., 2010; Ganopolski and Calov, 2011). Other groups perform similar experiments (Wang and Mysak, 2002; Kageyama et al., 2004; Fyke et al., 2011).

GCMs can be used in long-term simulations when an asynchronous coupling is implemented. In such simulations, the climate model is run repeatedly for intervals of one to 50 years, and then the climate is used to drive the ice sheet for a substantially longer time span. The resulting ice sheet is fed back into the climate model (Pollard et al., 1990; Ridley et al., 2005). Since the ice sheets change comparatively slow, the climate remains in a quasi-equilibrium with the ice sheets. The asynchronous coupling becomes problematic, when the climate model includes an ocean component, since the ocean has a timescale between atmosphere and ice sheets. One option in this case is to run ocean and ice sheets synchronously coupled and couple the atmosphere asynchronously (e. g. Mikolajewicz et al., 2007b).

A series of studies use coupled AOGCM ice sheet model systems to investigate the future development of the Greenland Ice Sheet and its impact on the AMOC.

Early studies (Huybrechts et al., 2002; Fichefet et al., 2003) only fed back the freshwater fluxes but kept the Greenland topography constant in the AOGCM. The first study with a full bidirectional coupling between an AOGCM and an ice sheet model was performed by Ridley et al. (2005). It was followed by studies by Mikolajewicz et al. (2007b,a); Vizcaíno et al. (2008, 2010) that also include the Antarctic Ice Sheet. The experiments presented in Mikolajewicz et al. (2007b) and Vizcaíno et al. (2010) were the first AOGCM–ISM studies to use an energy balance model for the surface mass balance of the ice sheet and the first to operate without anomaly maps. This was a substantial improvement in the physical representation of the coupling. A recent study by Gregory et al. (2012) used the AOGCM FAMOUS, a fast version of HADCM3 in combination with the ice sheet model GLIMMER to study the last glacial inception. None of the published studies address glacial maximum conditions or model the full northern hemisphere.

1.7. Objectives and structure of this study

The aim of this study is to advance our knowledge about glacial ice sheet–climate interactions focusing on Heinrich events. To study these interactions, we performed coupled ice sheet–climate model experiments under pre-industrial as well as LGM boundary conditions. Ice sheets are not yet standard components of climate models. Therefore this study has a strong technical component in developing a coupled model system and is a test of the applicability of the coupled system to pre-industrial climate, glacial climate, and Heinrich events.

For the experiments, we adapted the Parallel Ice Sheet Model (PISM) for the use in coupled ice sheet–climate simulations and coupled it to the atmosphere ocean general circulation model (AOGCM) ECHAM5/MPIOM/LPJ. We describe the models, the necessary modifications, as well as the setup in chapter 2. With the coupled setup we performed long-term experiments under constant pre-industrial as well as LGM boundary conditions. The mean states of these experiments are analyzed in chapter 3. The main focus of this study, the variability in the coupled model is analyzed in chapter 4. We summarize the main findings and draw the final conclusions in chapter 5.

CHAPTER 2

Model description

We have coupled the atmosphere–ocean general circulation model (AOGCM) ECHAM5/MPIOM/LPJ with a northern hemisphere setup of the ice sheet model (ISM) mPISM. In the following, we first describe the AOGCM, then the ISM, and finally the coupling between the two models.

2.1. ECHAM5/MPIOM/LPJ

ECHAM5 (Roeckner et al., 2003) is a spectral atmosphere general circulation model. For long-term simulations, the triangular spectral truncation at wavenumber 31 ($\sim$ 3.75°) in combination with 19 vertical hybrid-σ-levels reaching up to 10 hPa is a very good compromise between model speed and accuracy. This setup is therefore employed in all experiments described in the following. The land hydrology scheme (HD model, Hagemann and Dümenil 1998; Hagemann and Gates 2003) operates on a 0.5° grid. For the HD model, we use the present-day routing directions in combination with the LGM land-sea-mask. The land surface properties are modeled using the Lund-Potsdam-Jena (LPJ) vegetation model (Sitch et al., 2003). Its use in combination with ECHAM is described in Schurgers et al. (2007) and Mikolajewicz et al. (2007a).

MPIOM (Marsland et al., 2003) is a primitive equation ocean model operating on a curvilinear grid with variable resolution. In the setup employed in the following, the grid has two poles, located over Greenland and Antarctica and a nominal resolution of 3°. This results in an increased resolution in the deep water formation areas, and a relatively coarse resolution in the equatorial areas.

The atmosphere and ocean are coupled using the OASIS coupler (Valcke et al., 2004). The performance of a higher-resolution version of the coupled model is described in Jungclaus et al. (2006). Results of the Paleoclimate Modelling Intercomparison Project Phase 2 (PMIP-2) participation can be found in the PMIP-2 database at `http://pmip2.lsce.ipsl.fr`.

2.2. mPISM

mPISM is based on the Parallel Ice Sheet Model (PISM) version 0.3 from the University of Alaska, Fairbanks (Bueler and Brown, 2009; the PISM authors, 2013). Several aspects of the model needed to be changed for the coupling to the climate model and for obtaining pulsating ice streams. PISM uses the Shallow Ice Approximation (SIA) and the Shallow Shelf Approximation (SSA) to compute flow velocities. It uses an enthalpy method to handle polythermal ice (Aschwanden et al., 2012). Details about the model can be found in the literature given above.

In the following, we describe the modifications made in mPISM. We use the term PISM 0.3 when referring to the base version, mPISM when referring to the modified version, and PISM when referring to aspects of the base version that also apply to the modified version. PISM-PIK is a branch of PISM that was developed

at the Potsdam Institute for Climate Impact Research (PIK) and merged into PISM 0.4.

To make the model mass conservative, we changed the transport scheme in mPISM from the non-conservative 2nd order scheme used in PISM 0.3 to a mass conserving 1st order upwind scheme (e. g. Morton and Mayers, 2005). This was accepted into PISM-PIK (Winkelmann et al., 2011) and on this way into PISM 0.4. We use the combined velocities and the upwind scheme for the mass transport as well as for the horizontal enthalpy transport. The upwind scheme needs a staggered (Arakawa C type) grid (Arakawa and Lamb, 1977) with the flow velocities on the cell boundaries. PISM calculates the SIA velocities on this staggered grid while it calculates the SSA velocities on an collocated (Arakawa A) grid with the velocities on the grid cell centers.

For solving the SIA equations, ice thickness and temperature are needed on the staggered grid. The standard approach in PISM 0.3 is to average between the two adjacent grid cells. Since PISM uses a terrain following z-grid, this approach can lead to averaging between ice filled and air filled grid cells and thereby to too cold *mixed* temperatures that cause artificially high viscosity values and thereby too slow ice flow. To avoid this problem, and to better represent the concave down shape of ice sheets, we use the enthalpy and thickness values of the upwind grid cell on the cell boundary. This has very little influence in the interior of the ice sheet, but considerably increases flow speeds at the margins of the ice sheet.

Interpolating the SSA sliding velocities onto the staggered grid can induce artifacts. The algorithm that yielded the best results in our experiments, was to base the decision whether sliding is allowed on a grid boundary on the question whether the upwind cell is sliding. If and only if there is sliding in the upwind grid cell, we take the arithmetic mean of upwind and downwind velocity as the velocity on the cell boundary. Elseways, there is no sliding. If we would allow sliding on a grid boundary, where the upwind cell is not sliding because of freeze-on, the ice in the upwind grid cell would be drawn down fast. This would lead to a high downward velocity of the ice. This downward velocity would advect coldness and the basal temperature would drop even further, solidifying the freeze-on. A similar problem arises on the transition between ice stream and ice shelf. Here, we use the ice velocity of the inland grid point as velocity for the cell boundary. If we would use the mean velocity, the ice on the inland side of the transition would be drawn down considerably by the fast-sliding ice shelf, and the inland grid point would freeze on.

Another measure to better represent the stream-shelf-transition is that we use downwind gradients at the ice shelf side of the stream-shelf transition to compute the driving stress, because we assume that a large fraction of the driving stress in the ice stream is balanced within the ice stream and not by the ice shelf.

Since the SSA velocities are computed using central differences, the model grid can decouple to some degree, resulting in checkerboard patterns. To solve this problem, we impose a slight (5%) penalty for ice flow going against the direction of the surface slope. Possible errors in the velocities introduced by this penalty are far smaller than those introduced by the uncertainties in the stress-strain relationship of the ice, and the modeled surface topography clearly improves.

For solving the SSA stress balance, PISM 0.3 covers the ice-free areas with a 50 m thick layer of $-20°$C cold *sea ice*, that – for viscosity calculations – has a spreading rate of 10^{-3}/yr. The backstress from this *sea ice* causes the ice shelves to slow down towards the outer rims. We thinned it to 1 m. This thinning increases

ice shelf velocities and computational costs. Further thinning did not change the ice shelf velocities substantially, but did substantially increase the computational costs.

Since PISM uses explicit time stepping for the horizontal mass and enthalpy transports, the timestep has to be adapted to the velocities. This is done on a per-timestep-basis with criteria stemming from the SIA and the SSA velocities respectively. We halved the maximum time step permissible from the stability condition for the SIA transports since the upwind mass transport scheme can empty a grid cell twice as fast as the default PISM transport scheme, that used the SIA velocities in combination with the mean of the ice thicknesses of the adjacent grid points. We also impose a stricter criterion from the SSA velocities. We add up the outflows from a grid cell and do not permit more outflow than 1/4 of the cell contents, neglecting the inflow. The choice of 1/4 is – to some degree – arbitrary, but tests showed that 1/4 yields smoother solutions than 1/2. It thereby caused less oscillations between long and short timesteps. Therefore the mean timestep size actually increased while the results improved. Further sharpening the timestep criterion did not yield substantial further improvements.

Following Calov et al. (2002), we use a linear sliding law that allows sliding if there is basal water and deformable sediment available to lubricate the ice sheet. The availability of the sediment is based on the dataset from Laske and Masters (1997) with a cutoff value of 5 cm. The resulting distribution of till-covered areas, where sliding is possible when basal water is present, and bare-bedrock areas, where, in our model, no sliding is possible at any time is marked in fig. 2.1.

We spread out half of the heat flux from basal friction on a 1 grid cell square around each grid cell. This slightly heats the grid cells adjacent to an ice stream.

We had to modify the basal boundary condition of the enthalpy scheme to make it more stable under large friction values. We do not allow the existence of basal water when the ice sheet base is cold. If there is basal water below a cold base, we let it refreeze immediately and add its enthalpy to the lowest grid cell of the ice sheet. The enthalpy scheme then distinguishes between two main cases of the ice-bedrock interface. If the interface temperature is below the pressure melting point, we use the PISM default solver for a combined system of ice and bedrock. If it is at the pressure melting point, we solve ice and bedrock as separate Dirichlet problems and prescribe full water saturation at the base of the ice sheet. Next, we compute the energy balance of the basal water layer. Constituents of this balance are the heat flux from the bedrock Q_B, the basal friction Q_F, the heat flux into the ice Q_I, and the basal melt rate M of the ice sheet:

$$Q_B + Q_F - Q_I - ML\rho_I = 0, \tag{4}$$

where L is the latent heat of melting and ρ_I is the ice density. From the melt rate, we compute a new basal water level. If it is non-negative, we move on, if it is negative, the grid cell refreezes. We compute the enthalpy that corresponds to the missing basal water and subtract it from the enthalpy corresponding to waterless ice at pressure melting point.

We separate the basal water into a small locally bound fraction and an advectable fraction that we advect with the basal ice velocity and apply the same upwind scheme as used for ice and enthalpy transport. The locally bound fraction is responsible for the stiffness of the basal till and thereby for the sliding behavior.

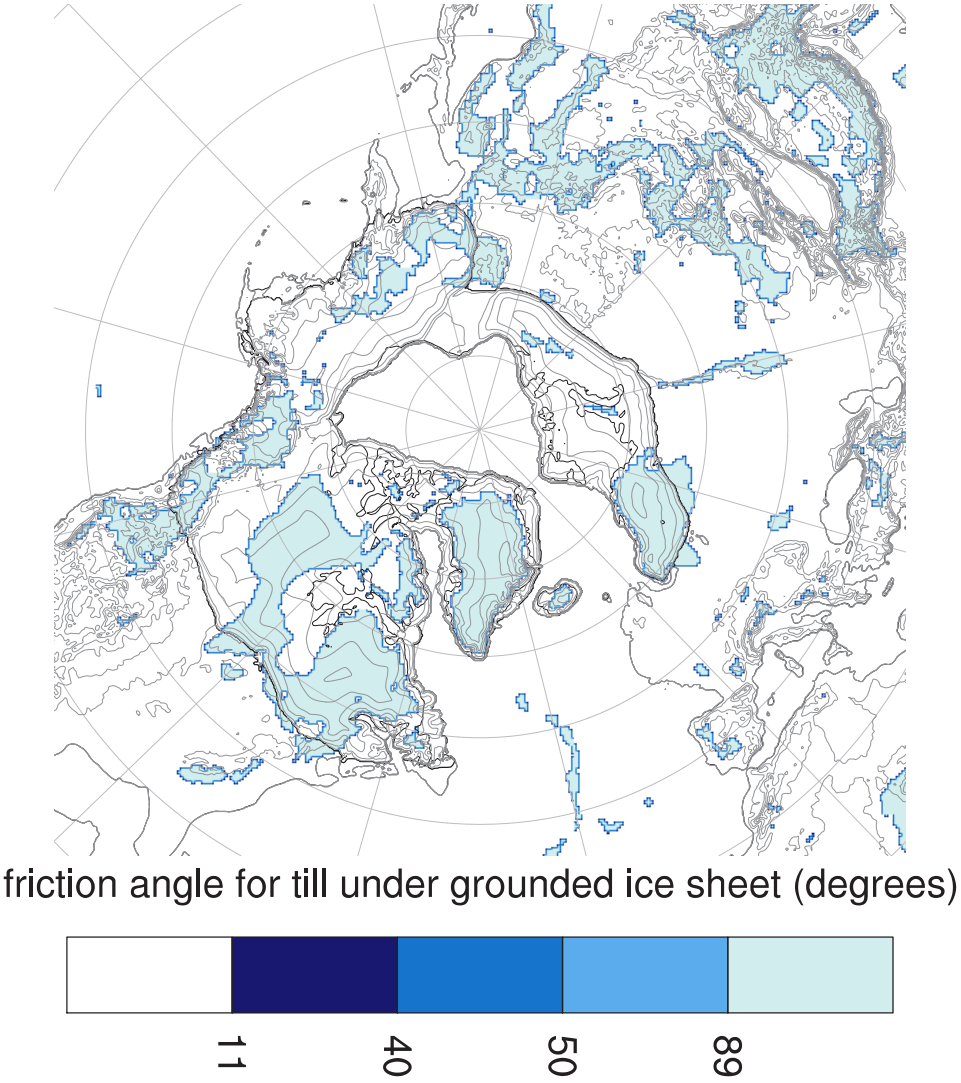

FIGURE 2.1. Till friction angles. Values below 11 (white in the plot) allow for very fast sliding, values above 89 (light blue) correspond to bare bedrock and practically completely prohibit sliding. Surface elevation is outlined in light gray for orientation. The ice sheet outlines are marked in black. The till friction angle distribution is constant over time.

For the bedrock deformation, we use an Local Lithosphere Relaxed Asthenosphere model (e. g. Le Meur and Huybrechts, 1996) with a rebound timescale of 3 kyrs.

We dynamically compute the change in sea level that is caused by the ice sheets and use it to adjust the sea level in the ice sheet model and in the climate model.

Our setup (e. g. fig. 2.1) uses a Cartesian coordinate system that is a Polar Stereographic projection of the Northern Hemisphere reaching southward to 36.7°N in all directions and to 19.1°N in the corners. The resolution is 20 km in both directions (625×625 grid cells). This grid contains all northern hemisphere regions we can possibly expect to grow large-scale ice sheets under glacial conditions (including the

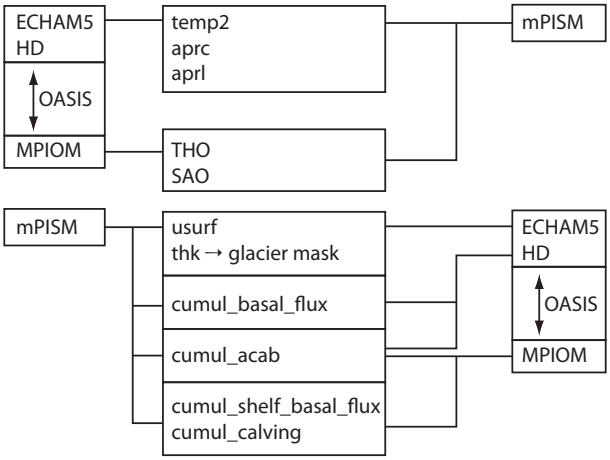

FIGURE 2.2. The fields being transferred between the models. Read from left to right. Variable names are: `temp2`: 2 m air temperature, `aprc`: convective precipitation, `aprl`: large-scale precipitation, `THO`: ocean potential temperature, `SAO`: ocean salinity, `usurf`: ice sheet surface topography, `thk`: ice sheet thickness, `cumul_basal_flux` ice sheet basal mass flux, `cumul_acab`: ice sheet surface mass balance, `cumul_shelf_basal_flux`: ice sheet shelf basal flux, `cumul_calving`: ice shelf calving flux.

Himalayans). Outside of the mPISM domain, we prescribe the ICE-5G topography matching the time slice of interest.

2.3. The coupling from the climate to the ice sheet

The coupling scheme between ECHAM5, MPIOM and mPISM is responsible for computing the ice sheet mass balance and surface temperature from ECHAM5 and MPIOM output fields and for transferring surface topography, glacier mask and mass fluxes from mPISM back to ECHAM5 and MPIOM. It is sketched in fig. 2.2. In this section we lay out the path from the climate model to mPISM.

To compute the mass balance for the ice sheet, we have to use a high spatial resolution that resolves the temperature distribution at the ice sheet margins. We use the 20 km grid of mPISM for the mass balance calculations. It is still impossible to run an atmosphere model at such a high spatial resolution for long time spans. Therefore we have to work with coarse resolution (in this case T31) atmospheric data, regrid them to the high-resolution ice sheet model grid, and apply corrections to account for unresolved features. To save computational time, we compute monthly averages of the atmospheric quantities and annual averages of the ocean variables before regridding them to the ice sheet model grid. These regridded high-resolution fields are used in the ice sheet model to determine the mass balance. The scheme we use to process temperatures and precipitation from ECHAM5 for the use in mPISM is sketched in fig. 2.3 and is described in detail in the following. It is based on the standard scheme employed in SICOPOLIS (Calov, 1994), that stems from Braithwaite and Olesen (1989).

The temperatures are highly correlated to the altitude at a local scale, so we can account for some of the temperature variations not resolved by ECHAM5 by applying an altitude correction with a fixed lapse rate. As lapse rate, we use 5 K/km as suggested by Abe-Ouchi et al. (2007). In a small sensitivity study, this proved to

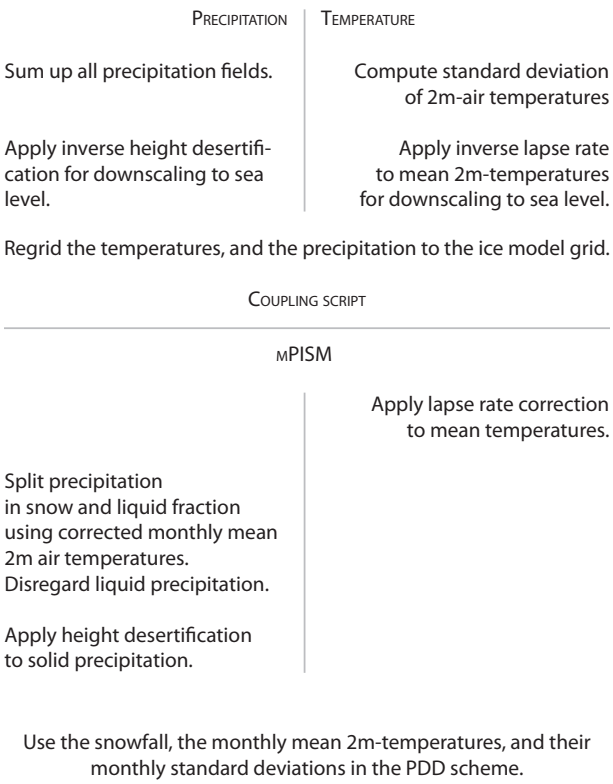

FIGURE 2.3. The modifications of the atmospheric coupling fields up to the PDD mass balance calculation.

be a good compromise between too high melt at low lapse rates and too widespread glaciation at high lapse rates.

We use the corrected monthly mean temperatures to partition the precipitation into solid and liquid fractions using a linear transition between $-10°\mathrm{C}$ and $+7°\mathrm{C}$ as in Marsiat (1994). The solid fraction is used as accumulation, the liquid fraction is discarded as runoff.

To account for the reduced precipitation at high altitudes, we apply a height desertification parametrization as in Budd and Smith (1979):

$$P = P_{\text{solid}} \cdot \begin{cases} 1 & , h \leq h_0 \\ \exp\left(-\lambda(h - h_0)\right) & , h > h_0, \end{cases} \tag{5}$$

where $h_0 = 2000\,\mathrm{m}$ and $\lambda = \log(2)/1000\,\mathrm{m}$. In standalone ice sheet simulations with a temperature deviation forcing ΔT from ice core or similar data, the precipitation is multiplied by

$$1 + (\Delta T \cdot 4.2857 \cdot 10^{-2}/\mathrm{K})$$

to represent the effect of the air temperature on the specific humidity.

We use temperatures and precipitation in a Positive Degree Day (PDD) model to determine the surface mass balance. As an extension of Fausto et al. (2011), we compute monthly temperature standard deviation maps from the 6-hourly climate model output and use them in mPISM to better represent the temperature variability. This is a compromise between computing the PDDs from the full 6-hourly

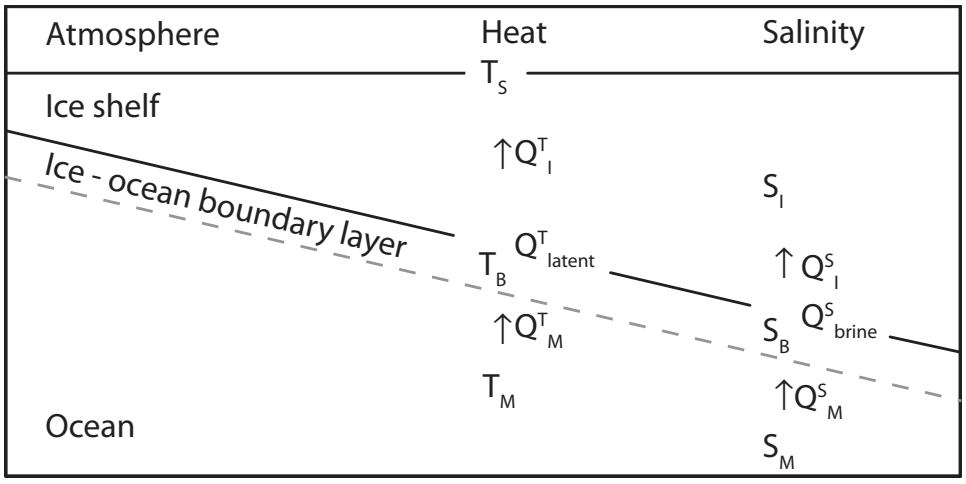

FIGURE 2.4. The variables used in the shelf coupling scheme. Variables are listed in table 2.1. Redrawn after Holland and Jenkins (1999).

temperature data on the highly resolved ice grid (which would be more computationally demanding) and the standard approach of prescribing a fixed standard deviation in the full model domain.

The PDD scheme employs the Calov-Greve integral method (Calov and Greve, 2005) to compute PDDs from monthly mean temperatures and standard deviations. Then, from these PDD, and the snow accumulation, the actual mass balance is computed according to the scheme from Reeh (1991):

> *The available positive degree-days (PDD) as calculated by means of equation (4)* [of Reeh (1991)]*, are used to melt snow and ice in the following order:*
> (1) *Snow (if present) is melted. The meltwater is supposed to percolate into the snowcover and refreeze as superimposed ice. Runoff does not occur until the amount of superimposed ice exceeds a given fraction (PMAX) of the snowcover.*
> (2) *The superimposed ice is melted.*
> (3) *Glacier ice is melted.*

This is summed up in the following equation:

$$\text{acc - melt} = \text{acc} - \min[0, (\text{PDD} - \text{acc}/m_{\text{snow}} \cdot \text{PMAX})] \cdot m_{ice}, \tag{6}$$

where m_{snow} and m_{ice} are the melt rates of snow and ice. They are empirical constants that need to be prescribed. We chose $m_{\text{snow}} = 3.2\,\text{mm/K/day}$ and $m_{\text{ice}} = 12.9\,\text{mm/K/day}$.

For the basal ice shelf melt (or growth), we use the three equation scheme described in Holland and Jenkins (1999). This scheme computes the ice shelf basal mass balance and properties of a thin boundary layer from ocean salinity and temperature as well as the ice shelf basal temperature gradient. Holland and Jenkins (1999) construct a model consisting of an ice layer, a boundary layer between ice and ocean and the mixed layer in the ocean. The definitions of the fluxes are sketched in fig. 2.4 and the variables used are listed in table 2.1. The behavior of this scheme is shown in fig. 2.5. In the boundary layer, they assume the ocean temperature to be at the freezing point. The salinity depends on the ice melt/refreeze rate and the entrainment velocity with which ocean water is entrained into the boundary layer.

TABLE 2.1. Variables and constants used in the ice shelf basal mass balance. All but κ taken from Holland and Jenkins (1999). $^*\kappa$ is taken from Hellmer and Olbers (1989)

Variables used in the Shelf coupling			
Naming			
$(\cdot)_S$	$(\cdot)$ at the ice surface		
$(\cdot)_I$	$(\cdot)$ in the ice shelf		
$(\cdot)_B$	$(\cdot)$ in the boundary layer		
$(\cdot)_M$	$(\cdot)$ in the Ocean		
T	Temperature		°C
S	Salinity		psu
p	Pressure		Pa
ρ	Density		kg/m^3
Fluxes			
Q_I^T	Heat flux into the ice		W/m^2
Q_{latent}^T	Heat flux from the boundary, $Q_{\text{latent}}^T < 0 =$ melt		W/m^2
Q_M^T	Heat flux from the ocean into the boundary layer		W/m^2
Q_I^S	Salinity flux into the ice		psu/m^2/s
Q_{brine}^S	Salinity flux from brine production		psu/m^2/s
Q_M^S	Salinity flux from the ocean into the boundary layer		psu/m^2/s
w_B	Melt rate, $w_B > 0 =$ melt		m/s
Constants			
a	Salinity coefficient of freezing equation	-5.73×10^{-2}	°C/psu
b	Constant offset for freezing equation	9.39×10^{-2}	°C
c	Pressure coefficient for freezing equation	-7.53×10^{-8}	°C/psu
c_{pI}	Ice heat capacity at constant pressure	2009	J/kg/K
c_{pM}	Ocean heat capacity at constant pressure	4170	J/kg/K
L_F	Latent heat of freezing	3.34×10^5	J/kg
γ_T	Thermal exchange velocity	1×10^{-4}	m/s
γ_S	Salinity exchange velocity	1×5.05^{-7}	m/s
κ	Thermal conductivity of ice	1.54×10^{-6}	m^2/s

The defining equations are

$$T_B = aS_B + b + cp_B \tag{7}$$

$$Q_I^S = Q_M^S + Q_{\text{brine}}^S \tag{8}$$

$$Q_M^S = -\rho_M \gamma_S (S_B - S_M) \tag{9}$$

$$Q_{\text{brine}}^S = \rho_M w_B (S_I - S_B) \tag{10}$$

$$Q_I^T = Q_M^T + Q_{\text{latent}}^T \tag{11}$$

$$Q_I^T = -\rho_I c_{pI} \kappa \frac{\partial T_I}{\partial z} \tag{12}$$

$$Q_M^T = -\rho_M c_{pM} \gamma_T (T_B - T_M) \tag{13}$$

$$Q_{\text{latent}}^T = -\rho_M w_B L_F \tag{14}$$

Using $\frac{\partial T_I}{\partial z} \approx \frac{T_i - T_B}{\Delta z}$, where T_i is the ice temperature Δz above the shelf base, we define the following shorthands

$$M := \rho_M w_B; \qquad \alpha := b + cp_B$$

$$K_S := -\rho_M \gamma_S; \quad K_T := -\rho_M c_{pM} \gamma_T; \quad K_I := -\frac{\rho_I c_{pI} \kappa}{\Delta z}$$

By combining (8), (9) and (10), we obtain

$$S_B = \frac{Q_I^S - MS_I + K_S S_M}{K_S - M}.$$

Now we can combine (11) with (14), solve for M, insert (12) and (13), replace S_B, and rearrange to obtain

$$\begin{aligned} -M^2 L_F + M \overbrace{[K_S L_F + (K_T + K_I)(aS_I + \alpha) - K_T T_M - K_I T_I]}^{\Phi} \\ = \underbrace{(K_T + K_I)(a(Q_I^S + K_S S_M) + \alpha K_S) - K_S(K_T T_M - K_I T_I)}_{\Psi} \end{aligned} \tag{15}$$

Solving for M yields

$$M = \frac{\Phi}{2L_F} \pm \sqrt{-\frac{\Psi}{L_F} + \frac{\Phi^2}{4L_F^2}} \tag{16}$$

From this, we take the positive branch. The negative branch yields obviously wrong values. We force this model with the average temperature and salinity of the top 12 layers (203m) from the ocean model.

We employ a simple calving scheme that operates on a grid cell and its eight neighbors. If less than three of the nine cells have an ice thickness above 200m, and the relaxed bedrock topography is below sea level, then the ice is calved. This allows shelves to dynamically grow and retreat, and prevents one grid cell wide ice tongues.

2.4. The coupling from the ice sheet to the climate

In the following, we describe how the output fields from mPISM are fed back into ECHAM5 and MPIOM. We first detail on the surface orography, then on the glacier mask, and finally on the mass fluxes.

The orography is fed back into ECHAM5 via the geoid surface potential and the gravity wave drag parametrization. For the areas outside of the mPISM domain, the mPISM surface field is combined with a background map matching the time slice of interest. The combined map is adjusted for sea level changes from the ice sheet. To keep the subgrid scale orography consistent, the background map is smoothed with respect to the standard topography map used for ECHAM5, so it matches the roughness of the ice-free areas of the remapped mPISM topography.

Since this smoother surface would significantly change climate in comparison to the standard model setup, we upscale the subgrid surface slopes by a factor of two. Furthermore, we decrease the resolution-dependent threshold for activating the gravity wave drag parametrization in ECHAM5 from 400 m to 300 m peak − mean elevation, so the gravity wave drag parametrization is active in about the same grid cells as in the original setup. These values were obtained by switching the maps in a pre-industrial setup and tuning the parameters until we obtained similar mean orographic slopes and a similar climate as in the original setup.

In the following paragraph we detail on the treatment of the glacier mask in the coupling scheme. All ice sheet model grid cells with an ice thickness above 10 m are treated as glaciated. We use conservative area remapping to interpolate the glacier mask to the ECHAM5 grid.

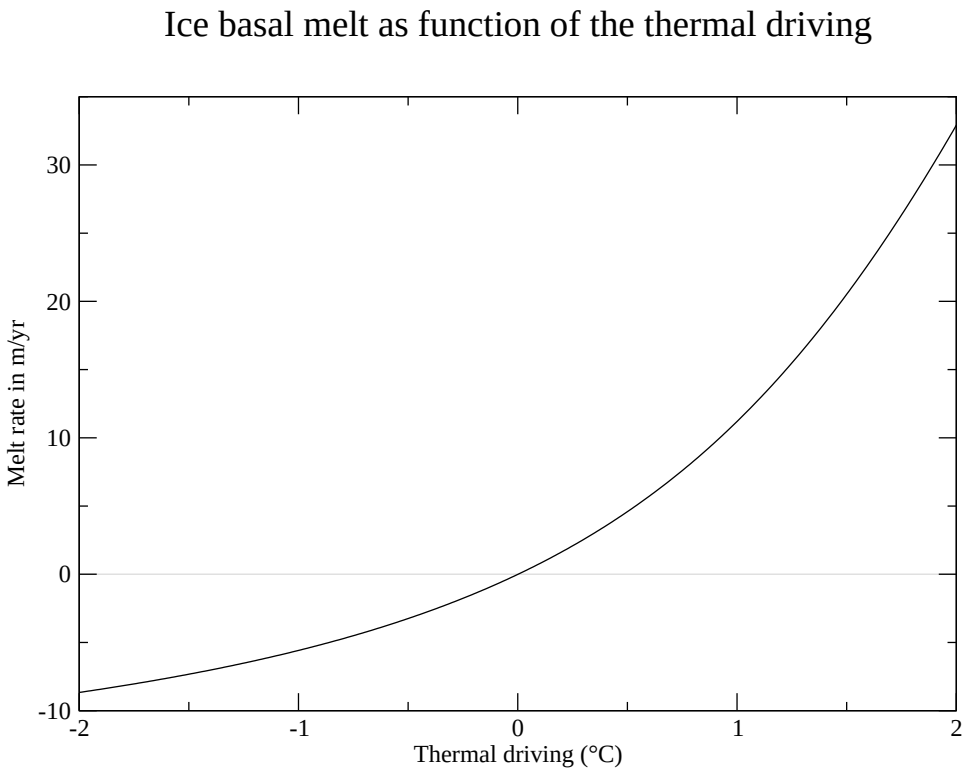

FIGURE 2.5. Shelf melt as a function of the thermal driving defined as $T_* = (T_M - T_B) - a(S_M - S_B)$. S_B is set to 34 psu, the ice thickness to 100 m and the air temperature to -20°C. This basically corresponds to the dashed line in Fig. 6 of Holland and Jenkins (1999).

ECHAM5 treats all grid cells with a fractional glacier mask value above 0.5 as fully glaciated. We modified the ECHAM5 albedo scheme, such that the albedo is computed based on a fractional glacier cover with a background albedo of 0.25 for the non-glaciated parts of the grid cell. For those grid cells that have a glacier fraction below 0.5 and are thus considered as non-glaciated, we reduce the forest (tree cover) fraction by the glacier fraction and compute a new background albedo α^{new} that represents the effects of the albedo of the glaciated parts:

$$forest = (1 - glacier)\, forest \tag{17}$$

$$\alpha^{new} = \alpha_{\mathrm{lpj}}\,(1 - \mathrm{glacier}) + \alpha_{\ \mathrm{glacier}}\,\mathrm{glacier}, \tag{18}$$

where *forest* is the forest fraction computed by LPJ, α_{lpj} is the albedo from LPJ, and $\alpha_{glacier}$ is a background albedo for glacier ice (0.5). The reduction of the forest fraction is important because it reduces the snow-masking effect in the albedo calculation of ECHAM5.

We average the mass fluxes of the surface mass balance, the basal melt and refreeze, the shelf basal melt and refreeze and the iceberg calving at every grid cell of mPISM over the coupling interval and split the fluxes according to mPISMs grounded/floating mask into land based fluxes that we feed into the surface runoff scheme of ECHAM5, and ocean based fluxes, that we feed into the nearest MPIOM grid cell. We associate fluxes from iceberg calving and shelf basal melt with a

TABLE 2.2. Main experiments performed and analyzed. For the boundary conditions see table 2.3. 1:10 coupling means 1 climate model (CM) year per 10 ice sheet model years. The coupling is done after each year of climate model integrations. For easy reference, ice sheet model years in ASYNC are ten times the corresponding climate model years, thus climate model year 6901 corresponds to ice model years 69 010 to 69 019.

Name	**Boundary Conditions**	**Coupling**	**Start year** (CM years)	**Duration** (CM years)
ASYNC	LGM	1:10	6901	2999
SYNC	LGM	1:1	1780	3220
ICE-5G	LGM	none		649
pre-ind	pre-ind	1:10	2800	1000

TABLE 2.3. Values differing between the LGM and pre-industrial setups.

Parameter	**LGM**	**pre-ind**
Topography	ICE-5G 21ka	ICE-5G 0ka
Eccentricity	0.0190	0.0167
Obliquity	22.95°	23.45°
Angle of Perihelion	294.4°	282.0°
CO_2 (ppm)	185	280
N_2O (ppm)	0.20	0.27
CH_4 (ppm)	0.35	0.67

negative enthalpy flux into the ocean, so that ice shelf basal melt and calving lead to ocean cooling and/or increased sea ice formation.

2.5. Setups and experiments

We performed four main experiments (table 2.2). Three of them (ASYNC, SYNC, ICE-5G) under LGM boundary conditions, one (pre-ind) under pre-industrial boundary conditions (table 2.3). ASYNC, SYNC, and pre-ind were done in coupled mode. Coupling was done after every year of climate model simulations.

SYNC was split off from ASYNC. As spin-up for ASYNC, the ISM was run for several tens of kyrs under prescribed glacial boundary conditions. Then it was coupled with the climate model and run for several thousand years during the different stages of the coupling and tuning process. The last 21 500 years of this process, the system was fully coupled. The climate model was started from an existing PMIP2-type LGM experiment (Arpe et al., 2011) and run for 3850 years during the coupling and tuning process (2150 years fully coupled) before ASYNC was started. The descriptions of the experiments are as follows:

ASYNC A fully coupled experiment under LGM boundary conditions. This experiment uses asynchronous coupling with 10 years of ISM integrations per year in the climate model. The experiments covers the climate model years 6901–9899 and the ice model years 69010–98999. We describe the mean state of this experiment in chapter 3 and the surges in chapter 4.

SYNC A synchronously coupled experiment, started from climate model year #8780 of ASYNC (renamed to year 1780 in SYNC) and integrated through

3220 years of the Hudson Strait Ice Stream surge. Both, the ice and the climate model cover the years 1780–4999.

ICE-5G A climate-only experiment, where we force the climate model with the ICE-5G topography under LGM boundary conditions as in the PMIP2 experiments. This experiment allows us to investigate the effects of the different ice sheet topographies and of the changes in freshwater fluxes caused by our coupling. This experiment was started from the same PMIP2 LGM experiment as ASYNC and integrated over 649 years. We analyze the last 100 years.

pre-ind An asynchronously coupled experiment under pre-industrial boundary conditions. The climate model was started from an existing pre-industrial experiment. The ISM was initialized with the present-day Greenland Ice Sheet shape using PISM's bootstrap methods. The experiment was run for 1000 years of climate model integration (10 000 years in the ISM) and the last 100 (1000) years are analyzed.

CHAPTER 3

Mean climates and long-term drift

In the following, we first discuss the pre-industrial experiment (pre-ind) and then the LGM mean state in ASYNC and the ICE-5G experiment (see section 2.5). Finally we describe the long-term drift in ASYNC. We discuss the climate in SYNC in chapter 4. Since SYNC only covers one surge phase of the Hudson Strait Ice Stream, we will focus on ASYNC.

3.1. The pre-industrial climate experiment

The pre-industrial simulation was integrated for 10 000 years in the ice sheet model and for 1000 years in the climate model. We discuss the state averaged over the last 1000 years in the ice sheet and the corresponding 100 years in the climate. The main purpose of this experiment is to show that our setup yields reasonable results under pre-industrial boundary conditions and to provide a reference state to compare the LGM climate against. We therefore limit the analysis of this experiment to key climate parameters and compare those to reanalysis and observational estimates. We first discuss the state of the atmosphere, then the ocean and finally the ice sheets.

3.2. The pre-industrial atmosphere

A comparison of the pre-industrial **2 m air temperatures** with the ERA INTERIM reanalysis for 1989 to 2010 (Dee et al. (2011), fig. 3.1(a)) shows that our pre-industrial model climate is colder than the present day climate (−0.6 K). As a comparison, we compute the difference between global mean temperature in the ERA-INTERIM period (20C3 and A1-B combined) and in the first thirty years (1860 to 1889) of the CMIP-3 20C3 experiment. These experiments were performed with a technically identical model and yield a global mean temperature difference of −0.56 K (pre-ind – present). So, we see perfect agreement of our global mean temperature and the observations. In fig. 3.1(a) we show the northern hemisphere summer season (JJA) temperature bias, since the summer season is decisive for the melt. The annual mean patterns are similar. The pattern in the temperature difference largely is a composite of the effect of the reduced CO_2 concentration in the pre-industrial model setup, and the effect of the smoothed-out T31 topography.

Typical for the reduced CO_2-concentration is the globally lower temperature, with a larger temperature change over land (−0.8 K) than over the ocean (−0.5 K). The change also is larger in the high latitudes (−3.2 K north of 45 °N, and −1.2 K south of 45 °S) than in the low latitudes, where, on the average, the temperature in our model is higher than in the ERA INTERIM reanalysis (+0.1 K between 45 °S and 45 °N).

The smoothed out T31 grid of ECHAM5 is lower than the T255 grid of ERA INTERIM in most mountain areas (the creation of the grid involves spectral smoothing and is not conservative, so the mean surface elevation is lower in a T31 grid

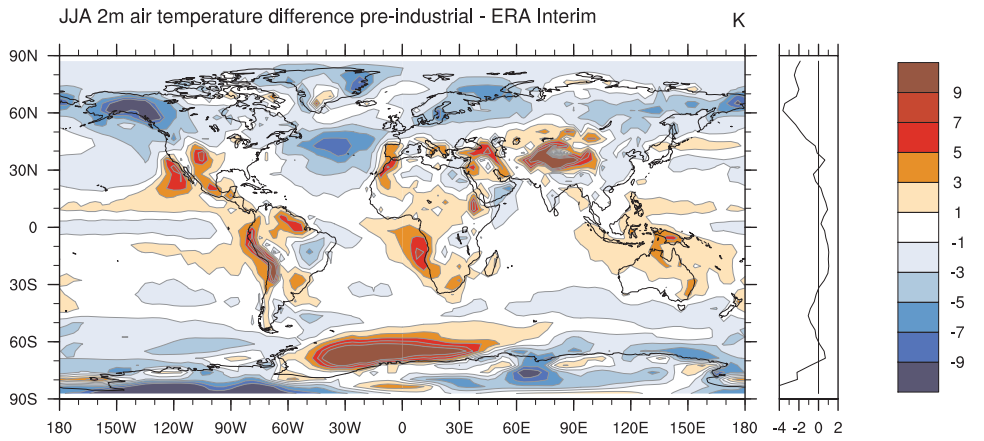

(a) Difference between modeled pre-industrial summer (JJA) 2 m air temperature and ERA INTERIM JJA 2 m air temperature.

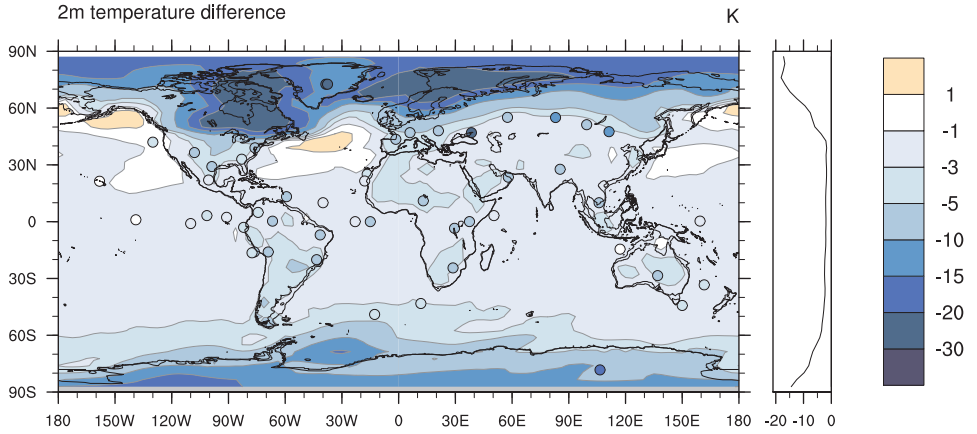

(b) Annual mean temperature difference between ASYNC and the pre-industrial run. Dots show proxy data for LGM - present day from Kim et al. (2008). Note the non-linear colorscale!

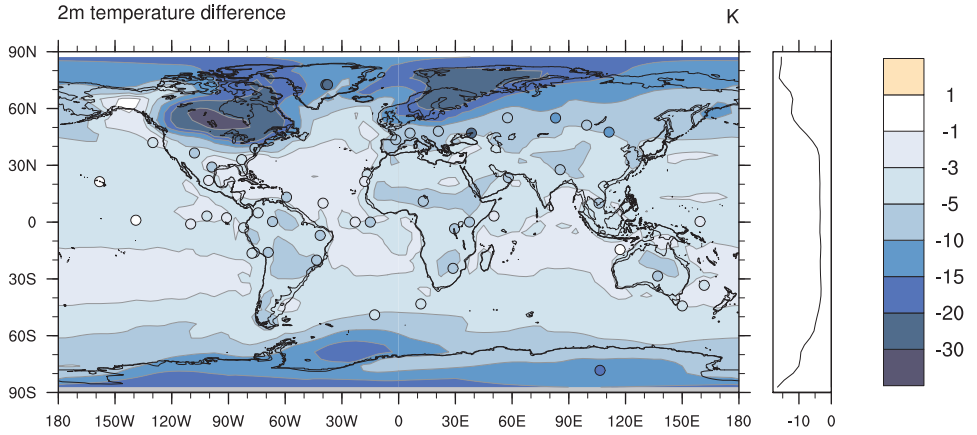

(c) Annual mean temperature difference between LGM with ICE-5G topograpy and pre-industrial run. Dots show proxy data for LGM - present day from Kim et al. (2008). Note the non-linear colorscale!

FIGURE 3.1. 2 m air temperature differences.

than in reality). The spectral smoothing causes mountains to be lower in T31 than in reality and creates trenches adjacent to them. Differences that can directly be traced back to the lower topography in the T31 resolution of the atmosphere model are the warm biases over the Andes and the Himalaya. Over the Himalaya, typical surface altitude differences between the two model setups are about 500 m to 1000 m on the T31 grid, over the Andes, they reach 2000 m, and over the southern tip of Greenland, they reach 1000 m. Assuming a lapse rate of 5 K/km, as it is used in our coupling scheme, this corresponds to 2.5–5 K temperature difference over the Himalaya, 5–10 K temperature difference over the Andes, and up to 5 K temperature difference over the southern tip of Greenland.

There is a cold bias over the northern Atlantic. It is a result of the North Atlantic Current taking a too southerly route. To correctly represent the path of the North Atlantic Current, the ocean model would have to resolve eddies, requiring a horizontal resolution of about 5 km in this region. This is not yet feasible for multi-millennial simulations.

There is a strong cold-bias over the Alaska range, that also occurs in stand-alone simulations (not shown) and becomes stronger because of ice-sheet growth in the coupled setup (fig. 3.2). This temperature bias, and thus the glaciation, can be reduced by increasing the climate model resolution (e. g. in the CMIP3-experiments that were performed with a very similar climate model version), but this is not yet feasible for multi-millennial experiments.

A comparison of the present day annual mean **precipitation** data from the GPCP dataset (Adler et al. (2003), fig. 3.3(a)) with the model results for the pre-industrial time (fig. 3.3(b)), yields a good agreement over Greenland. This is also reflected in the agreement of our Greenland mean surface accumulation values with those from regional modeling (table 3.2). Over the other polar areas, the values also closely match. The 2D as well as the zonal mean plots show that most of the precipitation differences occur in the tropics and southern mid-latitudes. The differences in the tropics are standard modeling artifacts and both regions are not of special interest for this study. In the global mean, the precipitation of 1.03 m/yr is 0.05 m/yr above the GPCP estimate, while north of 45 °N the modeled precipitation of 0.66 m/yr is 0.06 m/yr lower than the GPCP estimate.

3.3. The pre-industrial ocean

For the North Atlantic Deep Water (NADW) cell of the Atlantic Meridional Overturning Circulation (AMOC) (fig. 3.4(a)), the maximum strength is about 17.0 Sv at 32.5°N and a depth of 1020 m. This agrees with the estimate of 16 ± 2 Sv from Ganachaud (2003) and recent measurements of 18.7 ± 2 Sv at 26.5°N (Kanzow et al., 2010). The NADW is formed south of Greenland and in the Greenland/Iceland/Norwegian (GIN) Sea (not shown). The Antarctic Bottom Water cell reaches a maximum of 2.9 Sv at 30°S and a depth of 3570 m. The northward heat transport in the Atlantic of 0.8 PW at 30°N is lower than the present day estimates. Ganachaud and Wunsch (2003) obtain 1.27 ± 0.15PW at 24°N as a result of the world ocean circulation experiment, and Johns et al. (2011) obtain 1.33 ± 0.14 PW at 26°N from the RAPID mooring array measurements. A comparison of the modeled temperatures in the Atlantic and data from the WOCE experiment (Koltermann et al., 2011) shows that the deep water in our model is warmer than it is in reality. This explains why our model simulates less heat transport than the measurements indicate while the overturning strength is similar.

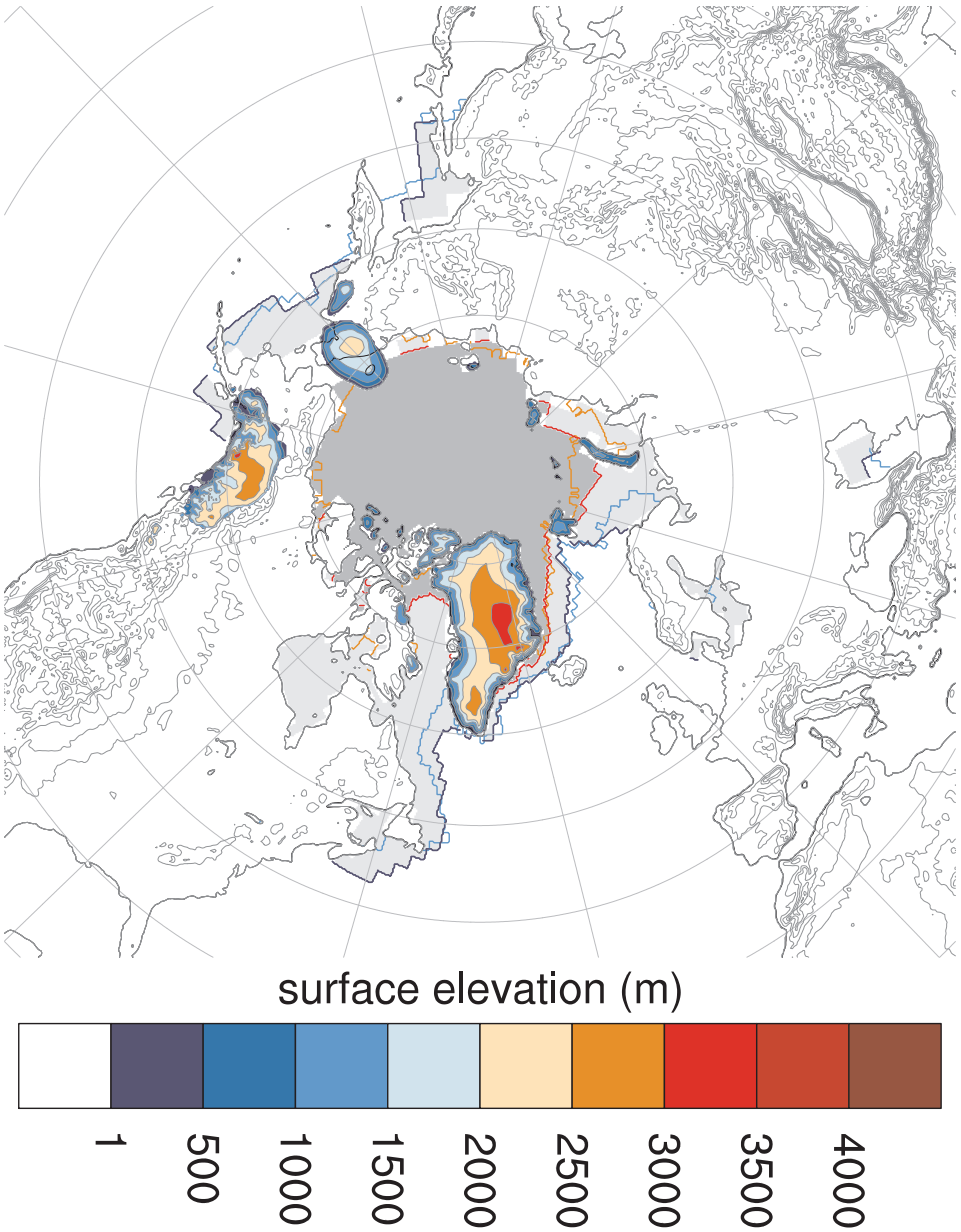

FIGURE 3.2. The surface topography in mPISM averaged over ice-model years 9000-10 000 of the coupled simulations. The thin isolines are every 500m, thick isolines every 1000m. Ice covered regions are colored. Over the ocean, dark gray with red outline indicates areas with perennial ice cover (15 % level) in more than 50 % of the model years. Light gray with dark blue outline indicates temporary ice cover in more than 50% of the model years. The Bering Strait appears to be ice-free because it is slightly displaced to the west in the ocean model. The orange outline marks areas which have permanent sea ice cover in more than 50% of the years 1870 to 2010 according to the HadISST sea ice data set (Rayner et al., 2003), the light blue outline marks areas that have temporary sea ice cover in more than 50% of these years according to HadISST.

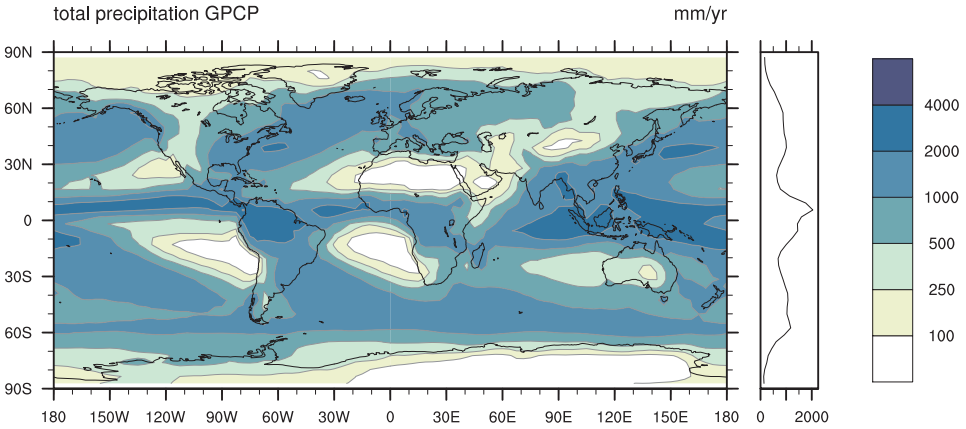

(a) Precipitation from GPCP satellite data.

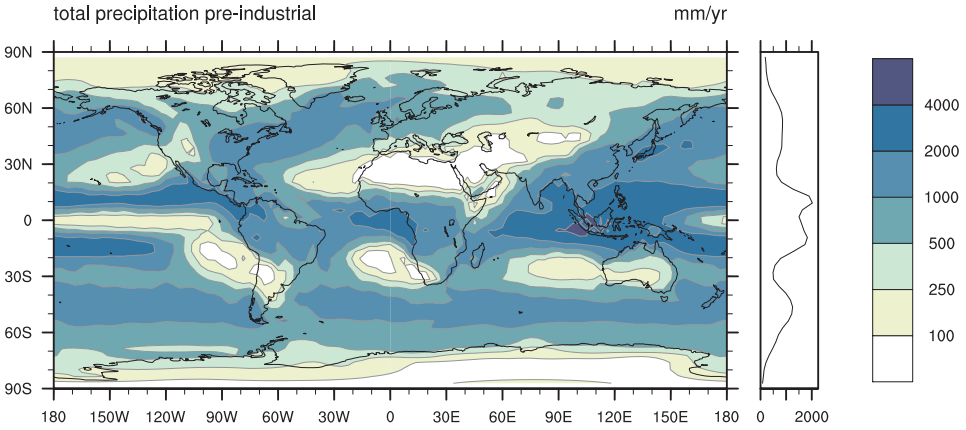

(b) Precipitation during the last 100 years of the pre-industrial experiment.

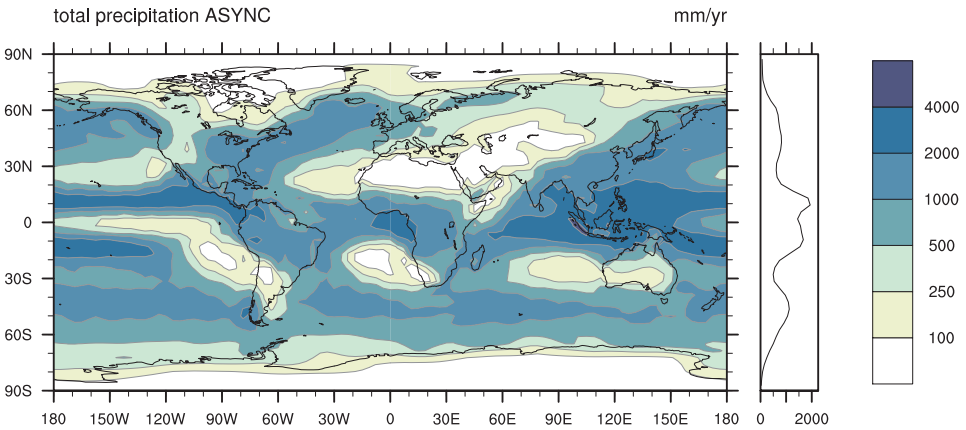

(c) Precipitation during the LGM. Averaged over the full ASNYC experiment.

FIGURE 3.3. Precipitation values from the GPCP dataset (Adler et al., 2003) and the averages from the pre-industrial and the ASYNC experiments.

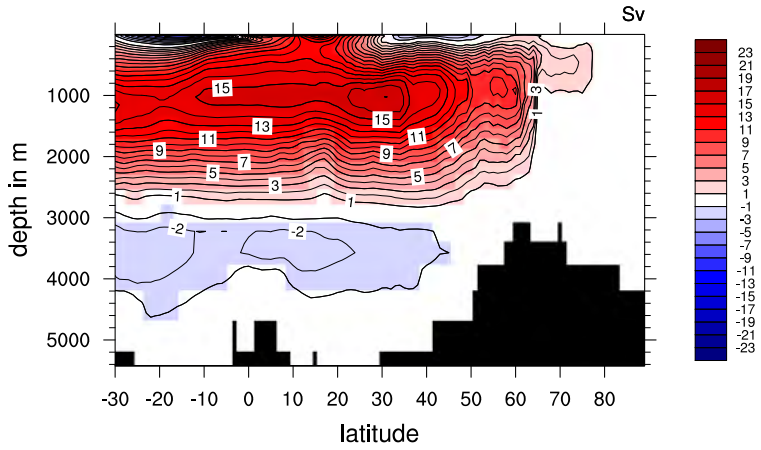

(a) AMOC stream function in the pre-ind experiment. Averaged over the last 100 years of the experiment.

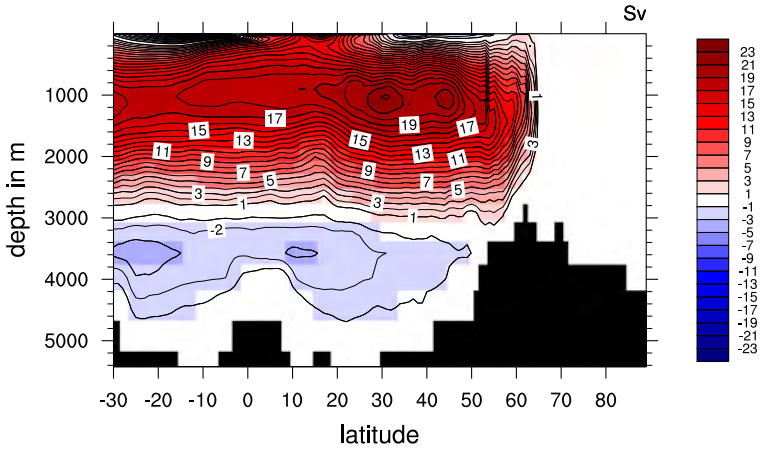

(b) Mean AMOC in ASYNC. Averaged over the full 3 kyrs. For the time variability see fig. 4.22.

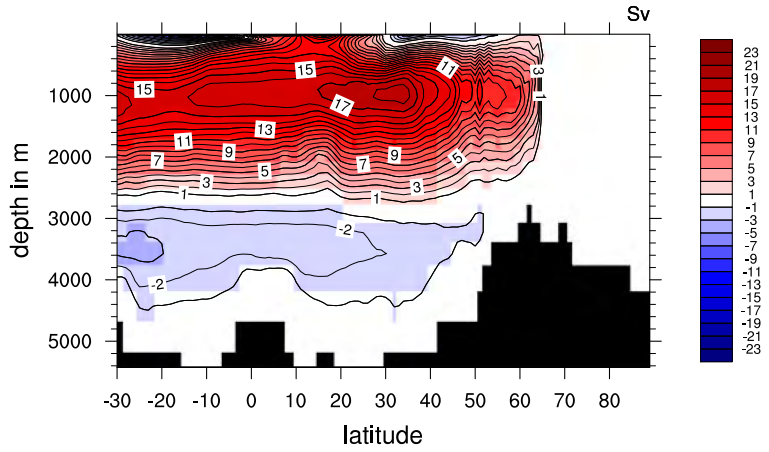

(c) Mean AMOC in the ICE-5G LGM experiment. Averaged over the last 100 years.

FIGURE 3.4. Atlantic Meridional overturning circulation stream functions for pre-industrial and LGM climate states.

TABLE 3.1. Pre-industrial ice sheet volumes and their changes averaged over years 9000 to 10 000. Greenland volume: Bamber et al. (2001). Glaciers outside of Greenland and Antarctica are estimated between 0.05 and 0.13 Mio km^3 in Lemke et al. (2007).

	Volume (Mio km^3)		Drift (km^3/yr)
Ice sheet	Present day	mPISM	mPISM
Greenland	2.93	3.65	−14
Canada and Alaska		1.2	+38
Siberia		0.94	+86
Arctic Islands		0.14	−0.1
Total		5.9	+106

The sea ice maximum and minimum (fig. 3.2) agree very well with the long-term average of the HadISST observational data set (Rayner et al., 2003). This data set covers the time period from 1870 to 2010. In the first 100 years, the observational data basis is very sparse. While the data basis improves over time, the sea ice cover decreases over time due to global warming. We decide to use the entire data set as a compromise between sparse data coverage of the right time slice and high data coverage quality of the wrong time slice.

3.4. The pre-industrial ice sheets

Fig. 3.2 shows the pre-industrial ice sheets averaged over the years 9000 to 10 000; fig. 3.5 shows the deviations from the reference topography. Fig. 3.6 shows the mean surface mass balance of the ice sheets. We obtain a northern hemisphere land ice volume of 5.9 Mio km^3, corresponding to 14.9 m of sea level equivalent (SLE). Of this volume, 3.65 Mio km^3 (9.2 m SLE) are stored in the **Greenland Ice Sheet**. Today's Greenland Ice Sheet (fig. 3.2) has a volume of 2.9 Mio km^3 (7.3 m SLE). The drift in Greenland Ice Sheet volume is −14 km^3/yr. It has a two dome structure; the main dome reaches a height of 3200 m above sea level (asl) (3300 m in reality (Bamber et al., 2001)) and a southern dome reaches 2700 m asl (2900 m in reality).

Along most of the coasts of Greenland, the model grows too much ice (fig. 3.5). At the northern and eastern coast, this is largely due to practically zero ablation from the PDD scheme. The glacier fraction in ECHAM is above 0.5 from the start of the experiment. The grid cells are therefore treated as glaciated, and the surface temperature in these grid cells cannot rise above 0°C. This substantially limits the 2 m air temperature and thus the melt in the PDD scheme. The sea ice along the northern and eastern coast maintains cold temperatures in the coastal ocean. The temperature is interpolated bilinearly when remapping from ECHAM5 to mPISM. The mean temperature between a sea ice covered grid cell and a glaciated grid cell cannot allow for substantial surface melt. Therefore, the surface mass balance is positive practically all the way to the coast, while substantial ice melt would be needed to stop the glaciers before the coast. There is substantial melt near the western coast where two grid cells with a glacier fraction below 0.5 remain that are considered as non-glaciated by ECHAM5. An energy balance scheme with detailed treatment of the different heat fluxes (Vizcaíno et al., 2010) could solve the problems at the east coast, but would have required substantial additional resources. Another way to improve the representation of the Greenland Ice Sheet margins is to use a

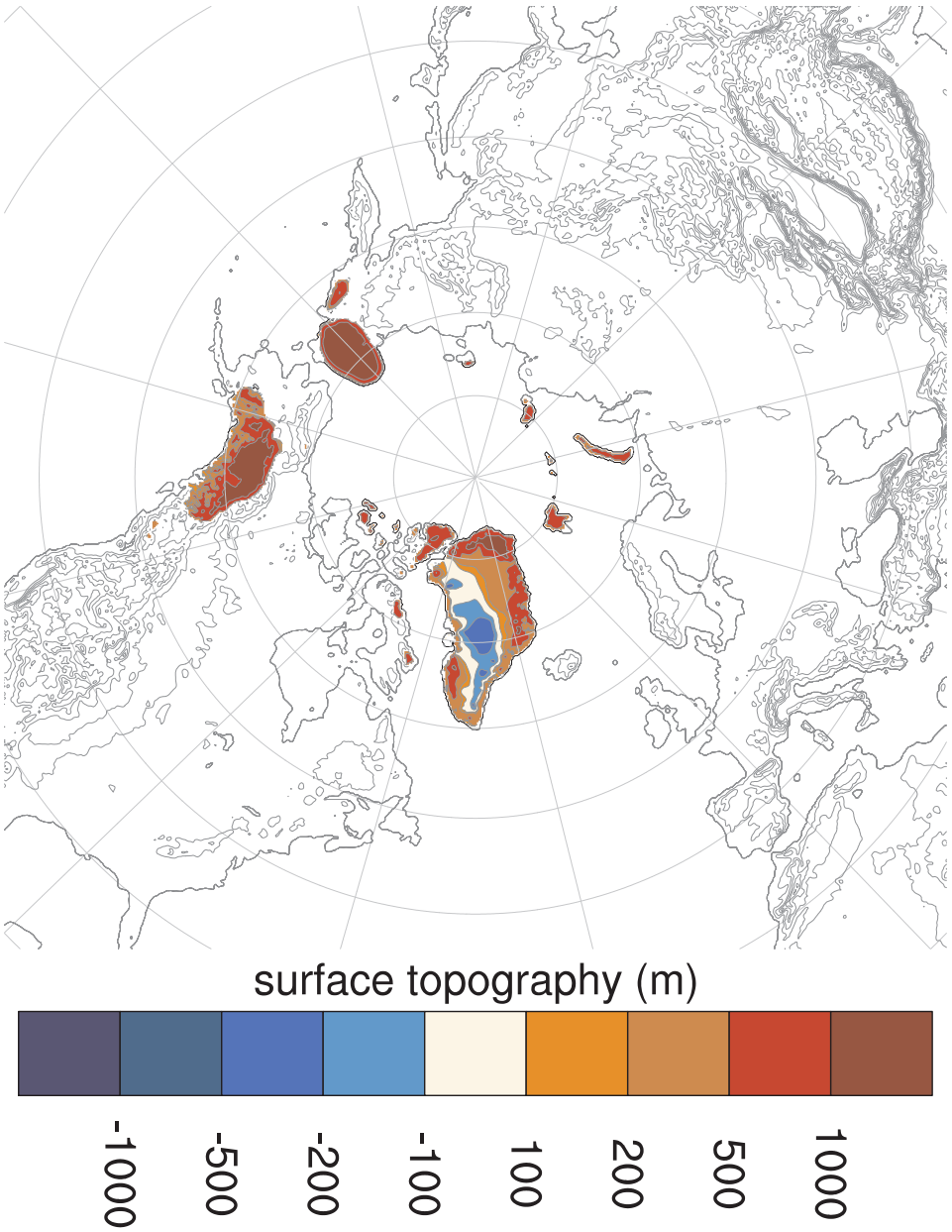

FIGURE 3.5. Topography difference between the surface topography in mPISM averaged over ice-model years 9000-10 000 of the pre-industrial experiment and the reference topography (a smoothed version of ETOPO1, Amante and Eakins (2009)).

very fine model resolution ($\ll 5$ km) in the ISM, that allows resolving the mountain ranges and the individual outlet glaciers.

The surface velocities in the northern part of the ice sheet agree reasonably well with the observations of Joughin et al. (2010a,b) (fig. 3.7). The ridge of the ice sheet can be seen as a low-velocity band and is very well captured in the northern part. In the central part of the East coast of Greenland, the model shows too much ice because of the lack of ablation described above. This leads to an eastward displacement of the ridge of the ice sheet. Since, at the east coast, the model

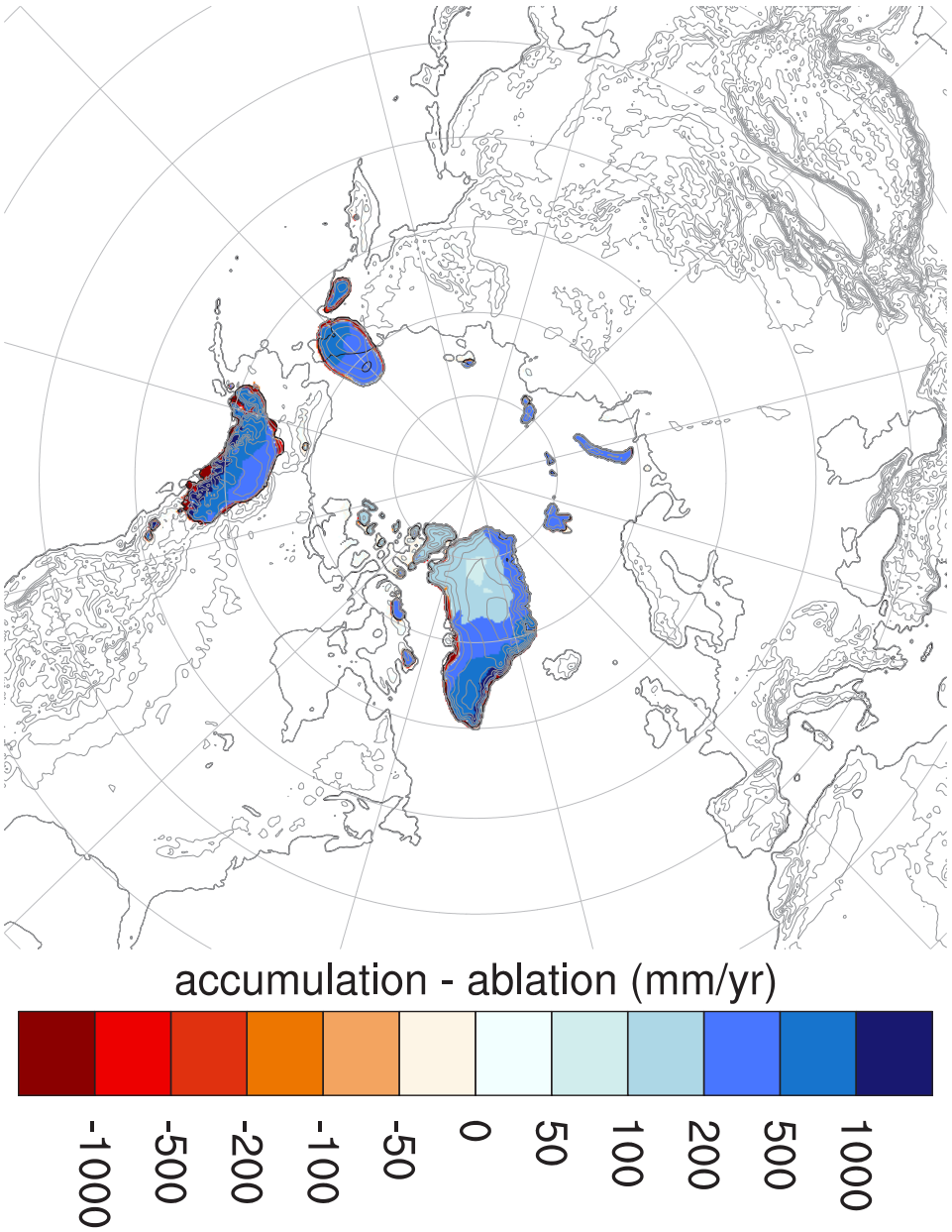

FIGURE 3.6. Ice sheet net surface mass balance averaged over the years 9000 to 10 000 of the pre-industrial simulation. Values are given as ice equivalent ($\rho = 910\,\mathrm{kg/m^3}$).

shows ice in areas that are not glaciated in reality, the flow velocities cannot be compared to observations in this region. In the southeast, there is a massive lack of observations, that prohibits a comparison. In the western part, we capture the general features well, although our velocities generally are too large and the ice sheet reaches further towards the coast than in reality (fig. 3.5). On the Arctic Islands, there are ice caps on Baffin Island and Ellesmere Island, Svalbard, Franz Josef Land, Novaya Zemlya, and Severnaya Zemlya. All of these regions presently also show glaciation.

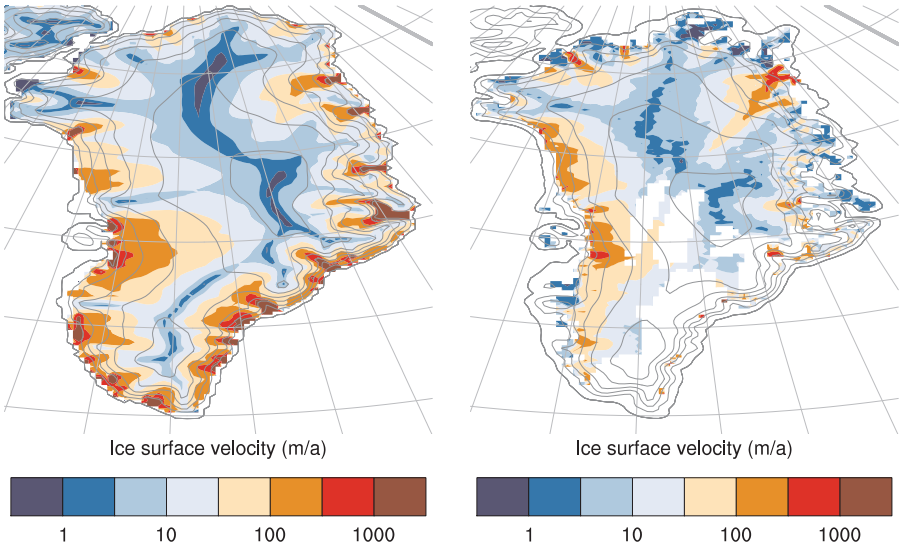

(a) Velocities from mPISM

(b) Observed velocities from Joughin et al. (2010b)

FIGURE 3.7. Observed and modeled Greenland Ice Sheet surface velocities.

TABLE 3.2. Greenland mass balance, RACMO2, Polar MM5 (PMM5) (Box et al., 2006), and MAR (Fettweis, 2007) data are for the period 1958–2007 (RACMO2, MAR), resp. 1958-2006 (PMM5) and are taken from Supplement S1 from Ettema et al. (2009).

	mPISM	RACMO2	PMM5	MAR
Accumulation (Gt/yr)	766.03	697	678	578
Ablation (Gt/yr)	271.23	228	322	290
Accumulation - Ablation (Gt/yr))	494.8	469	356	288

There are ice caps with a total volume of 0.94 Mio km^3 (+86 km^3/yr) growing in Northeast Siberia and there is an ice sheet with a volume of 1.1 Mio km^3 (+31 km^3/yr) in the Alaska Range and the northern Rocky Mountains. In these regions, our climate model shows a cold bias (fig. 3.1(a), section 3.2). This cold bias in regions, that are characterized by many separate glaciers in reality, leads to a glaciation in mPISM that quickly grows because of the positive feedbacks of increasing altitude and albedo. Once a grid cell is considered as glaciated by ECHAM5, this further reduces surface melt in mPISM and strengthens glacier growth. There is no melt in the interior of the Siberian ice caps and the Alaska Range ice sheet.

3.5. The LGM climate experiments

In the following, we discuss the mean state in our LGM model experiments. The results from the coupled experiment (ASYNC) are averaged over the full 3 kyrs for climate model data, corresponding to 30 kyrs of ice sheet model experiments. Unless explicitly stated otherwise, the description *the LGM experiment* refers to ASYNC in the discussion of the mean state. The mean ice sheet topography in ASYNC is displayed in fig. 3.8.

To further investigate the effects of the modeled ice sheets, we performed a comparison climate-only experiment with prescribed ice sheets from the ICE-5G reconstruction of Peltier (2004) (fig. 3.9). This experiment was performed according to the PMIP2 specifications and will be called ICE-5G in the following. The ICE-5G experiment was started from a previous PMIP2-experiment and integrated over 649 years. The results displayed in the following were averaged over the last 100 years. For details of the setups see section 2.5.

The discussion starts with the atmosphere, then continues with the ocean, and the ice sheets. In addition to the description of the mean state in ASYNC, we provide information about the long-term drift in sections 3.9 through 3.11.

3.6. The LGM atmosphere

The change from the pre-industrial to the LGM climate can largely be attributed to the combination of the changes induced by the higher topography and albedo over glaciers and those changes induced by the lower greenhouse gas concentrations. It is, however, difficult to ascribe particular effects in the climate system to particular causes, since there are many interacting and competing effects acting at the same time. We nonetheless describe changes and their causes, taking into account insights from sensitivity experiments performed with the standalone climate model.

In ASYNC, the global annual mean temperature is reduced by $-3.5\,\mathrm{K}$ compared with the pre-industrial experiment (fig. 3.1(b)). Over the oceans, the reduction is -2.5 K, while over the land it is $-5.4\,\mathrm{K}$. Over the areas that are glaciated during the LGM, the temperature difference is $-11\,\mathrm{K}$. Over non-glaciated land, it is $-3.3\,\mathrm{K}$.

In ASNYC, some regions show a warming compared to the pre-industrial conditions (fig. 3.1(b)). These are the northern Pacific, the Atlantic south of the sea ice cover, and, during summer, Siberia. The warming over the northern Pacific can be explained by changes in the stationary eddies which cause an enhanced advection of warm air from the south and by a reduction in the cloud cover in practically all regions north of 45°N allowing for higher shortwave absorption. The warming over the Atlantic can be explained by an increase in the oceanic heat transport and release (see section 3.7). The warming over Siberia is caused by a decrease in cloud cover that results in more shortwave radiation reaching the ground and overcompensates for the effect of the albedo, that is higher during the LGM than during the pre-industrial.

In the ICE-5G setup, the cooling is larger than in ASYNC with a mean temperature difference of $-5.3\,\mathrm{K}$ (fig. 3.1(c)). Over the oceans, the ICE-5G experiment shows a cooling of $-4.1\,\mathrm{K}$, while over the land it is $-7.7\,\mathrm{K}$. Over the areas that are glaciated in the LGM, the temperature difference is $-14\,\mathrm{K}$, while over non-glaciated land, it is $-5.4\,\mathrm{K}$.

To understand the temperature differences between ASYNC and the ICE-5G experiment, we performed a set of sensitivity experiments. Simply replacing the topography of the ICE-5G experiment with that of the coupled run and keeping the glacier mask constant leads to an increase in the global mean 2 m air temperature of $0.87\,\mathrm{K}$ in years 60 to 90 compared with the same years of the ICE-5G experiment. Most of the northern Pacific shows a strong warming. Over the western part, this is largely a downwind effect of higher temperatures in Asia, while over the eastern part, the picture is less clear with strong regional differences in the partitioning of the heat fluxes (not shown). The higher topography over the Canadian Arctic

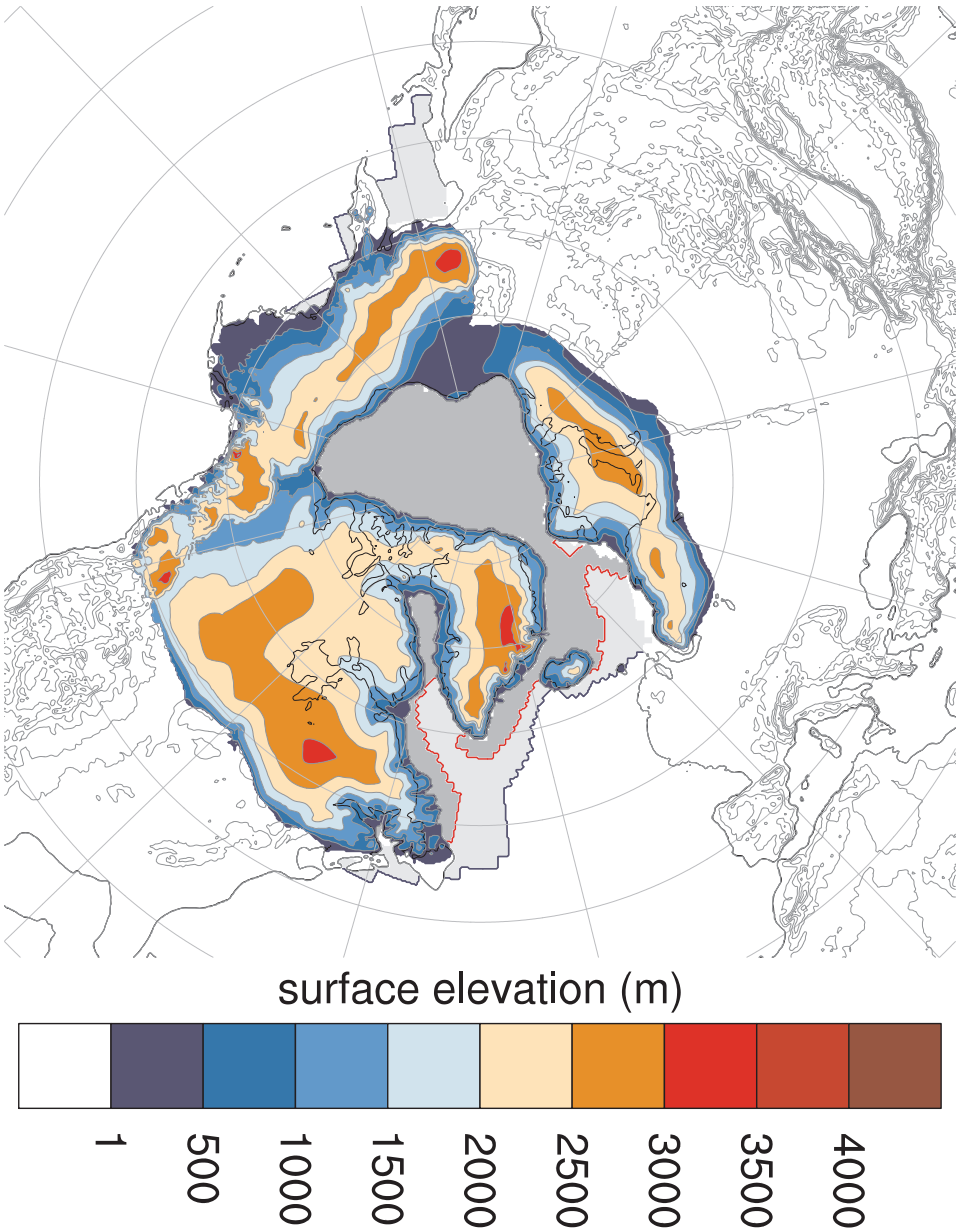

FIGURE 3.8. The surface topography in mPISM averaged over the full 30 kyrs of ASYNC. Outside the ice sheets, the thin isolines mark the topography at 500 m intervals, thick isolines at 1000 m intervals. Ice covered regions are colored. Over the ocean, dark gray with red outline indicates areas with perennial ice cover (15% level) in more than 50% of the model years. Light gray with blue outline indicates temporary ice cover in more than 50% of the model years.

Archipelago and Greenland causes a cooling in these regions, and following from that over the GIN Sea and the Arctic Ocean.

The global mean **precipitation** in ASYNC (figs. 3.3(c), 3.10) of 0.96 m/yr is lower than in the pre-industrial experiment (−0.068 m/yr). This difference is especially pronounced in the regions north of 45°N, where the precipitation is 0.54 m/yr (−0.12 m/yr). The difference in precipitation between the ICE-5G experiment and

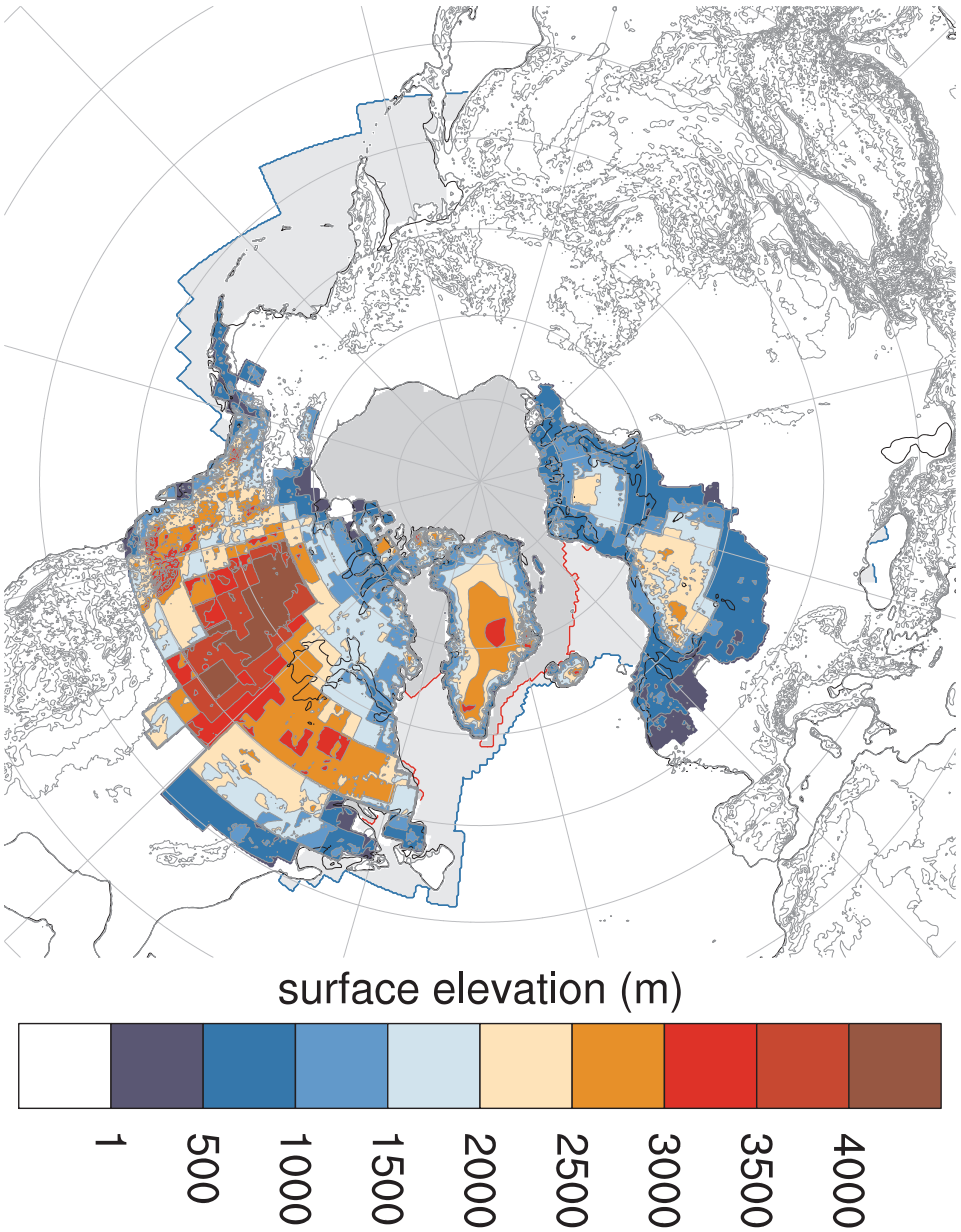

FIGURE 3.9. The surface topography from the ICE-5G reconstruction of Peltier (2004). Ice-covered regions are colored. The thin isolines are every 500 m, thick isolines every 1000 m. Sea ice is taken from ICE-5G experiment. Over the ocean, dark gray with red outline indicates areas with perennial ice cover (15% level) in more than 50% of the model years. Light gray with blue outline indicates temporary ice cover in more than 50% of the model years.

the pre-industrial experiment is larger (-0.11 m/yr globally, and -0.2 m/yr north of 45°N) matching the lower temperature and the thus lower atmospheric moisture content.

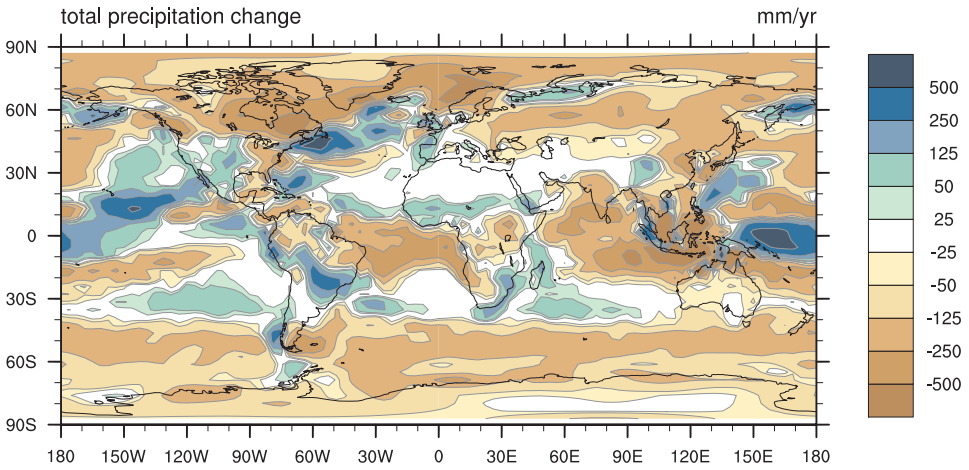

FIGURE 3.10. Precipitation changes in ASYNC compared to the pre-industrial experiment.

3.7. The LGM ocean

There are substantial differences in the **ocean circulation** and oceanic heat transport between the LGM and the pre-industrial experiments. The NADW formation in ASYNC occurs mainly southeast of Iceland (fig. 4.14). The NADW cell of the AMOC (fig. 3.4(b)) has a strength of 22.1 Sv (pre-ind: 17.0 Sv) and has its maximum at 32.5°N and a depth of 1020 m. For the time evolution of the NADW strength, see section 3.11 and section 4.4 (fig. 4.22(c)). The NADW cell reaches approximately 65°N. In contrast to pre-ind, there is hardly any deep water formation in the GIN sea, and thus the NADW cell does not extend north of Iceland. The Antarctic Bottom Water cell also increases in strength and reaches a maximum of 3.6 Sv at 21.5°S and a depth of 3570 m. The ocean heat transport reaches 1.1 PW at 23°N (0.8 PW in pre-ind).

In the ICE-5G experiment, the NADW cell is shallower and weaker than in ASYNC (fig. 3.4(c)). It only reaches 18 Sv at 35.5°N and a depth of 1020 m. It still is stronger than in pre-ind, and, as in ASYNC, it does not extend beyond Iceland. The AABW cell is slightly stronger (3.8 Sv) than in ASYNC and fills the space freed by the smaller NADW cell. The maximum Atlantic heat transport of 1.0 PW at 28°N lies in between the values of pre-ind (0.8 PW) and ASYNC (1.1 PW).

The barotropic circulation (fig. 3.11) in the GIN Sea is weaker in ASYNC than in the pre-industrial setup. The North Atlantic Subpolar Gyre weakens in ASYNC compared to pre-ind. At the same time, the Subtropical Gyre strengthens and the front between the two Gyres is moved northward by increased surface wind stress from the Westerlies (not shown). The ICE-5G simulation shows a weakening of the GIN Sea circulation. In contrast to ASYNC, it has a stronger North Atlantic Subpolar Gyre than the pre-industrial experiment.

The **sea ice** in ASYNC reaches further south in the Atlantic Ocean than in pre-ind (compare fig. 3.8 and fig. 3.2). It reaches Iceland during the entire year and covers much of the deep water formation areas of pre-ind. The winter sea ice margin is located at about 63°N east of Iceland and reaches south to about 43°N at the American east coast. A part of the Labrador Sea becomes ice-free during summer. In the ICE-5G experiment, the winter sea ice is very similar to that of ASYNC. The summer sea ice margin is clearly shifted to the north and the open

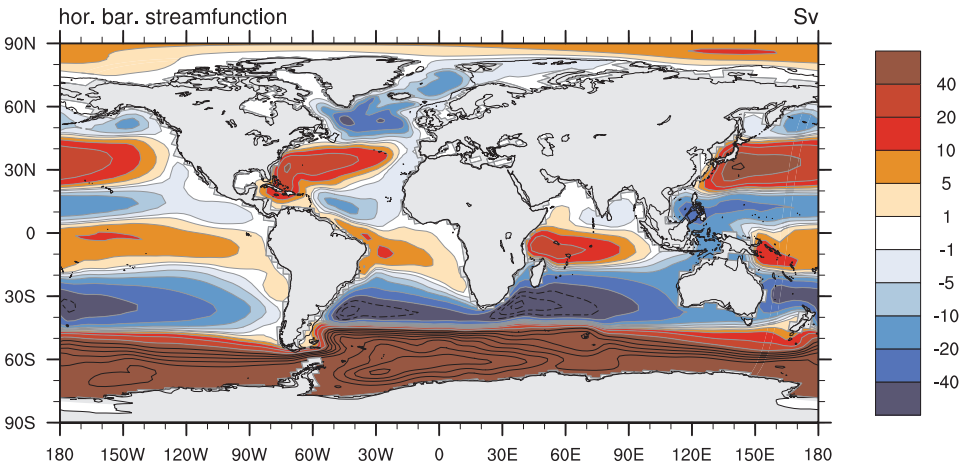

(a) pre-ind (averaged over the last 100 years).

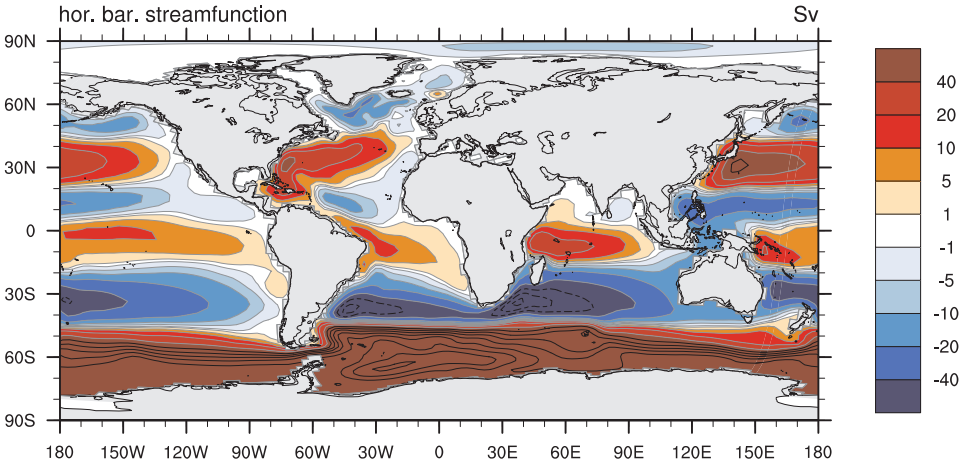

(b) ASYNC (averaged over the full 3 kyrs).

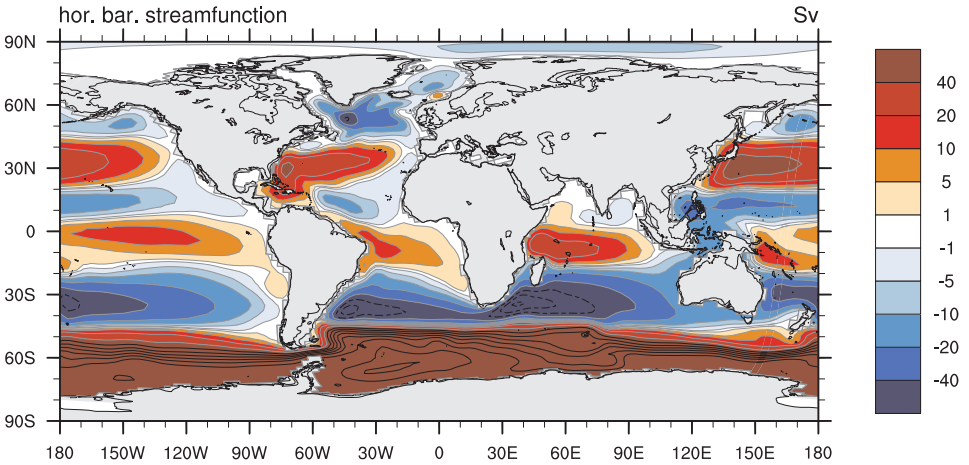

(c) ICE-5G (averaged over the last 100 years).

FIGURE 3.11. LGM barotropic circulation. For values beyond ±40 Sv, black contour lines are drawn at intervals of 20 Sv starting at ±60 Sv. The time variability of the North Atlantic Subtropical Gyre and the North Atlantic Subpolar Gyre is displayed in fig. 4.24.

TABLE 3.3. Heat budget of the Arctic Ocean.

Flux	pre-ind	ASYNC	ICE-5G
Atmosphere–Ocean (TW)	−32.3	−29.6	−34.7
Ice sheet–Ocean (TW)	−1.1	−12.7	0
Sea ice export (mSv)	85.6	125.3	100.1
Heat export corresponding to sea ice export (TW)	23.1	33.8	27.0
Cooling of the ocean water (TW)	10.3	8.4	7.7

TABLE 3.4. LGM Ice sheet volumes and drift. For the ICE-5G-reconstruction see Peltier (2004).

	Volume (Mio km^3)		Drift (km^3/yr)
Ice sheet	ICE-5G	mPISM	mPISM
Greenland	4.3	5.8	−2.6
Iceland	0.17	0.28	+1.2
Laurentide	36	31	+28
Siberia	0	9.3	+108
Fennoscandian	8.2	11.6	+156
Total	48.7	60	+233

area in the Labrador Sea is larger (fig. 3.9). The difference between the two sea ice extents could be due to the ice input from the ice sheet into the ocean, that cools the oceans in ASYNC, and is omitted in the forced experiment.

The role of the heat flux from glacier calving and shelf basal melt in cooling the oceans becomes obvious from the heat budget of the Arctic Ocean (table 3.3). In ASYNC, calving and shelf basal melt from the glaciers contribute 30% of the total cooling of the Arctic Ocean. Because the sea ice cover in ASYNC is thicker than in the ICE-5G experiment, the atmosphere–ocean heat fluxes are reduced in ASYNC compared with the ICE-5G experiment (−15%), although the Arctic air temperature is lower in ASYNC. The sea ice export through the Fram Strait is increased by 25% in ASYNC compared to the ICE-5G experiment. This corresponds roughly to the amount of sea ice formed in the Arctic Ocean from ice sheet calving and sub-shelf melt (compare fig. 4.2). The total heat loss from the Arctic Ocean is lower in pre-ind than in the two LGM experiments, and, in pre-ind, a larger fraction of the heat loss is required to cool the ocean water to the freezing point. Therefore less is available for sea ice formation and export.

3.8. The LGM ice sheets

The total modeled land ice volume in the northern hemisphere is 60 Mio km^3, corresponding to 150 m of sea level change. In table 3.4 we show how this ice volume is distributed among the different ice sheets, fig. 3.12 shows the mask used for this analysis.

Of the 60 Mio km^3 northern hemisphere ice volume, the **Greenland Ice Sheet** contains 5.8 Mio km^3 (14.5 m SLE) compared to 4.3 Mio km^3 (10.8 m SLE) in the ICE-5G reconstruction (Peltier, 2004). It shows a drift of −2.7 km^3/yr averaged

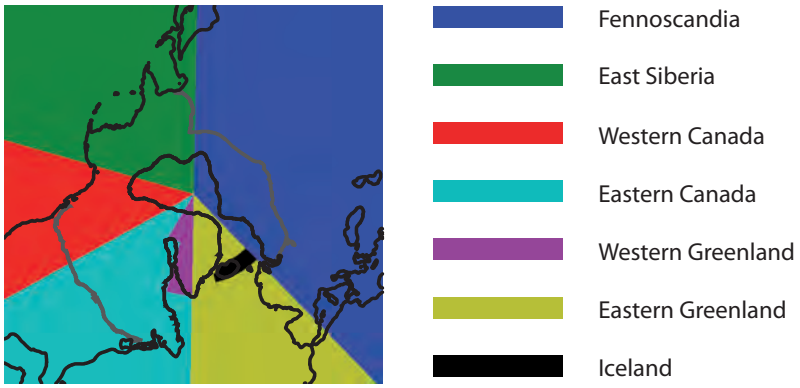

FIGURE 3.12. Regions defined for the analysis of ice sheet volumes. Overlain are the LGM mean coastlines and the southern ice sheet margins on land from ASYNC.

over the full 30 kyrs. The Greenland Ice Sheet is wider in all directions than in the pre-industrial experiment and covers the continental slopes. Its two-dome structure closely resembles that of the pre-industrial experiment. The height of the northern dome is at 3150 m (100 m lower than in the pre-industrial setup). The southern dome profits clearly from the cold climate and the wider ice sheet. It reaches a height of 2850 m (150 m above the value in the pre-industrial setup). The ICE-5G reconstruction also shows a wider and flatter Greenland Ice Sheet during the LGM than at the present, but there is less ice at the margins in the reconstruction than in ASYNC.

The mass balance of the Greenland Ice Sheet switches to a state, where the accumulation is entirely balanced by losses to the ocean. The annual mean accumulation is 558.14 Gt/yr. Fig. 3.13 shows the spatial distribution of the net surface mass balance of the LGM ice sheets averaged over the years 85 500 to 87 500 (the reference period we will use for the analysis of SYNC in the following chapter). We choose a rather short time window, because the surface mass balance strongly depends on the topography and thus the plot is more meaningful if we average over a time window with only small changes in the topography than if we average over the entire experiment.

Fig. 3.14(a) provides an overview of the active ice streams. On the continental shelf, the Northeast Greenland Ice Stream surges repeatedly. Another stream that is active only part of the time follows a trough in front of Kejser Franz Joseph Fjord (73° N) matching Wilken and Mienert (2006). South of it, at Scoresby Sund (70.5° N), an ice stream is continuously active matching with massive glacial deposits found in this area (Wilken and Mienert, 2006). Straight west of Iceland, Kangerdlugssuaq glacier drains into the Atlantic. Further Glaciers follow on the East coast. On the West coast, ice streams undergo recurring surges in the region of Jakobshaven Isbrae (E) and the trough north of it matching proxy observations in Roberts et al. (2009). Further north, in the region of Kong Oscar Glacier (F), two tributaries show surge-type activity. Since the sediment mask we use in mPISM (see section 2.2 and fig. 2.1) does not allow for sliding in the interior of Greenland, the ice streams are limited to the continental shelf. This does not prohibit fast-flowing ice as can be seen for pre-ind in fig. 3.7, where ice flows fast in areas where the ice cannot slide in our model because there are no basal sediments. This fast flow then happens purely by internal deformation. The inclusion of temperate ice

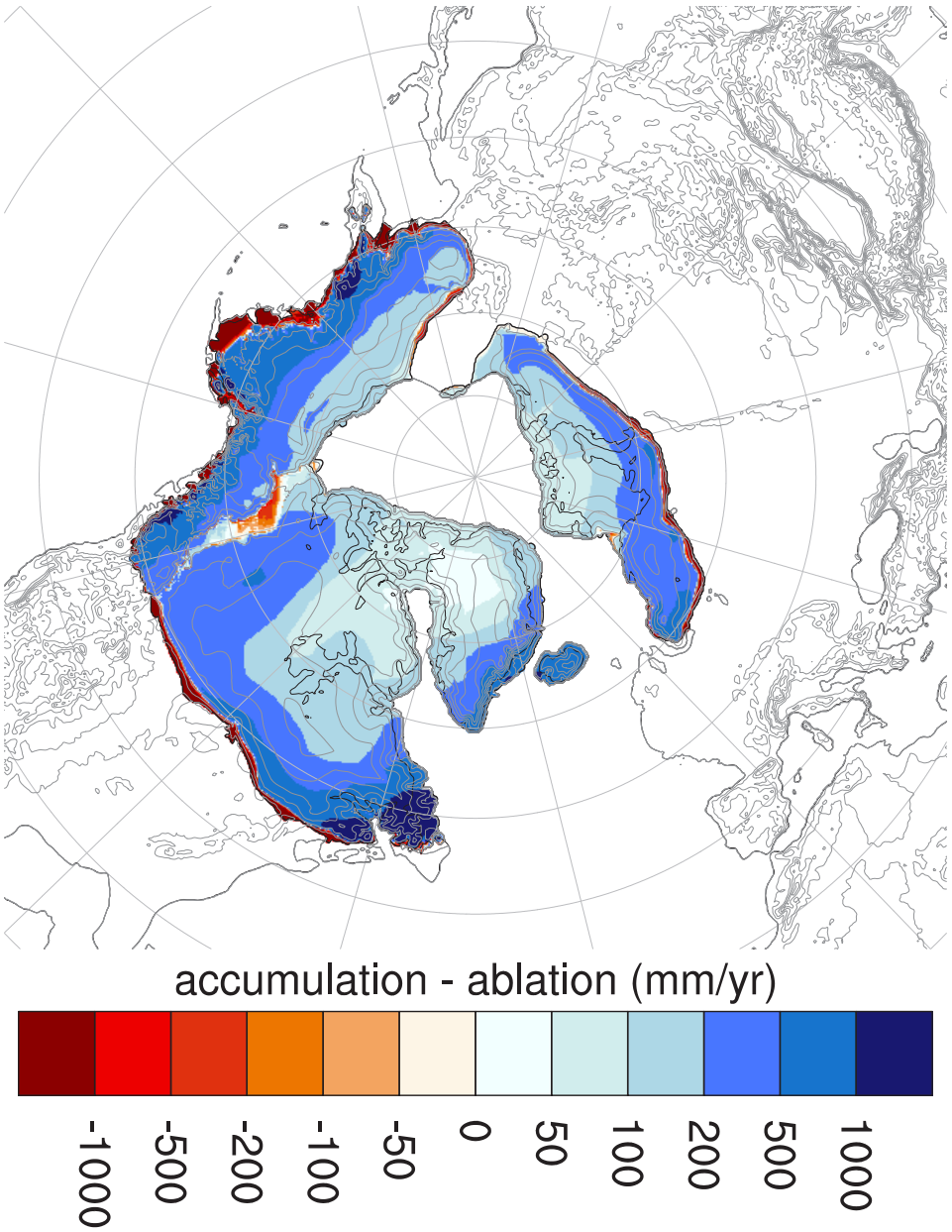

FIGURE 3.13. Surface mass balance of the ice sheets averaged over the years 85 500 to 87 500 of ASYNC.

in PISM allows for a very low viscosity, so the ice can reach high speeds by pure internal deformation without basal sliding.

Baffin Island and **Ellesmere Island** are fully glaciated in ASYNC and connect the Greenland Ice Sheet to the Laurentide Ice Sheet. The **Laurentide Ice Sheet** covers present-day Canada and has a mean volume of 31 Mio km^3 (ICE-5G: 36 Mio km^3), corresponding to 78 m of sea level (ICE-5G: 90.7 m SLE). In the west, it terminates inland of the coast, while in the east and north, it fully covers the coasts. The southern boundary is approximately at 50°N in the west and at 45°N in the east. The Laurentide Ice Sheet is split into a main part and a western

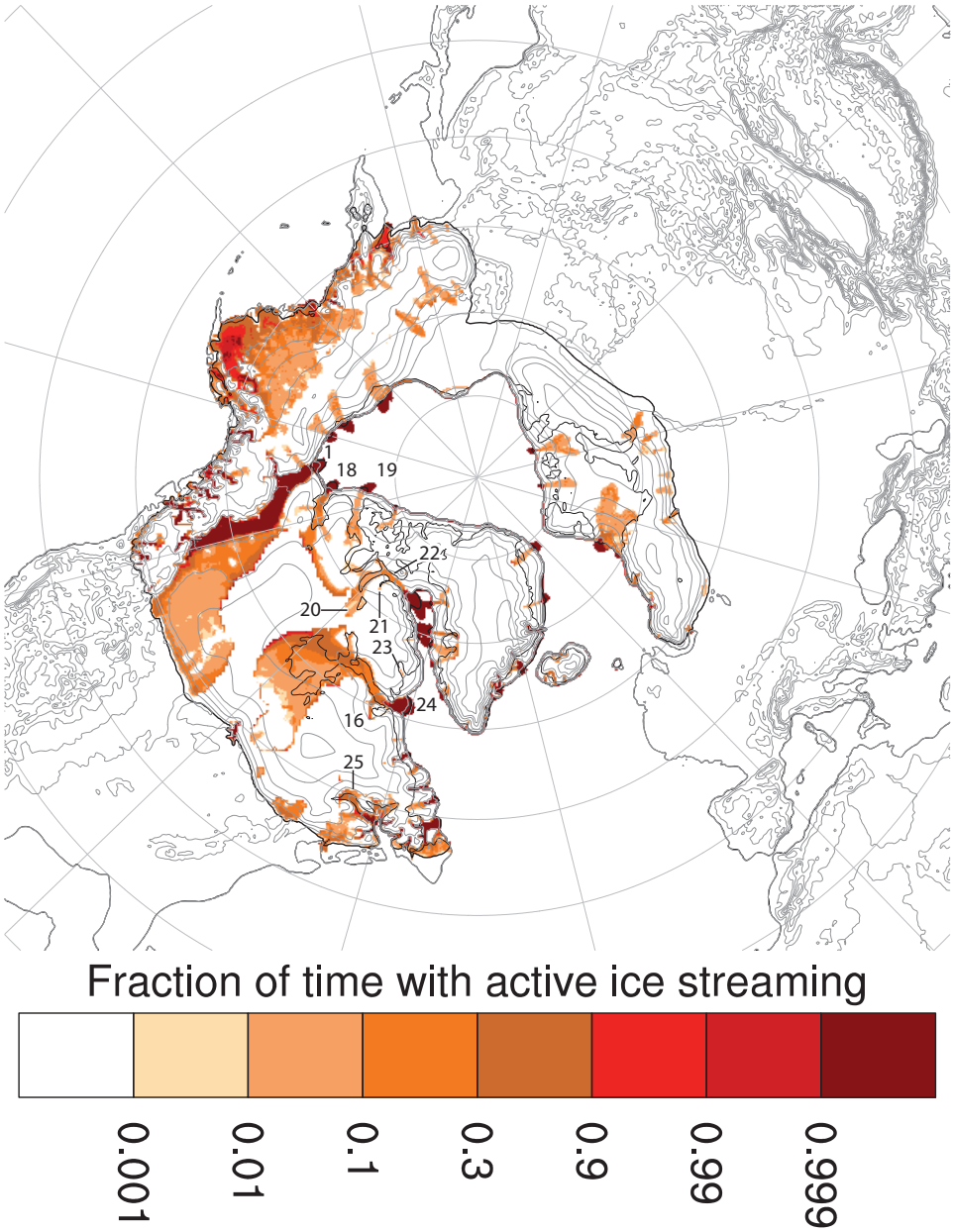

(a) Fraction of time that a specific grid cell is sliding at more than 1 m/yr. Only the time when the grid cell is ice-covered is taken into consideration. Ice shelves count as constantly sliding. Numbers match the Ice Stream numbering in Stokes and Tarasov (2010) and are as follows: 1 Mackenzie, 16 Ungava Bay, 18 Amundsen Gulf, 19 M'Clure Strait, 20 Gulf of Boothia, 21 Admirality Inlet, 22 Lancaster Sound, 23 Cumberland Sound, 24 Hudson Strait, 25 Laurentian.

cordilleran part by the Mackenzie Ice Stream. This ice stream cuts down to below 1500 m asl. and is in continuous operation with an average strength of 694 Gt/yr (21 mSv water equivalent). For the time evolution of the ice stream strength see fig. 4.2. Over large time fractions, Mackenzie Ice Stream shows net surface melt in its northern part (fig. 3.13). This area is characterized by very low surface elevations. The main part of the Laurentide Ice Sheet has two domes that are separated

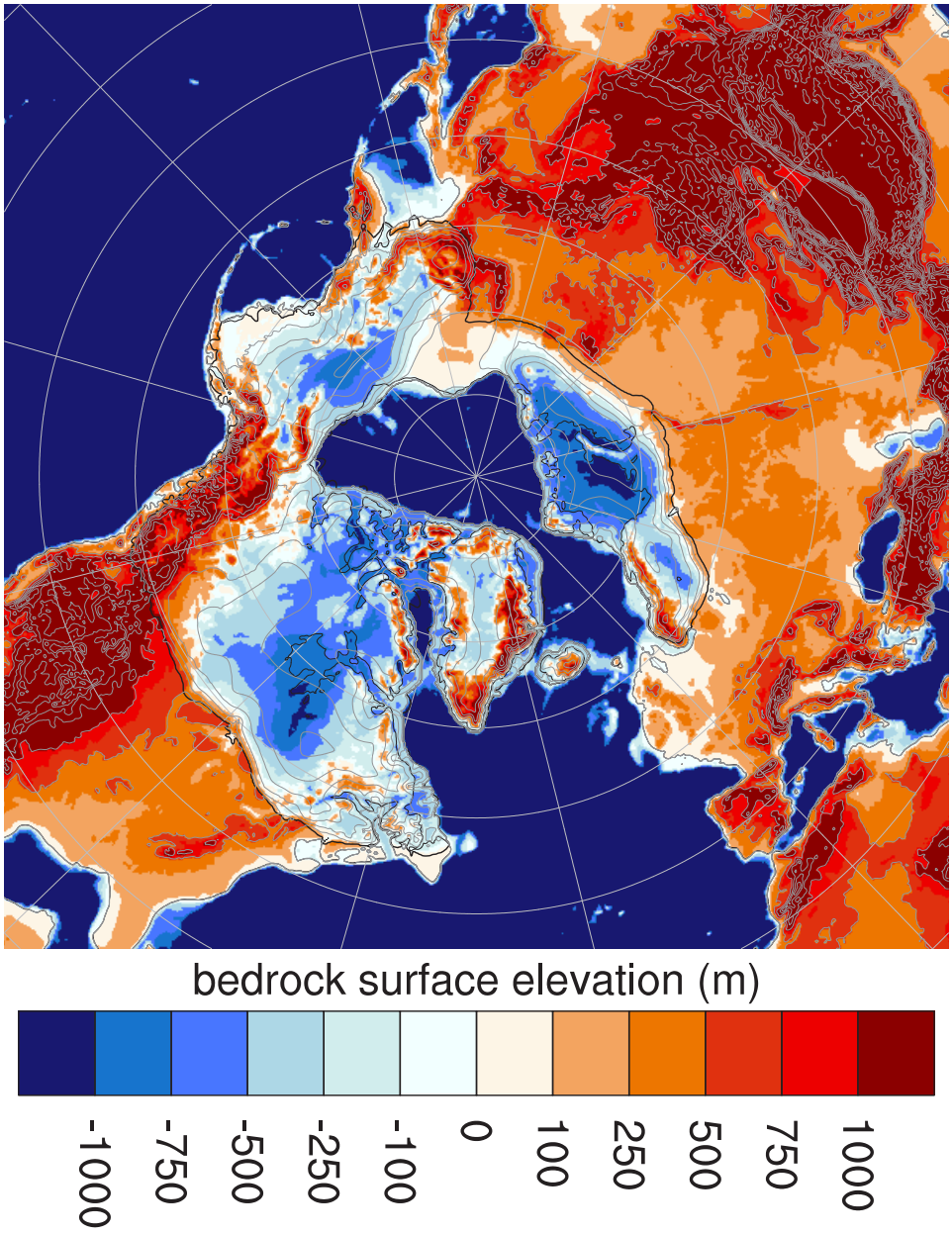

(b) Mean bedrock topography in ASNYC.

FIGURE 3.14. The ice streams and bedrock topography in ASYNC.

by the Hudson Bay. The maximum height of the eastern dome is 3200 m (3600 m of ice thickness), the maximum height of the western dome is 3150 m (also 3600 m of ice thickness). The Hudson Bay area is largely drained by the Hudson Strait Ice Stream that every 7000 years flushes ice into the Labrador Sea. Unless otherwise noted, we average over this oscillation in this chapter. Details of the oscillation and its implications in the climate system are covered in chapter 4. The main part of the Laurentide Ice Sheet loses ice by surface melt at its southern boundary and by calving into the ocean at the eastern and northern boundaries (fig. 3.13).

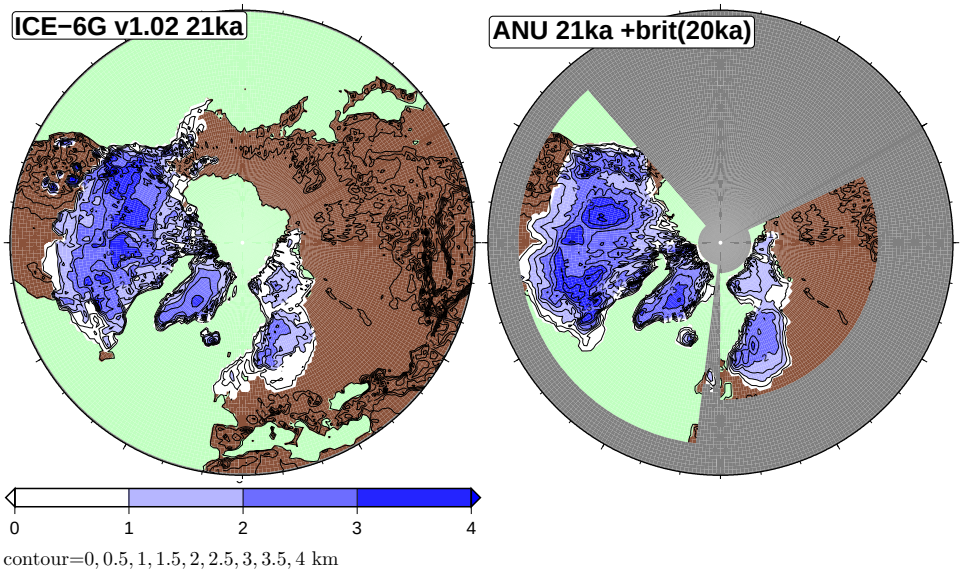

FIGURE 3.15. The PMIP3 comparison plot of the ice sheet surface reconstructions by Peltier (ICE-6G) and Lambeck (ANU). Adapted from: `https://pmip3.lsce.ipsl.fr/wiki/lib/exe/fetch.php/pmip3:design:21k:icesheet:gnh5.pdf`

The cordilleran part of the Laurentide Ice Sheet reaches heights of up to 3550 m, but these elevations are reached only on high mountains, so the thickness there is only around 1000 m. In valleys, the thickness reaches up to 2700 m, with surface heights of up to 2800 m. The surface accumulation of the cordilleran part of the Laurentide Ice Sheet is balanced by the Mackenzie Ice Stream on the eastern side and by surface melt on the western side. The melt on the western side is possible because of the high temperature in the northern Pacific, that can exceed pre-industrial levels.

We compare our results to four reconstructions. The widely used ICE-5G reconstruction (fig. 3.9, Peltier (2004)), its follow-up ICE-6G as provided by the PMIP-3 project (fig. 3.15), the latest reconstruction by Lev Tarasov (fig. 3.16, Tarasov and Peltier (2003); Tarasov et al. (2012) (labeled as Tarasov in the following) and the reconstruction by Kurt Lambeck as provided by the PMIP-3 project[1] (fig. 3.15, ANU in the following). None of the reconstructions show an ice-free west coast. They differ in the southern boundary and in the details of the structure of the interior of the ice sheet. All four reconstructions agree with our model in putting the south-western edge further to the north than the eastern edge, with values for the south-western edge between 42°N (ANU and ICE-6G) and 50°N (Tarasov) (50°N in our model). For the south-eastern edge the values are between 35°N (ANU and ICE-6G) and 40°N (Tarasov and ICE-5G), while our model yields 45°N. Considering our climate model has a resolution of about 3.75°, this is a good match.

In the interior of the Laurentide Ice Sheet, ICE-5G shows a massive mountain range between 90°W and 120°W, reaching about 4500 m asl. This range is smaller in the follow-up ICE-6G, and also in the ANU and Tarasov reconstructions.

The ANU reconstruction features the clear split into a western and a central part that also occurs in our model with the Mackenzie Ice Stream separating the

[1]Kurt Lambeck, Australian National University, unpublished, see `https://pmip3.lsce.ipsl.fr/wiki/lib/exe/fetch.php/pmip3:design:21k:icesheet:gnh5.pdf`

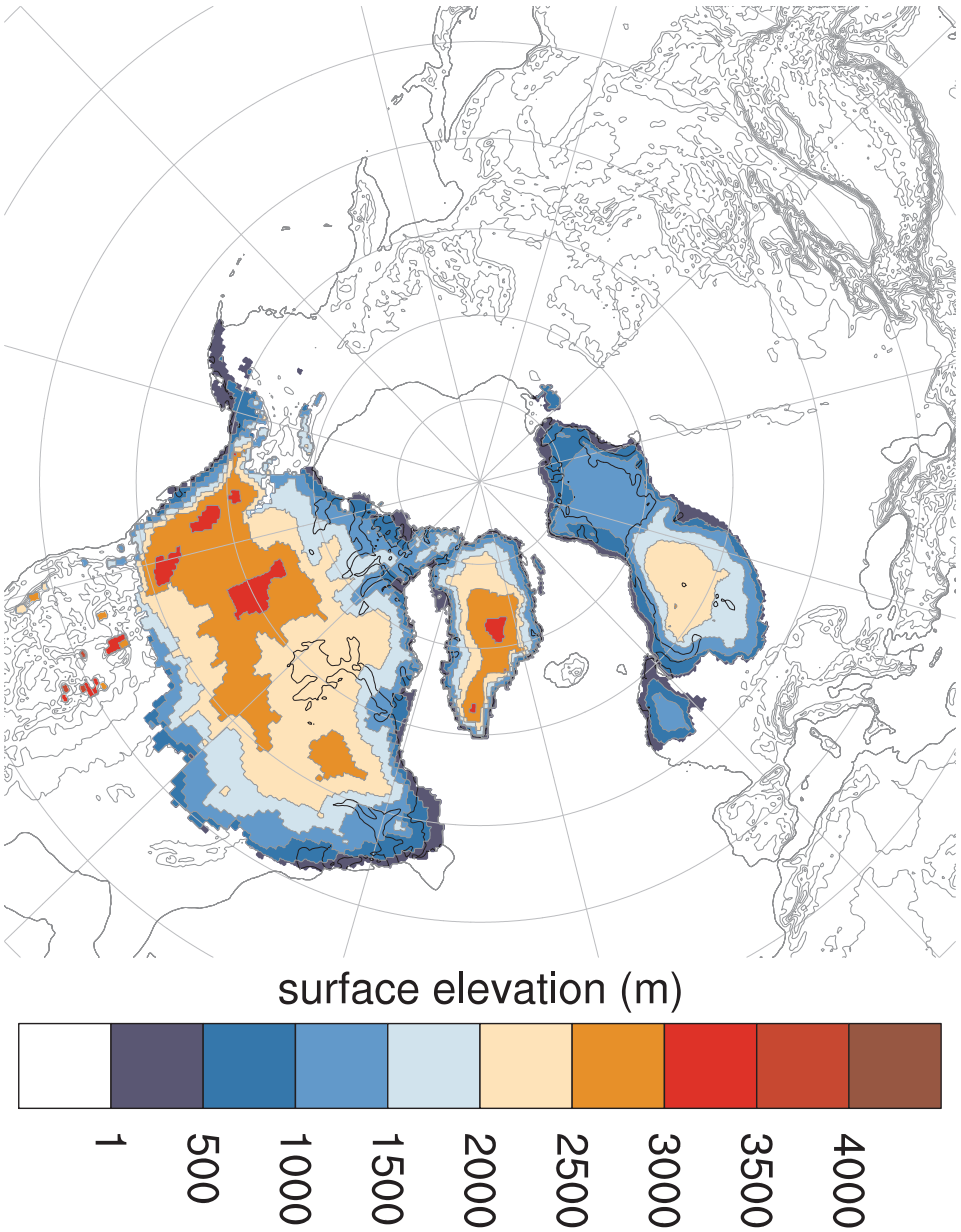

FIGURE 3.16. The LGM topography provided by Lev Tarasov. Ice-covered regions are colored.

two parts of the ice sheet. In ICE-5G and in the Tarasov reconstruction this split also exists, although the stream is less well represented. It is hardly discernible in ICE-6G.

In the central part, the ANU reconstruction shows a higher surface elevation than our model, but the structure is very similar with a rather low surface elevation in the region of the Hudson Bay and higher surface elevation south and west of it. A similar structure can be seen in the Tarasov reconstruction. West of the Hudson bay, ICE-5G, shows a massive mountain range between 90°W and 120°W, reaching about 4500 m asl, while ICE-6G has a peak exactly in the Hudson Bay area.

A comparison of the ice streams observed in the model (fig. 3.14(a)) with those found in proxy records (Stokes and Tarasov, 2010) shows several ice streams, where models and reconstructions agree. In the following, numbers relate to the numbering in Stokes and Tarasov (2010) and are employed in fig. 3.14(a). The central Laurentide Ice Sheet is drained into the Arctic Ocean by Mackenzie Ice Stream (1). There are two major ice streams in the Canadian Arctic Archipelago, the Amundsen Gulf ice stream (18) just to the east of Mackenzie, and M'Clure Strait (19) north of Amundsen Gulf Ice Stream. Both show surge behavior. So does Lancaster Sound Ice Stream (22) with its tributaries, the Admirality Inlet (21) and the Gulf of Boothia ice stream (20). They drain the north-eastern part of the Laurentide Ice Sheet into Baffin Bay. Further to the south, hardly represented, the Cumberland Sound Ice Stream (23) surges into the Davis Strait. South of Cumberland Sound and well represented, the Hudson Strait Ice Stream (24) drains the Hudson Bay into the Labrador Sea. The Hudson Strait is not the only possible ice stream route for draining the Hudson Bay. The sediment distribution allows for a more northerly route joining the Lancaster Sound ice stream and draining into the northern corner of Baffin Bay (fig. 2.1). However, this route does not become active in our experiments (fig. 3.14(a)). Directly south of the main Hudson Strait, an ice stream drains the Ungava Bay (16) into the Hudson Strait. In the Gulf of St Lawrence, a large ice stream system forms in the Laurentian Channel (25) and neighboring tributaries.

The Laurentide Ice Sheet connects via Alaska to an ice sheet in eastern Siberia, that did not exist in reality. This **East Siberian Ice Sheet** has a maximum height of 3300 m and a volume of 9.3 Mio km^3, corresponding to 24 m SLE. The drift is +108 km^3/yr. In the model, the East Siberian Ice Sheet closes the gap between the Laurentide Ice Sheet in the East, and the Fennoscandian ice sheet in the West. Krinner et al. (2011) came to the conclusion that two important factors for not glaciating eastern Siberia are (1) the low snow albedo that is caused by dust deposition, and (2) moisture blocking by the Fennoscandian ice sheet. We do not use a locally varying glacier albedo, so the first effect is not represented in our setup. Our Fennoscandian ice sheet does not reach as far south as indicated by the reconstructions and the low resolution of the Atmosphere model does not allow for a realistic simulation of the moisture blocking. Furthermore, we run the model under LGM boundary conditions for a long time span, so our (steady-state) response must be expected to be very different from a transient simulation. The East Siberian Ice Sheet loses mass by surface melt along all margins except for the Arctic Ocean coast, where the losses occur purely by calving and shelf basal melt. Further calving and shelf basal melt occur at the pacific coast (fig. 3.13).

The **Fennoscandian Ice Sheet** has a volume of 11.6 Mio km^3 (29.2 m SLE; ICE-5G: 8.2 Mio km^3, 20.7 m SLE) and shows a drift of +156 km^3/yr. It consists of two main parts. One part covering the Barents, Kara and Laptev sea shelves and the islands in this region up to Svalbard in the northwestern corner, and one part over Scandinavia south to 60°N. The eastern part starts with a peak height of 2600 m. During the experiment, the ice sheet expands southward, and the peak shifts to the south and grows to 3000 m. The western part starts with a peak height of 2730 m, decreases to 2600 m during the first 10 000 years and then stabilizes. Along the southern border and parts of the Norwegian Sea coast, there is surface melt. At the Arctic Ocean coast, all losses occur directly into the ocean (fig. 3.13).

Among the reconstructions of the Fennoscandian Ice Sheet, ICE-5G and ICE-6G show the largest low-thickness zones. Such zones are hard to obtain as a steady state solution in an dynamical ice sheet model, where there are positive feedbacks

for ice sheet growth, until either height desertification or a nearby coast limit the ice sheet height. They are easier to obtain as a transient state. The closure of the gap between the Fennoscandian ice sheet and the East Siberian ice sheet at the end of the coupled experiment shows such a large, flat zone, that is growing by surface accumulation. ICE-5G contains a Fennoscandian ice sheet that reaches far to the south and features surface height below 1000 m in its southern parts. In the ANU and reconstruction, the region between 50°N and 60°N is covered with substantially thicker ice exceeding 1500 m in large parts and even exceeding 2500 m over Norway. The surface elevations in the Tarasov reconstruction are lower over Norway and the Barents Sea than in the ANU reconstruction, but the reconstructions largely agree. Over the Barents, Kara, and Laptev Seas, our model places much more ice than the reconstructions. The locations of the ice streams with massive streaming happening between Norway and Svalbard and further streams between the present-day islands at the northern margin of the ice sheet (β, γ) match well with proxy records (Denton and Hughes, 1981). The southern margin ice streams cannot be compared to the reconstructions, since the margin is too far in the north.

Iceland is covered by an ice cap with a volume of 278 000 km^3 (0.7 m sle, ICE-5G: 172 000 km^3, resp. 0.43 m sle) and a maximum height of 2450 m (1400 m ice thickness).

3.9. Long-term changes in the ice sheets

Fig. 3.17 shows the time evolution of the ice sheets in ASYNC, fig. 3.18 shows the evolution of their volumes. In the following, we describe the long-term changes in the ice sheets. The recurring surges are covered in chapter 4.

As mentioned before, the eastern part of the Fennoscandian ice sheet slowly expands southward. This allows the ridge to shift southward and increase in altitude. For the first 20 000 ice model years, the snow in the region between the Fennoscandian and the Siberian ice sheets melts during the summer, except for a few cold years, when it survives the summer melt. The ice sheets slowly grow into this area by advective ice transport and start closing the gap from the sides (fig. 3.19). After this time, the winter snow in the gap between the ice sheets survives the summer melt and the gap between the ice sheets is largely closed by glacier growth from local accumulation.

The closing of the gap between the ice sheets has implications for the atmospheric transports into and out of the Arctic, since after closing this gap, the GIN Sea becomes the only free passage into and out of the Arctic.

There is a second example of fast increase in ice sheet area. The Bering Sea shelf is flooded with Ice from Alaska between years 9 000 and 11 000. The ice stream surges transport vast amounts of ice into the region (fig. 3.14(a)) and, in the first years, have to compensate for strong surface melt. Over time, the ice sheet in this region stabilizes.

The other regions show little long-term drift. This does not preclude repeating surge-type behavior that is covered in chapter 4.

3.10. Long-term changes in the atmosphere

To provide an overview of the largest long-term changes in the atmosphere, we show the differences in key variables between the mean state of the last millennium and the first millennium of ASYNC. The surface air temperature (fig. 3.20) north of 70°N generally decreases with the strongest changes in the areas of the expansion of the Fennoscandian and East Siberian Ice Sheets. The expansion of the ice sheets

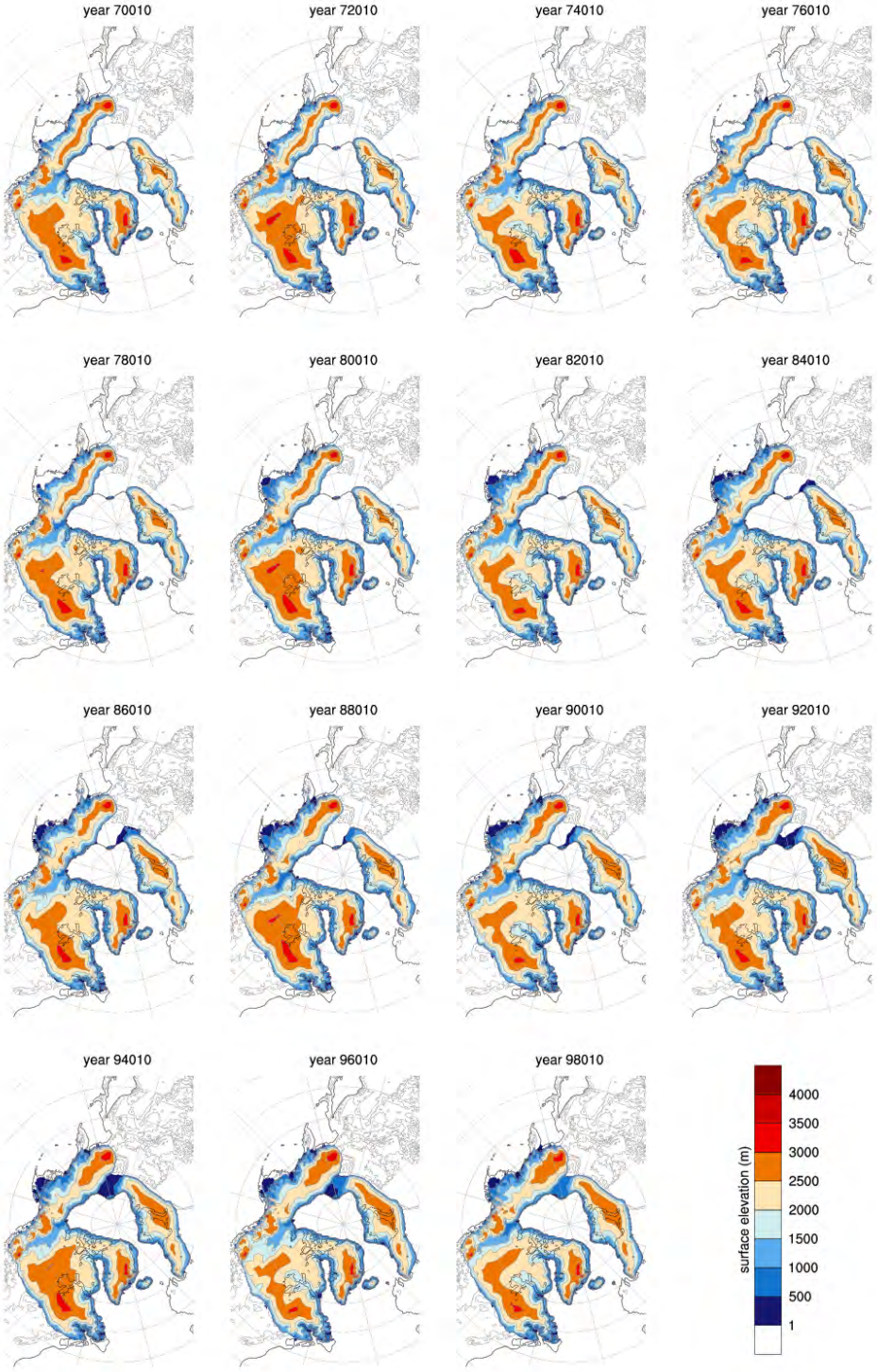

FIGURE 3.17. Ice sheet surfaces throughout ASYNC.

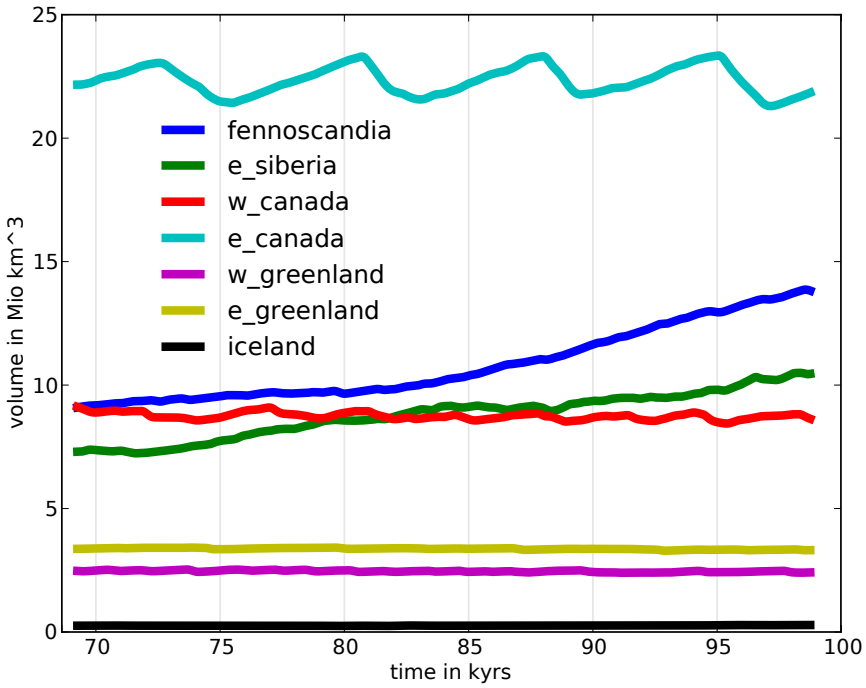

FIGURE 3.18. Development of the ice sheet volumes in ASYNC.

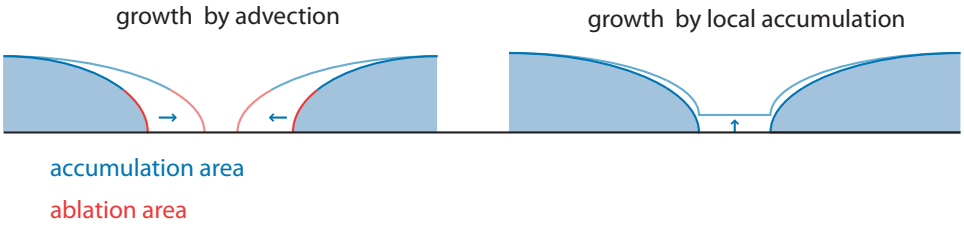

FIGURE 3.19. Growth modes the gap between the Fennoscandian and the east Siberian ice sheet. In advective growth, the ice sheet brings more ice into the ablation area than is molten during the summer season. The flanks of the ice sheet have the typical steep shape that stems from the strong thickness dependence of ice transport. When the climate cools strong enough to permit the ice between the glaciers to survive the summer season, the ice between the two ice sheets builds up as one flat surface. See fig. 3.17.

strongly increases the albedo (not shown) and thereby reduces the absorption of incoming shortwave radiation (fig. 3.21). Over the GIN Sea, we sea a strong cooling. This is caused by an increase in the the sea ice cover (fig. 3.26). The additional sea ice reduces the shortwave absorption during summer and reduces the ocean heat loss during winter. Especially during the second half of the experiment, the northerly wind over the GIN Sea strengthens (fig. 3.22). The air cools up to a height of 300 hPa (fig. 3.23), the SST decreases (fig. 3.27) and the ice covered area grows. The northern Laurentide Ice Sheet cools largely because there is less heat transported there by the atmosphere (fig. 3.24). The ocean and air temperatures south of Greenland are dominated by the ice stream surges, but there is a slight trend towards higher temperatures. This matches with the increasing strength of the AMOC (fig. 4.22).

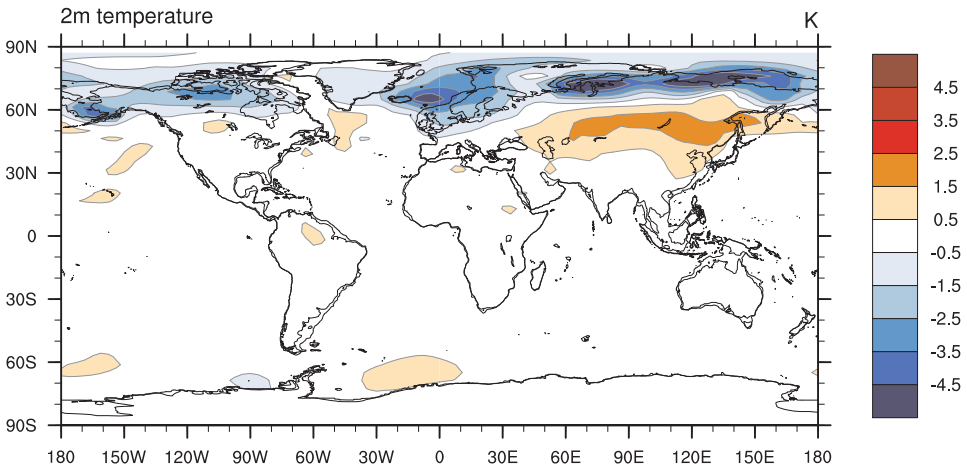

FIGURE 3.20. Change in 2 m air temperatures between last and the first millennium of ASYNC (years 8900 to 9899 – years 6901 to 7900).

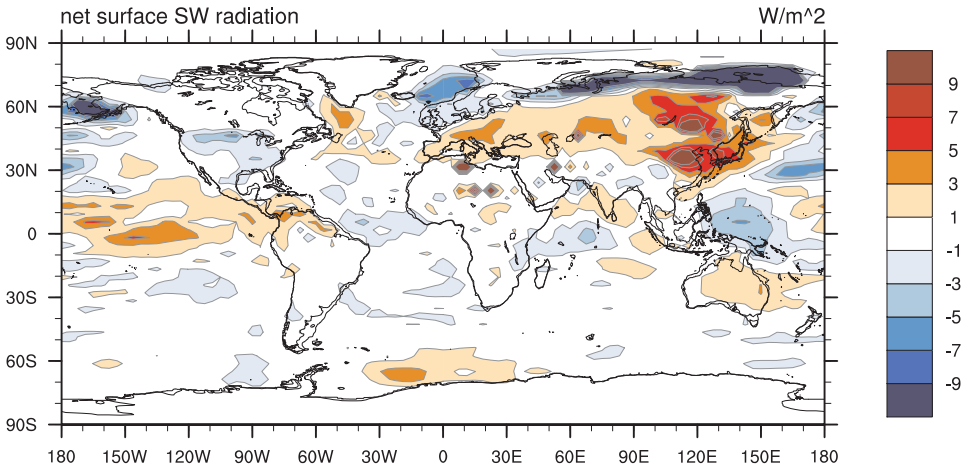

FIGURE 3.21. Change in surface net shortwave radiation between the last and the first millennium of ASYNC (years 8900 to 9899 – years 6901 to 7900).

In Siberia, there is a large-scale warming south of the ice sheets. In this region, more shortwave radiation reaches the surface (not shown) and is absorbed (fig. 3.21). The atmospheric heat transports into this region show smaller changes than the radiative changes and rather lead to a redistribution in the area than to an increased transport into it.

There is a warming over the Atlantic sector of the Arctic Ocean, where the sea ice cover decreases.

3.11. Long-term changes in the ocean

With the growing meridional temperature gradient over the Atlantic, the NADW cell of the AMOC grows in strength (fig. 4.22(c)), while the AABW cell shows no long-term drift separable from the variability (fig. 4.22(d)).

The stratification in the Arctic Ocean and the GIN Sea weakens over time. We show this for the Arctic Ocean in fig. 3.29. The temperature maximum of the Atlantic inflow is slowly eroded and the deep water warms over time. At the

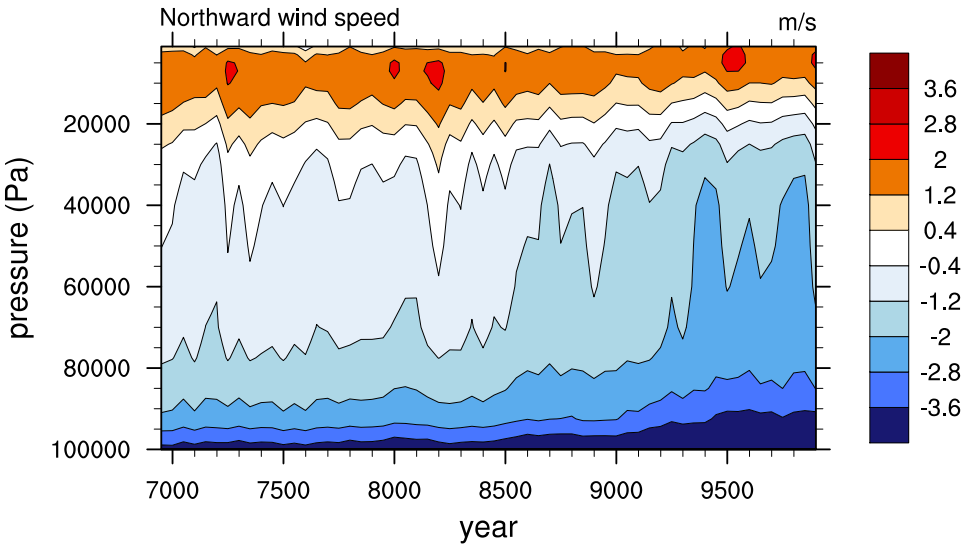

FIGURE 3.22. Annual mean northward wind velocities over the GIN Sea region (20°W to 20°E, 65°N to 80°N)

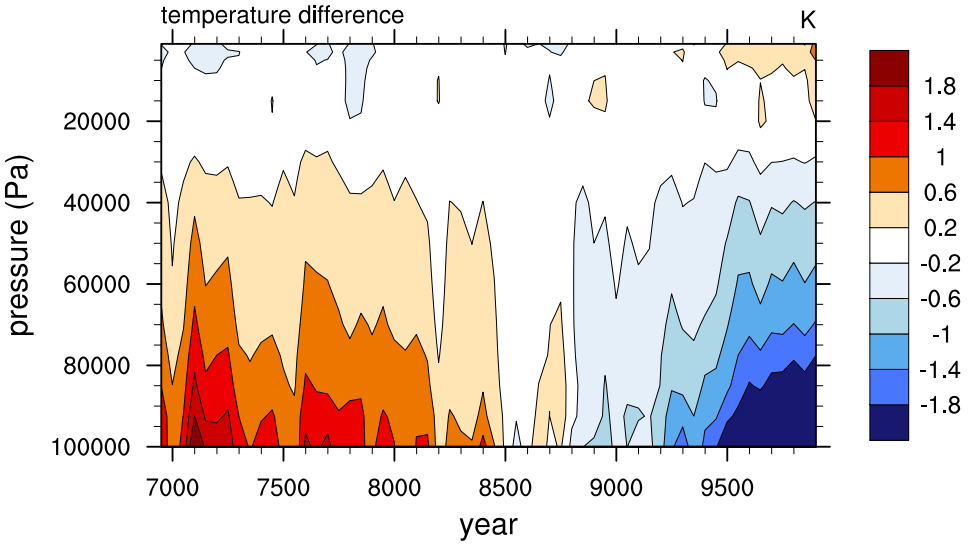

FIGURE 3.23. Temperature difference to the experiment mean over the GIN Sea region (20°W to 20°E, 65°N to 80°N).

same time, the salinity of the deep water decreases and the salinity at the surface increases. Deep water is formed southwest of Svalbard in the Greenland Sea.

While the SST in the GIN Sea decreases, the deep sea temperature keeps rising until deep convection, which is basically absent in the GIN Sea in the first half of the experiment, starts again (not shown).

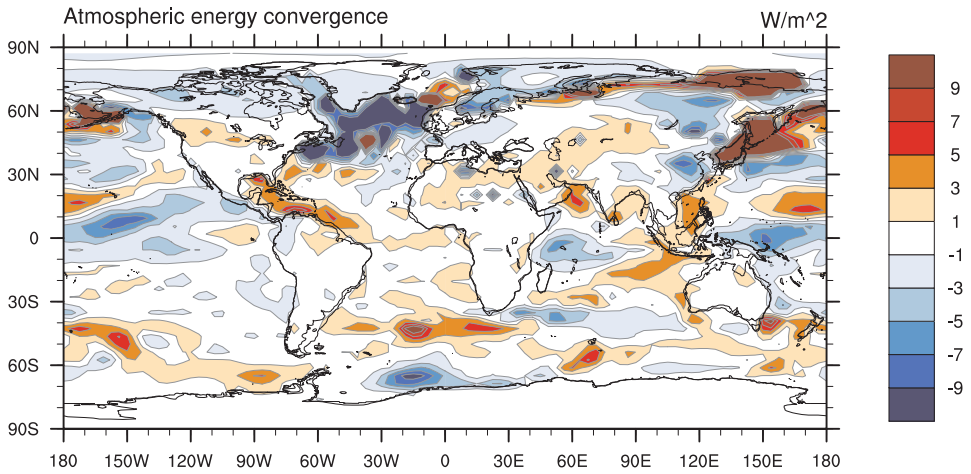

FIGURE 3.24. Change in atmospheric energy convergence between the last and the first millennium of ASYNC (years 8900 to 9899 – years 6901 to 7900). Positive values indicate more heat being transported into a region in the last millenium.

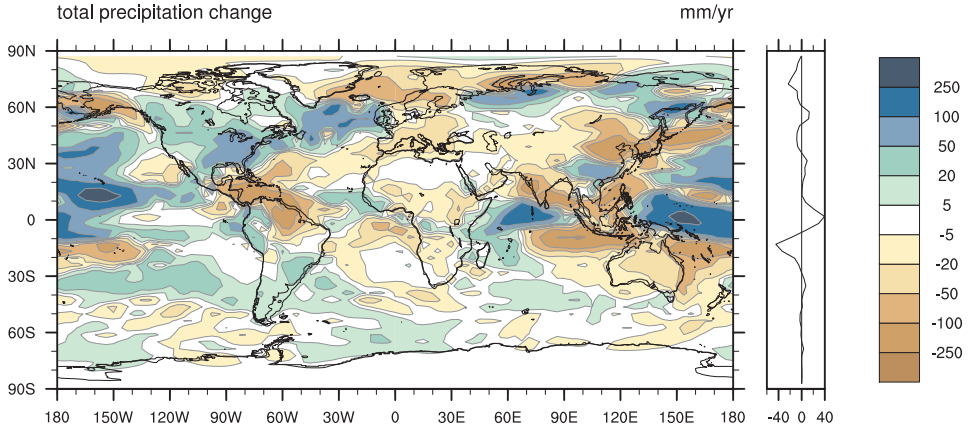

FIGURE 3.25. Precipitation difference between the last millennium and the first millennium of ASYNC (8900 to 9899 – 6901 to 7899).

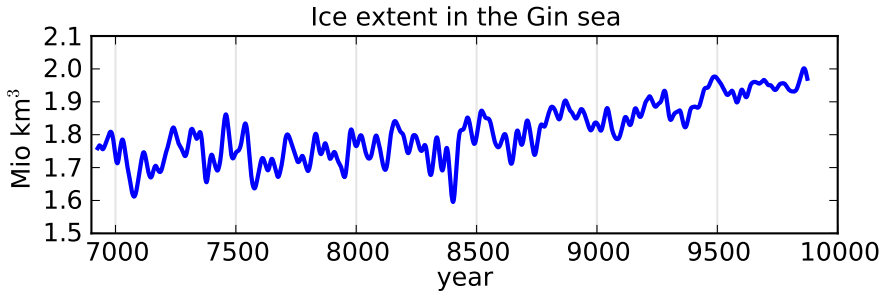

FIGURE 3.26. 50 year running mean of the sea ice extent in the GIN Sea. The total area of the GIN Sea in our setup is 2.1 Mio km^3.

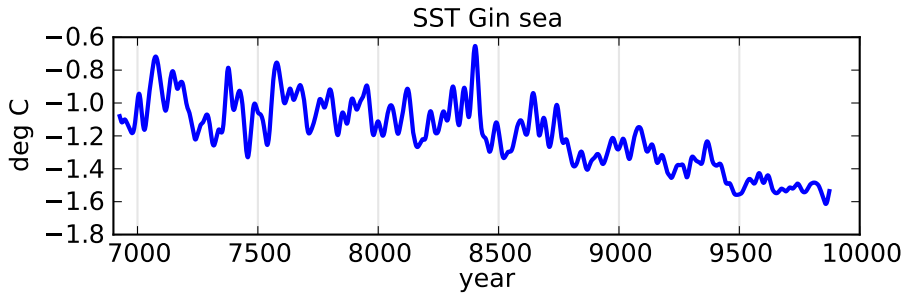

FIGURE 3.27. 50 year running mean sea surface temperature in the GIN Sea.

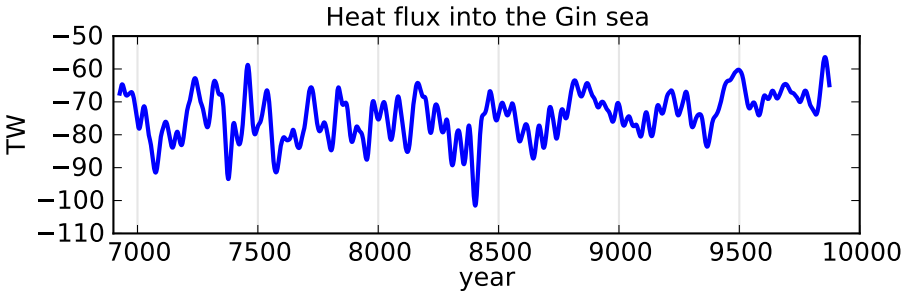

FIGURE 3.28. 50 year running mean of the heat gain in the GIN Sea. Includes energy into and out of the sea ice. The heat loss decreases over time

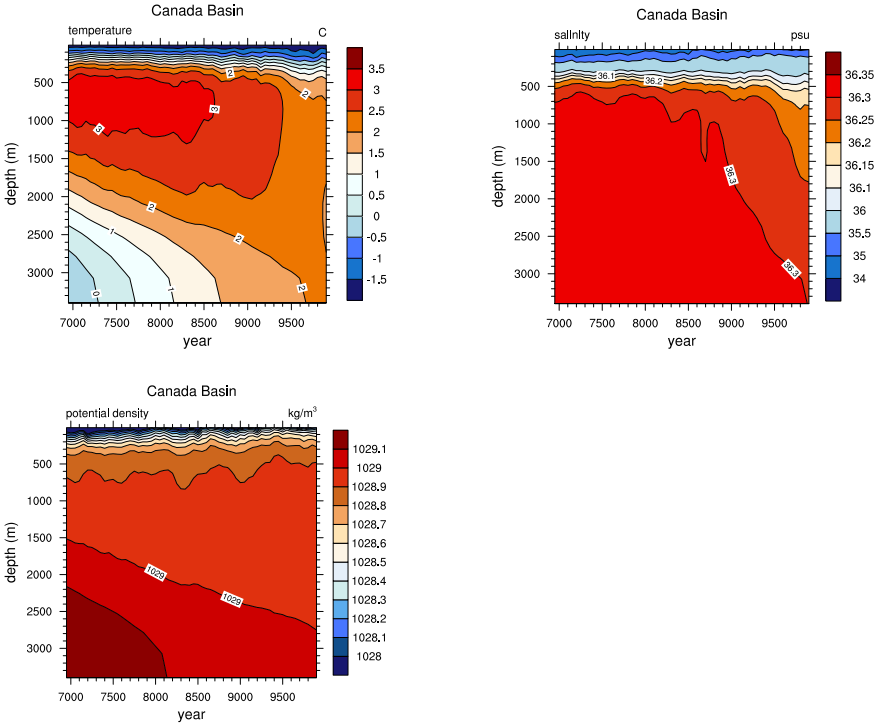

FIGURE 3.29. Temperature, salinity, and potential density in the Canada basin in ASYNC.

3.12. Comparison to other model coupling studies

Technically, this study extends the work by Vizcaíno et al. (2008, 2010). While these studies focus on the response of the Greenland Ice Sheet to a global warming scenario and the effects of the increased ice melt in the climate system, our focus is on glacial climate dynamics. To represent the physics that is relevant in a glacial setup, we add ocean-ice interaction and use the more advanced ice sheet model mPISM instead of SICOPOLIS. mPISM solves the shallow ice approximation (SIA) and shallow shelf approximation (SSA). By applying the SSA to ice streams and shelves, mPISM resolves the membrane stresses that are relevant in these areas and thus has a substantially better representation of ice streams and shelves than the SIA-only model SICOPOLIS. We do not model the Antarctic Ice Sheet, and choose a setup that covers all parts of the northern hemisphere that are relevant for glaciation under glacial maximum conditions. In comparison to Vizcaíno et al. (2010), we have to go one step back in the calculation of the surface mass balance and use a Positive Degree Day (PDD) model instead of the more advanced Energy Balance Model (EBM). The EBM computes the ablation from 6-hourly climate data after remapping to the ice sheet grid. Running the EBM on a hemispheric scale would have been very costly and increased the duration of the experiments substantially. The PDD method is much faster and also is widely used in glaciological and coupled model studies (e. g. Gregory et al., 2012).

We are not aware of published studies where a coupled AOGCM–ISM system is run on a hemispheric scale under last glacial maximum boundary conditions. There are studies that come close to this, such as the AOGCM–ISM experiments presented in Gregory et al. (2012), where the AOGCM FAMOUS (a fast version of HadCM3) is coupled with the ice sheet model GLIMMER in a setup that covers the Canadian Arctic Archipelago and Scandinavia to investigate feedbacks in the last glacial inception. Their model is coupled in a way that maximizes glaciation and thus yields substantial glaciation under pre-industrial boundary conditions. Other studies, e. g. Fyke et al. (2011) focus on Greenland and Antarctica. Limiting the modeled area to areas, where glaciation is wanted lifts a massive restriction on the coupling and mass balance codes. While it is fairly easy to construct a coupling scheme that yields a reasonable glacier distribution over Greenland, it is much more difficult to obtain ice sheets in the correct places while keeping other areas from glaciating immediately without explicitly introducing a location-dependency in the coupling scheme. While Siberia does glaciate in our model, this process occurs very slowly over several millennia and largely by advection of ice into this area. This could be avoided by taking the effect of dust depositions on temperatures and melt rates into account (Krinner et al., 2011), or by performing a transient simulation.

Using the EMIC CLIMBER coupled with the ice sheet model SICOPOLIS Calov et al. (2002) study Heinrich events and Ganopolski and Calov (2011) model full glacial cycles. Since CLIMBER has a very coarse atmosphere resolution, they employ a full EBM to compute the surface mass balance and use a moisture balance model to represent effect of slope convection. While the group at PIK performs impressive experiments with CLIMBER and SICOPOLIS that strongly contribute to the understanding of glacials and their climate, the atmosphere and ocean dynamics in CLIMBER are highly parametrized and thus CLIMBER cannot be used for detailed studies of atmosphere and ocean dynamics. This can only be done in coupled AOGCM–ISM experiments.

3.13. Summary of the mean states

Coupled AOGCM–ISM systems capable of long-time experiments are only beginning to be developed. Therefore, we have modified the state-of-the-art ISM PISM into mPISM, a model that can be used in coupled ice sheet – climate simulations. We have coupled it to the AOGCM ECHAM5/ MPIOM/ LPJ. Both models, as well as the coupling, work without anomaly maps or flux correction. Thus, they can much better represent the nonlinear dynamics of the climate system than models that employ such methods and commonly assume the correction patterns to stay constant under varying climate conditions. In comparison to simulations using earth system models of intermediate complexity (EMICs), AOGCMs are able to represent processes of the ocean circulation and atmosphere dynamics in a much more detailed way and with higher spatial and temporal resolution. In contrast to previous AOGCM–ISM simulations (e. g. Gregory et al., 2012), the ISM covers all relevant parts of the northern hemisphere. mPISM is a shallow ice approximation (SIA) – shallow shelf approximation (SSA) hybrid model and thus able to model ice streams more realistically than conventional SIA-only ISMs. In both directions, the coupling includes the fluxes between ice and atmosphere as well as the fluxes between ice and ocean, enabling the study of the full interactions between the ice sheets and the climate system.

With our model system, we performed the first fully coupled multi-millennial steady-state AOGCM–ISM simulations under LGM boundary conditions. We validated our setup by also performing steady-state experiments under pre-industrial boundary conditions. In both cases, our results agree reasonably well with the observational data. In the pre-industrial state, an additional ice sheet in the Alaska Range forms. This is due to a resolution dependent cold bias in the atmosphere model. In the LGM setup, a spurious ice sheet forms in eastern Siberia and Alaska. This is at least partly due to neglecting the albedo effect of dust on snow and ice in our model (Warren and Wiscombe, 1980; Krinner et al., 2011). Further advances could be made by using a sophisticated energy balance scheme for the surface mass balance (e. g. Calov et al., 2005a; Vizcaíno et al., 2010).

CHAPTER 4

Ice stream surges

As described in the introduction, it is commonly assumed that during some of the Dansgaard-Oeschger Stadials, the so-called Heinrich Stadials, massive ice discharges from the Laurentide Ice Sheet into the Labrador Sea occurred. In the ocean, these ice masses broke up into icebergs that released freshwater into the ocean. The freshwater weakened the meridional overturning circulation. The climate changes that occurred during these periods, were recorded in proxies practically all over the globe (see Clement and Peterson (2008) for a recent review).

To study the processes leading to and caused by such ice sheet collapses, we performed two experiments. First, we performed an asynchronously coupled experiment (ASYNC) spanning four ice sheet buildup-collapse cycles (30 000 years of ISM simulation and 3000 years of AOGCM simulation) and then a synchronously coupled experiment (SYNC) covering one single collapse period from ASYNC (3200 years). For details of the setup see section 2.5. In ASYNC, we investigate the cyclic behavior of the ice streams. In SYNC, we focus on the evolution of the climatic changes during the collapse. We compare the climate changes occurring in SYNC with those in ASYNC.

In both experiments, the collapses cause strong signals in the Atlantic Ocean temperature and salinity. The changes in salinity can globally be traced in the deep oceans, where the background variability is lower than at the surface. The effects of the ice sheet collapses on the atmosphere are mostly confined to the Laurentide Ice Sheet and the adjacent North Atlantic and the Arctic Ocean, but there are some far-reaching signals in surface air temperature and precipitation. In section 4.1 we describe some of the general processes during ice stream surging that we need in order to understand the behavior of the large ice streams covered in section 4.2. Following the description of the ice stream behavior in ASYNC, section 4.3 covers the sequence of events in SYNC. The knowledge of this sequence is necessary to understand their consequences in the ocean (section 4.4) and atmosphere (section 4.5). Finally we discuss the surge mechanisms (section 4.6) and our findings by comparing them with other simulations and with proxy-data (section 4.7).

4.1. Ice stream surging and ice sheet collapses

One of the most intriguing features of glaciers are surges. Within days to months, a glacier speeds up and the velocities change from a few meters per year to hundreds of meters or even kilometers per year. This can happen with or without an obvious external trigger (Benn and Evans, 2010). During the surge, the ice surface is drawn down and after some time (typically years) the surge stops and the glacier returns to its quiescent flow. As described in the introduction and in section 2.2, during the surge, the base of the glacier needs to be temperate to permit the presence of basal water that lubricates the flow. The lubrication becomes much more effective if the glacier is sediment bedded, since these sediments can be deformed more easily than the basal ice layer. As described in section 2.2, we base

the decision whether the ice slides in the model on the availability of basal sediments and basal water. If and only if both are present, the ice slides.

The need for basal water and thus a temperate base severely restricts the ice flow over mountains, where the ice sheet base is generally colder than in the neighboring valleys. Since the ice sheet surface generally is very smooth, over mountains the ice is thinner than in the surrounding areas. This has two negative implications for the basal temperature. (1) The thinner ice provides less thermal insulation, and (2) there is less heating by internal shear P_{shear}. The driving stress τ_d depends linearly on the product of the ice sheet thickness *thk* and surface slope m. The shear rate D is proportional to the third power of the driving stress. Thus, for a constant surface slope, the heat production grows with the fourth power of the ice thickness

$$\tau_d \sim m\, thk\ ;\ D \sim \tau_d^3 \Rightarrow P_{shear} = D : \tau_D \sim (m\, thk)^4\ . \tag{19}$$

Therefore ice streams mainly develop in valleys and do not spread to the neighboring mountains (compare fig. 3.14(a) and fig. 3.14(b)).

The details of surge propagation and termination are fields of active research and even the basic structure of a *correct* sliding law is still subject to discussion (Benn and Evans, 2010), but cyclic ice sheet surging is a process that is covered in the literature, e. g. MacAyeal (1993); Fowler and Schiavi (1998). Once a surge is active, there are heating and cooling processes competing for the development of the basal temperature and water level. The sliding generates heat that melts ice and keeps the surge running. This melting increases the vertical advection of cold ice into the basal zone. Even more importantly, at the back end of a developing surge, the ice stretches horizontally and cold ice is drawn down.

If the drainage basin of an ice stream is large enough and the passage to the sea (or ablation area in the case of land-terminating ice streams) is narrow enough to limit the outflow in the ice stream to the amount of ice restored by precipitation, a constantly operating ice stream can develop. This is the case for Mackenzie Ice Stream in our model. It drains a major part of the Laurentide Ice Sheet. If however, the ice stream drains the basin faster than it is refilled, the ice stream draws down the ice sheet substantially and then refreezes. This reduces the drainage of the basin, the ice sheet regrows and a new surge can start. In our model, the Hudson Strait Ice Stream, is a prime example for this behavior. An analog of varying the size of the accumulation area is varying the accumulation rate. The ISMIP-HEINO experiments (Calov et al., 2010) show exactly the behavior described above. With all other parameters held fixed, three out of seven models models are only able to obtain surges for low accumulation rates, not for high ones (additionally, one model was only run for one ablation rate value and one did not surge at all with the default air temperature and basal friction coefficient).

One of the decisive parameters for the processes at the base of the ice sheet is the basal friction coefficient. If the friction coefficient is high, even little sliding produces enough heat to keep an ice stream active. Furthermore, a high friction coefficient reduces the flow speed and increases the probability that the precipitation can keep up with the drainage and keep the ice stream running. The effect of varying the sliding coefficient has been demonstrated for SICOPOLIS in Calov et al. (2002) and for a variety of ice sheet models in Calov et al. (2010). Van Pelt and Oerlemans (2012) study sliding for an idealized glacier with PISM. They find long-period oscillations for low friction coefficients, fast oscillations for intermediate friction coefficients and constant flow for high friction coefficients. While Calov

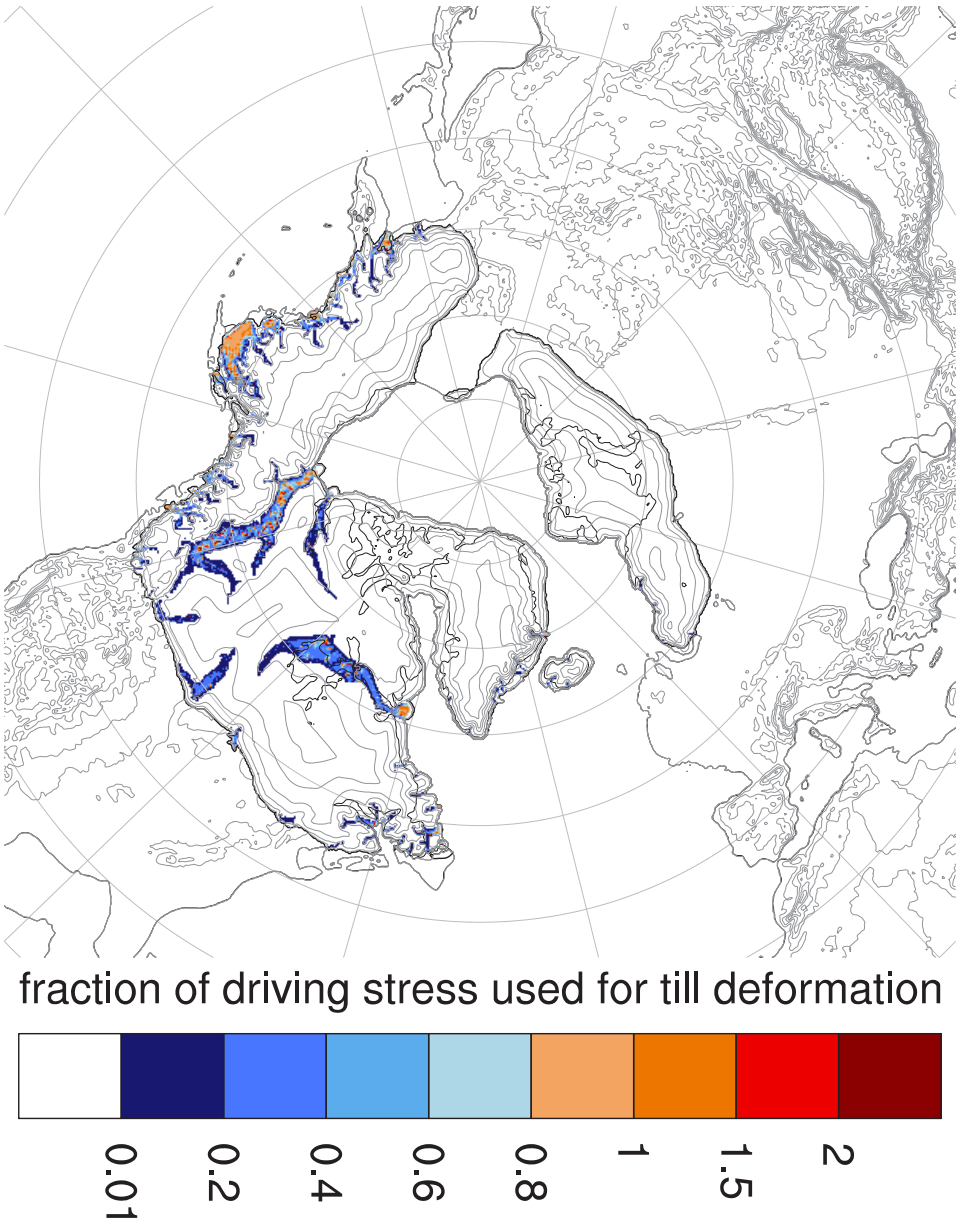

FIGURE 4.1. Translation of driving stress into shear of basal till. Values below 0.01 (white) mark regions where there is practically no deformation of basal sediments. Values between 0.01 and 1 mark regions where stress is diverted away by membrane stresses in the ice sheet. Values above 1 mark regions where stress is concentrated. The data stems from year 2350 of SYNC.

et al. (2002) use a sliding coefficient (1 / friction) of 0.1 m/yr/Pa, we have to use 1 m/yr/Pa to obtain robust oscillations. The difference in the sliding coefficient that is necessary to obtain robust oscillations in part stems from the use of the shallow shelf approximation in PISM. In the narrow passages, about two thirds of the driving stress is diverted into the walls of the ice stream by the membrane stresses and only one third actually contributes to basal stress (fig. 4.1).

4.2. The major ice streams

In the following, we describe the behavior of four major ice stream systems that are most relevant for the freshwater budget of the North Atlantic and the Arctic Ocean. For their positions see fig. 3.14(a). These are (1) the Barents Sea Ice Streams draining into the Norwegian Basin, (2) the Mackenzie Ice Stream draining along the east side of the Rocky Mountains into the Arctic Ocean, (3) the Amundsen Gulf Ice Stream to the east of the northern part of the Mackenzie Ice Stream also draining into the Arctic Ocean and (4) the Hudson Strait Ice Stream draining the surroundings of the Hudson Bay into the Labrador Sea. This description is based on the behavior of the ice streams in the ASYNC experiment. The discharge rates of the ice streams are displayed in fig. 4.2. (1) The part of the Fennoscandian ice sheet covering the Barents Sea is drained by four ice streams. Two of them flow into the Norwegian Basin. Both of these show surge-type behavior (figs. 3.14(a) and 4.2). Some of their surges occur simultaneous in both ice streams, but there is no clear phase-locking between the two streams. They surge rather frequently with discharge amounts up to 25 mSv and surge durations on centennial timescale (fig. 4.2). The other two, also surging, ice streams flow from the Barents Sea into the Arctic Ocean in the troughs between Svalbard and Franz-Josef-Land and between Franz-Josef-Land and Severnaya Zemlya (fig. 3.14(a)) They also surge frequently and reach discharge strengths up to 25 mSv (fig. 4.2).

(2) The Mackenzie Ice Stream constantly drains along the eastern margin of the Rocky Mountains. It has annual mean surface air temperatures exceeding 260 K in the southern parts. In the northern parts, it even reaches a negative surface mass balance. The huge drainage basin and the high surface (and thus ice-) temperatures allow the ice stream to stay in constant operation. The upstream regions that contribute keep changing over time (fig. 3.14(a)) and the ice discharge into the Arctic Ocean varies between about 10 mSv and 30 mSv. There is no clear periodicity and the spectrum of the ice discharge shows broad peaking between 1000 and 4000 years cycle duration (fig. 4.2).

(3) Just east of the Mackenzie Ice Stream, the Amundsen Gulf Ice Stream periodically drains a part of the northeastern Laurentide Ice Sheet into the Arctic Ocean. In contrast to the Mackenzie Ice Stream, it has periodic surge/buildup cycles that (after some irregularities in the first 8000 yrs) have a period of 3500 yrs with the active phase lasting between 1000 and 1500 years (fig. 4.2). Each surge starts with a very fast upstream propagation of the sliding area reflected in a fast growing discharge that typically peaks between 20 mSv and 25 mSv after 100 to 200 years and then slowly decreases to the background level of 0.2 mSv as the ice surface lowers and the supply of ice gradually decreases (fig. 4.2). In the last part of the surge, the ice stream refreezes from the upstream end to the downstream end. Because of its very clear peaks and periodicity, the Amundsen Gulf Ice Stream discharge can easily be seen in the Arctic Ocean sea ice volume and in the Fram Strait sea ice export (fig. 4.2).

(4) The Hudson Strait Ice Stream periodically drains the Hudson Bay area into the Labrador Sea. The surges recur with a period between 7000 and 8000 years (table 4.1, fig. 4.2) and last between 1700 and 2800 years. The ice discharge from the Hudson Strait varies between background values of about 5 mSv (stemming mainly from the almost constantly operating Ungava Bay Ice Stream that also feeds into the Hudson Strait) and peak discharges between 50 mSv and 70 mSv during the surges of the Hudson Strait Ice Stream. In each surge, the volume of the

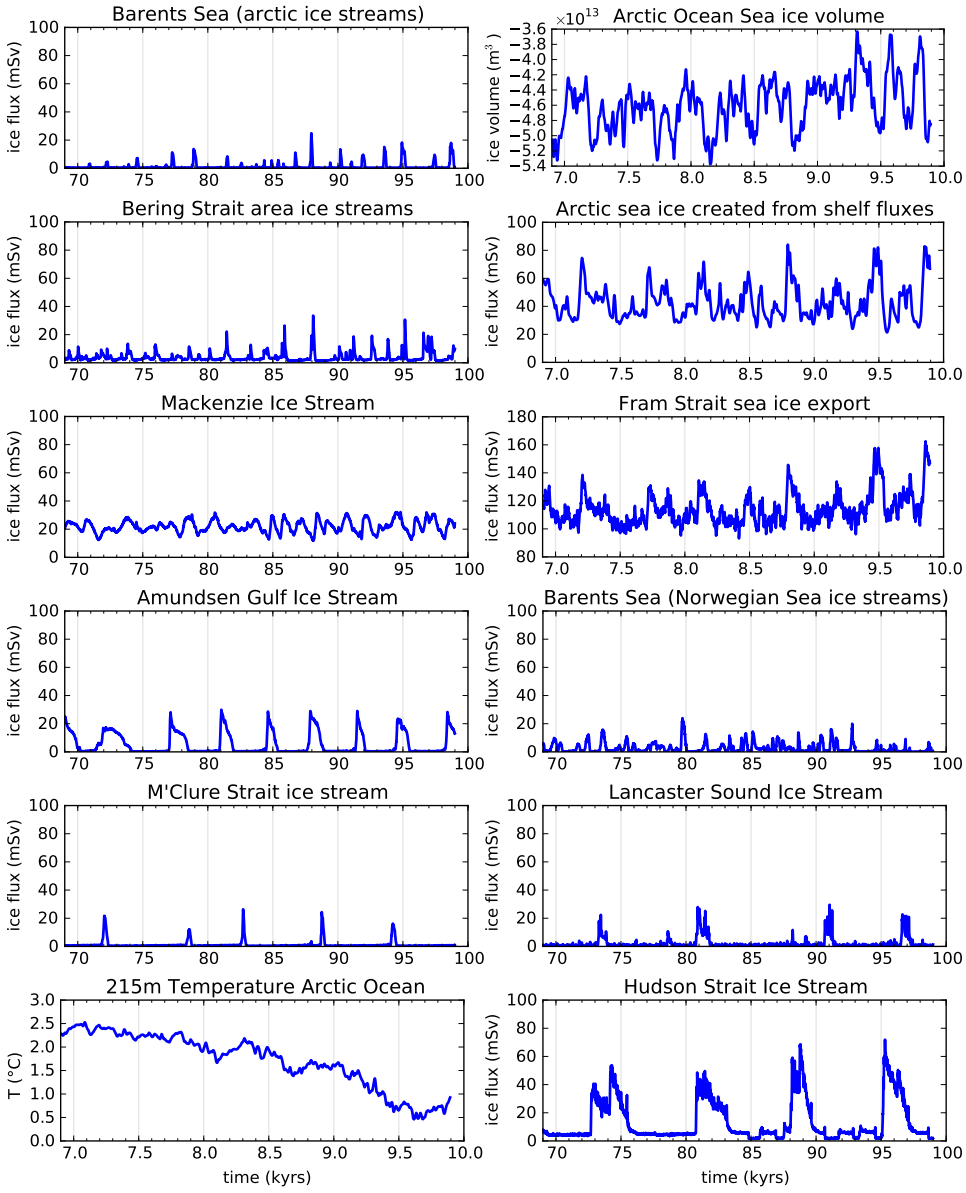

FIGURE 4.2. Glacier ice and sea ice fluxes as well as the Arctic Ocean 215 m potential temperature and the Arctic Ocean sea ice volume in ASYNC. All fluxes are running averages over 10 years. For easy comparison of the variability, all fluxes are plotted with a vertical scale spanning 100 mSv. For SYNC see fig. 4.3. All glacier fluxes are given at freshwater density. The sea ice fluxes are given at ice density $\rho = 910\,\mathrm{kg/m^3}$.

eastern Laurentide Ice Sheet (for the definition of the area see fig. 3.12) decreases by between 1.5 Mio km^3 and 2 Mio km^3 (3.75–5 m sea level equivalent) in 1700–2800 yrs (see table 4.1 and fig. 3.18).

In our experiments, the width of the Hudson Strait Ice Stream in the Hudson Strait is constrained by the adjacent mountains. It does not spread over the full width of the sediment covered region, but narrows down to a with of about 60 km near the mouth of the Hudson Strait (compare fig. 3.14(a) with fig. 3.14(b) and fig. 2.1). This strongly limits the ice discharge.

TABLE 4.1. Ice sheet collapses. Note that the mean loss rate significantly differs from the maximum flux into the Labrador Sea. Volumes and fluxes are given as ice Volume changes of the eastern section of the Laurentide Ice Sheet (fig. 3.12) ($\rho = 910\,\mathrm{kg/m^3}$). The time evolution of the ice sheet volumes for ASYNC is shown in fig. 3.18. Key fluxes are shown in fig. 4.2 for ASYNC and in fig. 4.3 for SYNC. *The second listing of SYNC is the same experiment as the first listing, but putting the end of the surge at year 4000, when the first two surge phases, that also occur in ASYNC have finished.

Experiment	Start year	Duration (years)	Volume released ($10^6\,\mathrm{km^3}$)	mean loss rate (mSv)
ASYNC	72 700	2800	1.6	18
ASYNC	80 750	2400	1.7	23
ASYNC	88 000	1700	1.5	29
ASYNC	95 000	2000	2.0	31
SYNC	1937	2833	2.1	23
SYNC	1937	2063*	1.8	27

Because of the large drainage basin and the narrow passage it is difficult to avoid constant streaming in the Hudson Strait Ice Stream in model simulations. In the experiments of Álvarez Solas et al. (2011) a constantly streaming ice stream develops when a constant shelf melt rate is applied and the SSA is used to compute the ice flow velocities in the ice stream. In contrast, Calov et al. (2002) obtained recurring surges. The ISMIP-HEINO experiment (Calov et al., 2010) show that, even under simplified conditions, the sliding behavior is highly model dependent and nonlinear. Obtaining a pulsing behavior of the Hudson Strait Ice Stream under constant boundary conditions was one of the major challenges in this project. It proved that whether the Hudson Strait Ice Stream is in constant operation or pulses, strongly depends on the choices made in the model setup, and on the parametrizations chosen.

With our setup, the surges of the Hudson Strait Ice Stream are a robust feature of the simulations and their existence is independent of the exact climate forcing. mPISM shows the surges as an internal oscillation under perfectly constant climate forcing as well as in the coupled simulations. Reducing the resolution from 20 km to 40 km leads to constant streaming, as do higher basal friction coefficients.

In the experiments, there is constant sliding in the western Hudson Bay and east of Mackenzie Ice Stream (fig. 3.14(a)). This is largely due to the high thickness of the ice sheet in this area and, following from that, the constant supply of temperate ice from the sediment-free zone between the Hudson Bay and the Mackenzie Ice stream. The ice in this sediment-free zone cannot slide because of the lacking sediments, so the ice sheet stays thick and the base of the ice sheet stays at the pressure melting point.

The first surge of the Hudson Strait Ice Stream starts from the constantly sliding zone on the western side of the Hudson Bay and propagates downstream. The second surge also starts from the upstream side, but, when the surge front already is propagating down the Hudson Strait and is increasing the surface gradients in this area, the last 100 km of the connection are covered by an upstream propagating extension of the Ungava Bay Ice Stream surge. The third and forth surges start from the already surging Ungava Ice Stream and propagate upstream into the Hudson Bay. The downstream propagation of the surges is caused a bug in the

basal boundary condition. We removed it during the second surge of the Hudson Strait Ice Stream. Rerunning the same surge with the debugged model version still shows an expansion of the surging area in the interior of the bay, but this time the surge starts from the downstream end and propagates upstream through the entire Hudson Strait. Rerunning the third surge with the old model code and the forcing fields from ASYNC yields an upstream propagating surge, just as the debugged code version does. The interval between the surges is not substantially affected by this race between upstream and downstream surge initiation. It is mainly set by the accumulation rate over the Laurentide Ice Sheet.

One effect by which surges propagate upstream as well as the downstream is increasing the surface gradient. In the case of an upstream propagation, the surge removes ice downstream of the surge front. In a downstream propagating surge, ice is piled up upstream of the front. The higher surface gradient increases the driving stress and thereby the heat production rate from the internal ice deformation (see equation (19)). A higher ice temperature decreases the viscosity and causes faster ice flow. This behavior was described in Calov et al. (2002) for the upstream propagating surges of the Hudson Strait Ice Stream in their SICOPOLIS setup. In all events, until the connection to the ocean is made, the sliding inside the Hudson Bay remains fairly slow with speeds of up to 200 m/yr (below 50 m/yr in the debugged model). In the first two events, the surge propagating down the strait reaches ice velocities of up to 1 km/yr. This is due to the surface gradients (and thus the driving stress) being higher near the coast than in the interior of the ice sheet. Once the connection to the ocean is made, in all experiments, the sliding speed in the Hudson Bay increases strongly with maximum speeds in the Hudson Bay of about 1 km/yr, growing to 10 km/yr in the middle of the Hudson Strait and to values near 30 km/yr in narrowest parts of the mouth of the Hudson Strait. Downstream of this narrow passage, the ice spreads out and forms a shelf with lower velocities (fig. 4.4).

All surges of the Hudson Strait Ice Stream show multiple discharge peaks (fig. 4.2). These are the results from different parts of the Hudson Bay surging at different times, some of them twice. In fig. 4.3–4.5, we show this for the surge in SYNC.

Calov et al. (2002) use CLIMBER and SICOPOLIS coupled via the atmosphere. They get robust oscillations under a variety of sliding coefficients, with a linear and also with a quadratic sliding law. The surges have an amplitude of 0.1 Sv to 0.2 Sv and thus are between twice and three times as strong as those in our model (figs. 4.2, 4.3). Comparing fig. 3 in Calov et al. (2002) with fig. 3.14(a), indicates that they obtain a substantially wider ice stream in the Hudson Strait than we do. This allows for a much faster discharge of the ice. The wider ice stream might partially be caused by the coarser model resolution of 1.5° longitude by 0.75° latitude compared with $20 \times 20\,\mathrm{km}^2$ in our setup. While the models in principle remain anonymous in the ISMIP-HEINO comparison paper of Calov et al. (2010), results of the experiments with SICOPOLIS were published in Greve et al. (2006). A comparison of the two publications shows that SICOPOLIS is one of only two models that obtains surges in all setups tested in Calov et al. (2010). This demonstrates that SICOPOLIS is very well suited for obtaining robust oscillations. A key factor that could contribute to this is the use of σ-coordinates in the vertical in combination unequally spaced model levels that increase the vertical resolution near the ice sheet base. This allows to model the downward advection of cold ice during a surge very precisely.

The initiation of the surges in the Hudson Strait allows for ocean based triggering mechanism as demonstrated by Calov et al. (2002). This is taken to the extreme in Álvarez Solas et al. (2011) (see section 1.4). In their model, the ice discharge from the Hudson Strait Ice Stream is modulated by the (non-) existence of an ice shelf covering the Labrador Sea. They obtain the pulsed discharge as an anomaly to a constantly surging Hudson Strait Ice Stream. The additional discharge amount of 60 mSv and the total duration of the enhanced discharge of 3000 years agrees very well with our results.

4.3. The surges in SYNC

In the following we describe the sequence of ice stream surges in SYNC. Fig. 4.4 shows the vertically averaged ice velocities, fig. 4.5 shows the corresponding surface elevations, and fig. 4.3 shows the discharge rates. At the start of the experiment, the Amundsen Gulf and the Ungava Bay Ice Streams are surging. The surge of the Amundsen Gulf Ice Stream quickly propagates upstream and causes a strong ice discharge into the Arctic ocean (fig. 4.3). During the surge of the Amundsen Gulf Ice Stream, ice streams on the Barents Shelf and in the Bering Strait area become active and discharge into the Arctic Ocean (fig. 4.3). The two-peak structure in the discharges from the Bering Strait area results from different ice streams surging at different times (fig. 4.4).

One of the key questions related to Heinrich events is whether surges of different ice sheets can trigger each other via oceanic or atmospheric teleconnections. One prime suspect here is a rising sub-surface Ocean temperature causing increased sub-shelf melt. The increased melt reduces the buttressing effect of the ice shelf and the ice stream behind it starts surging or speeds up (e. g. Álvarez Solas et al. (2010)). In the Arctic Ocean, the sub-surface ocean temperature rises during the ice stream surges (see section 4.4, fig. 4.10(a)). We investigate whether these temperatures trigger the surges of the ice streams on the Barents Shelf and near the Bering Strait in a sensitivity experiment. In this sensitivity experiment, we force mPISM with the same atmospheric forcing fields as in SYNC and constant ocean boundary conditions averaged over years 3000–3099 of SYNC, when the Arctic ocean is in a cold state (fig. 4.7), and the Labrador Sea is in a warm state. The basic structure of the Arctic ice stream fluxes is identical to that of SYNC (fig. 4.6). The total amount of ice discharged into the Arctic ocean is lower in the first 500 years of the sensitivity experiment than in SYNC, but the same ice streams are active as in SYNC. Their discharge rate is lower. The lower discharge rate matches with the lower ice shelf basal melt that allows for thicker ice shelves and thus more buttressing. Towards the end of the sensitivity experiment, Mackenzie Ice Stream becomes stronger than in SYNC. The surge of the Hudson Strait Ice Stream is not substantially affected by the warm ocean conditions in the Labrador Sea, but rather delayed slightly. However, the processes related to the surges are highly non-linear, and this delay is well within the range of responses we can expect for small, random forcings. The small sensitivity of the Hudson Strait Ice Stream to the ocean temperature is due to the very small ice shelf that offers a very small area where shelf basal melt can occur and provides hardly any buttressing. All in all, the differences between the sensitivity experiment and SYNC show that the ice sheet is influenced by the ocean in our experiments, although, in this case, the ocean does not trigger the surges.

The surging Ungava Ice Stream draws down the ice sheet surface in the Hudson Strait. This increases the surface gradient here and initiates the upstream propagation of the surge activation wave between years 1900 and 2000 (see Calov et al.

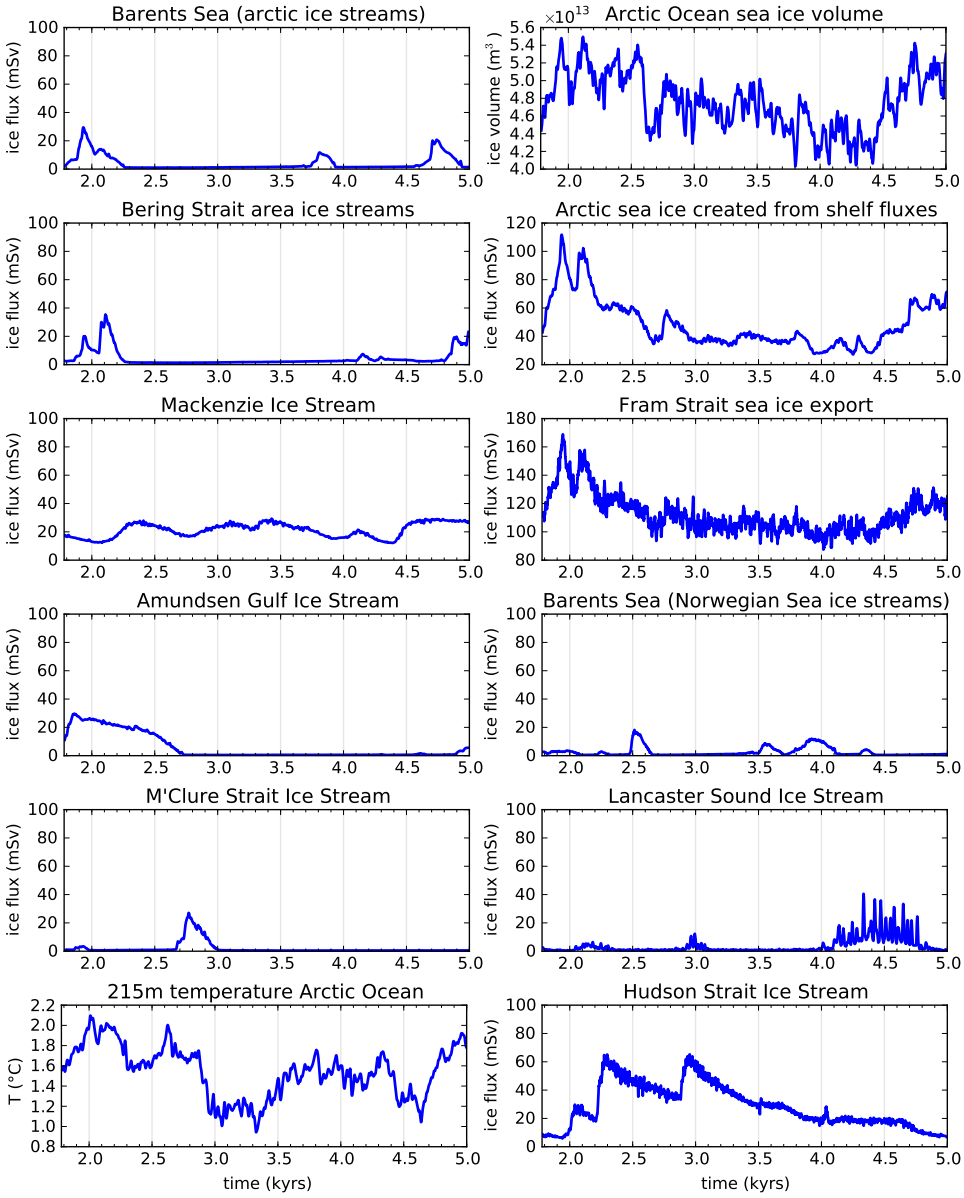

FIGURE 4.3. Glacier ice and sea ice fluxes as well as the Arctic Ocean 215 m potential temperature and the Arctic Ocean sea ice volume in SYNC. All fluxes are running averages over 10 years. For easy comparison of the variability, all fluxes are plotted with a vertical scale spanning 100 mSv. For ASYNC see fig. 4.2

(2002)). Once the surge has reached the Hudson Bay, it first propagates southward along the eastern margin of the bay. It draws down the ice sheet surface on the eastern side of the bay and thereby increases the surface gradients towards the west. This prepares the connection to the already sliding western margin of the Hudson Bay. Between years 2200 and 2210, the sliding zone in the west of the Bay expands and connects to the Hudson Strait Ice Stream. In the years 2210 to 2860, the western zone is slowly drained and the southern part refreezes. In the mean time, between the years 2400 and 2600, the southern Barents Sea Ice stream surges into the Norwegian sea. Between years 2860 and 2920, the surge in the Hudson

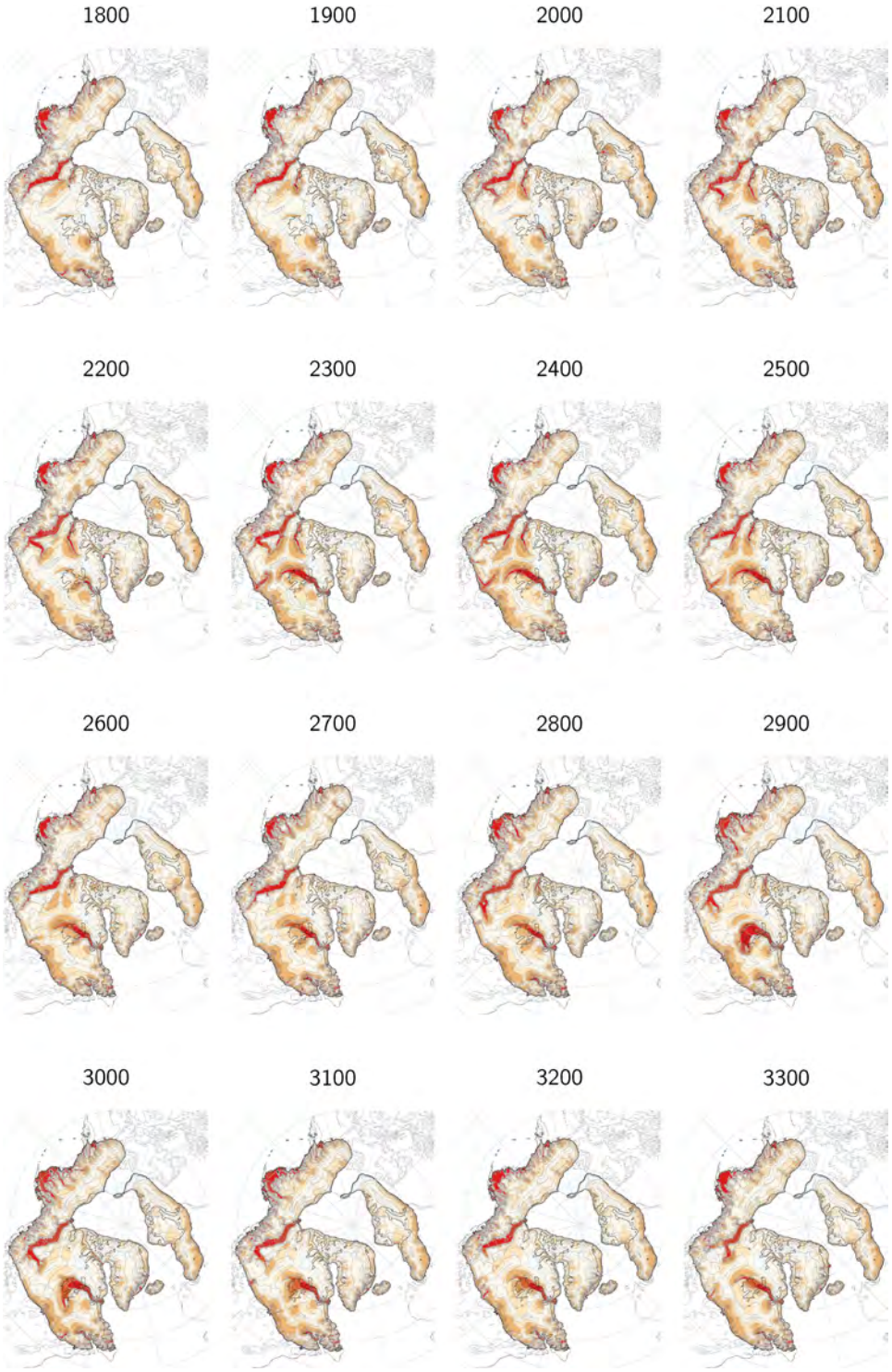
1800
1900
2000
2100
2200
2300
2400
2500
2600
2700
2800
2900
3000
3100
3200
3300

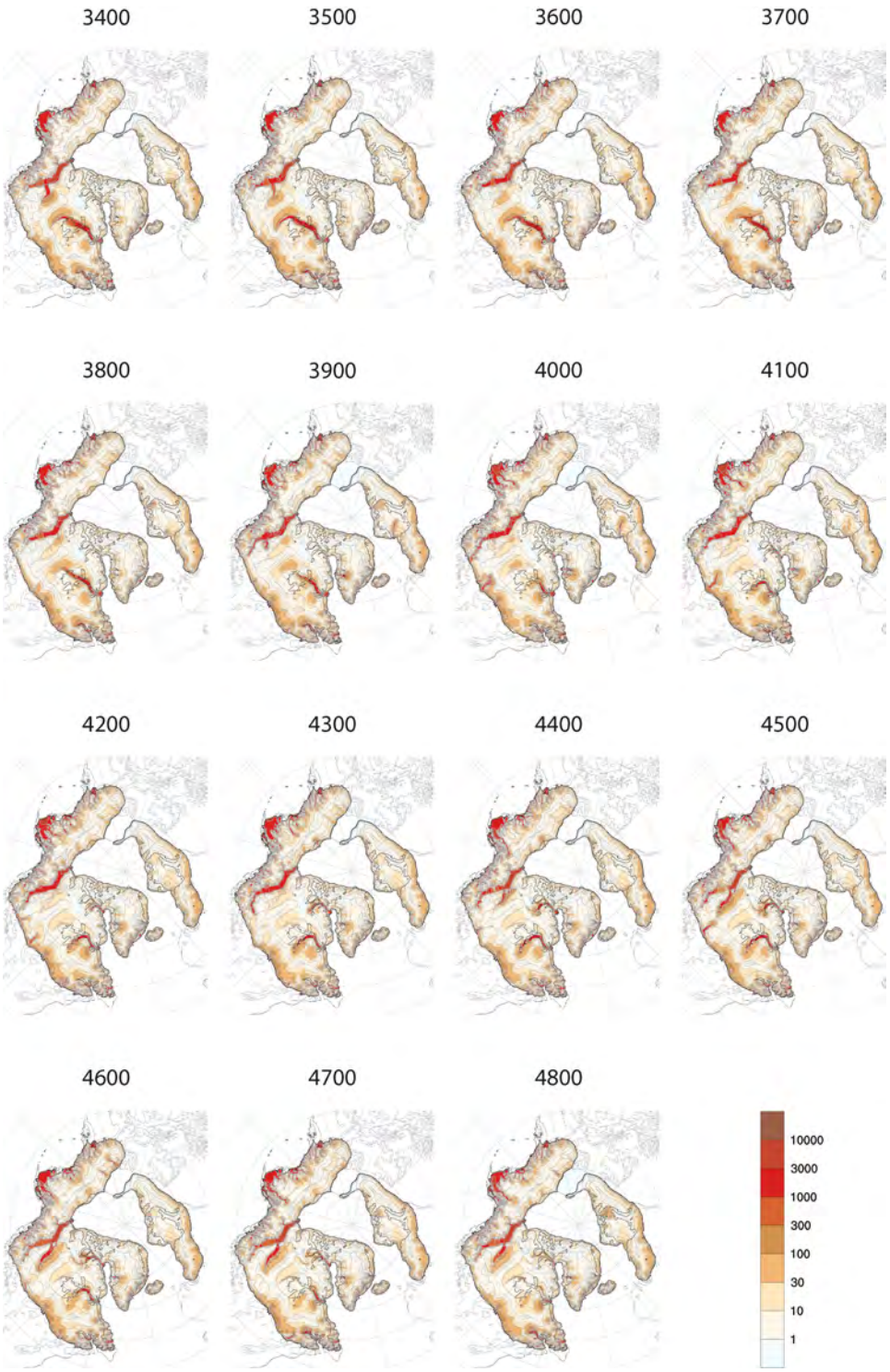

FIGURE 4.4. Vertically averaged ice velocities in SYNC.

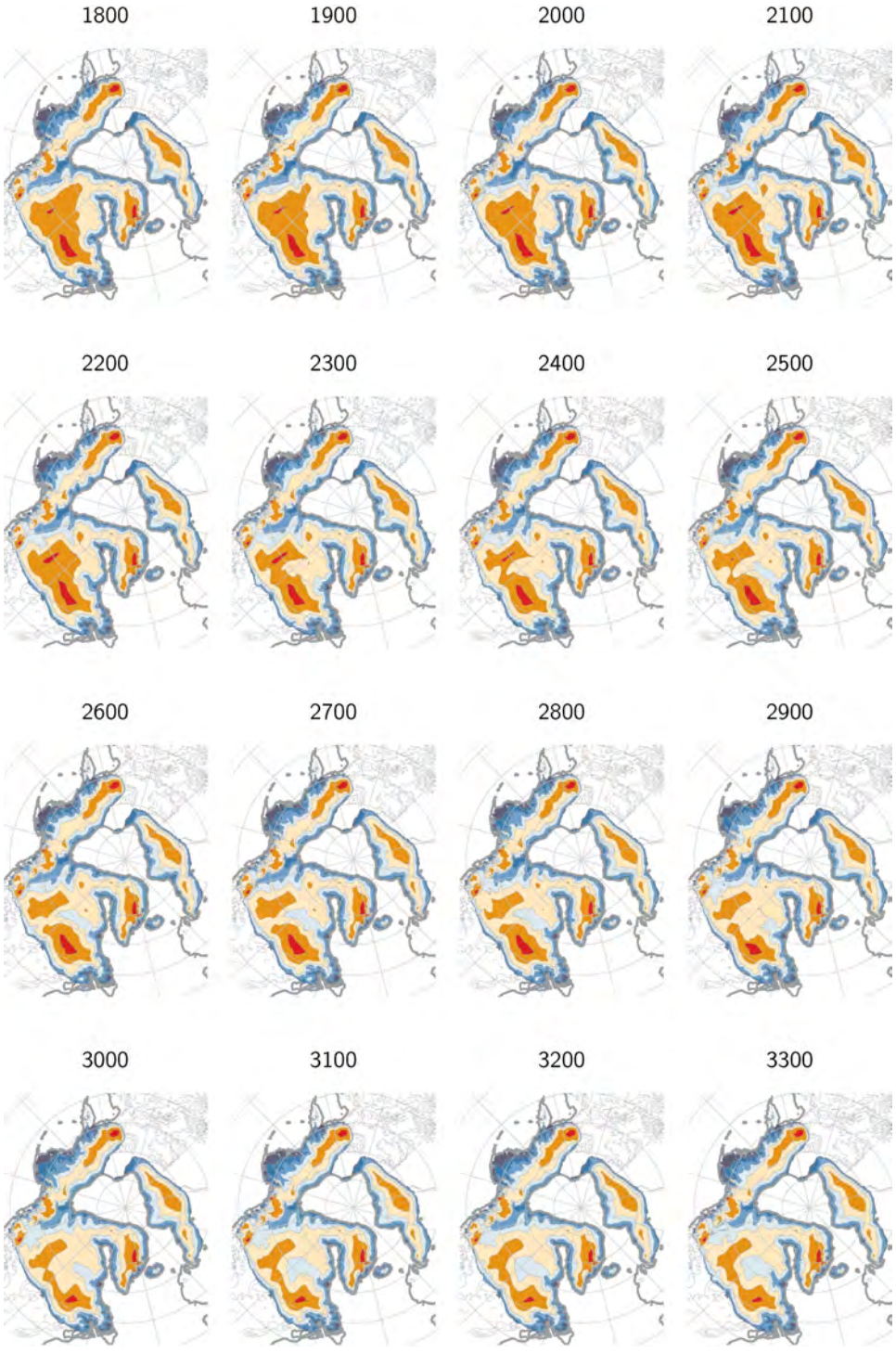
1800
1900
2000
2100
2200
2300
2400
2500
2600
2700
2800
2900
3000
3100
3200
3300

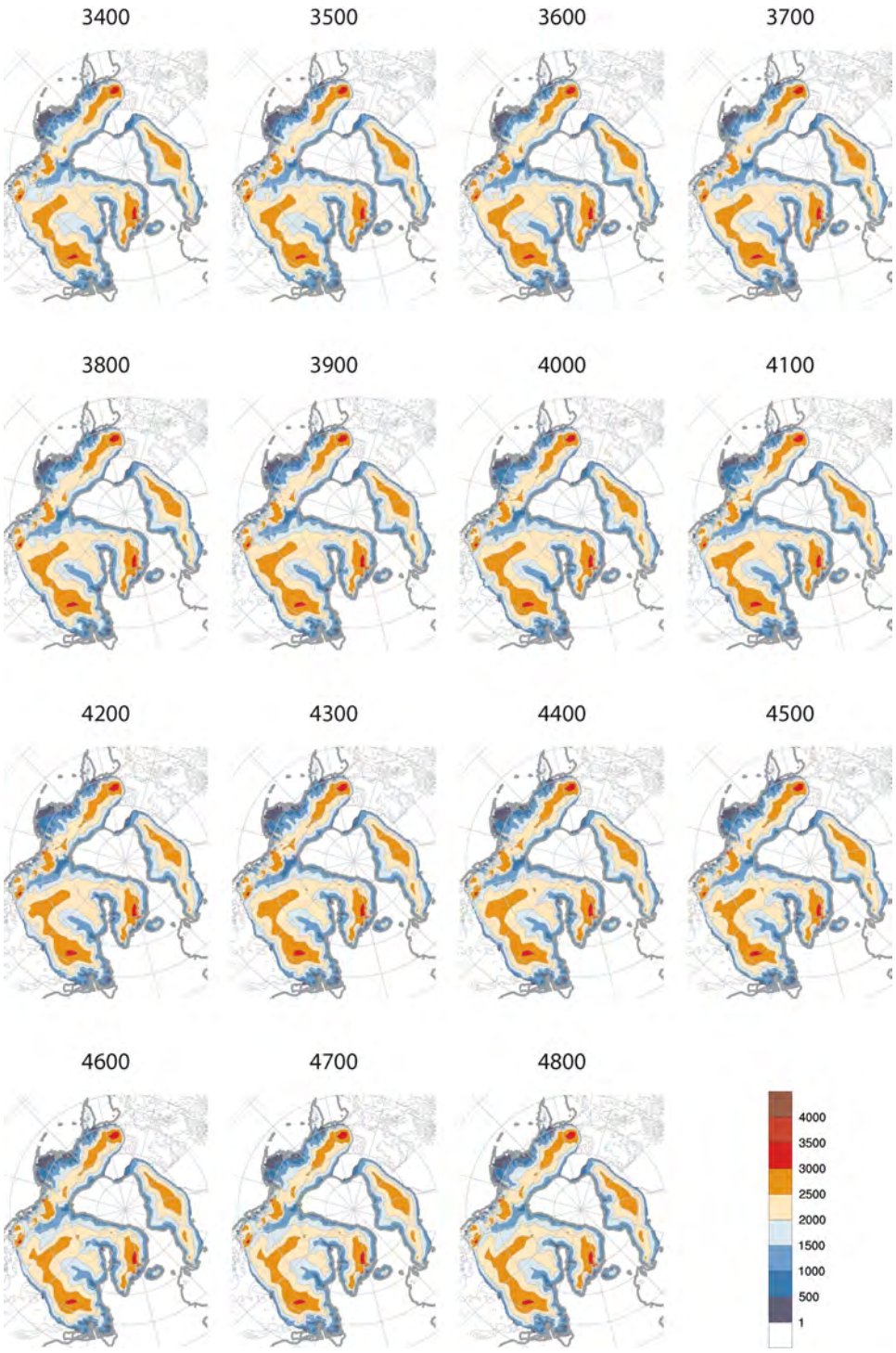

FIGURE 4.5. Ice surface elevations in SYNC.

Bay again spreads southward and reaches further into the southern parts of the bay. This causes the second large pulse in the ice discharge (fig. 4.3). The ice in the Hudson Bay slowly refreezes and by the year 4000, only the Hudson Strait remains active. In contrast to ASYNC, this is not the end of the surge in SYNC, but the

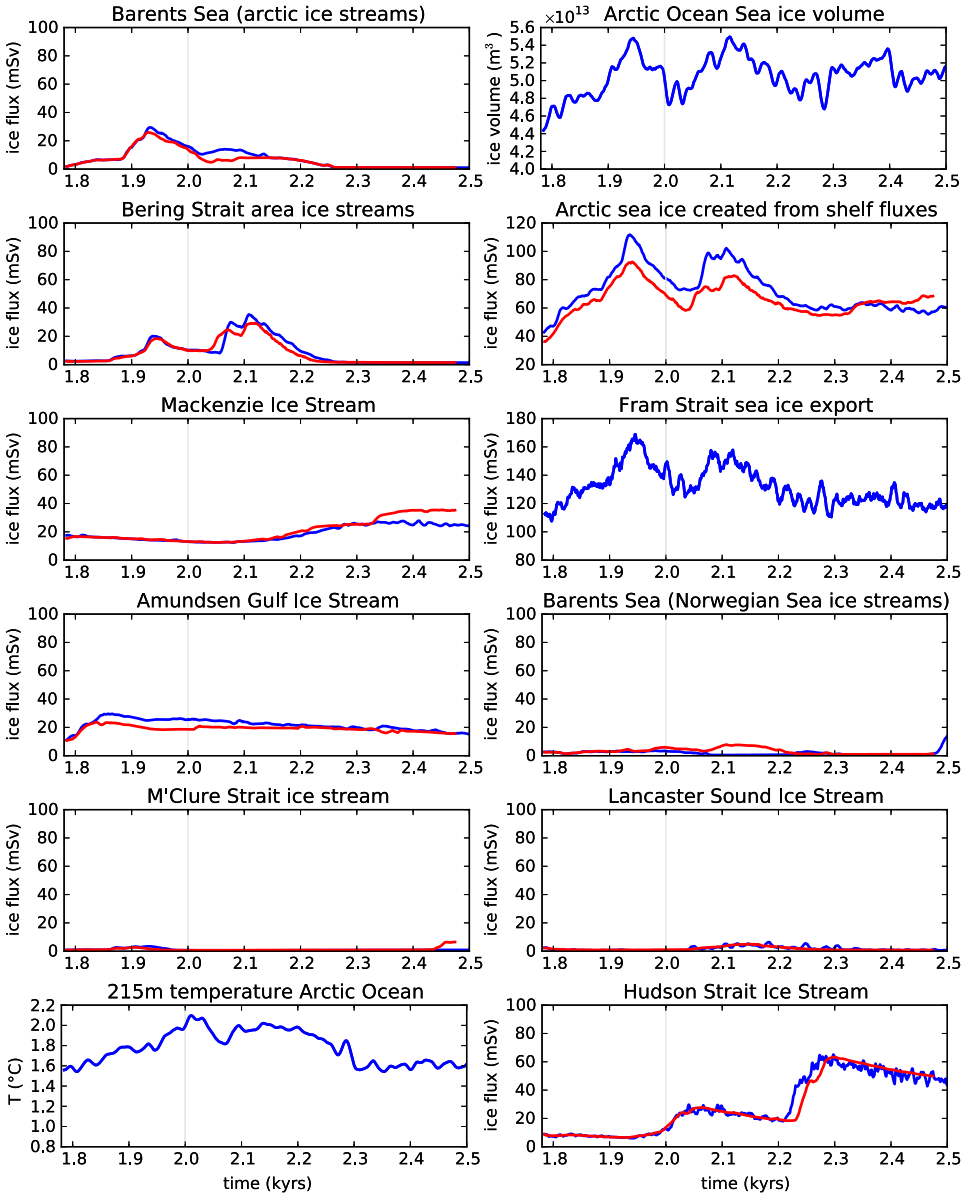

FIGURE 4.6. Ice stream fluxes in a sensitivity experiment that is forced with the ocean state averaged over years 3000–3099 of SYNC (fig. 4.7) and time-varying atmospheric fields of SYNC (red), and in SYNC (blue). The sensitivity experiment features a cold Arctic Ocean and a warm Labrador Sea.

eastern margin of the Hudson Bay starts a new surge phase. The volume of ice mobilized in this surge is fairly low, but the surge phase lasts for another 770 years. Between the years 4000 and 4200, the Lancaster Sound Ice Stream surges into the Baffin Bay (figs. 4.4–4.3).

There are several minor ice streams in the model. Minor in this case still implies a width of at least one grid cell (20 km) and up to about 100 km (fig. 3.14(a)). These ice streams are smaller than the continental-scale Mackenzie and Hudson Strait Ice Streams but still of massive size by present day standards. Several of them show a pulsing behavior. The surges start at the downstream end and propagate upstream.

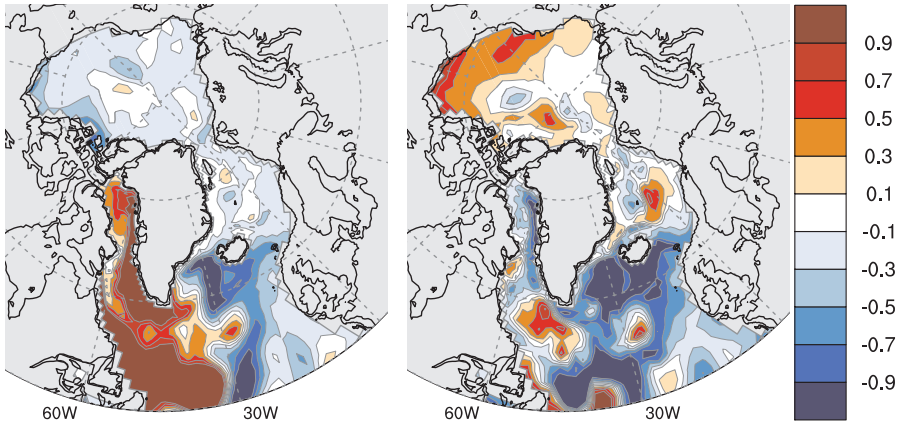

(a) Sensitivity study (b) Arctic ice stream surges

FIGURE 4.7. Temperature anomalies in the forcing used for mPISM in the sensitivity study compared to the reference period. For comparison the mean anomaly during the surges of the arctic ice streams (averaged over years 2050–2099 of SYNC) is presented.

The refreeze usually starts at the upstream end and then propagates downstream. Which ice streams show a surging behavior and which are in constant operation can be told from the time fraction they spend sliding displayed in fig. 3.14(a). For a comparison of the modeled ice streams to proxy data see section 3.8.

4.4. The response of the ocean

In the following, we focus on the ocean response to the ice stream surges in SYNC (a rerun of the third collapse ASYNC) and point out similarities and differences in ASYNC. In SYNC, the Amundsen Gulf Ice Stream already is surging at the beginning of the experiment (fig. 4.3). This shows a clear imprint on the climate. Therefore we cannot use the SYNC to obtain a reference period. Thus, we take the years 8550 to 8749 from ASYNC as reference period (year 8780 in ASYNC corresponds to year 1780 in SYNC).

We start the discussion by describing the changes in sea ice volumes, transports and cover. From there, we move on to the changes in ocean temperature and salinity and finally to the changes in the ocean circulation. We start with the surges of the Arctic ice streams in the first 400 years of SYNC. These surges occur in two pulses, the first between years 1900 and 2000, the second between 2000 and 2200 (left column and, as a sum of the Arctic fluxes, the second plot on the right in fig. 4.3). We start with the effects in the Arctic Ocean and then follow the ice on its route through the GIN Sea into the Iceland and Irminger Basins and from there to the Labrador Sea.

A large fraction of the mass discharge from the surging ice streams occurs in the form of iceberg calving. As described in section 2.4, the calved ice is modeled as sea ice in MPIOM. The conversion of glacier ice into sea ice works best for the surges into the Arctic Ocean. Since the Arctic Ocean surface layer perennially is at the freezing point, the calved ice is entirely converted into sea ice and transported from the Arctic Ocean to the GIN Sea via the Fram Strait (figs. 4.3, 4.8). The variability in the shelf basal and calving fluxes (second plot on the right in figs. 4.2 and 4.3) explains for almost all of the variability in the Fram Strait sea ice

export (third on the right in the above mentioned figures) on centennial and longer time scales. In ASYNC, the correlation coefficient (r) between the 10 year running means of the ice stream discharge and the sea ice export is 0.85 with the sea ice export lagging behind the ice discharge by 5 years ($r = 0.82$ at zero lag, $r = 0$ at about ± 60 years). In SYNC r is 0.76 with a flat plateau. The difference between the behaviors is caused by the asynchronous coupling in ASYNC. The variability of the ice discharge is compressed by a factor of 10 in ASYNC compared to SYNC. This can be seen by the autocorrelation of the ice discharge timeseries from ASYNC falling below 0.8 for a shift of about 10 years, while for SYNC it takes a shift of about 100 years for this to happen. Scaling time by a factor of 10 leads to largely identical autocorrelation functions.

During the surges of the Arctic ice streams, the ice thickness in the Arctic Ocean grows (+1.3 m on the average (2050 to 2099 – reference)). This reduces the heat loss to the atmosphere and thus reduces the sea ice formation rate. The reduction in sea ice formation causes a reduction in brine rejection and thus a reduction in sea surface salinity. The water column stabilizes, the surface cools and the subsurface temperature rises (see fig. 4.10(a) and the bottom left plot in fig. 4.3). For the consequences of the higher sub-surface ocean temperatures for the ice sheets see section 4.3.

In the GIN Sea, the additional sea ice mainly stays in the Greenland Sea, and follows the East Greenland Current (fig. 4.8). In the Greenland Sea, the sea ice concentration in the reference period perennially is above 90%, so there is little change in ice concentration during the Arctic ice stream surges (fig. 4.8(c)). The ice thickness in the Greenland Sea increases from about 2 m by about 0.6 m (fig. 4.8(a), years 2050–2099 vs. reference) with slightly larger changes in the summer season and smaller changes in the winter season.

In the Norwegian Sea, the sea ice concentration increases by about 10% in summer and fall during the second pulse of the Arctic ice streams (years 2050–2099). As in the Greenland basin, the winter sea ice concentration is close to or at 100%, therefore there is no noticeable change in the winter sea ice concentration. The ice thickness in the reference period varies between 0.4 m during summer and 1 m during the winter season. During the years 2050–2099, it increases by 0.1 m. As in the Greenland Sea, the thickness changes are slightly larger in the summer season than in the winter season.

The major part of the additional sea ice in the GIN Sea travels through the GIN Sea in the East Greenland Current and reaches the Irminger Basin via the Denmark Strait. A smaller fraction crosses the Iceland-Faroe Ridge or the Faroe-Shetland-Ridge and melts in the Iceland Basin. In the Irminger Basin, a large part of the sea ice melts, the remainder flows into the Labrador Sea.

The Labrador Sea and the Irminger Basin already show partial ice cover before the surges of the Arctic ice streams. With the additional sea ice brought here by the East Greenland Current during the surges, the sea ice cover increases further (fig. 4.8). In contrast, the Iceland basin is more strongly influenced by the North Atlantic Current and stays practically ice free. Only a narrow band of sea ice on the southern side of the Iceland-Faroe Ridge can form.

The changes in sea ice are directly reflected in changes in the ocean heat uptake (fig. 4.9). Where the sea ice cover increases (fig. 4.8), the ocean loses less heat to the atmosphere in the cold seasons, while the deep water formation areas south of Iceland lose more heat (fig. 4.9) and the water temperature decreases (see fig. 4.10(a) for the 150 m temperatures, the surface cooling is stronger). At the same time,

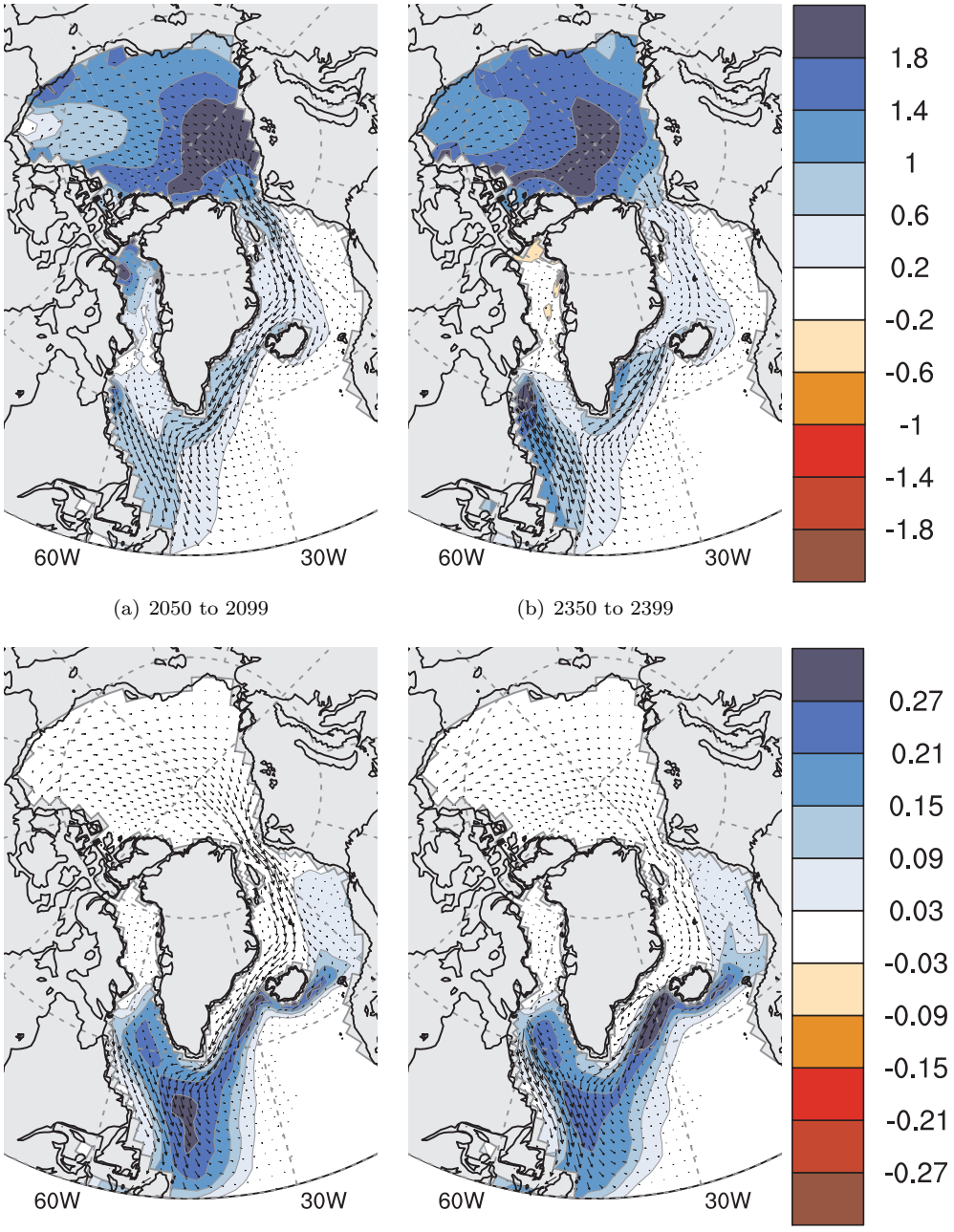

(a) 2050 to 2099 (b) 2350 to 2399

(c) 2050 to 2099 (d) 2350 to 2399

FIGURE 4.8. Sea ice thickness (a, b, color coded, in m), concentration (c, d) and transport (vectors) anomalies compared to the reference period (7550 to 7749 in ASYNC).

the water freshens because of the freshwater from the melting sea ice. With the Subpolar Gyre, the colder than normal water from south of Iceland moves toward Greenland and is subducted below the low salinity surface water of the East Greenland Current (see fig. 4.11 for the layering along 60°N). This causes a cooling in the subsurface water in the East Greenland Current. The stratification in the current remains stable (fig. 4.14) because of the light low salinity surface water. The

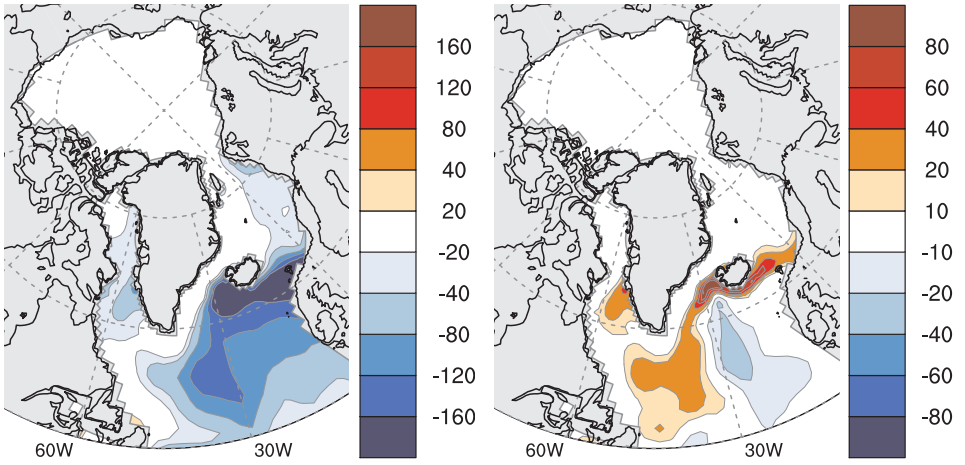

(a) Ocean heat uptake in the reference period (b) Change in ocean heat uptake (2050 to 2099 – reference)

FIGURE 4.9. Ocean heat uptake and change during the surge event. The flux is defined as the net energy flux into the ocean/sea ice system and given in W/m^2. The effects of glacier calving and shelf basal melt are removed.

subducted water flows into the Labrador Sea and causes a subsurface cooling and freshening there in the years up to 2300 (figs. 4.10(a) and 4.12). When interpreting the transports in fig. 4.10(a), it is important to consider the shape of the isopycnals in the North Atlantic and the adjacent basins (figs. 4.11 and 4.13), since the water does not necessarily stay at one depth level, but follows the isopycnals.

With the weakening of the North Atlantic Subpolar Gyre (see below, fig. 4.24(a)) the water throughput of the Labrador sea is reduced from 20.5 Sv during the reference period via 17.5 Sv (2050 to 2099) to 12.1 Sv (2350 to 2399) (all values computed from the outflow across a transect from Greenland (61.5°N, 50°W) to Newfoundland, (48°N, 55°W)).

With the onset of the main phase of the surge of the Hudson Strait Ice Stream at year 2200, the surface water freshening in the Labrador basin increases and exceeds 0.5 psu (fig. 4.12(b)). This freshening is largely restricted to the top 100 m, but a small signal persists throughout the entire water column. The stratification further stabilizes and a warm water anomaly develops, centering at 150 m to 200 m of depth (figs. 4.10(b) and 4.12(a)). While the sub-surface water in the East Greenland Current in the northern Irminger Basin still is colder than in the reference period (and than during the surges of the Arctic ice streams, fig. 4.10), at the southern tip of Greenland the sub-surface water is warmer than in the reference period. This is an effect of mixing with Atlantic water. One reason why the Atlantic water entrained in the current is warmer is that, on its way to the southern tip of Greenland, the Atlantic water flowing northward takes a more direct approach to the Irminger Basin (figs. 4.10 and 4.13), being less exposed to deepwater formation (fig. 4.14) and thus reaches the Irminger Basin warmer. The circulation of the water in the Labrador Sea also changes, which contributes further to the warming. We visualize this in fig. 4.13 for isopycnals that lie between 150 and 180 m of depth in the northern Labrador Sea. Since the density of the Labrador Sea water changes over time, we have to pick different potential densities in the different time frames. In the reference period and during the surges of the Arctic ice streams, these isopycnals

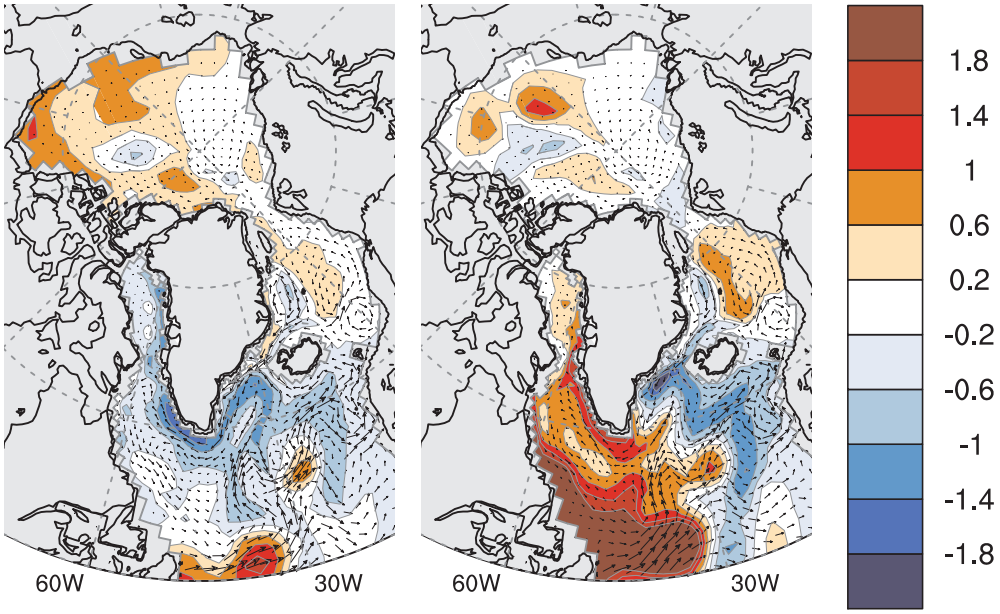

(a) 2050 to 2099 – reference (b) 2350 to 2399 – reference

FIGURE 4.10. Temperature change (in K) in 153 m depth during (a) the surges of the Arctic ice streams and (b) the surge of the Hudson Strait Ice Stream. The vectors show the ocean velocity at 153 m depth during the periods displayed.

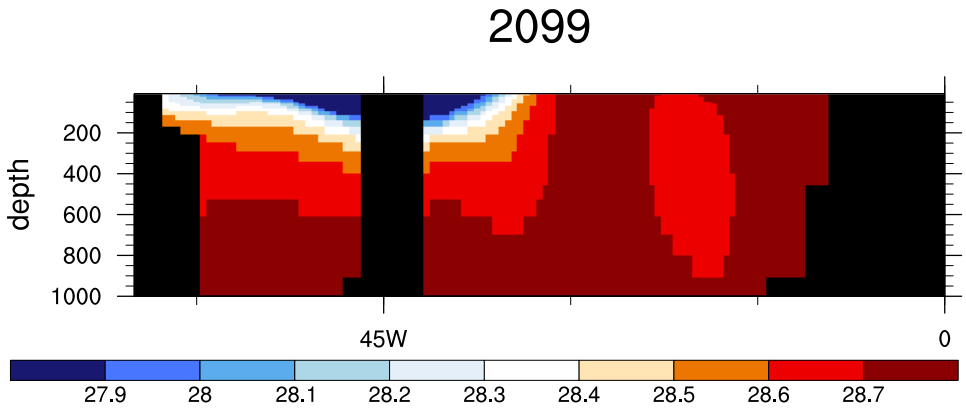

FIGURE 4.11. Atlantic Ocean potential density σ_θ in the top 1000 m at 60°N during March averaged over the years 2050 to 2099.

rise to 90 to 120 m in the southern Labrador sea. During the surge of the Hudson Strait Ice Stream the isopycnal stays deeper than 150 m. This is a consequence of the stronger stratification of the Labrador Sea and reduces the heat loss to the atmosphere. The subsurface warming strengthens during the two main peaks of the Hudson Strait Ice Stream surge (compare the Hudson Strait Ice Stream flux in fig. 4.3 with fig. 4.12(a)). This warm layer also develops in ASYNC, but, due to the asynchronous coupling and the thus shorter duration of the surges in ASYNC, the warming is less pronounced there. From the timing, we can clearly tell, that the

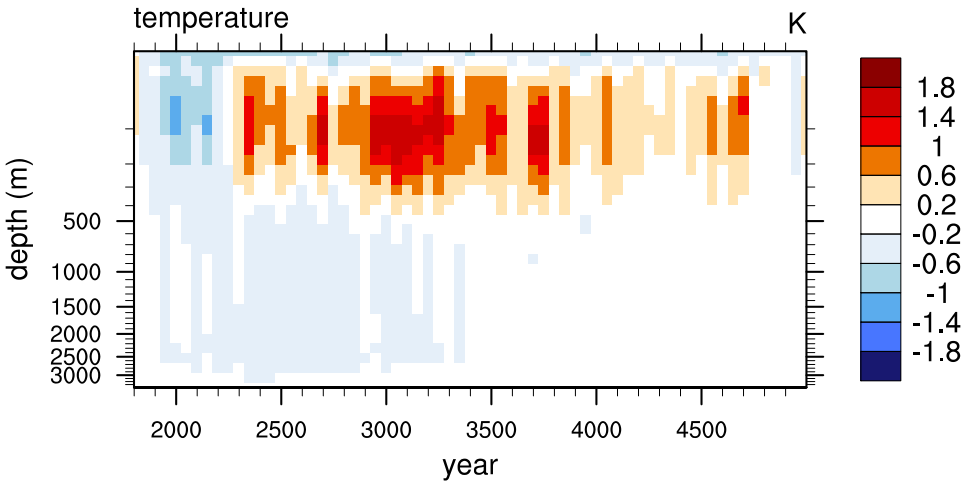

(a) Temperature change.

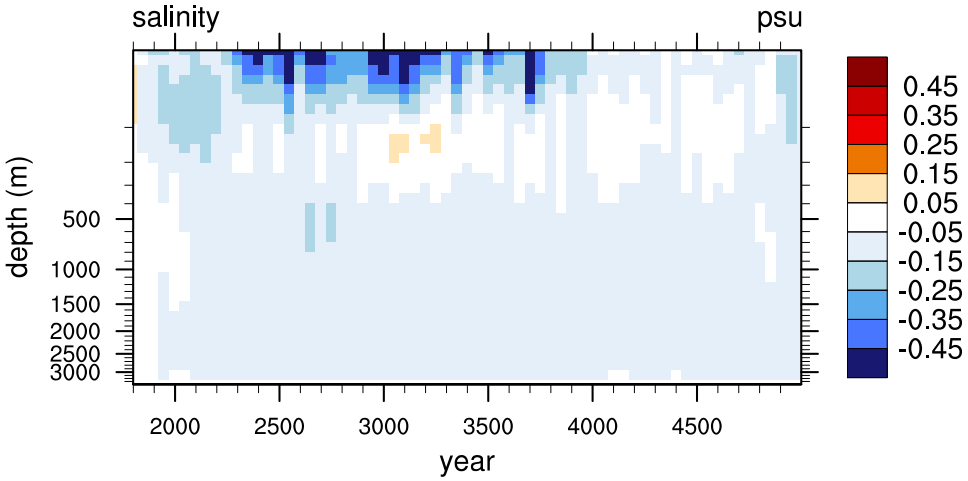

(b) Salinity change.

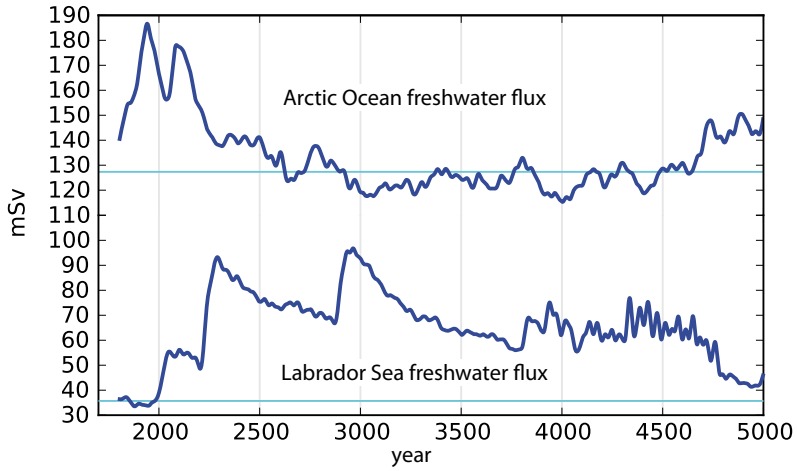

(c) Freshwater fluxes into the Arctic Ocean and the Labrador Sea (as defined in fig. 4.17). The light blue horizontal lines mark the values during the reference period.

FIGURE 4.12. Temperature and salinity changes in the Labrador Sea at 60°N, 55°W in SYNC compared to the reference period (years 7550 to 7749 of ASYNC). Note the non-linear vertical scale giving equal weight to each model level. For easy comparison, the freshwater fluxes are plotted below.

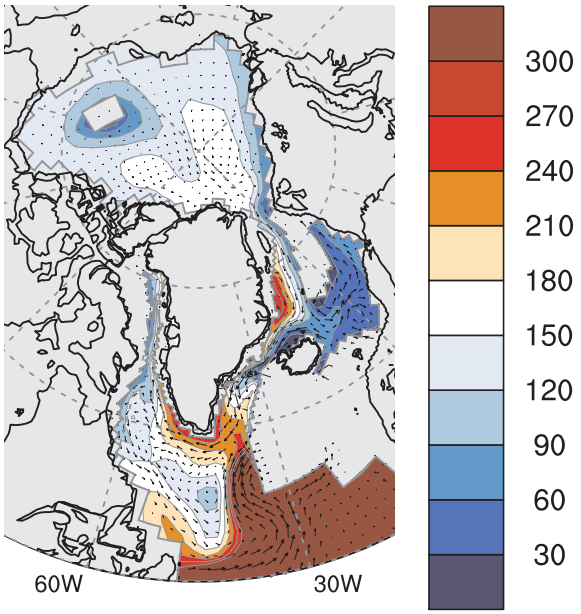

(a)

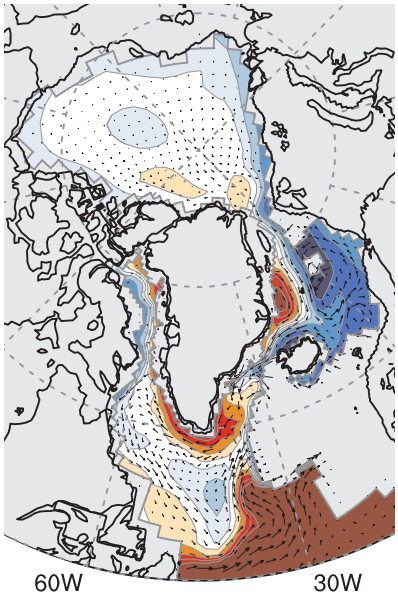

(b)

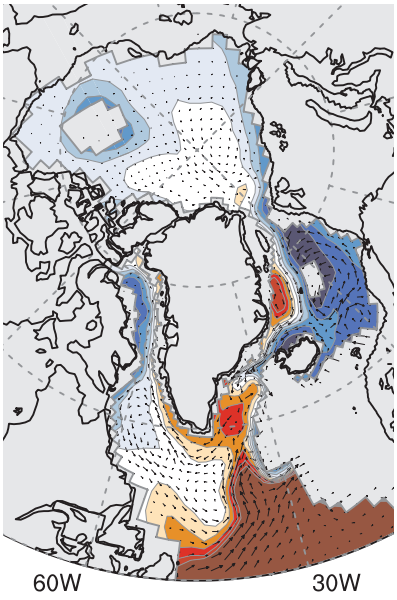

(c)

FIGURE 4.13. Depth (in m) of March potential density σ_θ (reference level = surface) isopycnals for (a) the reference period ($\sigma_\theta = 1028.56$), (b) the Arctic ice stream surges (years 2050–2099, $\sigma_\theta = 1028.5$), and (c) the Hudson Strait Ice Stream surge (years 2350–2399, $\sigma_\theta = 1028.43$). The densities were chosen such, that the surfaces have a similar depth in the interior of the Labrador Sea.

development of the warm subsurface water layer is a consequence of the surge, and not its trigger.

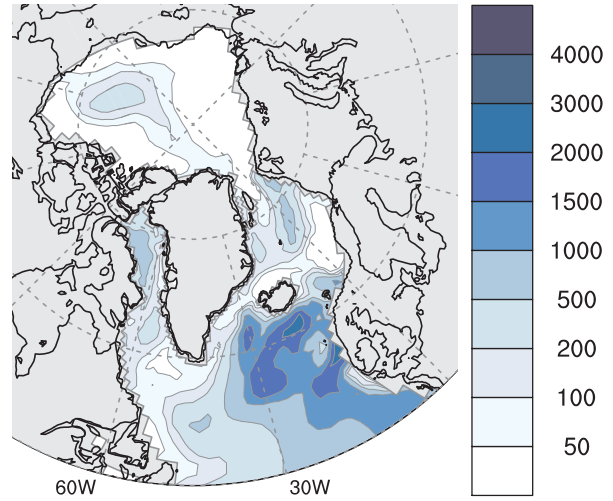

(a) reference

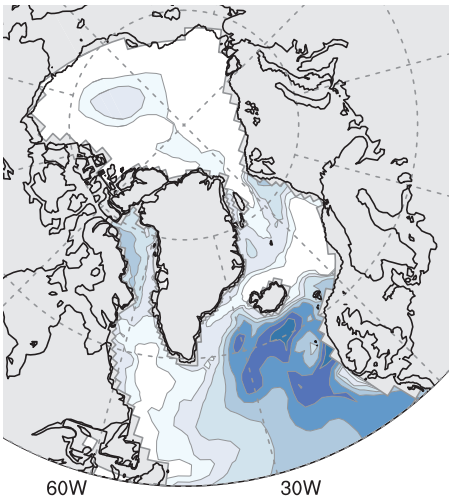

(b) 2050 – 2099

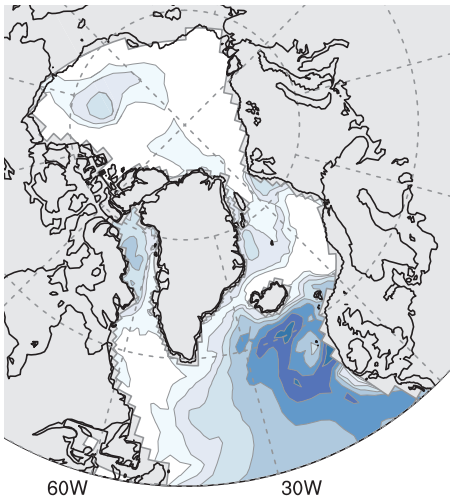

(c) 2350 – 2399

FIGURE 4.14. Mixed layer depths (in m) before and during ice sheet collapse in the Hudson bay. The monthly means were averaged over the displayed time intervals, then the maximum was taken for each grid point.

The horizontal and vertical sections in figs. 4.15, 4.18, and 4.19 show the distribution of the freshwater anomaly in the Atlantic. A part of the freshwater sinks in the deep water formation areas south of Iceland (fig. 4.14). It follows the deep western boundary current at depths around 2000 m to 3000 m to the southern ocean and, as part of the normal route of the NADW, joins the Antarctic Circumpolar Current on its voyage to the East (fig. 4.15(c)). While the salinity in the deep Antarctic Ocean is growing at the start of the surge, this trend stops around year 2050 and, after the year 2350, the salinity decreases. We show this for the depth level centering at 4198 m in fig. 4.16. The freshening in the deep layers of the Atlantic is strongest in the north at the overflows from the GIN and Labrador Seas. In ASYNC, the correlation between the salinity in the Antarctic Circumpolar Current at 2200 m depth and the freshwater flux into the Labrador Sea (both as defined

in fig. 4.17) is $r = -0.6$ for a lag of about 200 years, the time it takes the salinity anomaly to travel through the Atlantic (both time series detrended and smoothed with a 20 year running mean).

The freshening in the southern Atlantic is strongest at depths between 1500 m and 3000 m and up to about 10°from the coast (fig. 4.19). Over time, it spreads over the entire width of the Atlantic basin. Figs. 4.15(a) and 4.19(b) show an increase in sea surface salinity. There is considerable variability in the SSS, and the sign of the anomaly changes over time, but, averaging over the years 2000 to 2999 yields a positive mean anomaly, while the deeper ocean freshens. Fig. 4.19(b) shows an increase in salinity around 1000 m of depth. A comparison with figs. 4.18(a) and 4.19(a) shows that this caused by a slight upward shift of the border between the NADW and the Antarctic Intermediate Water.

At larger distances from the Labrador Sea, the surface signal is much smaller than the background climate variability, but in the deep ocean, that has a very long time scale, we can detect small changes very easily. In the Pacific, the salinity decrease caused by the ice sheet collapses is only 0.005 psu at 2200 m depth, but, in ASYNC, even this small change stands out strongly against the background variability. At greater depths, the signal does not appear against the background drift.

The freshwater that does not sink in the deep water formation areas follows the Subtropical Gyre, and sinks down to intermediate depths west of the French and Spanish coasts as part of the ventilation of the thermocline (Luyten et al., 1983). With the subtropical Gyre, it is brought to the Gulf of Mexico (fig. 4.15).

In the Atlantic, there is hardly any change in the in situ density. The reduction in salinity is practically completely compensated for by a reduction in ocean temperature that reaches 1 K in the center of the Mediterranean Water. The Salinity of the Mediterranean Water decreases in the deep layers of the Strait of Gibraltar (not shown) as well as in the Atlantic (fig. 4.15). The depth of the Mediterranean water tongue in the Atlantic increases as can be seen from the dipole anomaly in fig. 4.18(c), where there is a slight increase in salinity just below the depth of the maximum salinity of the Mediterranean water. When interpreting the strength of the salinity increase, one has to take the general freshening of the north Atlantic into account.

During the surges of the Arctic ice streams, the zonal wind stress from the westerlies over the North Atlantic increases at the eastern coast, while it weakens at the American coast (fig. 4.20(a)). The westward wind stress south of Iceland decreases but the multi-annual variability is of a similar magnitude as the change. With the surge of the Hudson Strait Ice Stream, the pattern changes and the wind stress caused by the westerlies at the European coast decreases in strength. For an extreme 50-year average see fig. 4.20(b). The difference between maximum and minimum zonal wind stress over the North Atlantic varies around the reference value during the surges of the Arctic ice streams (fig. 4.21). During the surge of the Hudson Strait Ice Stream, it drops below this value and stays there for the remainder of the experiment.

During the ice stream surges, the NADW cell (fig. 3.4(b) for the mean state and fig. 4.22(a) for the variations during the ice stream surges), the North Atlantic Subpolar Gyre (ASPG) and the Subtropical Gyre (fig. 4.23) weaken. The Antarctic Bottom Water cell in the Atlantic is hardly influenced, and rather weakens than strenghens in SYNC, while in ASYNC, it strengthens during the ice stream surges. In the following we detail on the different aspects of the ocean circulation.

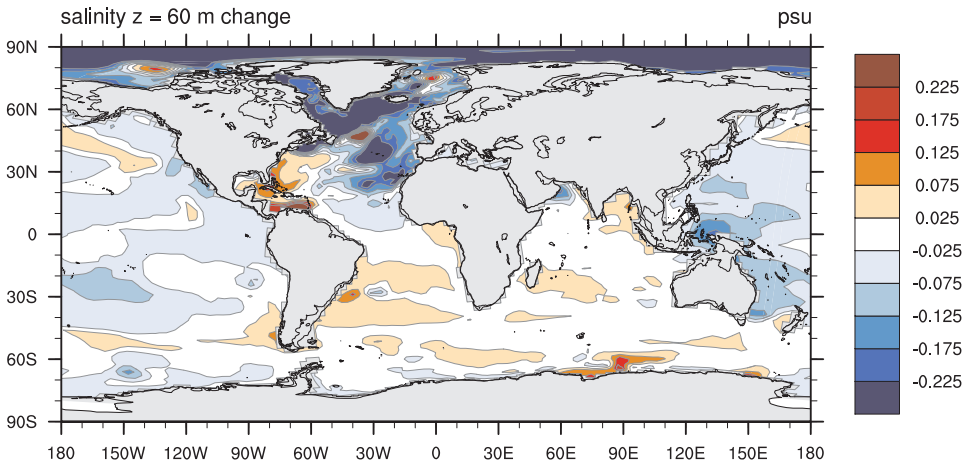

(a) Salinity change in 60 m depth

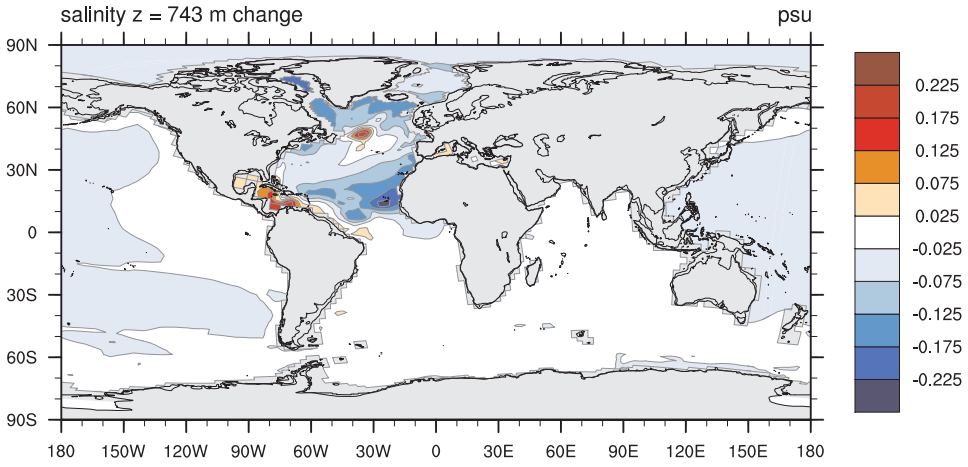

(b) Salinity change in 750 m depth

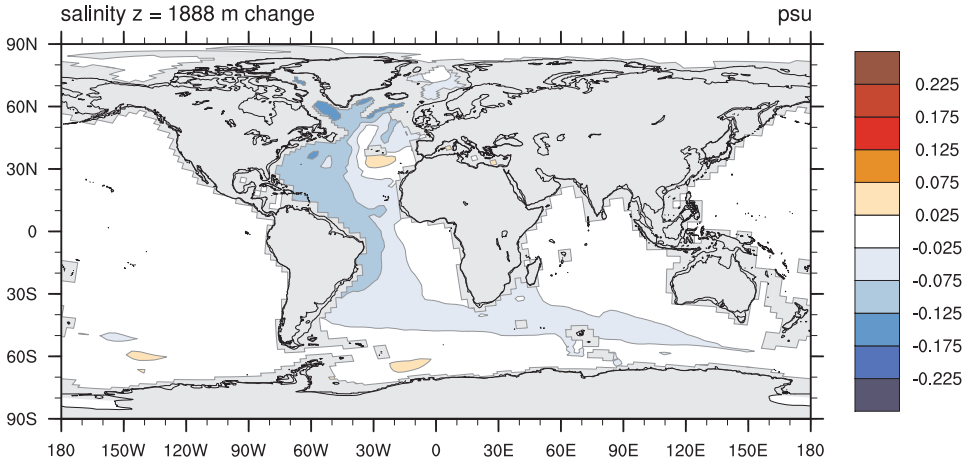

(c) Salinity change in 1900 m depth

FIGURE 4.15. Atlantic salinity changes during the Hudson Strait Ice Stream surge in SYNC. Averaged over the years 2350 to 2399 for the surge and years 8550 to 8749 from ASYNC as reference state.

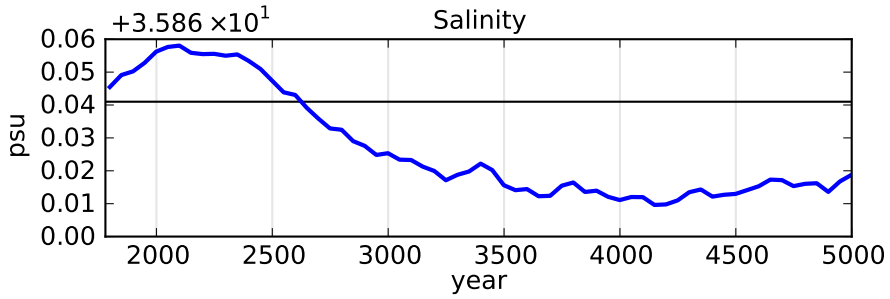

FIGURE 4.16. Salinity in the Antarctic Circumpolar Current in the depth level centering at 4198 m. The black line indicates the value during the reference period. For the definition of the region see fig. 4.17.

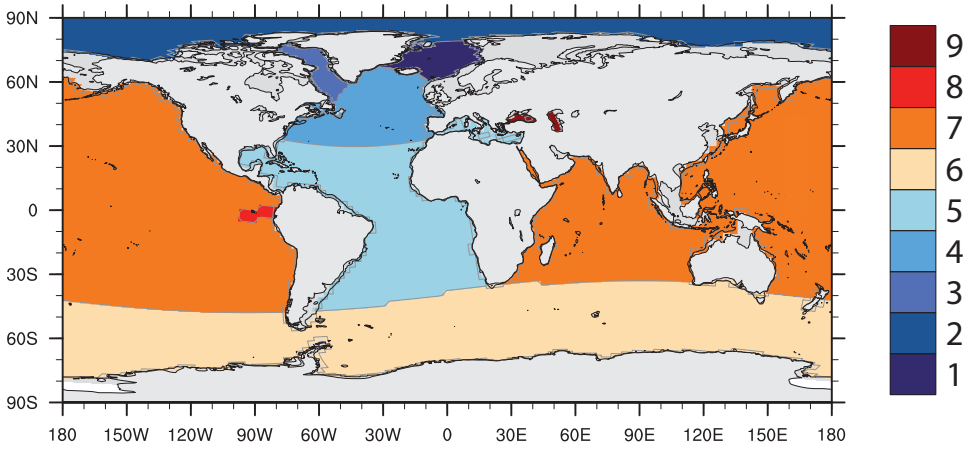

FIGURE 4.17. Basins used for time series and basin averages: 1: GIN Sea, 2: Arctic Ocean, 3: Labrador Sea, 4: northern Atlantic, 5: tropical and southern Atlantic, 6: Antarctic Circumpolar Current, 7: Indian Ocean and Pacific, 8: El Niño area, 9: Lakes and inland seas.

The NADW cell (fig. 4.22) has a mean strength of 23.4 Sv during the reference period. During the collapse it does not exceed 22.5 Sv and most of the time it is below 22 Sv. The first two minima for the intervals 1900–1949 and 2050–2149 correspond to the two main pulses from the Arctic ice streams. They are followed by the two strongest minima as low as 20.5 Sv during the first maximum period of the surge of the Hudson Strait Ice Stream around years 2250 to 2400 and during the surge of the Barents Sea Ice Stream between years 2500 and 2600. After the surge of the Barents Sea Ice stream, the circulation partially recovers to about 21.5 Sv and is hardly affected by the second phase of the Surge of the Hudson Strait Ice Stream. With the slow-down of the surge, the NADW cell strengthens again (fig. 4.22), but does not regain its full strength. In ASYNC the NADW exhibits a similar behavior of with decreases in strength matching with the ice stream surges (fig. 4.22(c)). In ASYNC, the correlation between the NADW cell strength and the global freshwater flux is $r = -0.63$ at a lag of 25 years (0.5 at zero lag, both timeseries detrended and averaged with a running mean of 20 years).

The AABW cell (fig. 4.22) shows values between 3.4 Sv and 3.7 Sv during the reference period. During the surges, it first slightly increases and then decreases

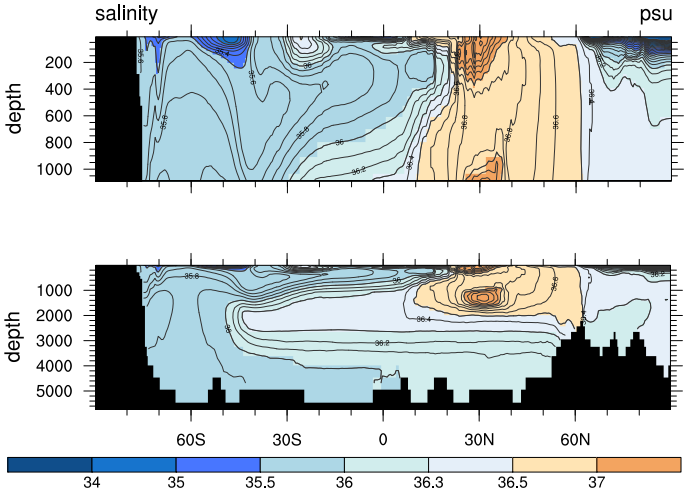

(a) Atlantic ocean salinity in the reference period (years 8550 to 8749 of ASYNC). Isolines are drawn every 0.1 psu.

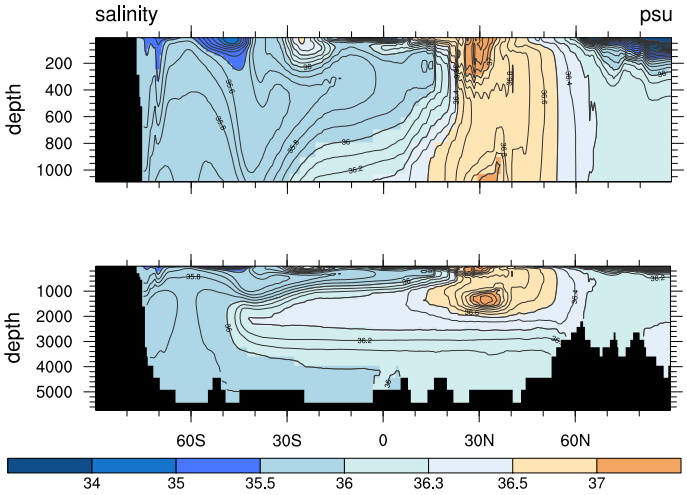

(b) Years 2350 to 2399. Isolines are drawn every 0.1 psu.

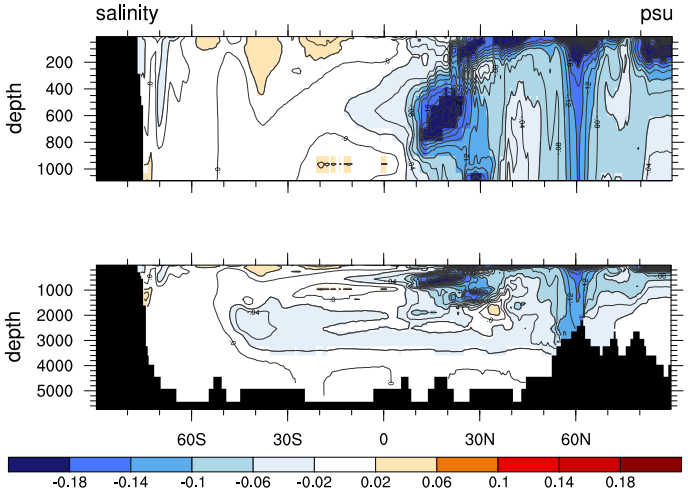

(c) Years 2350 to 2399 of SYNC – years 8550 to 8749 of ASYNC. Isolines are drawn every 0.02 psu.

FIGURE 4.18. Atlantic salinity in the reference period and during the Hudson Strait Ice Stream surge in SYNC. The data is averaged over the Atlantic and Arctic Ocean from 30°W to 30°E.

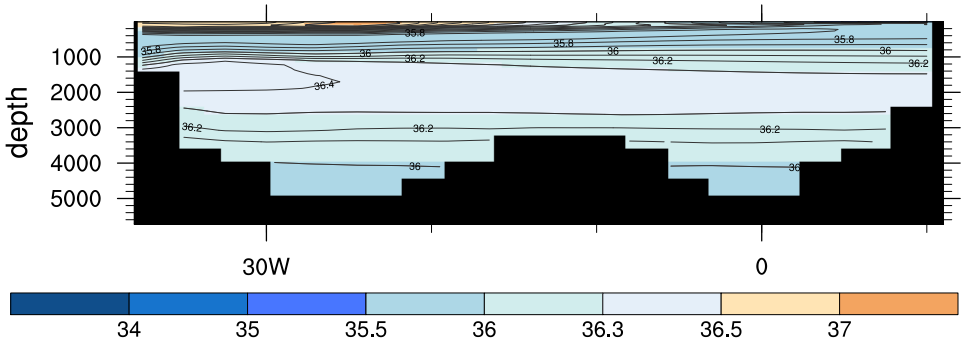

(a) Salinity during the reference period (years 8550 to 8749 of ASYNC). Isolines are drawn at 0.1 psu intervals.

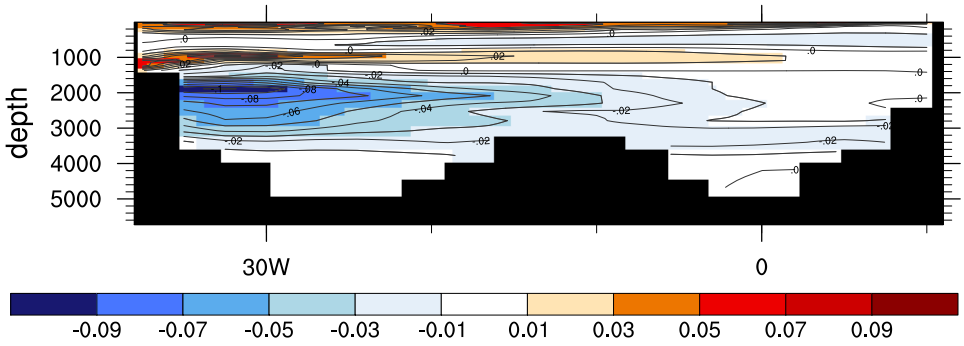

(b) Salinity difference between years 2350 to 2399 of SYNC and 8550 to 8749 of ASYNC. Isolines are drawn at 0.01 psu intervals.

FIGURE 4.19. Salinity in the Atlantic at 20°S during the reference period and salinity change during the Hudson Strait Ice Stream surge. Salinity Values are in psu. Depth values are in m.

below the reference value. This behavior is interesting because the AABW cell cannot profit from the weakness of the NADW cell in SYNC, and this behavior contrasts with the behavior observed in ASYNC where the AABW cell strengthens in times with a strong NADW cell (fig. 4.22, r=0.53 on the 50-year means with the AABW leading the NADW by one 50 year block, and r=0.45 for the zero-lag match). The leading of the AABW can be interpreted as the AABW being only shortly affected by the freshening. This would also explain why there is hardly any, or a reverse effect in SYNC. The correlation of the AABW cell strength with the global freshwater flux is $r = 0.4$ for a 25 year lag (r=0.32 for zero lag), a slightly delayed strengthening of the AABW cell when the freshwater fluxes into the ocean increase (both timeseries detrended and smoothed with a 20-year running average).

In the reference period, the ASPG strength varies between 34.5 Sv and 37.5 Sv (figs. 4.23, 4.24(c)). During the first and second surge phases of the Arctic ice streams, it decreases to about 32 Sv (fig. 4.24(a)). During the surge of the Hudson Strait Ice Stream, it varies between 34 Sv and 28.5 Sv with minima at the peaks of the surges of the Hudson Strait Ice Stream and the Barents Sea Ice Stream (fig. 4.23(b)). There is a last strong decrease in Gyre strength around year 3700, then it recovers to pre-surge values. In ASYNC, the ASPG weakens in the first

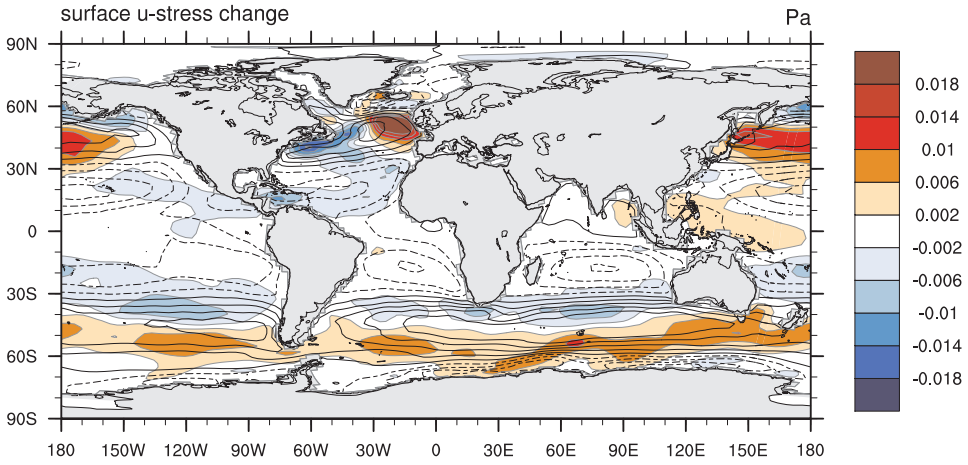

(a) 2050 to 2099

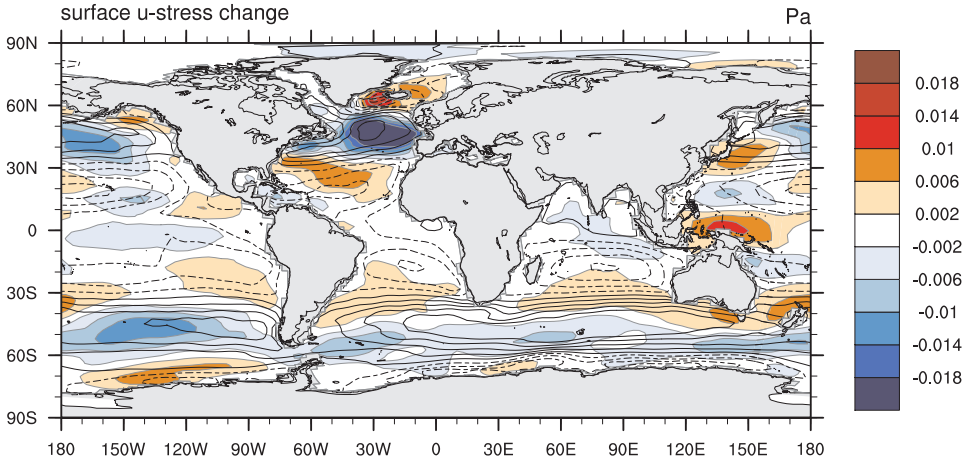

(b) 4000 to 4049

FIGURE 4.20. Change in zonal wind stress during the ice stream surges in SYNC compared to the reference period (8550 to 8749 of ASYNC). Overlain is the zonal wind Stress in the reference period with contour levels of 0.04 Pa starting at ±0.02 Pa. Dashed outlines indicate negative values.

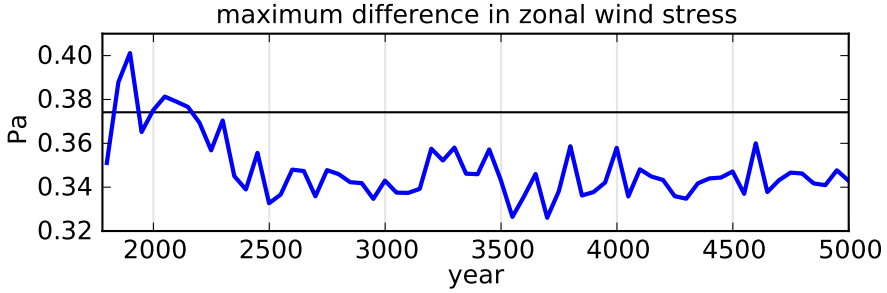

FIGURE 4.21. Maximum wind stress difference (max - min) over the North Atlantic (including GIN Sea, Arctic Ocean and Labrador Sea). Computed from 50-year monthly means. The black line marks the value in the reference period.

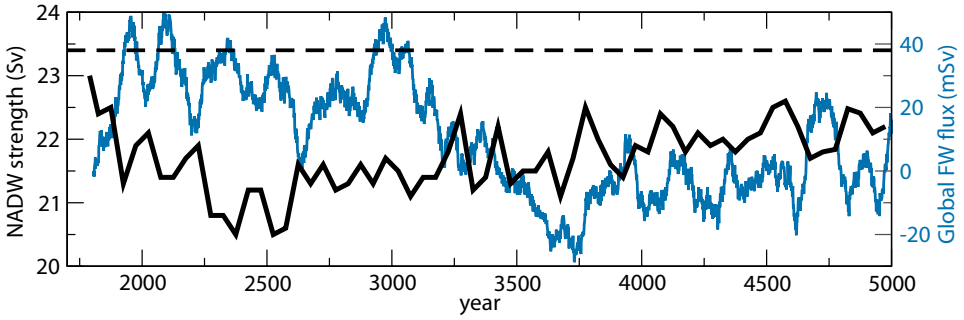

(a) Strength of the NADW cell in SYNC.

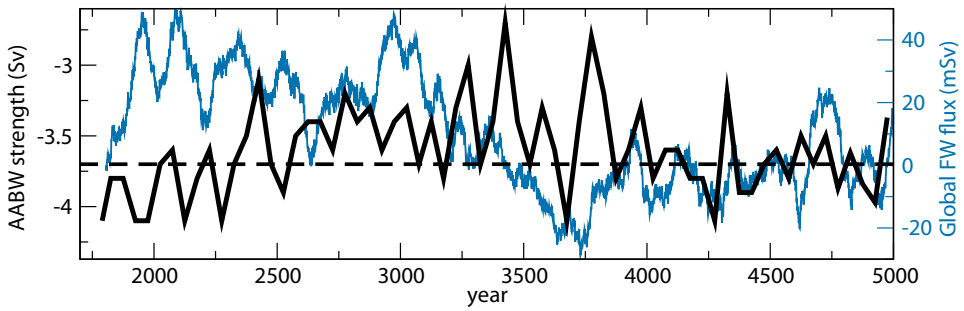

(b) Strength of the AABW cell in SYNC.

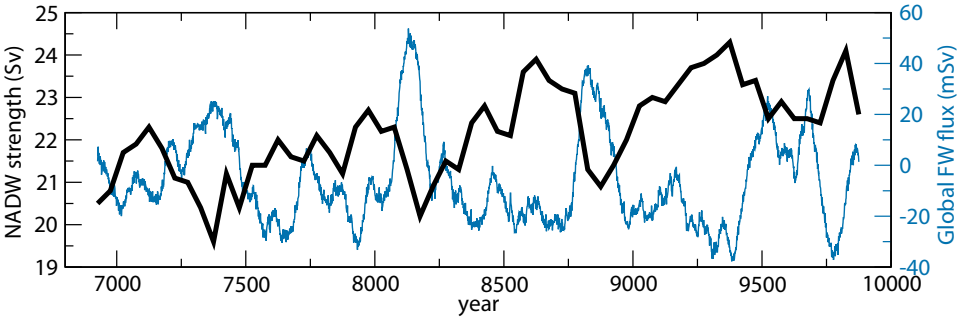

(c) Strength of the NADW cell in ASYNC.

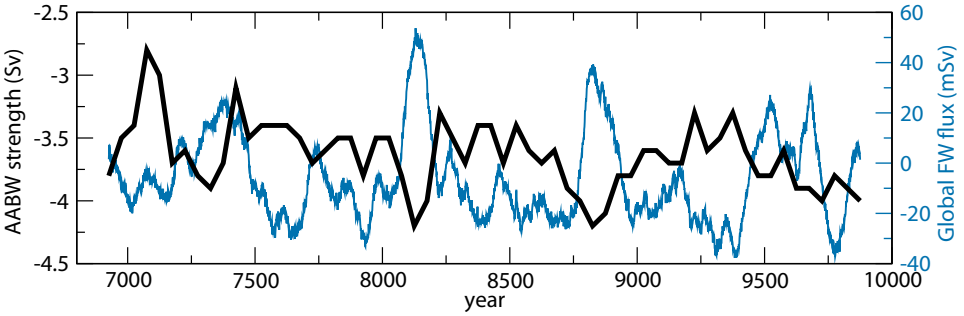

(d) Strength of the AABW cell in ASYNC.

FIGURE 4.22. Maximum and minimum Atlantic Meridional Overturning Circulation streamfunction computed for 50-year intervals of SYNC and ASYNC. In the background, the 50-year running mean of the global freshwater flux into the ocean is shown in blue. The dashed lines in (a) and (b) show the mean strength in the reference period.

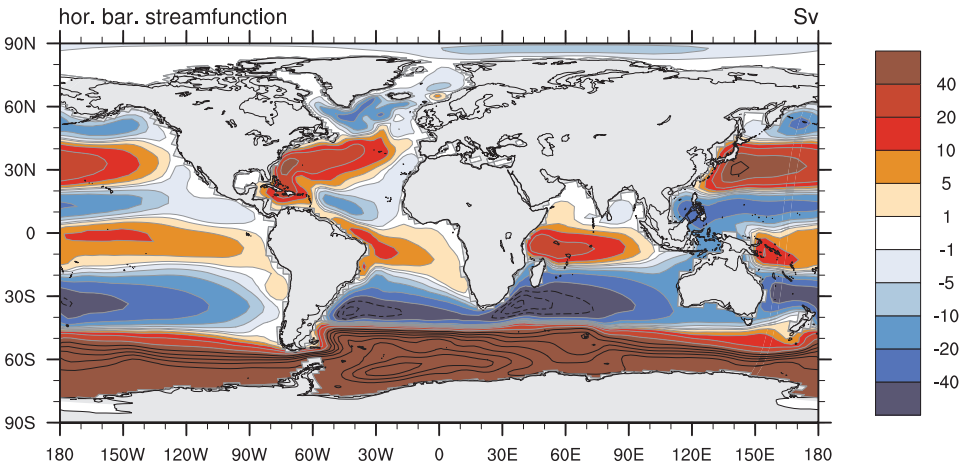

(a) Barotropic stream function before the ice sheet collapse. Averaged over years 8550 to 8749 of SYNC. For values beyond ±40 Sv, black contour lines are drawn at intervals of 20 Sv starting at ±60 Sv.

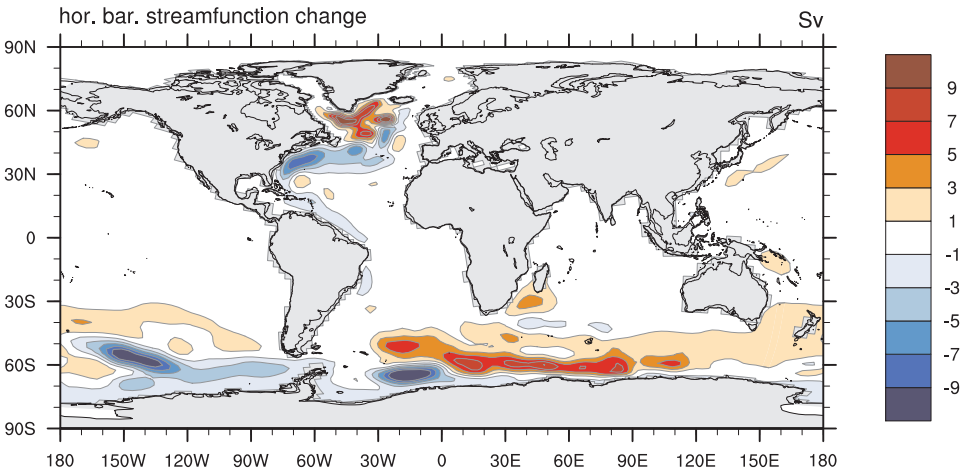

(b) Barotropic stream function change during the ice sheet collapse. Difference between the years 2350 to 2399 and the reference period shown above.

FIGURE 4.23. Change in barotropic ocean circulation.

three Hudson Strait Ice Stream surges, while it remains practically constant during the last surge.

During the reference period, the North Atlantic Subtropical Gyre (fig. 4.23, fig. 4.24(b)) has a strength varying between 51.7 Sv and 53.5 Sv. In SYNC, it shows a first minimum of 49.5 Sv during the first surge phase of the Arctic ice streams. As the ASPG it shortly recovers and weakens again to the same level in the second surge phase. From this, it does not recover but it further weakens to 46 Sv when the Hudson Strait Ice Stream becomes active around year 2200. During the remainder of the surge it varies between 46 Sv and 50 Sv with maxima around year 2600 and between years 3100 and 3300. After 3300 it falls back to about 47 Sv and then slowly recovers to values around 50 Sv at year 5000.

The overall behavior is qualitatively similar in the first three out of the four surge events in ASYNC. The fourth event, starting at climate model year 9500,

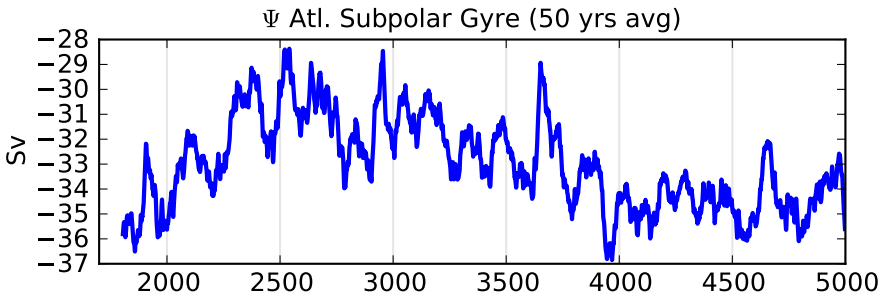

(a) SYNC.

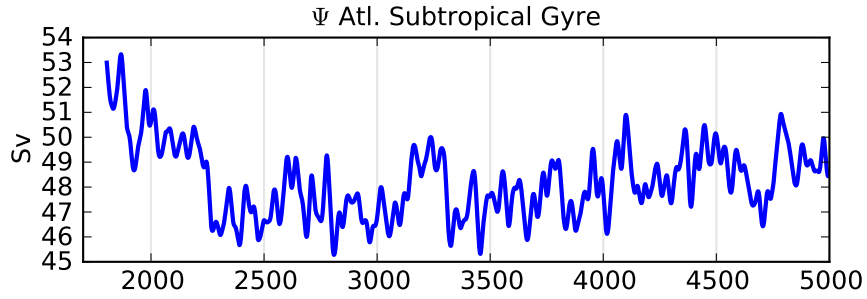

(b) SYNC

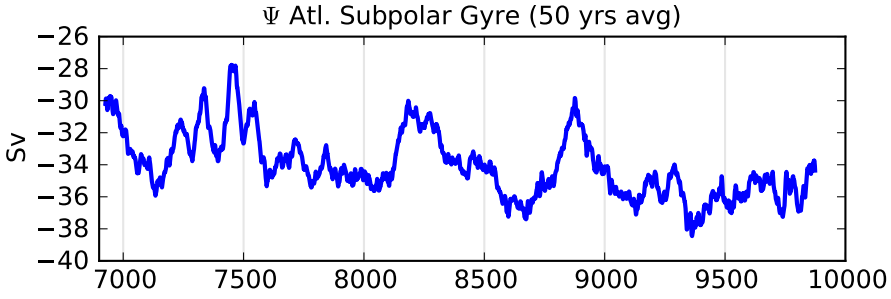

(c) ASYNC

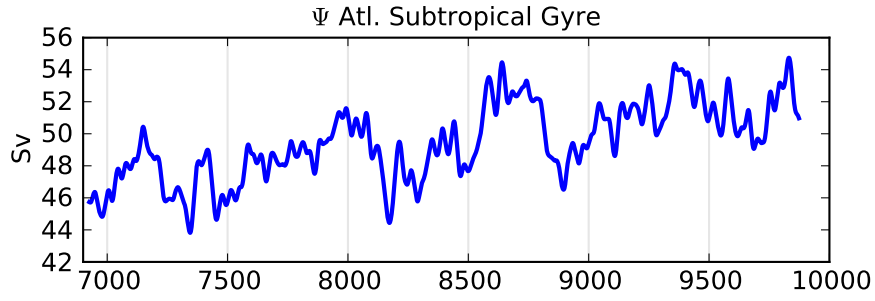

(d) ASYNC

FIGURE 4.24. Atlantic Subpolar and Subtropical Gyre stream function maximum (minimum). Note the sign difference between the two gyre systems. The surges in ASYNC start at years 72 000, 80 750, 88 000, and 95 000.

yields hardly any changes in the ocean circulation, while the changes in the salinity structure are largely similar to the other events. Due to the asynchronous coupling, these events are too short to analyze the detailed structure and timings of the different minima.

4.5. The response of the atmosphere

In the following, we describe the changes in air temperatures, precipitation, energy balance, and atmospheric transports during the ice stream surges in SYNC (see fig. 4.5 for surface elevations and fig. 4.3 for the fluxes). The seasonal analysis, especially of the radiation balances, is obstructed because the calendar of ECHAM5. The calendar follows the Gregorian calendar in high detail and contains the different leap year cycles as well as the long-term drift of the timing of the equinoxes and solstices. So, while the annual mean TOA incoming shortwave flux is constant, the timing of the season within a year varies on several levels. We show this in fig. 4.25 for the March TOA incoming solar radiation at 60°N averaged over the 50 year blocks that we use for the analysis of the climate data. There are three patterns in the radiation. (1) an alternating between higher and lower radiation because of the missing leap day every 100 years, (2) a sawtooth with a period of 400 years, because of the extra-leap day every 400 years, and (3) a long-term increase in March TOA incoming solar radiation corresponding to a calendar shift of about 2 days in 6000 years. Therefore, a comparison of radiative fluxes on sub-year base for different years practically always shows a hemispheric signal. Patterns that are not zonally symmetric can be interpreted with good confidence that they are not an artifact of the calendar, as can patterns that go against the trend expected from the pattern in the incoming shortwave radiation. Zonally rather symmetric pattern that match the trend expected from the incoming shortwave radiation have to be considered with great caution.

As the ocean, the atmosphere already responds to the surges of the Arctic ice streams before the Hudson Strait Ice Stream starts surging. Starting with the year 1800, there is a cooling centering over the Labrador Sea (figs. 4.26(a) and 4.27(a)). It stretches to the west over the Laurentide Ice Sheet and to the east into the GIN Sea. Over the Labrador Sea, the annual mean 2 m air temperature decreases by more than 4 K while over the Laurentide Ice Sheet and western Greenland, the cooling is limited to about 1 K. Over the GIN Sea, it can reach values up to 2 K. The cooling over the Labrador and GIN Sea is strongest in SON and DJF with slightly stronger cooling during SON.

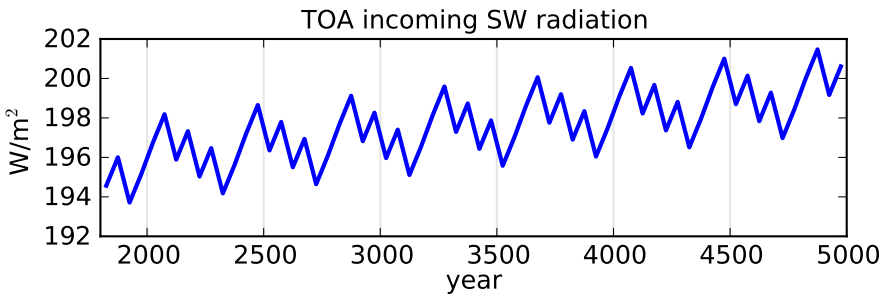

FIGURE 4.25. The effect of the calendar drift visualized using the TOA incoming shortwave at 60°N during March. Averaged in 50 year blocks ([0;49] and [50;99] respectively).

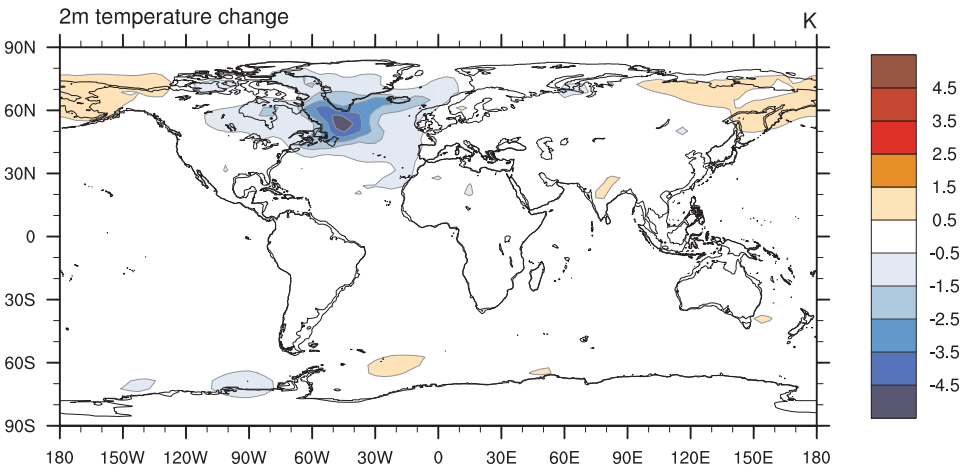

(a) 2 m air temperature changes during the surge of the Arctic ice streams (years 2050 to 2099 of SYNC minus reference (years 8550 to 8749 of ASYNC)).

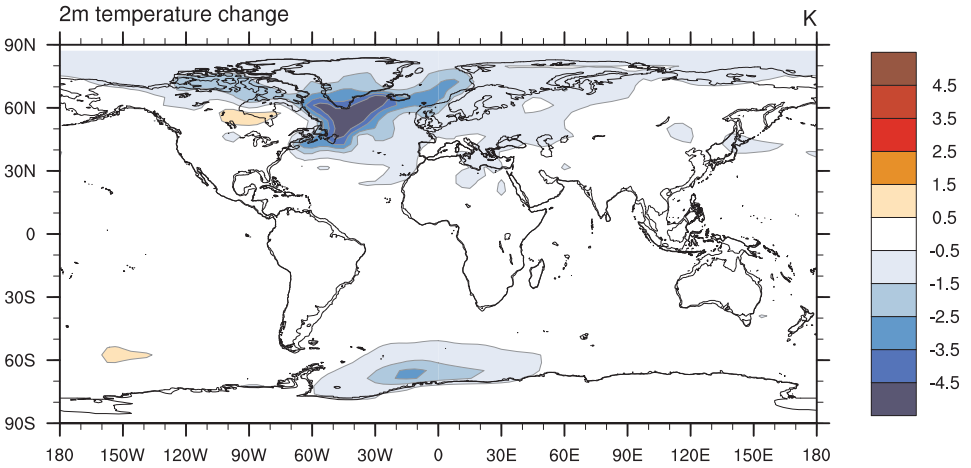

(b) The 2 m air temperature changes during the surge of the Barents Sea Ice Stream into the Norwegian Sea (years 2500 to 2549 of SYNC – reference).

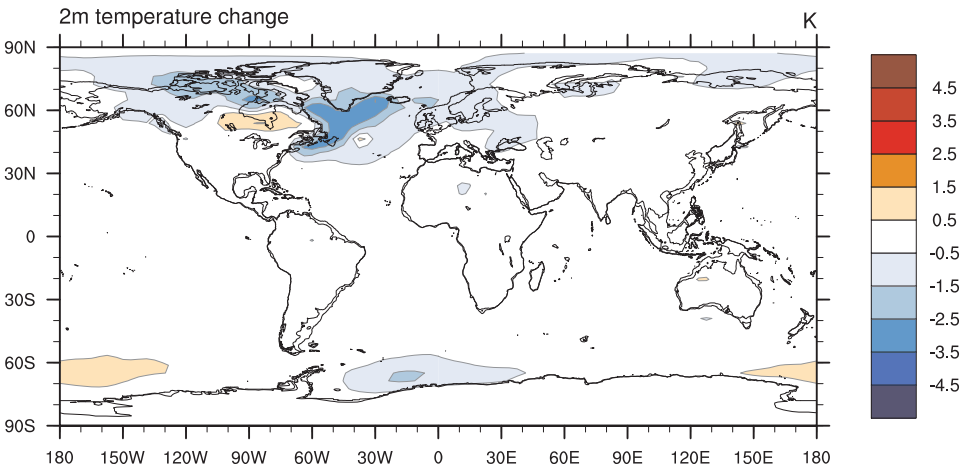

(c) The 2 m air temperature changes during the second part of the surge of the Hudson Strait Ice Stream (years 2900 to 2949 of SYNC – reference).

FIGURE 4.26. Changes in 2 m air temperature during different stages of the ice sheet collapse.

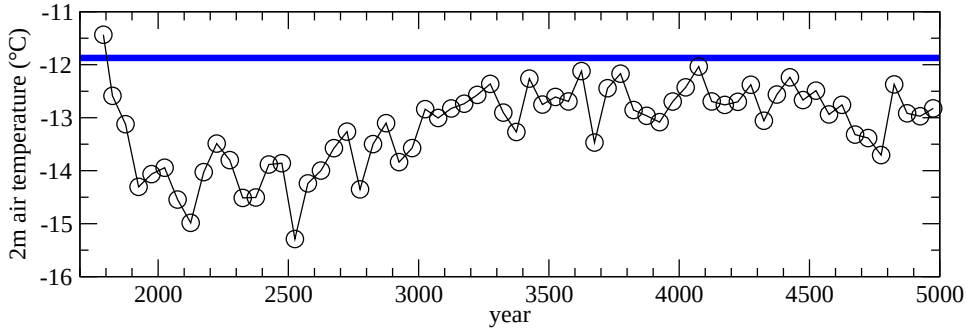

(a) SYNC.

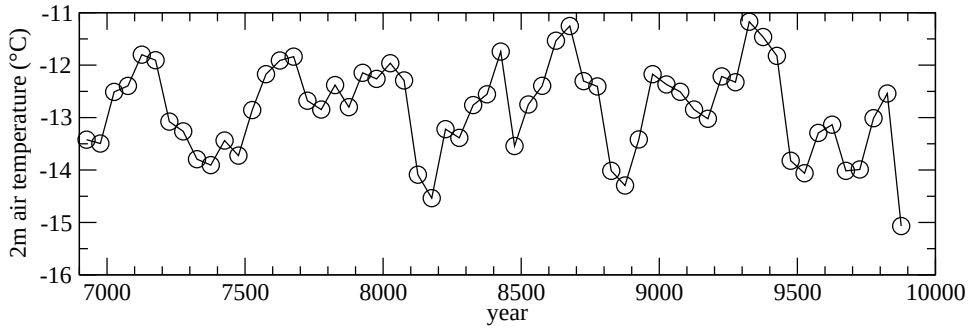

(b) ASYNC.

FIGURE 4.27. The 2 m air temperatures in the region from 30 °W to 60 °W and from 45 °N to 75 °N. The blue line in fig (a) marks the mean of the temperatures during the reference period (years 8550 to 8749 of ASYNC)

The cooling over the Labrador Sea is caused by the increased sea ice cover (compare fig. 4.26(a) with fig. 4.8(c)). The extra sea ice reduces the heat flux from the ocean, and increases the albedo (over the Labrador sea, albedo changes exceed +0.2 in JJA and SON). The increased albedo causes a reduction in shortwave absorption over the southern Labrador Sea, that causes a decrease in the top of atmosphere net shortwave radiation (fig. 4.28). From the Labrador Sea, the cooling spreads by reduced advection of heat over Greenland and over the Laurentide Ice Sheet. Over the eastern Laurentide Ice Sheet, the surface elevations at this stage of the experiment are higher than in the reference period because the ice sheet is still building up for the surge of the Hudson Strait Ice Stream. The higher surface elevation contributes further to the cooling.

With the surge of the Hudson Strait Ice Stream, the cooling over the Labrador Sea and Irminger Basin intensifies (fig. 4.27). The cooling reaches its first maximum with the peak of the surge of the Hudson Strait Ice Stream around year 2300. Then it weakens again, as the surge weakens. When the Barents Sea Ice Stream surges around year 2500, the cooling reaches its absolute maximum between years 2500 and 2550 (fig. 4.26(b)). Then, the temperatures partially recover and only a limited cooling remains. The second surge phase of the Hudson Strait Ice Stream starting around year 2900 only shows a mild impact on the temperatures (figs 4.26(c), 4.27(a)).

While the Atlantic sector of the (sub-) polar regions cools, there is a slight (1 K) warming trend over Northeast Siberia, Kamchatka, and Alaska (fig. 4.26(a)). Over

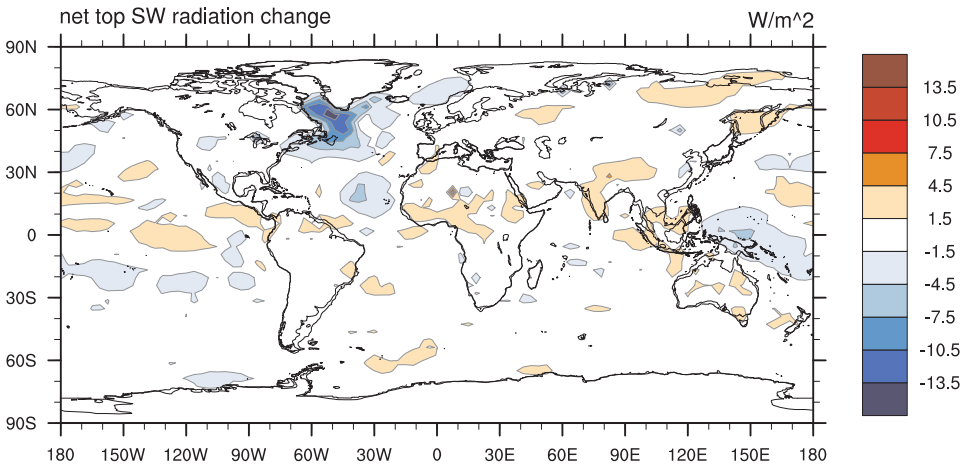

FIGURE 4.28. Top of atmosphere net shortwave radiation change during the Arctic ice stream surges. (2050 to 2099 of SYNC – 8550 to 8749 of ASYNC).

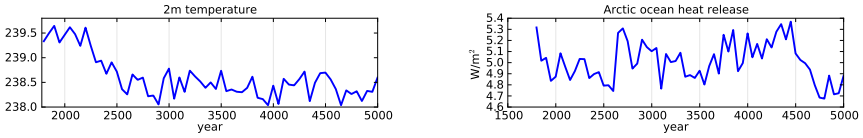

(a) 2 m air temperature over the Arctic Ocean. (b) Heat release from the Arctic Ocean

FIGURE 4.29. Arctic Ocean 2 m air temperature and heat release from the ocean.

the western part of the temperature anomaly in Northeast Siberia, the warming is largely due to less clouds and therefore more sunlight reaching the surface in summer (fig. 4.28). From this region, heat is transported downwind towards Alaska. The warming over Kamchatka is also caused by a reduction in clouds and is strongest in SON. The strength of the warming in SON could partly be caused by the calender shift pushing autumn two days further into summer and removing two winter days. The annual mean signal is not caused by the calendar of ECHAM5. Over the other parts of the world temperature changes are mostly minor ($< 0.5\,\mathrm{K}$).

The 2 m air temperature over the Arctic Ocean, that remains constant during the surge of the Arctic ice streams, decreases by 1 K to 238.5 K when the Hudson Strait Ice Stream starts surging in year 2200 (fig. 4.29(a)). It remains at this value until the end of the experiment. The cooling is caused by small decreases in top of atmosphere (TOA) net shortwave flux, and in atmospheric advection. The ocean heat release does not contribute to the temperature trends (fig. 4.29(b)).

With the progressing surge of the Hudson Strait Ice Stream, the surface elevation over the Hudson Bay decreases (fig. 4.5). This leads to a lapse-rate related temperature increase, that is, however, restricted to the southern part of the Hudson Bay (fig. 4.26). The northern Hudson Bay and the Canadian Arctic Archipelago (CAA) cool throughout the experiment. For the following quantification, we average over the region from 120°W to 75°W and from 60°N to 75°N. The surface temperature decreases from an average of 243.1 K in the reference period to 241.7 K averaged over the years 4000 to 5000. In the years up to 2250, the cooling is relatively constant at about 0.6 K and we can partially explain it by an increase in

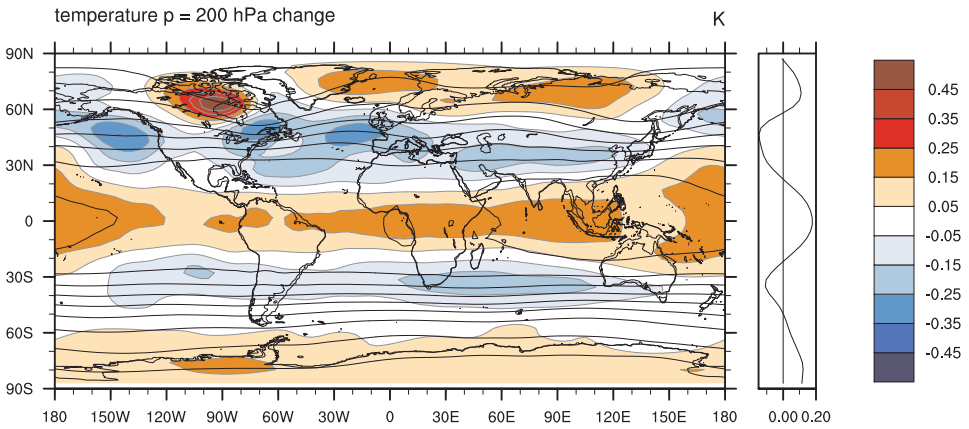

FIGURE 4.30. Change in 200 hPa temperatures averaged over the years 3000 to 3999 of SYNC compared to years 8550 to 8749 of ASYNC. To show the mean circulation, the 200 hPa geopotential height contour lines at intervals of 200 m are overlaid in black.

surface elevation of (on the average) 50 m compared to the reference period. Later, the surface elevation over the CAA decreases but the temperatures keep falling. One factor that contributes to this cooling is a reduction in cloud cover (`aclcov`) from 78% in year 2250 to 73% in year 4000. This reduction is present in all seasons and leads to higher net shortwave gains in summer ($+0.4\,\mathrm{W/m^2}$ in the annual mean, while the increase in SW reaching the surface is about $3\,\mathrm{W/m^2}$) but also to less reflection of outgoing longwave (LW) radiation in all seasons ($-4\,\mathrm{W/m^2}$ change in downward LW reaching the surface in the annual mean). The atmospheric transport of heat into the region decreases from $99\,\mathrm{W/m^2}$ in the reference period via $98\,\mathrm{W/m^2}$ until year 3000 to values between $97.5\,\mathrm{W/m^2}$ and $97\,\mathrm{W/m^2}$ in the years from 4000 to 5000.

At a height of 200 hPa a banded, zonal signal with warming over the tropics and polar areas and cooling over the mid-latitudes emerges (fig. 4.30). The warming over the subpolar regions has three maxima, one over the northwestern Hudson Bay stretching northwest from there, one over eastern Greenland and the Greenland Sea and one over northern Siberia at about 120 °E. The warming over the northwestern Hudson Bay can be explained by a decrease in southward wind in this area (fig. 4.31, the area of the maximum in southward wind decreases clearly). Over the GIN Sea, the northward component of the mean flow is strengthened by about 0.4 m/s (3000 to 3999 – reference). West of the Ural, the northward wind speed increases slightly, possibly contributing to the warming over northern Siberia. The temperature pattern is less pronounced in ASYNC. The northern subpolar warming and the cooling in the mid-latitudes during and after the Hudson Strait Ice Stream surges are present in ASYNC, but the cooling over the southern mid-latitudes is not present in ASYNC. The dominant signal over the tropics in ASYNC is a warming starting at year 8800, the start of SYNC, and lasting until the end of the experiment. Therefore the emergence of this signal in SYNC probably is more related to model drift than to the ice stream surges.

The **precipitation** shows substantial variability on a multidecadal time scale. Therefore averaging over several centuries is necessary to distinguish between changes induced by the ice stream surges and the multidecadal variability of the Atmosphere–Ocean system. In fig. 3.3(c) we show the mean precipitation in ASYNC. All precipitation changes during the ice sheets surges are small compared to the total

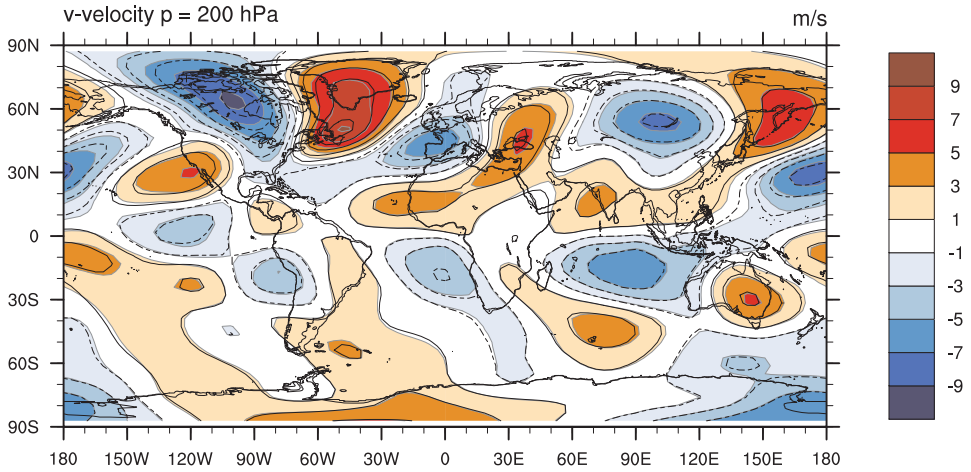

FIGURE 4.31. 200 hPa zonal wind velocities. Colors: years 3000 to 3999, black contour lines: reference period with same contour levels. Negative values are drawn with dashed outlines.

precipitation. We show the precipitation changes in fig. 4.32. They are averaged over (a) the years 2000 to 3000 and (b) 3000 to 4000 of SYNC. The mean precipitation change in the years 4000 to 5000 is very similar to that of 3000 to 4000. We therefore do not plot it. To test the significance of the changes, we compute the standard deviation σ of 200 year averages (the duration of our reference period) of the precipitation between years 3000 and 5000 of SYNC. We draw the 2σ contour lines as dashed lines in fig. 4.32. Precipitation changes beyond 2σ very likely are not random variability, but either are long-term drift in the model or are caused by the ice stream surges. Since the model shows considerable long-term drift in ASYNC (fig. 3.25), we discuss the precipitation changes in SYNC by comparing them to the long-term changes in ASYNC.

In the long term drift of ASNYC (fig. 3.25) as well as in SYNC (fig. 4.32), a dipole pattern develops over the North Atlantic with drier conditions in the northern part of the dipole and wetter conditions in the southern part. The spatial extents of the positive and negative anomalies differ between the two experiments, with a precipitation reduction in ASYNC that is limited to the GIN Sea and a precipitation reduction in SYNC, that extends further to the south and includes the Irminger Basin, the Iceland Basin and parts of the Labrador Sea. The details will be described in the following.

In both experiments, the sea ice cover in the GIN Sea expands (see fig. 3.26 for the timeseries of ASYNC and fig. 4.8 for maps of selected periods of SYNC). The increased sea ice cover reduces the evaporation and thereby causes a reduction in precipitation. In SYNC, a dipole pattern in the net precipitation – evaporation (P-E) flux develops. Over the Norwegian Sea, where most of the increase in sea ice cover occurs, the reduction in evaporation outweighs the reduction in precipitation and the change in the P-E flux is positive throughout SYNC, while over the Greenland and Iceland Seas, that already are largely ice covered before the surges, there is a net reduction in the P-E flux. In contrast, in ASYNC the P-E flux is reduced over the entire GIN Sea. This matches with the increasingly southward blowing wind in ASYNC (fig. 3.22).

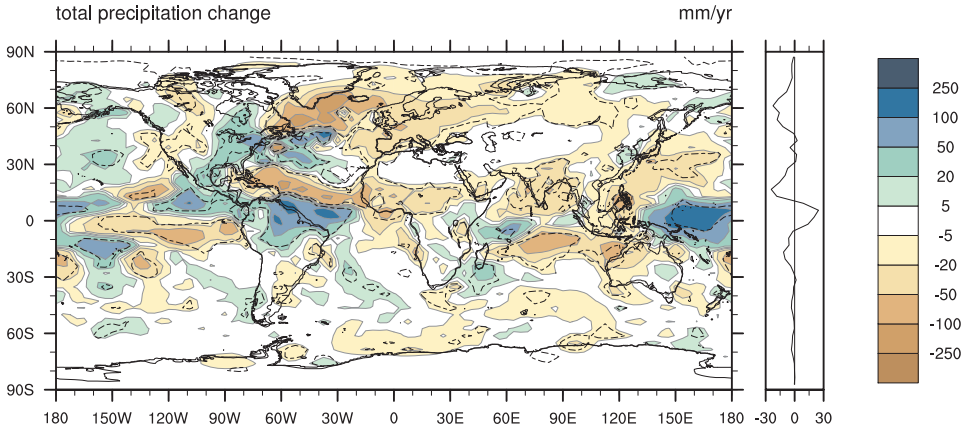

(a) 2000 – 3000

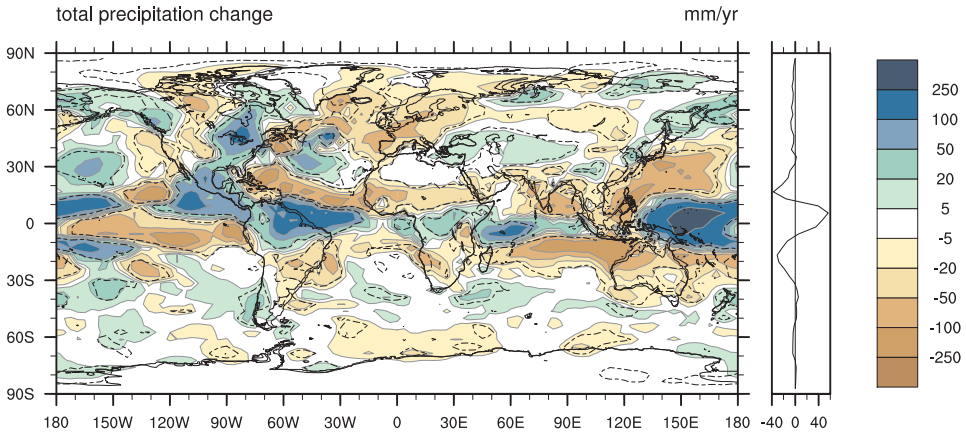

(b) 3000 – 4000

FIGURE 4.32. Precipitation changes averaged over different phases of SYNC. Reference period are the years 8550 to 8749 of ASYNC. Dashed lines mark regions, where the changes exceed 2 standard deviations computed from 200 year means of the preciptiation in the years 3000 to 5000 of SYNC.

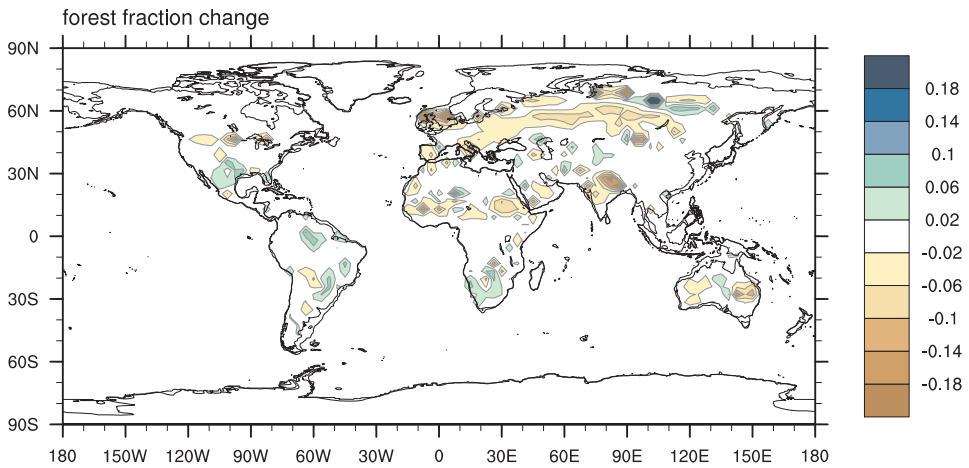

FIGURE 4.33. Forest cover changes (2500 to 2549 – reference).

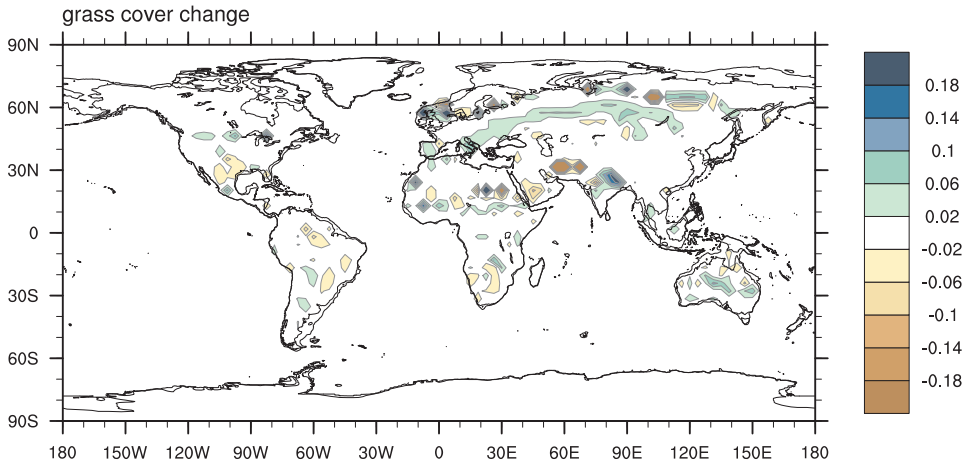

FIGURE 4.34. Changes in grassland and steppe (2500 to 2549 – reference).

Over the Labrador Sea, the precipitation decreases in the years 2000 to 2999 of SYNC. During the years 3000 to 3999, the precipitation stays low over the southern part of the Labrador Sea, while it increases over the northern part. The increase in precipitation over the northern Labrador Sea matches with a general increase in precipitation over the eastern Laurentide Ice Sheet.

The precipitation over the Irminger Sea weakens during the surge of the Hudson Strait Ice Stream. As in the GIN Sea, the P-E flux is split into a net decrease in the west, that is already largely sea ice covered before the surge, and a net increase in the east, where the increasing sea ice cover reduces the evaporation. The drift in ASYNC shows an increase in precipitation over the Irminger Sea, so the different signals between SYNC and the drift in ASYNC together with the physical reason give confidence that this change is caused by the ice stream surge. Over the Iceland Basin, a similar pattern as in the Irminger Sea emerges. The evaporation is reduced over the northern part, where the sea ice cover increases, and the precipitation is reduced over the entire basin.

Over northern America, the precipitation changes show a dipole pattern with a decrease in precipitation in the middle part and an increase in the eastern part. Especially during the later years, there is increased precipitation over the Rocky Mountains and Alaska.

The drier conditions over the northern Atlantic spread into Europe and frequently reach far into Siberia (this dry band is responsible for the above mentioned warming in eastern Siberia). Over southern Europe, the reduction in precipitation locally exceeds 50 mm/yr (10% of the annual rain fall in the reference period).

In the years 2000 to 3000, there is a decrease in zonal mean precipitation north of 50°N (see zonal mean diagram in fig. 4.32(a)). Between 50°N and 60°N, about one quarter of this change is caused by a reduction in net P-E flux (and thus by advective processes), while three quarters of the precipitation decrease can be explained by a matching evaporation decrease (not shown). North of 60°N, the change in net P-E flux becomes increasingly important. In the following 1000 years (after year 3000), the zonal mean of the precipitation north of 30°N practically matches the values from the reference period. During this period, the decrease in precipitation over Europe is compensated for by an increase in precipitation over the Pacific and over the eastern Laurentide Ice Sheet.

Over the northern part of the North Atlantic Subtropical Gyre, the precipitation generally increases indicating a slight southward shift of the mid-latitudes rain band. The ITCZ slightly shifts to the southwest causing a dipole pattern in the precipitation anomalies with a precipitation increase over the northern parts of Southern America. While, during the years 2000 to 3000, there only is a reduction in precipitation over the Sahel region, in the following millennia, the rainfall in the tropical rain band over Africa increases and a dipole pattern develops.

A three-band-structure with drier conditions over India, wetter conditions just south of it and then a drier band spanning from Indonesia and northern Australia to Madagascar exists through a large part of SYNC. Northeast of Australia, the precipitation increases. These precipitation changes are very similar to those observed in ASYNC and could simply be model drift. While the drying over Australia and the increased precipitation northeast of Australia also appear as long-term drift in ASYNC, but a very similar signal also exists in the ECHAM5/MPIOM *COSMOS-S* hosing experiment in Kageyama et al. (2013), that is probably the simulation of this set that is closest to our experiment. This suggests that this pattern is an actual consequence of the ice stream surges.

In ASYNC, several precipitation changes from SYNC are not reproduced. The drying over the Northern Atlantic is mostly limited to the Labrador Sea, and the associated increase in precipitation between 30°N and 45°N is missing. The dipole pattern of decreased precipitation between the Gulf of Mexico and the African west coast, and increased precipitation to the south is hardly captured in the fist collapse event, but clearly present in all three following events. The precipitation decrease in Europe is also missing in the first event, but captured in the following three, although it does not extend far into Siberia. The changes over India and the Indian ocean in SYNC are hardly reproduced during the Hudson Strait Ice Stream surges ASYNC.

Due to the cooling (fig. 4.26(b)), the forests in the region of present day Great Britain shrink slightly. Due to the decreasing precipitation, the forest cover in southern and eastern Europe, and in a large band over Siberia slightly decreases as well fig. 4.33. With the southward shift of the ITCZ, the forests in the Sahel region slightly shifts southward, In Eurasia the forests are replaced by steppe, in the Sahel zone, this is not the case.

4.6. Discussion of the surge mechanisms

To what degree the processes related to the fast propagation of the sliding zones and to the refreeze at the end of the surge in ice sheet models are real physics or a numerical artifact is still debated (Calov et al., 2010; Soucek and Martinec, 2011). They are very sensitive to the exact numerical implementation as the multi-model comparison in Calov et al. (2010) shows and to variations in the implementation of the basal sliding criterion, as Soucek and Martinec (2011) show. Using PISM, Van Pelt and Oerlemans (2012) find long-period oscillations in an idealized valley glacier setting for sufficiently low friction coefficients and faster oscillations for intermediate friction coefficient values. For high friction coefficients, they obtain steady flow. Hindmarsh (2011) regards the basic problem of thermally controlled ice stream surges as well posed, but expects that the details of the surge propagation might be ill-posed under the shallow ice equation. We avoid this problem by modeling the sliding using the shallow shelf approximation.

However, in reality, we observe ice streams cycling between surging and non-surging phases. The processes at the base of these ice streams are very difficult to

study. Basal conditions vary on very small spatial scale, down to meters, making in-situ measurements challenging and difficult to upscale. The exact mechanisms of basal sliding and surge propagation still are fields of intensive research (see Benn and Evans (2010) for a detailed description of glacier surges and an extensive list of references). Furthermore, some glacier surges propagate in a shockwave style fashion with discontinuities in the surface height (Dowdeswell et al., 1991). So far, no ice sheet model is able to represent these features. Therefore, an implementation in a hemisphere-scale ice sheet model must mainly be judged on the basis of being physically consistent and yielding a reasonable model behavior.

By and large, this is the case for the sliding in mPISM. For parts of the collapse, the sliding area expands almost by one row of grid cells per timestep. This indicates a numerical artifact being at work. On the other hand, it does not exactly propagate with this velocity, and the propagation is limited to those parts of the Hudson Bay, that already are close to sliding before the surge starts. Therefore, the propagation – although it may be very fast – seems to follow basic physical principles and cannot be discarded as a pure numerical artifact.

Because of the very low basal resistance, the flow speed of the ice is mainly limited by the limits on its horizontal internal deformation. Therefore the stress balance of the shallow shelf approximation becomes important (fig. 4.1). In contrast to SIA only models, where this would be a 1:1 relationship, models that include the lateral stresses only balance a part of the driving stresses locally and transfer most of the stress into adjacent grid points that do not slide, or have a very high basal sliding resistance.

In the margins of the ice sheet, where the driving stresses are especially high, the ice in valleys can reach surface velocities well in excess of 100 m/yr because of the high internal deformation rates that temperate ice can reach under high driving stresses. This leads to the formation of ice-stream-like structures that *slide* on a basal layer of fast deforming ice, as is the case for the Northeast Greenland Ice Stream in fig. 3.7(a). This effect mitigates some of the very harsh cutoff we impose with the use of the basal sediment mask.

4.7. Comparison to freshwater hosing experiments and climate proxies

In the following, we compare our results to those of other coupled model studies as well as to proxy data. For comparisons with hosing experiments, we will mainly focus on the intercomparisons of Stouffer et al. (2006) and Kageyama et al. (2013) (see also section 1.5). We draw the references for the proxy data mainly from Broecker and Hemming (2001), Otto-Bliesner and Brady (2010), and Chikamoto et al. (2012).

As for all models in Stouffer et al. (2006) and in Kageyama et al. (2013), the AMOC in our experiments weakens (fig. 4.22). The reduction by 10–15% in our model is on the lower end of the results obtained in the above cited intercomparisons (6–62% for a 0.1 Sv freshwater forcing in Stouffer et al. (2006), and 20–95% for varying freshwater forcings in Kageyama et al. (2013)) just as the freshwater release of 0.06 Sv from the ice sheet is lower than the forcings used in the model intercomparisons. The growth of the strength of the response with the strength of the forcing has been shown in various experiments, e. g. Maier-Reimer and Mikolajewicz (1989); Otto-Bliesner and Brady (2010), and, using ECHAM5/MPIOM under LGM boundary conditions, Zhang et al. (2012, submitted). Zhang et al. (2012, submitted) obtain a reduction in AMOC by about 70% for a freshwater pulse of 0.2 Sv applied over 150 years and an almost complete shutdown for a freshwater pulse of

1 Sv. A difference between our simulations and most hosing experiments is, that in our simulations the freshwater is injected locally at the Hudson Strait, while in most hosing experiments, it is spread out over the possible deepwater formation areas.

Proxy studies suggest a complete shutdown or at least a very strong reduction of the NADW formation during Heinrich event 1 (H1) (Vidal et al., 1997, McManus et al., 2004, Stanford et al., 2011 and the references therein). While our experiments are clearly far away from a collapsed NADW cell, there is growing evidence that the AMOC reduction was present before the deposition of the ice rafted debris (Gutjahr and Lippold, 2011; Stanford et al., 2011). Furthermore, H1 is special, because it took place during the already beginning deglaciation. For H4, Vidal et al. (1997) find that the NADW cell was reduced, but still active outside the zone of maximum iceberg melting.

Some of the models in the pre-industrial multi-model hosing experiment in Stouffer et al. (2006) show a northward migration of the deepwater formation into areas that are not subject to the hosing. Because of the heat released by the convection, the SST rises in these new deepwater formation areas. None of the models in Kageyama et al. (2013) show this behavior. In ASYNC, for some 50-year time frames, we see a similar behavior with subsurface warming and heat release in areas that are not strongly affected by the ice stream surge. In SYNC, there is no warming in the high latitudes. The surges of the Arctic ice streams just before the surge of the Hudson Strait Ice Stream cause an increase in the already high sea ice cover and a freshening of the surface layer. Both effects strongly counteract a northward migration of the deepwater formation areas.

With the weakening NADW formation, practically all models in Stouffer et al. (2006) and Kageyama et al. (2013) show a high-latitude cooling centering over the Atlantic. The exact shape and strength of this pattern varies considerably, but the basic feature is robust. In the 0.1 Sv AOGCM-ensemble of Stouffer et al. (2006), the temperatures over Europe sink by 0.5 to 1 K. In Kageyama et al. (2013) the temperature changes tend to be stronger. This matches with 5 out of 11 models being subjected to a freshwater forcing exceeding 0.1 Sv. In SYNC, the cooling over Europe largely is between 0.5 and 1.5 K during the surge of the Hudson Strait Ice Stream (fig. 4.26). Thus, taking the different freshwater forcing strengths into account, our results are consistent with those from the hosing experiments.

Our model shows a cooling over Greenland that largely is between 0.5 and 1.5 K. The signal in the Greenland ice cores is dominated by the Dansgaard-Oeschger variability and Heinrich Stadials appear not colder than other stadials there. Ganopolski and Rahmstorf (2001) explained this with a southward shift of the deepwater formation areas in normal stadials that would cut Greenland from the Atlantic heat fluxes even without Heinrich event. The further retreat during a Heinrich Stadial then would not have any further substantial effect on Greenland. The models in Stouffer et al. (2006) largely agree with our model in simulating a moderate cooling, while some models in Kageyama et al. (2013) show a very pronounced cooling. The comparison with the proxy data is very difficult, because there are no AOGCM simulations of Dansgaard-Oeschger events. It is possible to obtain Dansgaard-Oeschger-event like features by prescribing negative freshwater forcings (e. g. Ganopolski and Rahmstorf (2001), see Kageyama et al. (2010) for a review), but they do not appear as internal oscillations of climate models, yet. Therefore, most freshwater hosing experiments start with an intermediate state and, if the

AMOC is shut down, show a strong cooling. Thus, while being difficult to compare to proxy evidence, our results agree with those from modeling studies.

At the Iberian Margin, Heinrich (1988) found an increase in cold-water planktic foraminifera in sediment cores from Dreizack Mountain (47.3°N, 19.5°W) in times of increased ice-rafting. Depending on the calibration method, Bard et al. (2000) obtain SST reductions between 3 and 9 K for H1 and between 2 and 5 K for H2 from a sediment core from the Iberian margin. They obtain a reduction in SSS by 1 to 3 psu for H1. For the same location, we observe a SST decrease by about 0.6 K and a reduction in SSS by 0.2 to 0.3 psu. The trend matches and considering that H1 is very strong and influenced by the deglaciation, the results are consistent with the proxy data. On land, pollen records from around the Mediterranean and western Europe (e. g. Tzedakis et al., 2004; Fletcher and Sánchez Goñi, 2008; Fletcher et al., 2010), show a correlation between the Dansgaard-Oescheger cycles and tree types and cover. The pollen indicate relatively cold, arid climates during stadials and relatively warm, humid climates during the interstadials. Among the stadials, the Heinrich Stadials are the coldest and most arid. In the model, we observe colder, and, over large parts of Europe also drier conditions during the ice stream surges (fig. 4.32), matching the trend in the proxies.

Schönfeld and Zahn (2000) put the Mediterranean Outflow Water (MOW) during the LGM at 1600 to 2200 m depth. Skinner and Elderfield (2007) find indications for influence of MOW at a depth of 2637 m during Heinrich Stadials. In our LGM simulation, the core of the MOW is centered at a depth of 1300 m and reaches down to 1800 m (fig. 4.18). It slightly deepens during the ice stream surges (fig. 4.18(c)). With this effect, we capture the trend in the observations.

For the time of H1, Flower et al. (2004) find the deglacial warming and a decrease in SSS by with spikes reaching 2–4 psu in the Gulf of Mexico. However, the picture in their data is not very clear. SYNC shows a reduction in SSS reaching 0.4 psu in the same area. Lea et al. (2003) find no statistically significant changes in SST in a core from the Cariaco basin (northern Venezuelan shelf), but a slight tendency towards cooling. In our model, the trend in this region depends on the grid cell chosen, and in any case is close to zero. Rühlemann et al. (2004) find a rapid warming of 1–3 K for intermediate depth (1299 resp. 426 m) waters at 17 ka in benthic foraminifera from sediment cores from the Carribean Sill and Angolan coast. From two sediment cores from similar locations, Vidal et al. (1999) find an increase in the SST during H1, H4 and H5. In our model, we find 0.2 K cooling on the Caribbean Sill during the Arctic ice stream surges, followed by a 0.2 K warming and, at the Angolan coast slight cooling during Arctic ice stream surges, followed by a 0.15 K warming. Stanford et al. (2011) date the start of the freshwater releases related to H1 at 19 ka and the start of the IRD deposition at 17.5 ka. Giving a 2 kyr lead for the freshwater discharge we also obtain a warming trend. Regardless of the timing, the signal in our simulation is very weak.

Grimm et al. (1993, 2006) find an increase in pine tree pollen and indication for an increased lake level in Lake Tulane (central Florida). In SYNC this is on the southern limit of the zone of increased precipitation so this result agrees with the trend, although the signal in our simulation is very small. In ASYNC there is rather less than more precipitation central Florida, but the signal is very small and patchy around Florida in most Heinrich event time slices so one should not over-interpret it.

The southward shift of the ITCZ over southern America, that we observe in the model, is confirmed by proxy data. Hessler et al. (2010) summarize proxy data

from the tropics. They find a indication for a southward ITCZ shift in southern America. The data coverage in Africa is too poor and the trends are too diverse for a clear picture to emerge. Similarly Arz et al. (1998) find increased deposition of terrigenous sediments, indicating wetter conditions, around the times of Heinrich events a sediment core from the Brazilian continental margin, but the dating uncertainty is substantial.

The EPICA Community Members (2006) present data from the Byrd (80°S, 110.5°W), EPICA Dronning Moud Land (EDML, 75°S, 0°E), and EPICA Dome C (75°S, 123.3°E) ice cores. They show warming trends during the Dansgaard-Oeschger Stadials reaching values between 0.5 and 3 K. The warmings last especially long (and thus reach higher values) during the Heinrich Stadials. At Dome C, SYNC shows a cooling compared to the reference value at the start of the experiment that is followed by a warming trend. ASYNC has relatively warm periods during the second and third Hudson Strait Ice Stream surge, but the signal hardly reaches out of the noise. The changes in both experiments on the order of 0.3 K. At the locations of Byrd ice core, and EDML, there are no trends in our experiments. On average, the models in Stouffer et al. (2006) simulate a warming between 0 and 0.3 K over the Antarctic continent for a freshwater forcing of 0.1 Sv. This is below one standard deviation from the model simulations. In Kageyama et al. (2013), about half of the models simulate a warming above 0.5 K (for different freshwater forcings). There is hardly any cooling exceeding 0.5 K. Some models show a cooling exceeding 0.5 K over parts of the Antarctic Circumpolar Current, while for most parts of the southern hemisphere there are more models showing warming than cooling. Summarizing, there is a Dansgaard-Oeschger dominated pattern in the proxy data while the hosing intercomparisons show a mixed picture and our model shows hardly any changes.

For the eastern Pacific, Seki et al. (2002) find evidence for post-Heinrich event SST increases by 3–4 K for H1, H3, H4, and H5 in ODP Hole 1017E (34.5°N, 121°W). While this in part is to be ascribed to the Dansgaard-Oeschger warming cycle that is visible in this core for all Dansgaard-Oeschger events, there is a clear cooling during stadials, that is a bit more obvious for the (longer) Heinrich Stadials. At the same location, we find a slight (0.1 to 0.2 K) cooling in SYNC. Considering that we are not modeling Dansgaard-Oeschger cycles, our results reasonably agree with the proxies.

All in all, the changes our model simulates are not exceedingly strong, but, considering that in the Greenland ice cores, the Heinrich Stadials differ from the other stadials mainly in terms of duration, but not in strength, and, that at least for Heinrich event 1, the proxies indicate that most of the weakening of the AMOC occurred pre-collapse and might have actually triggered the ice-sheet collapse (see sec. 1.4), the mild response of the ocean model is in accordance with the proxy data. Our results also are consistent with the results of previous freshwater hosing experiments using moderate forcings.

4.8. Summary of the ice stream surges

The experiments analyzed in this chapter are not only the first steady state AOGCM–ISM LGM experiments, but, at the same time, they are the first set of experiments with a coupled AOGCM–ISM system where Heinrich event style surges occur as internal, model generated variability. We obtain surges of the Hudson Strait Ice Stream with a period of 7 kyrs, matching the reconstructions from proxy data (e. g. Hemming, 2004). The repeated ice stream surges are internal oscillations

of the ice sheets. While substantial work on the ice sheet model was necessary to obtain these oscillations, their occurrence adds confidence in the model of MacAyeal (1993) and matches with the experiments of Calov et al. (2002). As in these studies, in our experiments, the timescale of 7 kyrs is set by the accumulation rate over the Hudson Bay area. In this respect, our results contrast with the results of Álvarez Solas et al. (2011), who get time varying ice discharge only when they force the model with time varying shelf melt rates. Even with a time varying melt rate, a critical question for our understanding of the ice–climate system is, whether the increased shelf melt triggers a surge caused by an internal oscillation of the ice sheet (Calov et al., 2002), or whether the time varying melt rate is really the cause of the surges (Álvarez Solas et al., 2011). Our results support the theory of internal oscillations that can be triggered externally.

In our model, the surges of the Hudson Strait Ice Stream cause freshwater discharge rates peaking at about 0.06 Sv, and the modeled ice volume changes lie between 1.5 and 2.1 Mio km^3, corresponding to 3.8–5 m sea level rise. Proxy estimates for Heinrich events (including the Younger Dryas event) vary greatly and range from 0.06–0.12 Sv to 0.15–1 Sv depending on the study and the discharge duration assumed (Clement and Peterson, 2008). While our results are on the lower end of this range, they are within the margin of uncertainty. The occurrence of Heinrich events as part of some Dansgaard-Oeschger stadials complicates a comparison of model output and proxy data since the two effects of Dansgaard-Oeschger cycles and Heinrich events are combined in proxies, while the model only shows the effects of the ice stream surges. By and large, the modeled changes agree with the reconstructions from the proxy data. The reduction in north Atlantic deepwater formation by 10 to 15 % is consistent with the results of AOGCM freshwater hosing experiments (Stouffer et al., 2006; Kageyama et al., 2013), considering the lower freshwater discharge in our model and the localized release in contrast to a spreading directly over the deepwater formation areas in the idealized freshwater hosing studies. The modeled reduction in AMOC, the cooling over the Atlantic that reaches into Eurasia, the reduced precipitation over Eurasia, and the southward shift of the ITCZ have the same sign as the climate changes inferred from proxies but are of a smaller magnitude than the proxy-derived estimates. The fact that we do not observe a clear bipolar see-saw effect with southern hemisphere warming can be attributed to the very stable AMOC in the AOGCM and is likely to be related to the lack of Dansgaard-Oeschger cycles.

The ISM shows strong surge behavior not only in the Hudson Strait, but in several regions. This agrees with geological evidence for multiple sources of ice rafted debris on the Atlantic seafloor (e. g. Hemming, 2004; Stanford et al., 2011). In SYNC, the surges of the Arctic ice streams cause a sub-surface warming in the Arctic Ocean. The surges furthermore cause an enhanced ice export through the Fram Strait. This enhanced ice export weakens the deepwater formation and thus the AMOC. A plausible hypothesis would be that this would lead to a sub-surface warming, that could trigger ice discharges from the Hudson Strait Ice Stream (e. g. Álvarez Solas et al., 2011), but the effect is dominated by an sea ice-induced cooling in the surface waters of the GIN Sea and the north Atlantic. The Atlantic surface water is subducted below the low salinity water of the East Greenland Current and reaches the Labrador Sea as cold sub-surface water. Only during the surge of the Hudson Strait Ice Stream, the stratification in the Labrador Sea stabilizes strongly enough to cause a sub-surface warming. Such interactions can only be observed in three-dimensional coupled atmosphere–ocean models.

While the ice sheet collapse events lead to massive ice discharges, and this massive streaming is not part of the default behavior of PISM, the crucial process not occurring in the default setup of PISM and challenging most ice sheet models is the termination of a surge (see the results in Calov et al., 2010). The fact that the ice sheet models by default do not exhibit the catastrophic ice sheet collapses that are assumed to have occurred during Heinrich events, might imply that the models portray the future ice sheets as more stable than they are, but the difficulty ice sheet models have with yielding recurring surges of the Hudson Strait Ice Stream (e. g. Álvarez Solas et al., 2011) and the results of Calov et al. (2010) show that stabilizing processes that can stop a collapse can be hard to model and might be poorly represented in ice sheet models.

CHAPTER 5

Summary and conclusion

The topic of this study was the investigation of glacial climate variability with an interactively atmosphere–ocean coupled general circulation model (AOGCM) – ice sheet model (ISM) system, focusing on Heinrich events. Modeling the last glacial is an important step for assessing the credibility of projections of future climate change, because we can test whether our models are able to correctly represent a climate that strongly differs from the present day climate. Furthermore, the Dansgaard-Oeschger and Heinrich events, periods of rapid climate change during the last glacials, are commonly attributed to ice sheet – climate interactions. By modeling Heinrich events, we can expand our understanding of the climate system and assess the ability of our models to predict future ice sheet – climate interactions.

For the experiments, we have modified the state-of-the-art ISM PISM into mPISM, a model that can be used in coupled ice sheet – climate simulations. We have coupled it to the AOGCM ECHAM5/ MPIOM/ LPJ. Both models, as well as the coupling, work without anomaly maps or flux correction. Therefore they can much better represent the nonlinear dynamics of the climate system than models that employ such methods and commonly assume the correction patterns to stay constant under varying climate conditions. In comparison to simulations using earth system models of intermediate complexity (EMICs), AOGCMs are able to represent processes of the ocean circulation and atmosphere dynamics in a much more detailed way and with higher spatial and temporal resolution. In contrast to previous AOGCM–ISM simulations (e. g. Gregory et al., 2012), the ISM covers all relevant parts of the northern hemisphere. mPISM is a shallow ice approximation (SIA) – shallow shelf approximation (SSA) hybrid model and thus able to model ice streams more realistically than conventional SIA-only ISMs. In both directions, the coupling includes the fluxes between ice and atmosphere as well as the fluxes between ice and ocean, enabling the study of the full interactions between the ice sheets and the climate system.

With our model system, we performed the first fully coupled multi-millennial steady-state AOGCM–ISM simulations under last glacial maximum (LGM) boundary conditions. We validated our setup by also performing steady-state experiments under pre-industrial boundary conditions. In both cases, our results agree reasonably well with the observational data. In the pre-industrial state, an additional ice sheet in the Alaska Range forms. This is due to a resolution dependent cold bias in the atmosphere model. In the LGM setup, a spurious ice sheet forms in eastern Siberia and Alaska. This is at least partly due to neglecting the albedo effect of dust on snow and ice in our model (Warren and Wiscombe, 1980; Krinner et al., 2011). Further advances could be made by using a sophisticated energy balance scheme for the surface mass balance (e. g. Calov et al., 2005a; Vizcaíno et al., 2010). Another reason for the buildup of too much ice in Siberia is the long-time constant LGM forcing that allows for a slow and steady build-up of the ice sheets.

Our LGM experiments are not only the first steady state AOGCM–ISM LGM experiments, but, at the same time, they are the first set of experiments with a coupled AOGCM–ISM system where Heinrich event style surges occur as internal, model generated variability. We obtain surges of the Hudson Strait Ice Stream with a period of 7 kyrs, matching the reconstructions from proxy data (e. g. Hemming, 2004). The repeated ice stream surges are internal oscillations of the ice sheets. While substantial work on the ice sheet model was necessary to obtain these oscillations, their occurrence adds confidence in the model of MacAyeal (1993) and matches with the experiments of Calov et al. (2002). As in these studies, in our experiments, the timescale of 7 kyrs is set by the accumulation rate over the Hudson Bay area. In this respect, our results contrast with the results of Álvarez Solas et al. (2011), who get time varying ice discharge only when they force the model with time varying shelf melt rates. Even with a time varying melt rate, a critical question for our understanding of the ice–climate system is, whether the increased shelf melt triggers a surge caused by an internal oscillation of the ice sheet (Calov et al., 2002), or whether the time varying melt rate is really the cause of the surges (Álvarez Solas et al., 2011). Our results support the theory of internal oscillations.

In our model, the surges of the Hudson Strait Ice Stream cause freshwater discharge rates peaking at about 0.06 Sv, and the modeled ice volume changes lie between 1.5 and 2.1 Mio km^3, corresponding to 3.8–5 m sea level rise. Proxy estimates for Heinrich events (including the Younger Dryas event) vary greatly and range from 0.06–0.12 Sv to 0.15–1 Sv depending on the study and the discharge duration assumed (Clement and Peterson, 2008). While our results are on the lower end of this range, they are within the margin of uncertainty. The occurrence of Heinrich events as part of some Dansgaard-Oeschger stadials complicates a comparison of model output and proxy data since the two effects of Dansgaard-Oeschger cycles and Heinrich events are combined in proxies, while the model only shows the effects of the ice stream surges. By and large, the modeled changes agree with the reconstructions from the proxy data. The reduction in north Atlantic deepwater formation by 10 to 15 % is consistent with the results of AOGCM freshwater hosing experiments (Stouffer et al., 2006; Kageyama et al., 2013), considering the lower freshwater discharge in our model and the localized release in contrast to a spreading directly over the deepwater formation areas in the idealized freshwater hosing studies. The modeled reduction in AMOC, the cooling over the Atlantic that reaches into Eurasia, the reduced precipitation over Eurasia, and the southward shift of the ITCZ have the same sign as the climate changes inferred from proxies but are of a smaller magnitude than the proxy-derived estimates. The fact that we do not observe a clear bipolar see-saw effect with southern hemisphere warming can be attributed to the very stable AMOC in the AOGCM and is likely to be related to the lack of Dansgaard-Oeschger cycles.

The ISM shows strong surge behavior not only in the Hudson Strait, but in several regions. This agrees with geological evidence for multiple sources of ice rafted debris on the Atlantic seafloor (e. g. Hemming, 2004; Stanford et al., 2011). In SYNC, the surges of the Arctic ice streams cause a sub-surface warming in the Arctic Ocean. The surges furthermore cause an enhanced ice export through the Fram Strait. This enhanced ice export weakens the deepwater formation and thus the AMOC. A plausible hypothesis would be that this would lead to a sub-surface warming, that could trigger ice discharges from the Hudson Strait Ice Stream (e. g. Álvarez Solas et al., 2011), but the effect is dominated by an sea ice-induced cooling in the surface waters of the GIN Sea and the north Atlantic. The Atlantic surface

water is subducted below the low salinity water of the East Greenland Current and reaches the Labrador Sea as cold sub-surface water. Only during the surge of the Hudson Strait Ice Stream, the stratification in the Labrador Sea stabilizes strongly enough to cause a sub-surface warming. Such interactions can only be observed in three-dimensional coupled atmosphere–ocean models.

For moderate forcings, the climate model as well as the default version of PISM do not show sudden, strong responses, or switching behavior between different steady states. This of course makes it easier to tune the models to present day (or pre-industrial) conditions. While reproducing the present-day conditions is a crucial test for the models and a prerequisite for prediction runs, this requirement may have led to models portraying the climate (including the ice sheets) as more stable than it actually is. Parametrizations that lead to sudden, unwanted climate changes during the tuning or in a control run have to be removed or substantially dampened in the tuning process. EMICs have the advantage of running much faster than the comprehensive models and thereby larger parameter spaces can easily be scanned while tuning them, making a moderate behavior less crucial for the tuning process. Furthermore, the use of semi-physical parametrizations, such as flux corrections, that allow to force the model into a desired state, is commonly accepted with EMICs but not with AOGCMs. This makes tuning EMICs easier. The reduced need for a stable behavior might explain why several EMICs show the AMOC bistability lacking in AOGCMs.

While the ice sheet collapse events lead to massive ice discharges, and this massive streaming is not part of the default behavior of PISM, the crucial process not occurring in the default setup of PISM and challenging most ice sheet models is the termination of a surge (see the results in Calov et al., 2010). The fact that the ice sheet models by default do not exhibit the catastrophic ice sheet collapses that are assumed to have occurred during Heinrich events, might imply that the models portray the future ice sheets as more stable than they are, but the difficulty ice sheet models face with simulating recurring surges of the Hudson Strait Ice Stream (e. g. Álvarez Solas et al., 2011) and the results of Calov et al. (2010) show that stabilizing processes that can stop a collapse can be hard to model and might be poorly represented in ice sheet models.

In summary, we have successfully built a coupled ice sheet climate model system that stands the test of modeling LGM as well as pre-industrial climates. mPISM displays large-scale ice stream surges in the Hudson Bay area as internal oscillations confirming the mechanism suggested by MacAyeal (1993). The time varying discharge from the ice sheets increases the climate variability on the longer timescales. The response of the climate system to the ice stream discharges shows the basic features that are characteristic for Heinrich events.

APPENDIX A

Acknowledgements

Technical

The computations for this thesis were performed on the *blizzard* supercomputer of the *Deutsches Klimarechenzentrum*. Most of the computational time was provided through BMBF project 675.

ERA INTERIM (Dee et al., 2011) climate reanalysis data was provided by the European Centre for midrange weather forecasts (ECMWF).

Precipitation data from the GPCP project was obtained through the integrated climate data center of the KlimaCampus Hamburg. The GPCP combined precipitation data were developed and computed by the NASA/Goddard Space Flight Center's Laboratory for Atmospheres as a contribution to the GEWEX Global Precipitation Climatology Project.

Personal

Now it is time to thank the people who have helped me on my way through this PhD. This is a humble attempt to catch the most important ones and by no means complete. Quite on the contrary, I'm sure, I've forgotten some people whose presence is so natural to me that they did not come to my mind, when writing this list.

First, and foremost, thank you, Uwe Mikolajewicz for *adopting* me and teaching me the art of climate modeling and model coupling. Without your guidance and advice I would never have been able to perform the experiments, nor to analyze them. Thanks for keeping me going and for numerous discussions about science, life in science and life in itself. I would also like to thank Victor Brovkin for important advice on the way and the supervision of my thesis. Victor, it is a pleasure to work with you.

The whole story would not have started, had Andreas Chlond not invited me to explore the world of glaciers. He brought me into this exciting field and gave me a beautiful start on the topic. His support continued through numerous panel meetings and he always had an open door when I visited him in his office. Thank you for all this.

In Andreas' Group, I had the pleasure to work with Nicole Sander and Otto Böhringer. Although Nicole left the group after a short while, it was a fun time with her and I learned a lot from her. Otto – well, hard to describe, but surely one of the most wonderful people I've ever met. Thank you for all your patience with me and for your patient and successful efforts in getting the ice models to work on blizzard. Without you, this project would have been impossible.

From the early days, I have to thank several people from the land department, Robert (then Getzieh, now Schuldt), my frequent roommate on conferences and institute retreats, Daniel Goll, Sebastian Bathiany, Helge Gössling, Freja Vamborg, and all the others who were around in coffee and lunch rounds. Special thanks to

Thomas Kleinen for taking care of us PhD students and for a lot of insights into science.

Moving on, I would like to express my gratitude to Conni and Antje from the IMPRS office for their support throughout the project, and Antje for constantly reminding me that the most important aspect of a PhD is to finish as soon as possible. Special thanks go to Bjorn for serving as my panel chair through all the meetings and always maintaining a perspective for finishing the project. Thank you, Jochem, for allowing me to join the ocean and your generic academic skills course. Thank you Martin for supporting me in continuing my work on the boundary between the land and the ocean.

Coming to the ocean department, I am deeply indebted to *my postdoc* Christian Rodehacke, for numerous discussions with and without coffee, where I learned so much about the ocean, modeling climate, and life. All the best in Copenhagen, I hope we'll have the pleasure to cooperate on various projects in the future. Special thanks go to Laura for loads of fun discussions, NCL quizzes, and improving pretty much every text I had to hand in somewhere. Among all the other people that made my time in the ocean department worthwhile, I want to mention my office-mates Fanny and Rosi, as well as Peter, Werner, Jan, Josianne, Ralf, Kornelia Müller, Andrea Franke, and, of course, my fellow icicles Philipp, Einar, and Iris.

Staying with the ice but moving to the university, I am deeply thankful to Thomas Kleiner, Nina Wilkens, Martin Rückamp, and Angelika Humbert. The ice-coffee rounds were a beautiful time and the only way to really understand a problem is discussing it. Further thanks go to all the other marvelous glaciologists and other climate scientists I met on conferences, workshops and summer and winter schools. Some that need special mentioning are Doug Benn, Richard Morris, Eric Larour, and the PISM groups at Alaska and PIK, especially Ed Bueler, Ricarda Winkelmann, Maria Martin and Torsten Albrecht.

Somewhere between the university and MPI is CIS, our IT department. Thanks for constant support, working computers, and especially for healing my poor little laptop. Special thanks of course go to Björn Bewersdorff for his premium-support and great friendship. At our bigger computer, I am deeply endowed to Niklas Röber for transforming my model output into three-dimensional pictures and movies. They make it much easier to understand what's going on in the model. Thanks to both, Niklas Röber and Moritz Hanke for loads of climbing and fun at the DAV gym. Staying with the climbing but returning to MPI, thank you Katrin, Peter, Steffen, Fanny, Irene, Thomas, and Marco.

A great friend from the turbulent levels of the atmosphere department is Cedrick. Preparing and running the climate course at the *Deutsche Schülerakademie* (DSA) was an incredible project that would not have been possible had it not been so much fun to work together. Since then it has always been a great pleasure to discuss all kinds of problems from the details of computer architecture to the basic questions of life and what you make of it. The DSA were (by now twice) 17 extreme days with a great cast. Thanks to everybody involved, especially of course to the AKL. Also related to the DSA and the atmosphere department: Thank you Vera for a lot of fun discussions and your work for the DSA, JGW, and the CDE.

Time to leave work. Well, almost. Cheers to the crew from my old times at the geophysical institute, especially Lea Scharff and Matthias Hort. Everywhere and nowhere at the same time, Carina is great fun to hang around with, when the pathes cross. Big hugs go to Lars Krieger and Rebecca Kittel, now in Australia. Time

spent with you guys is never wasted. From the Lars bunch, and also somebody one can always rely on is Jörg Schwöbel. It is a pleasure to have you around. Further cheers to Johannes, Tina, Sandra, Maren, Nataly, and Julia.

What would life be without sports and arts, and why should you not combine the two? Thanks to the Hamburg Juggling crew, especially Magali who brought me there and to André, Annedore, Bente, Björn, Daniela, Flo, Frauke, Frauke, Jana, Johanna, Justus, Karl, Livia, Magda, Mareike, Philipp, Stefan, Vera, and Victor. Why juggle balls and clubs when you can do acrobatics? Thanks for the most wonderful sport of them all, especially to Jonni and to my flyers Tanja, Daniela, Anne, Laura, Cathy, Nina, Maren, and to all the other acrobats, especially to Uli, Tyll, Anne, Caro Klein, Caro (groß) and Hanna Z.

Moving on to my longest-time hobby, saving the world with Greenpeace, thank you so much, Basti, Holger, Rainer, Anne (again), Hanna, Lisa, Daniel, Anat, Andi, Floppi, Sophie, Birte N., Sonja M., Güde, Schnick, Jenny, Kirstin, Karsten Smid, Sabine Walter and all the other people for the amazing fun, great cooperation and enormous efforts (and, of course, for the climbing to those who went climbing with me). Special thanks to Nicole Knapp for running the trainings and the facilitator program of Greenpeace. I learned a lot there.

Further thanks for the great time go to the smurfs, Linda and Matthias. I had a few more encounters with my wonderful flatmates Lisa, Mareike, Johanna, Arne, Adreas, and several more or less short time guests. Thanks for putting up with me!

Moving on to the pre-Hamburg times... although we don't meet often in person, a great thank you goes to Jul and Jörg from my last hometown, and to Anneka. People, I know, I can always blindly rely on. Thanks for all the good time and the friendship.

Last, but not least, thanks to my family. They contributed greatly in shaping me and bringing me where I am now.

THE END

Bibliography

Abe-Ouchi, A, T Segawa and F Saito, **2007**. Climatic Conditions for modelling the Northern Hemisphere ice sheets throughout the ice age cycle. *Climate of the Past*, 3(3):423–438. doi:10.5194/cp-3-423-2007.

Adler, Robert F, George J Huffman, Alfred Chang, Ralph Ferraro, Ping-Ping Xie, John Janowiak, Bruno Rudolf, Udo Schneider, Scott Curtis, David Bolvin, Arnold Gruber, Joel Susskind, Philip Arkin and Eric Nelkin, **2003**. The Version-2 Global Precipitation Climatology Project (GPCP) Monthly Precipitation Analysis (1979–Present). *J. Hydrometeor*, 4(6):1147–1167. ISSN 1525-755X. doi:10.1175/1525-7541(2003)004¡1147:TVGPCP¿2.0.CO;2.

Alley, R B, D D Blankenship, C R Bentley and S T Rooney, **1986**. Deformation of till beneath ice stream B, West Antarctica. *Nature*, 322(6074):57–59. doi:10.1038/322057a0.

Alley, Richard B., **2005**. Comment on "Catastrophic ice shelf breakup as the source of Heinrich event icebergs" by C. L. Hulbe et al. *Paleoceanography*, 20(1): 12–14. ISSN 0883-8305. doi:10.1029/2004PA001086.

Álvarez Solas, Jorge, Sylvie Charbit, Catherine Ritz, Didier Paillard, Gilles Ramstein and Christophe Dumas, **2010**. Links between ocean temperature and iceberg discharge during Heinrich events. *Nature Geoscience*, 3(2):122–126. ISSN 1752-0894. doi:10.1038/ngeo752.

Álvarez Solas, Jorge, M Montoya, Catherine Ritz, Gilles Ramstein, S Charbit, C Dumas, K Nisancioglu, T Dokken and Andrey Ganopolski, **2011**. Heinrich event 1: an example of dynamical ice-sheet reaction to oceanic changes. *Climate of the Past*, 7(4):1297–1306. doi:10.5194/cp-7-1297-2011.

Amante, C and B. W. **Eakins**. ETOPO1 1 Arc-Minute Global Relief Model: Procedures, Data Sources and Analysis. Technical report, NOAA Technical Memorandum NESDIS NGDC-24, **2009**.

Arakawa, A and V R **Lamb**. Computational design and the basic dynamical processes of the UCLA general circulation Model. In *Methods in Computatinonal Physics*, volume 17, pages 173–265. Academic Press, **1977**.

Arpe, Klaus, S A G Leroy and Uwe Mikolajewicz, **2011**. A comparison of climate simulations for the last glacial maximum with three different versions of the ECHAM model and implications for summer-green tree refugia. *Climate of the Past*, 7(1):91–114. doi:10.5194/cp-7-91-2011.

Arz, Helge W, Jürgen Pätzold and Gerold Wefer, **1998**. Correlated Millennial-Scale Changes in Surface Hydrography and Terrigenous Sediment Yield Inferred from Last-Glacial Marine Deposits off Northeastern Brazil. *Quaternary Research*, 50(2):157–166. ISSN 0033-5894. `http://www.sciencedirect.com/science/article/pii/S0033589498919925`.

Aschwanden, A, E Bueler, C Khroulev and H Blatter, **2012**. An enthalpy formulation for glaciers and ice sheets. *Journal of Glaciology*, 58(209):441–457. doi:10.3189/2012JoG11J088.

Bamber, J L, R L Layberry and S P Gogineni, **2001**. A new ice thickness and bed data set for the Greenland ice sheet 1. Measurement, data reduction, and errors. *J. Geophys. Res.*, 106(D24):33773–33780. ISSN 0148-0227. doi:10.1029/2001JD900054.

Bamber, Jonathan L, Riccardo E M Riva, Bert L A Vermeersen and Anne M LeBrocq, **2009**. Reassessment of the Potential Sea-Level Rise from a Collapse of the West Antarctic Ice Sheet. *Science*, 324(5929):901–903. doi:10.1126/science.1169335.

Bard, Edouard, Frauke Rostek, Jean-Louis Turon and Sandra Gendreau, **2000**. Hydrological Impact of Heinrich Events in the Subtropical Northeast Atlantic. *Science*, 289(5483):1321–1324. `http://www.sciencemag.org/content/289/5483/1321.abstract`.

Barker, Stephen, Gregor Knorr, Maryline J Vautravers, Paula Diz and Luke C Skinner, **2010**. Extreme deepening of the Atlantic overturning circulation during deglaciation. *Nature Geosci*, 3(8):567–571. ISSN 1752-0894. doi:10.1038/ngeo921.

Barnola, J M, D Raynaud, Y S Korotkevich and C Lorius, **1987**. Vostok ice core provides 160,000-year record of atmospheric CO2. *Nature*, 329(6138):408–414. doi:10.1038/329408a0.

Benn, D I and D J A **Evans**. *Glaciers and glaciation.* Hodder Education, **2010**. ISBN 978-0340905791. `http://www.hoddereducation.co.uk/Title/9780340905791/Glaciers_and_Glaciation_2nd_edition.htm`.

Bitz, C M, J C H Chiang, W Cheng and J J Barsugli, **2007**. Rates of thermohaline recovery from freshwater pulses in modern, Last Glacial Maximum, and greenhouse warming climates. *Geophys. Res. Lett.*, 34(7):L07708. ISSN 0094-8276. doi:10.1029/2006GL029237.

Blankenship, D D, C R Bentley, S T Rooney and R B Alley, **1986**. Seismic measurements reveal a saturated porous layer beneath an active Antarctic ice stream. *Nature*, 322(6074):54–57. doi:10.1038/322054a0.

Blatter, H, **1995**. Velocity And Stress-Fields In Grounded Glaciers - A Simple Algorithm For Including Deviatoric Stress Gradients. *Journal of Glaciology*, 41 (138):333–344.

Bond, G, H Heinrich, Wallace S Broecker, L Labeyrie, J Mcmanus, J Andrews, S Huon, R Jantschik, S Clasen, C Simet, K Tedesco, M Klas, G Bonani and S Ivy, **1992**. Evidence For Massive Discharges of Icebergs Into the North-atlantic Ocean During the Last Glacial Period. *Nature*, 360(6401):245–249. `http://dx.doi.org/10.1038/360245a0`.

Box, G E P. Robustness in the strategy of scientific model building. In **Launer**, R L and G N **Wilkinson**, editors, *Robustness in Statistics*, pages 201–236. Academic Press, **1979**. ISBN 0124381502. `http://oai.dtic.mil/oai/oai?verb=getRecord&metadataPrefix=html&identifier=ADA070213`.

Box, Jason E, David H Bromwich, Bruce A Veenhuis, Le-Sheng Bai, Julienne C Stroeve, Jeffrey C Rogers, Konrad Steffen, T Haran and Sheng-Hung Wang, **2006**. Greenland Ice Sheet Surface Mass Balance Variability (1988–2004) from Calibrated Polar MM5 Output. *J. Climate*, 19(12):2783–2800. ISSN 0894-8755. doi:10.1175/JCLI3738.1.

Braconnot, Pascale, Sandy P Harrison, Masa Kageyama, Patrick J Bartlein, Valerie Masson-Delmotte, Ayako Abe-Ouchi, Bette Otto-Bliesner and Yan Zhao, **2012**. Evaluation of climate models using palaeoclimatic data. *Nature Clim. Change*, 2(6):417–424. ISSN 1758-678X. doi:10.1038/nclimate1456.

Braithwaite, R J and O B **Olesen**. *Glacier fluctuations and climatic change*, pages 219–233. Kluwer, **1989**.

Broecker, Wallace S and Sidney R **Hemming**, **2001**. Paleoclimate - Climate swings come into focus. *Science*, 294(5550):2308–2309. doi:10.1126/science.1068389.

Broecker, Wallace S, Dorothy. M. Peteet and David Rind, **1985**. Does the Ocean-atmosphere System Have More Than One Stable Mode of Operation. *Nature*, 315(6014):21–26.

Broecker, Wallace S, Bond, M Klas, E Clark and J McManus, **1992**. Origin of the northern Atlantic's Heinrich events. *Climate Dynamics*, 6(3-4):265–273.

Bryan, Frank, **1986**. High-latitude salinity effects and interhemispheric thermohaline circulations. *Nature*, 323(6086):301–304. doi:10.1038/323301a0.

Budd, W F and I N **Smith**. The growth and retreat of ice sheets in response to orbital radiation changes. In *Proceedings of the Canberra Symposium, December 1979*, number 131 in IAHS Publ., pages 369–409, **1979**.

Bueler, Ed and Jed **Brown**, **2009**. Shallow shelf approximation as a sliding law in a thermomechanically coupled ice sheet model. *J. Geophys. Res.*, 114(F3): F03008. ISSN 0148-0227. doi:10.1029/2008JF001179.

Calov, Reinhard. *Das thermomechanische Verhalten des groenlaendischen Eisschildes unter der Wirkung verschiedener Klimaszenarien - Antworten eines theoretisch-numerischen Modells*. PhD thesis, Institut fuer Mechanik, Technische Hochschule Darmstadt, Germany, **1994**.

Calov, Reinhard and Ralf **Greve**, **2005**. A semi-analytical solution for the positive degree-day model with stochastic temperature variations. *J. Glaciol.*, 51:173–175.

Calov, Reinhard, Andrey Ganopolski, Vladimir Petoukhov, Martin Claussen and Ralf Greve, **2002**. Large-scale instabilities of the Laurentide ice sheet simulated in a fully coupled climate-system model. *Geophys. Res. Lett.*, 29. doi:10.1029/2002GL016078.

Calov, Reinhard, Andrey Ganopolski, Martin Claussen, Vladimir Petoukhov and Ralf Greve, **2005a**. Transient simulation of the last glacial inception. Part I: glacial inception as a bifurcation in the climate system. *Climate Dynamics*, 24 (6):545–561. ISSN 0930-7575. doi:10.1007/s00382-005-0007-6.

Calov, Reinhard, Andrey Ganopolski, Vladimir Petoukhov, Martin Claussen, Victor Brovkin and Claudia Kubatzki, **2005b**. Transient simulation of the last glacial inception. Part II: sensitivity and feedback analysis. *Climate Dynamics*, 24(6):563–576. ISSN 0930-7575. doi:10.1007/s00382-005-0008-5.

Calov, Reinhard, Ralf Greve, Ayako Abe-Ouchi, Ed Bueler, Philippe Huybrechts, Jesse V. Johnson, Frank Pattyn, David Pollard, Catherine Ritz, Fuyuki Saito and Lev Tarasov, **2010**. Results from the Ice-Sheet Model Intercomparison Project–Heinrich Event INtercOmparison (ISMIP HEINO). *Journal of Glaciology*, 56(197):371–383. ISSN 00221430. doi:10.3189/002214310792447789.

Carlson, Anders E, Peter U Clark, Brian a Haley, Gary P Klinkhammer, Kathleen Simmons, Edward J Brook and Katrin J Meissner, **2007**. Geochemical proxies of North American freshwater routing during the Younger Dryas cold event. *Proceedings of the National Academy of Sciences of the United States of America*, 104(16):6556–61. ISSN 0027-8424. doi:10.1073/pnas.0611313104.

Chappell, John, **2002**. Sea level changes forced ice breakouts in the Last Glacial cycle: new results from coral terraces. *Quaternary Science Reviews*, 21(10):1229–1240. ISSN 0277-3791. doi:10.1016/S0277-3791(01)00141-X.

Chikamoto, Megumi O., Laurie Menviel, Ayako Abe-Ouchi, Rumi Ohgaito, Axel Timmermann, Yusuke Okazaki, Naomi Harada, Akira Oka and Anne Mouchet, **2012**. Variability in North Pacific intermediate and deep water ventilation during Heinrich events in two coupled climate models. *Deep Sea Research Part II: Topical Studies in Oceanography*, 61-64:114–126. ISSN 09670645. doi:10.1016/j.dsr2.2011.12.002.

Clark, Peter U., Richard B. Alley and David Pollard, **1999**. Northern hemisphere ice-sheet influences on global climate change. *Science*, 286(November):1104–1111. `http://www.sciencemag.org/content/286/5442/1104.short`.

Claussen, Martin, L Mysak, A Weaver, M Crucifix, T Fichefet, M F Loutre, S Weber, J Alcamo, V Alexeev and A Berger, **2002**. Earth system models of intermediate complexity: closing the gap in the spectrum of climate system models. *Climate Dynamics*, 18(7):579–586. ISSN 0930-7575.

Clement, Amy C and Larry C **Peterson**, **2008**. Mechanisms of abrupt climate change of the last glacial period. *Rev. Geophys.*, 46(4):RG4002. ISSN 8755-1209. doi:10.1029/2006RG000204.

Crucifix, M, P Braconnot, S Harrison and Bette Otto-Bliesner, **2005**. Second phase of Paleoclimate Modelling Intercomparison Project. *EOS, Transactions, American Geophysical Union*, 86:264–265. doi:10.1029/2005EO280003.

Dansgaard, W, S Johnsen, H Clausen, D Dahl-Jensen, N Gundestrup, C Hammer and H Oeschger. North Atlantic climatic oscillations revealed by deep Greenland ice cores. In *Climate Processes and Climate Sensitivity*, volume 29 of *Geophys. Monogr. Ser.*, pages 288–298. AGU, Washington, DC, **1984**. ISBN 0-87590-404-1. doi:10.1029/GM029p0288.

Dansgaard, W, S J Johnsen, H B Clausen, D Dahl-Jensen, N S Gundestrup, C U Hammer, C S Hvidberg, J P Steffensen, A E Sveinbjornsdottir, J Jouzel and G Bond, **1993**. Evidence for general instability of past climate from a 250-kyr ice-core record. *Nature*, 364(6434):218–220. doi:10.1038/364218a0.

Darby, Dennis A and Paula **Zimmerman**, **2008**. Ice-rafted detritus events in the Arctic during the last glacial interval, and the timing of the Innuitian and Laurentide ice sheet calving events. *Polar Research*, 27(2):114–127. ISSN 08000395. doi:10.1111/j.1751-8369.2008.00057.x.

de Vries, Pedro and Susanne L **Weber**, **2005**. The Atlantic freshwater budget as a diagnostic for the existence of a stable shut down of the meridional overturning circulation. *Geophys. Res. Lett.*, 32(9):L09606—-. ISSN 0094-8276. doi:10.1029/2004GL021450.

Dee, D P, S M Uppala, A J Simmons, P Berrisford, P Poli, S Kobayashi, U Andrae, M A Balmaseda, G Balsamo, P Bauer, P Bechtold, A C M Beljaars, L van de Berg, J Bidlot, N Bormann, C Delsol, R Dragani, M Fuentes, A J Geer, L Haimberger, S B Healy, H Hersbach, E V Hólm, L Isaksen, P Kå llberg, M Köhler, M Matricardi, A P McNally, B M Monge-Sanz, J.-J. Morcrette, B.-K. Park, C Peubey, P de Rosnay, C Tavolato, J.-N. Thépaut and F Vitart, **2011**. The ERA-Interim reanalysis: configuration and performance of the data assimilation system. *Quarterly Journal of the Royal Meteorological Society*, 137(656):553–597. ISSN 1477-870X. doi:10.1002/qj.828.

Denton, G H and T J **Hughes**. *The Last Great Ice Sheets*, volume 1. Wiley, **1981**. ISBN 0471060062.

Denton, G H, R F Anderson, J R Toggweiler, R L Edwards, J M Schaefer and A E Putnam, **2010**. The Last Glacial Termination. *Science*, 328(5986):1652–1656. doi:10.1126/science.1184119.

Dowdeswell, J A, G S Hamilton and J O Hagen, **1991**. The duration of the active phase on surge-type glaciers: contrasts between Svalbard and other regions. *Journal of Glaciology*, 37(127):388–400. ISSN 0022-1430.

Duplessy, J. C., N. J. Shackleton, R. G. Fairbanks, L. Labeyrie, D. Oppo and N. Kallel, **1988**. Deepwater source variations during the last climatic cycle and their impact on the global deepwater circulation. *Paleoceanography*, 3(3):343. ISSN 0883-8305. doi:10.1029/PA003i003p00343.

Eamar, Joan, Heather Main, Natasha Webster, Lynn Nygaard and Edward Osmond-Jones, editors. *Global outlook for ice and snow*. United Nations Environment Programme, **2007**. ISBN 9789280727999.

EPICA Community Members, **2004**. Eight glacial cycles from an Antarctic ice core. *Nature*, 429(6992):623–628. ISSN 0028-0836. doi:10.1038/nature02599.

EPICA Community Members, **2006**. One-to-one coupling of glacial climate variability in Greenland and Antarctica. *Nature*, 444(7116):195–198. ISSN 0028-0836. doi:10.1038/nature05301.

Ettema, Janneke, Michiel R van den Broeke, Erik van Meijgaard, Willem Jan van de Berg, Jonathan L Bamber, Jason E Box and Roger C Bales, **2009**. Higher surface mass balance of the Greenland ice sheet revealed by high-resolution climate modeling. *Geophys. Res. Lett.*, 36(12). ISSN 0094-8276. doi:10.1029/2009GL038110.

Fausto, Robert S, Andreas P Ahlstrø m, Dirk van As and Konrad Steffen, **2011**. Present-day temperature standard deviation parameterization for Greenland. *Journal of Glaciology*, 57(206):1181–1183.

Fettweis, X, **2007**. Reconstruction of the 1979–2006 Greenland ice sheet surface mass balance using the regional climate model MAR. *The Cryosphere*, 1(1): 21–40. doi:10.5194/tc-1-21-2007.

Fichefet, Thierry, Chantal Poncin, Hugues Goosse, Philippe Huybrechts, Ives Janssens and Hervé Le Treut, **2003**. Implications of changes in freshwater flux from the Greenland ice sheet for the climate of the 21st century. *Geophys. Res. Lett.*, 30(17):1911. ISSN 0094-8276. doi:10.1029/2003GL017826.

Fletcher, William J and Maria Fernanda **Sánchez Goñi**, **2008**. Orbital- and sub-orbital-scale climate impacts on vegetation of the western Mediterranean basin over the last 48,000 yr. *Quaternary Research*, 70(3):451–464. ISSN 0033-5894. `http://www.sciencedirect.com/science/article/pii/S0033589408000975`.

Fletcher, William J, Maria Fernanda Sánchez Goñi, Judy R M Allen, Rachid Cheddadi, Nathalie Combourieu-Nebout, Brian Huntley, Ian Lawson, Laurent Londeix, Donatella Magri, Vasiliki Margari, Ulrich C Müller, Filipa Naughton, Elena Novenko, Katy Roucoux and P C Tzedakis, **2010**. Millennial-scale variability during the last glacial in vegetation records from Europe. *Quaternary Science Reviews*, 29(21–22):2839–2864. ISSN 0277-3791. `http://www.sciencedirect.com/science/article/pii/S0277379109003886`.

Flower, B P, D W Hastings, H W Hill and T M Quinn, **2004**. Phasing of deglacial warming and Laurentide Ice Sheet meltwater in the Gulf of Mexico. *Geology*, 32 (7):597–600. ISSN 0091-7613.

Fowler, A C and E **Schiavi**, **1998**. A theory of ice-sheet surges. *Journal of Glaciol-ogylaciology*, 44(146):104–118. `http://www.igsoc.org/journal.old/44/146/igs_journal_vol44_issue146_pg104-118.pdf`.

Fürst, J J, H Goelzer and P Huybrechts, **2013**. Effect of higher-order stress gradients on the centennial mass evolution of the Greenland ice sheet. *The Cryosphere*, 7(1):183–199. ISSN 1994-0424. doi:10.5194/tc-7-183-2013.

Fyke, J G, A J Weaver, D Pollard, M Eby, L Carter and A Mackintosh, **2011**. A new coupled ice sheet/climate model: description and sensitivity to model physics under Eemian, Last Glacial Maximum, late Holocene and modern climate conditions. *Geoscientific Model Development*, 4(1):117–136. doi:10.5194/gmd-4-117-2011.

Ganachaud, Alexandre, **2003**. Large-scale mass transports, water mass formation, and diffusivities estimated from World Ocean Circulation Experiment (WOCE) hydrographic data. *J. Geophys. Res.*, 108(C7). ISSN 0148-0227. doi:10.1029/2002JC001565.

Ganachaud, Alexandre and C **Wunsch**, **2003**. Large-scale ocean heat and freshwater transports during the World Ocean Circulation Experiment. *Journal of Climate*, 16(4):696–705. doi:10.1175/1520-0442(2003)016¡0696:LSOHAF¿2.0.CO;2.

Ganopolski, Andrey and Reinhard **Calov**, **2011**. The role of orbital forcing, carbon dioxide and regolith in 100 kyr glacial cycles. *Climate of the Past*, 7(4): 1415–1425. doi:10.5194/cp-7-1415-2011.

Ganopolski, Andrey and Stefan **Rahmstorf**, **2001**. Rapid changes of glacial climate simulated in a coupled climate model. *Nature*, 409(6817):153–158. ISSN 0028-0836. doi:10.1038/35051500.

Ganopolski, Andrey, Reinhard Calov and Martin Claussen, **2010**. Simulation of the last glacial cycle with a coupled climate ice-sheet model of intermediate complexity. *Climate of the Past*, 6(2):229–244. doi:10.5194/cp-6-229-2010.

Goldberg, D. N., C. M. Little, O. V. Sergienko, a. Gnanadesikan, R. Hallberg and M. Oppenheimer, **2012a**. Investigation of land ice-ocean interaction with a fully coupled ice-ocean model: 1. Model description and behavior. *Journal of Geophysical Research*, 117(F2):1–16. ISSN 0148-0227. doi:10.1029/2011JF002246.

Goldberg, D N, C M Little, O V Sergienko, A Gnanadesikan, R Hallberg and M Oppenheimer, **2012b**. Investigation of land ice-ocean interaction with a fully coupled ice-ocean model: 2. Sensitivity to external forcings. *J. Geophys. Res.*, 117(F2):F02038. ISSN 0148-0227. doi:10.1029/2011JF002247.

Gregory, J M, O J H Browne, A J Payne, J K Ridley and I C Rutt, **2012**. Modelling large-scale ice-sheet–climate interactions following glacial inception. *Climate of the Past*, 8(5):1565–1580. doi:10.5194/cp-8-1565-2012.

Greve, Ralf, **1997**. A continuum-mechanical formulation for shallow polythermal ice sheets. *Philosophical Transactions of the Royal Society London A*, 355:921–974.

Greve, Ralf, Ryoji Takahama and Reinhard Calov, **2006**. Simulation of large-scale ice-sheet surges : The ISMIP HEINO experiments. *Polar Meteorology and Glaciology*, 20:1–15. `http://hdl.handle.net/2115/29659`.

Grimm, Eric C, George L Jacobson, William A Watts, Barbara C S Hansen and Kirk A Maasch, **1993**. A 50,000-Year Record of Climate Oscillations from Florida and Its Temporal Correlation with the Heinrich Events. *Science*, 261(5118):198–200. `http://www.sciencemag.org/content/261/5118/198.abstract`.

Grimm, Eric C, William A Watts, George L Jacobson Jr., Barbara C S Hansen, Heather R Almquist and Ann C Dieffenbacher-Krall, **2006**. Evidence for warm wet Heinrich events in Florida. *Quaternary Science Reviews*, 25(17–18):2197–2211. ISSN 0277-3791. `http://www.sciencedirect.com/science/article/pii/S027737910600165X`.

Grousset, F E, L Labeyrie, J A Sinko, M Cremer, G Bond, J Duprat, E Cortijo and S Huon, **1993**. Patterns of Ice-rafted Detritus In the Glacial North-atlantic (40-degrees-55-degrees-n). *Paleoceanography*, 8(2):175–192.

Gudmundsson, G H, **2013**. Ice-shelf buttressing and the stability of marine ice sheets. *The Cryosphere*, 7(2):647–655. doi:10.5194/tc-7-647-2013.

Gudmundsson, G H, J Krug, G Durand, L Favier and O Gagliardini, **2012**. The stability of grounding lines on retrograde slopes. *The Cryosphere*, 6(6):1497–1505. ISSN 1994-0424. doi:10.5194/tc-6-1497-2012.

Gulley, J D, D I Benn, E Screaton and J Martin, **2009**. Mechanisms of englacial conduit formation and their implications for subglacial recharge. *Quaternary Science Reviews*, 28(19–20):1984–1999. ISSN 0277-3791. `http://www.sciencedirect.com/science/article/pii/S0277379109001176`.

Gutjahr, Marcus and Jörg **Lippold**, **2011**. Early arrival of Southern Source Water in the deep North Atlantic prior to Heinrich event 2. *Paleoceanography*, 26(2): PA2101. ISSN 0883-8305. doi:10.1029/2011PA002114.

Hagemann, S and L **Dümenil**, **1998**. A parametrization of the lateral waterflow for the global scale. *Climate Dynamics*, 14(1):17–31. ISSN 0930-7575. doi:10.1007/s003820050205.

Hagemann, S and L D **Gates**, **2003**. Improving a subgrid runoff parameterization scheme for climate models by the use of high resolution data derived from satellite observations. *Climate Dynamics*, 21(3):349–359. ISSN 0930-7575. doi:10.1007/s00382-003-0349-x.

Hawkins, E, R S Smith, L C Allison, Jonathan M Gregory, T J Woollings, H Pohlmann and B de Cuevas, **2011**. Bistability of the Atlantic overturning circulation in a global climate model and links to ocean freshwater transport. *Geophys. Res. Lett.*, 38(10). ISSN 0094-8276. doi:10.1029/2011GL047208.

Heinrich, Hartmut, **1988**. Origin and consequences of cyclic ice rafting in the Northeast Atlantic Ocean during the past 130,000 years. *Quaternary Research*, 29(2):142–152. ISSN 0033-5894. doi:10.1016/0033-5894(88)90057-9.

Hellmer, Hartmut and Dirk **Olbers**, **1989**. A two-dimensional model for the thermohaline circulation under an ice shelf. *Antarctic Science*.

Hellmer, Hartmut H, Frank Kauker, Ralph Timmermann, Jürgen Determann and Jamie Rae, **2012**. Twenty-first-century warming of a large Antarctic ice-shelf cavity by a redirected coastal current. *Nature*, 485(7397):225–8. ISSN 1476-4687. doi:10.1038/nature11064.

Hemming, Sidney R, **2004**. Heinrich events: Massive late Pleistocene detritus layers of the North Atlantic and their global climate imprint. *Rev. Geophys.*, 42. doi:10.1029/2003RG000128.

Hessler, Ines, Lydie Dupont, Raymonde Bonnefille, Hermann Behling, Catalina González, Karin F Helmens, Henry Hooghiemstra, Judicael Lebamba, Marie-Pierre Ledru, Anne-Marie Lézine, Jean Maley, Fabienne Marret and Annie Vincens, **2010**. Millennial-scale changes in vegetation records from tropical Africa and South America during the last glacial. *Quaternary Science Reviews*, 29(21–22):2882–2899. ISSN 0277-3791. `http://www.sciencedirect.com/science/article/pii/S0277379109004028`.

Hindmarsh, Richard C A, **2011**. Ill-posedness of the shallow-ice approximation when modelling thermo-viscous instabilities – Correspondence. *Journal of Glaciology*, 57 (206):1177–1178.

Hock, Regine, **2005**. Glacier melt: a review of processes and their modelling. *Progress In Physical Geography*, 29(3):362–391.

Holland, David M and Adrian **Jenkins**, **1999**. Modeling Thermodynamic Ice–Ocean Interactions at the Base of an Ice Shelf. *Journal of Physical Oceanography*, 29(8):1787–1800. ISSN 0022-3670. doi:10.1175/1520-0485(1999)029¡1787:MTIOIA¿2.0.CO;2.

Holland, Paul R., Adrian Jenkins and David M. Holland, **2008**. The response of ice shelf basal melting to variations in ocean temperature. *Journal of Climate*, 21(11):2558–2572. doi:10.1175/2007JCLI1909.1.

Howat, I. M., Ian Joughin, S. Tulaczyk and S. Gogineni, **2005**. Rapid retreat and acceleration of Helheim Glacier, east Greenland. *Geophysical Research Letters*, 32(22):L22502. ISSN 0094-8276. doi:10.1029/2005GL024737.

Hu, Aixue, Bette L Otto-Bliesner, Gerald A Meehl, Weiqing Han, Carrie Morrill, Esther C Brady and Bruce Briegleb, **2008**. Response of Thermohaline Circulation to Freshwater Forcing under Present-Day and LGM Conditions. *Journal of Climate*, 21(10):2239–2258. ISSN 0894-8755. doi:10.1175/2007JCLI1985.1.

Huisman, Selma E, Matthijs den Toom, Henk A Dijkstra and Sybren Drijfhout, **2010**. An Indicator of the Multiple Equilibria Regime of the Atlantic Meridional Overturning Circulation. *Journal of Physical Oceanography*, 40(3):551–567. ISSN 0022-3670. doi:10.1175/2009JPO4215.1.

Hulbe, Christina L, **1997**. An Ice Shelf Mechanism for Heinrich Layer Production. *Paleoceanography*, 12(5):711–717. ISSN 0883-8305. doi:10.1029/97PA02014.

Hulbe, Christina L, Douglas R MacAyeal, George H Denton, Johan Kleman and Thomas V Lowell, **2004**. Catastrophic ice shelf breakup as the source of Heinrich event icebergs. *Paleoceanography*, 19(1):PA1004—-. ISSN 0883-8305. doi:10.1029/2003PA000890.

Hutter, Kolumban, **1982**. DYNAMICS OF GLACIERS. *Annual Reviews of Fluid Mechanics*, 14:87–130.

Huybrechts, P, I Janssens, C Poncin and T Fichefet, **2002**. The response of the Greenland ice sheet to climate changes in the 21st century by interactive coupling of an AOGCM with a thermomechanical ice-sheet model. *Annals of Glaciology*, 35(1):409–415. ISSN 0260-3055.

Iken, Almut, **1981**. The effect of the subglacial water pressure on the sliding velocity of a glacier in an idealized numerical model. *Journal of Glaciology*, 27: 407–421. ISSN 0022-1430.

Jenkins, Adrian, Keith W Nicholls and Hugh F J Corr, **2010**. Observation and parameterization of ablation at the base of Ronne Ice Shelf, Antarctica. *Journal of Physical Oceanography*, 40(10):2298–2312. `http://journals.ametsoc.org/doi/full/10.1175/2010JPO4317.1`.

Johns, W E, M O Baringer, L M Beal, S A Cunningham, T Kanzow, H L Bryden, J J M Hirschi, J Marotzke, C S Meinen, B Shaw and R Curry, **2011**. Continuous, Array-Based Estimates of Atlantic Ocean Heat Transport at 26.5○N. *J. Climate*, 24(10):2429–2449. ISSN 0894-8755. doi:10.1175/2010JCLI3997.1.

Joughin, I, B Smith and I Howat, **2010a**. MEaSUREs Greenland Ice Sheet Velocity Map from InSAR Data. `http://nsidc.org/`.

Joughin, I, B Smith, I M Howat, T Scambos and T Moon, **2010b**. Greenland Flow Variability from Ice-Sheet-Wide Velocity Mapping. *Journal of Glaciology*, 56(197):415–430.

Jungclaus, J. H., N Keenlyside, M Botzet, Helmuth Haak, J.-J. Luo, Mojib Latif, Jochem Marotzke, Uwe Mikolajewicz and Erich Roeckner, **2006**. Ocean Circulation and Tropical Variability in the Coupled Model ECHAM5/MPI-OM. *Journal of Climate*, 19(16):3952–3972. ISSN 0894-8755. doi:10.1175/JCLI3827.1.

Kageyama, M, S Charbit, C Ritz, M Khodri and G Ramstein, **2004**. Quantifying ice-sheet feedbacks during the last glacial inception. *Geophys. Res. Lett.*, 31(24): L24203. ISSN 0094-8276. doi:10.1029/2004GL021339.

Kageyama, M, U Merkel, B Otto-Bliesner, M Prange, A Abe-Ouchi, G Lohmann, R Ohgaito, D M Roche, J Singarayer, D Swingedouw and X Zhang, **2013**. Climatic impacts of fresh water hosing under Last Glacial Maximum conditions: a multi-model study. *Clim. Past*, 9(2):935–953. ISSN 1814-9332. doi:10.5194/cp-9-935-2013.

Kageyama, Masa, André Paul, Didier M Roche and Cédric J Van Meerbeeck, **2010**. Modelling glacial climatic millennial-scale variability related to changes in the Atlantic meridional overturning circulation: a review. *Quaternary Science Reviews*, 29(21-22):2931–2956. ISSN 0277-3791. doi:10.1016/j.quascirev.2010.05.029.

Kanzow, T, S A Cunningham, W E Johns, J J M Hirschi, J Marotzke, M O Baringer, C S Meinen, M P Chidichimo, C Atkinson, L M Beal, H L Bryden and J Collins, **2010**. Seasonal Variability of the Atlantic Meridional Overturning Circulation at 26.5 degrees N. *Journal of Climate*, 23(21):5678–5698. doi:10.1175/2010JCLI3389.1.

Kim, Seong-Joong, Thomas Crowley, David Erickson, Bala Govindasamy, Phillip Duffy and Bang Lee, **2008**. High-resolution climate simulation of the last glacial maximum. *Climate Dynamics*, 31(1):1–16. ISSN 0930-7575. doi:10.1007/s00382-007-0332-z.

Kleman, Johan, Krister Jansson, Hernán De Angelis, Arjen P Stroeven, Clas Hättestrand, Göran Alm and Neil Glasser, **2010**. North American Ice Sheet build-up during the last glacial cycle, 115-21 kyr. *Quaternary Science Reviews*, 29(17-18):2036–2051. ISSN 0277-3791. doi:DOI: 10.1016/j.quascirev.2010.04.021.

Koltermann, K. P., Gouretski V. V. and K. Jancke. *Hydrographic Atlas of the World Ocean Circulation Experiment (WOCE). Volume 3: Atlantic Ocean*. International WOCE Project Office, Southampton, UK, **2011**. ISBN 090417557X.

Krinner, Gerhard, Bernhard Diekmann, Florence Colleoni and Georg Stauch, **2011**. Global, regional and local scale factors determining glaciation extent in Eastern Siberia over the last 140,000 years. *Quaternary Science Reviews*, 30(7-8): 821–831. ISSN 0277-3791. doi:10.1016/j.quascirev.2011.01.001.

Langen, P. L., A. M. Solgaard and C. S. Hvidberg, **2012**. Self-inhibiting growth of the Greenland Ice Sheet. *Geophysical Research Letters*, 39(12). ISSN 0094-8276. doi:10.1029/2012GL051810.

Laske, G and G **Masters**, **1997**. A Global Digital Map of Sediment Thickness. *EOS Trans. AGU*, 78.

Le Meur, Emmanuel and Philippe **Huybrechts**, **1996**. A comparison of different ways of dealing with isostasy: examples from modelling the Antarctic ice sheet during the last glacial cycle. *Annals of Glaciology*, 23:309–317. `http://epic.awi.de/2128/1/Meu1995a.pdf`.

Lea, David W, Dorothy K Pak, Larry C Peterson and Konrad A Hughen, **2003**. Synchroneity of Tropical and High-Latitude Atlantic Temperatures over the Last Glacial Termination. *Science*, 301(5638):1361–1364. doi:10.1126/science.1088470.

Lemke, Peter, J Ren, Richard B. Alley, I Allison, J Carrasco, G Flato, Y Fujii, G Kaser, P Mote, R.H. Thomas and T Zhang. Observations: Changes in Snow, Ice and frozen Ground. In *Climate Change 2007: The Physical Science Basis. Contribution of the Working Group I to the Fourth Assesmente Report of the Intergovernmental Panel on Climate Change*. Cambridge University Press,

Cambridge, United Kingdom and New York, NY, USA, **2007**.

Lippold, Jorg, Yiming Luo, Roger Francois, Susan E Allen, Jeanne Gherardi, Sylvain Pichat, Ben Hickey and Hartmut Schulz, **2012**. Strength and geometry of the glacial Atlantic Meridional Overturning Circulation. *Nature Geosci*, 5(11): 813–816. ISSN 1752-0894. doi:10.1038/ngeo1608.

Lisiecki, Lorraine E and Maureen E **Raymo**, **2005**. A Pliocene-Pleistocene stack of 57 globally distributed benthic δ^{18}O records. *Paleoceanography*, 20(1):PA1003. ISSN 0883-8305. doi:10.1029/2004PA001071.

Lliboutry, L, **1968**. General theory of subglacial cavitation and sliding of temperate glaciers. *Journal of Glaciology*, 7:21–58.

Luyten, J R, J Pedlosky and H Stommel, **1983**. The Ventilated Thermocline. *Journal of Physical Oceanography*, 13(2):292–309. ISSN 0022-3670. doi:10.1175/1520-0485(1983)013¡0292:TVT¿2.0.CO;2.

Lynch-Stieglitz, Jean, Jess F Adkins, William B Curry, Trond Dokken, Ian R Hall, Juan Carlos Herguera, Joël J.-M. Hirschi, Elena V Ivanova, Catherine Kissel, Olivier Marchal, Thomas M Marchitto, I Nicholas McCave, Jerry F McManus, Stefan Mulitza, Ulysses Ninnemann, Frank Peeters, Ein-Fen Yu and Rainer Zahn, **2007**. Atlantic Meridional Overturning Circulation During the Last Glacial Maximum. *Science*, 316(5821):66–69. doi:10.1126/science.1137127.

MacAyeal, D R, **1993**. Binge/Purge Oscillations of the Laurentide Ice Sheet as a Cause of the North Atlantic's Heinrich Events. *Paleoceanography*, 8. doi:10.1029/93PA02200.

MacAyeal, Douglas R, **1989**. Large-Scale Ice Flow Over a Viscous Basal Sediment: Theory and Application to Ice Stream B, Antarctica. *J. Geophys. Res.*, 94. doi:10.1029/JB094iB04p04071.

Maier-Reimer, Ernst and Uwe **Mikolajewicz**. Experiments with an OGCM on the Cause of the Younger Dryas. In **Wooster**, W. and Yá nez **Arancibia**, editors, *Oceanography 1988*. UNAM Press, México D F, **1989**.

Manabe, S and R J **Stouffer**, **1988**. Two Stable Equilibria of a Coupled Ocean-Atmosphere Model. *Journal of Climate*, 1(9):841–866. ISSN 0894-8755. doi:10.1175/1520-0442(1988)001¡0841:TSEOAC¿2.0.CO;2.

Manley, G, **1965**. Possible Climatic Agencies in the Development of Post-Glacial Habitats. *Proceedings of the Royal Society of London. Series B. Biological Sciences*, 161(984):363–375. doi:10.1098/rspb.1965.0008.

Marotzke, Jochem, **2012**. A grip on ice-age ocean circulation. *Nature*, 485(7397): 180–181. ISSN 0028-0836.

Marsh, Robert, Wilco Hazeleger, Andrew Yool and Eelco J Rohling, **2007**. Stability of the thermohaline circulation under millennial CO2 forcing and two alternative controls on Atlantic salinity. *Geophys. Res. Lett.*, 34(3):L03605—-. ISSN 0094-8276. doi:10.1029/2006GL027815.

Marshall, Shawn J and Michelle R **Koutnik**, **2006**. Ice sheet action versus reaction: Distinguishing between Heinrich events and Dansgaard-Oeschger cycles in the North Atlantic. *Paleoceanography*, 21. doi:10.1029/2005PA001247.

Marsiat, Isabelle, **1994**. Simulation of the northern hemisphere continental ice sheets over the last glacial-interglacial cycle: Experiments with a latitude-longitude vertically integrated ice sheet model coupled to a zonally averaged climate model. *Paleoclimates Data and Modelling*, 1(1):59–98. ISSN 1063-7176.

Marsland, S J, H Haak, J H Jungclaus, M Latif and F Röske, **2003**. The Max-Planck-Institute global ocean/sea ice model with orthogonal curvilinear coordinates. *Ocean Modelling*, 5(2):91–127. ISSN 1463-5003. doi:10.1016/S1463-5003(02)00015-X.

McManus, J F, R Francois, J M Gherardi, L D Keigwin and S Brown-Leger, **2004**. Collapse and rapid resumption of Atlantic meridional circulation linked to deglacial climate changes. *NATURE*, 428(6985):834–837. ISSN 0028-0836. doi:10.1038/nature02494.

Mercer, J H, **1969**. The Allerød Oscillation: A European Climatic Anomaly? *Arctic and Alpine Research*, 1(4):227–234. ISSN 00040851. `http://www.jstor.org/stable/1550111`.

Mikolajewicz, Uwe and Ernst **Maier-Reimer**, **1994**. Mixed boundary conditions in ocean general circulation models and their influence on the stability of the model's conveyor belt. *J. Geophys. Res.*, 99(C11):22633–22644. ISSN 0148-0227. doi:10.1029/94JC01989.

Mikolajewicz, Uwe, Ernst Maier-Reimer, Thomas J Crowley and Kwang-Yul Kim, **1993**. Effect of Drake and Panamanian Gateways on the Circulation of an Ocean Model. *Paleoceanography*, 8(4):409–426. ISSN 0883-8305. doi:10.1029/93PA00893.

Mikolajewicz, Uwe, Matthias Gröger, Ernst Maier-Reimer, Guy Schurgers, Miren Vizcaíno and Arne Winguth, **2007a**. Long-term effects of anthropogenic CO2 emissions simulated with a complex earth system model. *Climate Dynamics*, 28 (6):599–633. doi:10.1007/s00382-006-0204-y.

Mikolajewicz, Uwe, Miren Vizcaíno, Johann Jungclaus and Guy Schurgers, **2007b**. Effect of ice sheet interactions in anthropogenic climate change simulations. *Geophys. Res. Lett.*, 34. doi:10.1029/2007GL031173.

Milanković, Milutin. *Kanon der Erdbestrahlung und seine Anwendung auf das Eiszeitenproblem*. Poseńa izdanja Srpska akademija nauka. Königlich Serbische Akademie, Belgrad, **1941**.

Morlighem, M, E Rignot, H Seroussi, E Larour, H Ben Dhia and D Aubry, **2010**. Spatial patterns of basal drag inferred using control methods from a full-Stokes and simpler models for Pine Island Glacier, West Antarctica. *Geophys. Res. Lett.*, 37(14):L14502—-. ISSN 0094-8276. doi:10.1029/2010GL043853.

Morton, K W and D F **Mayers**. *Numerical Solution Of Partial Differential Equations: An Introduction*. Numerical Solution of Partial Differential Equations: An Introduction. Cambridge University Press, **2005**. ISBN 9780521607933.

Murray, Tavi, K Scharrer, T D James, S R Dye, E Hanna, A D Booth, N Selmes, A Luckman, A L C Hughes, S Cook and P Huybrechts, **2010**. Ocean regulation hypothesis for glacier dynamics in southeast Greenland and implications for ice sheet mass changes. *J. Geophys. Res.*, 115(F3). ISSN 0148-0227. doi:10.1029/2009JF001522.

Negre, Cesar, Rainer Zahn, Alexander L Thomas, Pere Masque, Gideon M Henderson, Gema Martinez-Mendez, Ian R Hall and Jose L Mas, **2010**. Reversed flow of Atlantic deep water during the Last Glacial Maximum. *Nature*, 468(7320): 84–88. ISSN 0028-0836. doi:10.1038/nature09508.

Oka, A, H Hasumi and A Abe-Ouchi, **2012**. The thermal threshold of the Atlantic meridional overturning circulation and its control by wind stress forcing during glacial climate. *Geophys. Res. Lett.*, 39(9). ISSN 0094-8276. doi:10.1029/2012GL051421.

Otto-Bliesner, Bette L and Esther C **Brady**, **2010**. The sensitivity of the climate response to the magnitude and location of freshwater forcing: last glacial maximum experiments. *Quaternary Science Reviews*, 29(1-2):56–73. doi:10.1016/j.quascirev.2009.07.004.

Otto-Bliesner, Bette L, Esther C Brady, Gabriel Clauzet, Robert Tomas, Samuel Levis and Zav Kothavala, **2006**. Last Glacial Maximum and Holocene Climate in CCSM3. *J. Climate*, 19(11):2526–2544. ISSN 0894-8755. doi:10.1175/JCLI3748.1.

Pardaens, A K, H T Banks, Jonathan M Gregory and P R Rowntree, **2003**. Freshwater transports in HadCM3. *Climate Dynamics*, 21(2):177–195. ISSN 0930-7575. doi:10.1007/s00382-003-0324-6.

Paterson, W S B. *Physics of Glaciers, Third Edition*. Butterworth-Heinemann, 3 edition, **1994**. ISBN 9780750647427.

Pattyn, F, **2003**. A new three-dimensional higher-order thermomechanical ice sheet model: basic sensitivity, ice stream development, and ice flow across subglacial lakes. *Journal of Geophysical Research*, 108(B8). ISSN 0148-0227.

Peck, V L, I R Hall, R Zahn, H Elderfield, F Grousset, Sidney R Hemming and J D Scourse, **2006**. High resolution evidence for linkages between NW European ice sheet instability and Atlantic Meridional Overturning Circulation. *Earth and Planetary Science Letters*, 243(3-4):476–488. doi:10.1016/epsl.2005.12.023.

Peltier, W R, **2002**. On eustatic sea level history: Last Glacial Maximum to Holocene. *Quaternary Science Reviews*, 21(1–3):377–396. ISSN 0277-3791. `http://www.sciencedirect.com/science/article/pii/S0277379101000841`.

Peltier, W R, **2004**. Global glacial isostasy and the surface of the ice-age earth: The ice-5G (VM2) model and grace. *Annual Review of Earth and Planetary Sciences*, 32:111–149. ISSN 0084-6597. doi:10.1146/annurev.earth.32.082503.144359.

Phillips, Thomas, Harihar Rajaram and Konrad Steffen, **2010**. Cryo-hydrologic warming: A potential mechanism for rapid thermal response of ice sheets. *Geophys. Res. Lett.*, 37(20):L20503—-. ISSN 0094-8276. doi:10.1029/2010GL044397.

Pollard, David, **2010**. A retrospective look at coupled ice sheet–climate modeling. *Climatic Change*, 100(1):173–194. ISSN 0165-0009. doi:10.1007/s10584-010-9830-9.

Pollard, David and Robert M **DeConto**, **2009**. Modelling West Antarctic ice sheet growth and collapse through the past five million years. *Nature*, 458(7236):329–332. ISSN 0028-0836. doi:10.1038/nature07809.

Pollard, David, Isabelle Muszynski, Stephen H. Schneider and Starley L. Thompson, **1990**. Asynchronous coupling of ice-sheet and atmospheric forcing models. *Annals of Glaciology*, 14:247–251.

Prange, Matthias, V. Romanova and Gerrit Lohmann, **2002**. The glacial thermohaline circulation: Stable or unstable? *Geophysical Research Letters*, 29(21). ISSN 0094-8276. doi:10.1029/2002GL015337.

Prentice, I Colin, Dominique Jolly and BIOME 6000 participants, **2000**. Mid-Holocene and glacial-maximum vegetation geography of the northern continents and Africa. *Journal of Biogeography*, 27(3):507–519. ISSN 1365-2699. doi:10.1046/j.1365-2699.2000.00425.x.

Pritchard, H D, S R M Ligtenberg, H a Fricker, D G Vaughan, M R van den Broeke and L Padman, **2012**. Antarctic ice-sheet loss driven by basal melting of ice shelves. *Nature*, 484(7395):502–5. ISSN 1476-4687. doi:10.1038/nature10968.

Rahmstorf, Stefan, **1994**. Rapid climate transitions in a coupled ocean–atmosphere model. *Nature*, 372(6501):82–85. doi:10.1038/372082a0.

Rahmstorf, Stefan, **1996**. On the freshwater forcing and transport of the Atlantic thermohaline circulation. *Climate Dynamics*, 12(12):799–811. ISSN 0930-7575. doi:10.1007/s003820050144.

Rahmstorf, Stefan, **2002**. Ocean circulation and climate during the past 120,000 years. *Nature*, 419(6903):207–214. ISSN 0028-0836. doi:10.1038/nature01090.

Rahmstorf, Stefan, Michel Crucifix, Andrey Ganopolski, Hugues Goosse, Igor Kamenkovich, Reto Knutti, Gerrit Lohmann, Robert Marsh, Lawrence A Mysak, Zhaomin Wang and Andrew J Weaver, **2005**. Thermohaline circulation hysteresis: A model intercomparison. *Geophys. Res. Lett.*, 32(23):L23605. ISSN 0094-8276. doi:10.1029/2005GL023655.

Rayner, N A, D E Parker, E B Horton, C K Folland, L V Alexander, D P Rowell, E C Kent and A Kaplan, **2003**. Global analyses of sea surface temperature, sea ice, and night marine air temperature since the late nineteenth century. *J. Geophys. Res.*, 108(D14):4407. ISSN 0148-0227. doi:10.1029/2002JD002670.

Reeh, Niels, **1991**. Parameterization of Melt Rate and Surface Temperature on the Greenland Ice Sheet. *Polarforschung*, 59/3:113–128.

Ridley, J K, P Huybrechts, J M Gregory and J A Lowe, **2005**. Elimination of the Greenland Ice Sheet in a High CO2 Climate. *Journal of Climate*, 18(17): 3409–3427. ISSN 0894-8755. doi:10.1175/JCLI3482.1.

Rignot, E, Jonathan L Bamber, M R Van Den Broeke, C Davis, Y H Li, W J Van De Berg and E Van Meijgaard, **2008**. Recent Antarctic ice mass loss from radar interferometry and regional climate modelling. *Nature Geoscience*, 1(2):106–110.

Roberts, David H, Antony J Long, Christoph Schnabel, Bethan J Davies, Sheng Xu, Matthew J R Simpson and Philipe Huybrechts, **2009**. Ice sheet extent and early deglacial history of the southwestern sector of the Greenland Ice Sheet. *Quaternary Science Reviews*, 28(25–26):2760–2773. ISSN 0277-3791. doi:10.1016/j.quascirev.2009.07.002.

Robinson, A, R Calov and A Ganopolski, **2010**. An efficient regional energy-moisture balance model for simulation of the Greenland Ice Sheet response to climate change. *The Cryosphere*, 4(2):129–144. ISSN 1994-0424. doi:10.5194/tc-4-129-2010.

Roeckner, Erich, G Bäuml, L Bonventura, Renate Brokov, Monika Esch, Marco Giorgetta, Stefan Hagemann, I Kirchner, Luis Kornblueh, E Manzini, A Rhodin, U Schlese, Uwe Schulzweida and A Tompkins. The atmospheric general circulation model ECHAM5 Part 1 Model description. Technical Report 349, Max-Planck-Institut für Meteorologie, **2003**.

Rooth, C, **1982**. Hydrology and ocean circulation. *Progress in Oceanography*, 11 (2):131–149. ISSN 00796611. doi:10.1016/0079-6611(82)90006-4.

Rühlemann, Carsten, Stefan Mulitza, Gerrit Lohmann, André Paul, Matthias Prange and Gerold Wefer, **2004**. Intermediate depth warming in the tropical Atlantic related to weakened thermohaline circulation: Combining paleoclimate data and modeling results for the last deglaciation. *Paleoceanography*, 19(1): PA1025. ISSN 0883-8305. doi:10.1029/2003PA000948.

Scambos, T A, J A Bohlander, C A Shuman and P Skvarca, **2004**. Glacier acceleration and thinning after ice shelf collapse in the Larsen B embayment, Antarctica. *Geophys. Res. Lett.*, 31(18):L18402. ISSN 0094-8276. doi:10.1029/2004GL020670.

Schönfeld, J and R **Zahn**, **2000**. Late Glacial to Holocene history of the Mediterranean Outflow. Evidence from benthic foraminiferal assemblages and stable isotopes at the Portuguese margin. *Palaeogeography, Palaeoclimatology, Palaeoecology*, 159(1–2):85–111. ISSN 0031-0182. `http://www.sciencedirect.com/science/article/pii/S0031018200000353`.

Schoof, Christian, **2006**. Variational methods for glacier flow over plastic till. *Journal of Fluid Mechanics*, 555(-1):299–320. doi:10.1017/S0022112006009104.

Schoof, Christian, **2007**. Ice sheet grounding line dynamics: Steady states, stability, and hysteresis. *Journal of Geophysical Research*, 112(F3):1–19. ISSN 0148-0227. doi:10.1029/2006JF000664.

Schurgers, Guy, Uwe Mikolajewicz, Matthias Groeger, Ernst Maier-Reimer, Miren Vizcaino and Arne Winguth, **2007**. The effect of land surface changes on Eemian climate. *Climate Dynamics*, 29(4):357–373. doi:10.1007/s00382-007-0237-x.

Seki, Osamu, Ryoshi Ishiwatari and Kohei Matsumoto, **2002**. Millennial climate oscillations in NE Pacific surface waters over the last 82 kyr: New evidence from alkenones. *Geophys. Res. Lett.*, 29(23):2144. ISSN 0094-8276. doi:10.1029/2002GL015200.

Sitch, S, B Smith, I C Prentice, A Arneth, A Bondeau, W Cramer, J O Kaplan, S Levis, W Lucht, M T Sykes, K Thonicke and S Venevsky, **2003**. Evaluation of ecosystem dynamics, plant geography and terrestrial carbon cycling in the LPJ dynamic global vegetation model. *Global Change Biology*, 9(2):161–185. ISSN 1365-2486. doi:10.1046/j.1365-2486.2003.00569.x.

Skinner, L C and H **Elderfield**, **2007**. Rapid fluctuations in the deep North Atlantic heat budget during the last glacial period. *Paleoceanography*, 22(1): PA1205. ISSN 0883-8305. doi:10.1029/2006PA001338.

Solomon, S, D Qin, M Manning, Z Chen, M Marquis, K B Averyt, M Tignor and H L Miller, editors. *The Physical Science Basis. Contribution of Working Group I to the Fourth Assessment Report of the Intergovernmental Panel on Climate Change*. Cambridge University Press, Cambridge, United Kingdom and New York, NY, USA, **2007**.

Soucek, O and Z **Martinec**, **2011**. ISMIP-HEINO experiment revisited: effect of higher-order approximation and sensitivity study. *Journal of Glaciology*, 57 (206):1158–1170. ISSN 0022-1430.

Stanford, J D, E J Rohling, S Bacon, A P Roberts, F E Grousset and M Bolshaw, **2011**. A new concept for the paleoceanographic evolution of Heinrich event 1 in the North Atlantic. *Quaternary Science Reviews*, 30(9-10):1047–1066. ISSN 0277-3791. doi:10.1016/j.quascirev.2011.02.003.

Stokes, Chris R and Lev **Tarasov**, **2010**. Ice streaming in the Laurentide Ice Sheet: A first comparison between data-calibrated numerical model output and geological evidence. *Geophys. Res. Lett.*, 37. doi:10.1029/2009GL040990.

Stokes, Chris R, Chris D Clark, Dennis A Darby and Douglas A Hodgson, **2005**. Late Pleistocene ice export events into the Arctic Ocean from the M'Clure Strait Ice Stream, Canadian Arctic Archipelago. *Global and Planetary Change*, 49(3–4): 139–162. ISSN 0921-8181. `http://www.sciencedirect.com/science/article/pii/S0921818105001232`.

Stommel, Henry, **1961**. Thermohaline Convection with Two Stable Regimes of Flow. *Tellus*, 13(2):224–230. ISSN 00402826. doi:10.1111/j.2153-3490.1961.tb00079.x.

Stouffer, R J, J Yin, Jonathan M Gregory, K W Dixon, M J Spelman, W Hurlin, A J Weaver, M Eby, G M Flato, H Hasumi, A Hu, J H Jungclaus,

I V Kamenkovich, A Levermann, M Montoya, S Murakami, S Nawrath, A Oka, W R Peltier, D Y Robitaille, A Sokolov, G Vettoretti and S L Weber, **2006**. Investigating the Causes of the Response of the Thermohaline Circulation to Past and Future Climate Changes. *Journal of Climate*, 19(8):1365–1387. doi:10.1175/JCLI3689.1.

Swingedouw, Didier, Christian B. Rodehacke, Erik Behrens, Matthew Menary, Steffen M. Olsen, Yongqi Gao, Uwe Mikolajewicz, Juliette Mignot and Arne Biastoch, **2012**. Decadal fingerprints of freshwater discharge around Greenland in a multi-model ensemble. *Climate Dynamics*. ISSN 0930-7575. doi:10.1007/s00382-012-1479-9.

Tarasov, Lev and W R **Peltier**, **2003**. Greenland glacial history, borehole constraints and Eemian extent. *Journal of Geophysical Research*, 108:2124–2143.

Tarasov, Lev and W Richard **Peltier**, **1997**. Terminating the 100 kyr ice age cycle. *J. Geophys. Res.*, 102(D18):21665–21693. ISSN 0148-0227. doi:10.1029/97JD01766.

Tarasov, Lev, Arthur S Dyke, Radford M Neal and W R Peltier, **2012**. A data-calibrated distribution of deglacial chronologies for the North American ice complex from glaciological modeling. *Earth and Planetary Science Letters*, 315–316 (0):30–40. ISSN 0012-821X. doi:10.1016/j.epsl.2011.09.010.

the PISM authors. PISM, a Parallel Ice Sheet Model, **2013**. `http://www.pism-docs.org`.

Timmermann, Ralph, Sergey Danilov, Jens Schröter, Carmen Böning, Dmitry Sidorenko and Katja Rollenhagen, **2009**. Ocean circulation and sea ice distribution in a finite element global sea ice–ocean model. *Ocean Modelling*, 27(3–4): 114–129. ISSN 1463-5003. `http://www.sciencedirect.com/science/article/pii/S1463500308001571`.

Tzedakis, P C, M R Frogley, I T Lawson, R C Preece, I Cacho and L de Abreu, **2004**. Ecological thresholds and patterns of millennial-scale climate variability: The response of vegetation in Greece during the last glacial period. *Geology*, 32 (2):109–112. doi:10.1130/G20118.1.

Valcke, Sophie, A Caubel, R Vogelsang and D Declat. OASIS3 User's Guide 5th Edition. Technical Report TR/CMGC/03/69, CERFACS, **2004**. `http://www.prism.enes.org/Publications/Reports/Report02.pdf`.

Valdes, Paul, **2011**. Built for stability. *Nature Geosci*, 4(7):414–416. ISSN 1752-0894. doi:10.1038/ngeo1200.

van de Berg, W J, M R van den Broeke, C H Reijmer and E van Meijgaard, **2006**. Reassessment of the Antarctic surface mass balance using calibrated output of a regional atmospheric climate model. *J. Geophys. Res.*, 111:—-. doi:10.1029/2005JD006495.

Van Pelt, Ward J J and J **Oerlemans**, **2012**. Numerical simulations of cyclic behaviour in the Parallel Ice Sheet Model (PISM). *Journal of Glaciology*, 58 (208):347–360. doi:10.3189/2012JoG11J217.

Vidal, L, L Labeyrie, E Cortijo, M Arnold, J C Duplessy, E Michel, S Becqué and T C E van Weering, **1997**. Evidence for changes in the North Atlantic Deep Water linked to meltwater surges during the Heinrich events. *Earth and Planetary Science Letters*, 146(1–2):13–27. ISSN 0012-821X. `http://www.sciencedirect.com/science/article/pii/S0012821X96001926`.

Vidal, L, R R Schneider, O Marchal, T Bickert, T F Stocker and G Wefer, **1999**. Link between the North and South Atlantic during the Heinrich events of the last glacial period. *Climate Dynamics*, 15(12):909–919 LA – English. ISSN 0930-7575.

doi:10.1007/s003820050321.

Vizcaíno, Miren, Uwe Mikolajewicz, Matthias Gröger, Ernst Maier-Reimer, Guy Schurgers and Arne Winguth, **2008**. Long-term ice sheet–climate interactions under anthropogenic greenhouse forcing simulated with a complex Earth System Model. *Climate Dynamics*, 31(6):665–690. doi:10.1007/s00382-008-0369-7.

Vizcaíno, Miren, Uwe Mikolajewicz, Johann Jungclaus and Guy Schurgers, **2010**. Climate modification by future ice sheet changes and consequences for ice sheet mass balance. *Climate Dynamics*, 34(2):301–324. ISSN 0930-7575. doi:10.1007/s00382-009-0591-y.

Waelbroeck, C, L Labeyrie, E Michel, J C Duplessy, J F McManus, K Lambeck, E Balbon and M Labracherie, **2002**. Sea-level and deep water temperature changes derived from benthic foraminifera isotopic records. *Quaternary Science Reviews*, 21(1–3):295–305. ISSN 0277-3791. `http://www.sciencedirect.com/science/article/pii/S0277379101001019`.

Wang, Zhaomin and Lawrence A **Mysak**, **2002**. Simulation of the last glacial inception and rapid ice sheet growth in the McGill Paleoclimate Model. *Geophys. Res. Lett.*, 29(23):2102. ISSN 0094-8276. doi:10.1029/2002GL015120.

Wang, Zhaomin and Lawrence A **Mysak**, **2006**. Glacial abrupt climate changes and Dansgaard-Oeschger oscillations in a coupled climate model. *Paleoceanography*, 21:—-. doi:10.1029/2005PA001238.

Warren, Stephen G and Warren J **Wiscombe**, **1980**. A Model for the Spectral Albedo of Snow. II: Snow Containing Atmospheric Aerosols. *Journal of the Atmospheric Sciences*, 37(12):2734–2745. ISSN 0022-4928. doi:10.1175/1520-0469(1980)037¡2734:AMFTSA¿2.0.CO;2.

Weaver, Andrew J, E S Sarachik and Jochem Marotze, **1991**. Freshwater flux forcing of decadal and interdecadal oceanic variability. *Nature*, 353(6347):836–838. `http://dx.doi.org/10.1038/353836a0`.

Weaver, Andrew J, Jan Sedláček, Michael Eby, Kaitlin Alexander, Elisabeth Crespin, Thierry Fichefet, Gwenaëlle Philippon-Berthier, Fortunat Joos, Michio Kawamiya, Katsumi Matsumoto, Marco Steinacher, Kaoru Tachiiri, Kathy Tokos, Masakazu Yoshimori and Kirsten Zickfeld, **2012**. Stability of the Atlantic meridional overturning circulation: A model intercomparison. *Geophys. Res. Lett.*, 39(20):L20709. ISSN 0094-8276. doi:10.1029/2012GL053763.

Weber, S L, S S Drijfhout, Ayako Abe-ouchi, M Crucifix, M Eby, Andrey Ganopolski, S Murakami, Bette L. Otto-Bliesner and W R Peltier, **2007**. The modern and glacial overturning circulation in the Atlantic ocean in PMIP coupled model simulations. *Climate of the Past*, 3(1):51–64. doi:10.5194/cp-3-51-2007.

Weertman, J, **1974**. Stability of the junction of an ice sheet and an ice shelf. *Journal Of Glaciology*, 13(67):3–11. `http://stuff.mit.edu/$\sim$heimbach/papers_glaciology/jglaciol_weertman_1974.pdf`.

Wilken, Manon and Juergen **Mienert**, **2006**. Submarine glacigenic debris flows, deep-sea channels and past ice-stream behaviour of the East Greenland continental margin. *Quaternary Science Reviews*, 25(7–8):784–810. ISSN 0277-3791. doi:10.1016/j.quascirev.2005.06.004.

Winkelmann, R, M A Martin, M Haseloff, T Albrecht, E Bueler, C Khroulev and A Levermann, **2011**. The Potsdam Parallel Ice Sheet Model (PISM-PIK) Part 1: Model description. *The Cryosphere*, 5:715–726. doi:10.5194/tc-5-715-2011.

Zhang, Sheng, Richard J Greatbatch and Charles A Lin, **1993**. A Reexamination of the polar Halocline Catastrophe and Implications for Coupled Ocean-Atmosphere Modeling. *Journal of Physical Oceanography*, 23(2):287–299. ISSN 0022-3670.

doi:10.1175/1520-0485(1993)023¡0287:AROTPH¿2.0.CO;2.

Zhang, X., G. Lohmann, G. Knorr and X. Xu, **2012**. Two ocean states during the Last Glacial Maximum. *Climate of the Past Discussions*, 8(4):3015–3041. ISSN 1814-9359. doi:10.5194/cpd-8-3015-2012.



ISSN 1614-1199